Energy Absorption of Macrocomposite Laminates

Ahmadnia, Ali

Energy Absorption of Macrocomposite Laminates

By

Ali Ahmadnia

This thesis is submitted for the degree of Doctor of Philosophy

in the Faculty of Engineering at the University of London

Department of Materials
Queen Mary and Westfield College
University of London

March 2000

Acknowledgements

I would like to express my thanks to my supervisor, Professor P. J. Hogg for his comments, suggestions and encouragement, freely offered during the course of this work.

Thanks also to Dr. Ata Yoosefinejad, Dr. Guogang Ren, Mr. Robert Neumann and Mr. Silvano Cauchi-Savona for their occasional advice and help, which is greatly appreciated.

Thanks also to Mrs Sandra Wells, Mrs Yvonne Johnson, Miss Catherine Pedley, all members of the lecturing staff, technicians and fellow students in the Materials Department who helped at one time or another with this work.

I am indebted to the Department of Metallurgy and Materials science at Cambridge University for allowing me to use their Mechanical testing facilities.

Thanks also to Scott Bader who provided the materials for this work.

Finally, I would like to thank my wife Farangis and my two sons Ehsan and Amin for their unfailing support and encouragement.

Dedicated To my wife and two sons

Farangis, Ehsan and Amin

Abstract

The aim of this project was two-fold. Firstly to provide an understanding of the behaviour of SMC when subjected to drop weight impact and secondly to investigate the effect of a surface layer of a metallic material (stainless steel, aluminium, brass and copper) and a layer of Ionomer on the impact behaviour of SMC.

Tensile, flexural, compression, shear, charpy and drop weight impact tests were carried out on SMC (Sheet Moulding Compound). The response of SMC and various combinations of SMC and metal sheet (stainless steel, aluminium, brass and copper) and SMC with a layer of Ionomer to impact load have been assessed using an Instrumented Falling Weight Impact test machine. Slow indentation tests and a variety of destructive and non-destructive test techniques were used to monitor the initiation and propagation of damage and relate them to the major features of typical force-time curves obtained during impact. The deformation of the metallic layer was compared under impact and slow test and a calibration curve was produced. By using the calibration curve the energy absorbed by SMC and SMC as a layer in SMC+metal laminate was compared and results were related to stiffness and ductility of the metallic layer. The energy absorbed by the SMC-metal laminates were analysed and the energy absorbed by each constituents was determined. The effect of impact damage on tensile and compressive residual strength was assessed by conducting tension and compression test on the damaged specimens. Finally, a number of simple models and finite element technique were used to predict the impact response of SMC and SMC-metal laminates to impact.

The results of the research programme indicated a strong macrocomposite effect resulting in greatly improved energy absorbing capabilities for SMC. The indications were that a metal layer was required that would be stiff, thereby putting the SMC into compression and also ductile in order to support extensive deformation in the SMC whereby microcracking could accumulate.

Contents

List of Figures vii

List of Tables xx

Chapter 1 Introduction 1

Chapter 2 Literature review 5

2.1 Introduction 5

2.2 Impact Test Methods 5

2.3 Charpy and Izod Test 6

2.4 Drop Weight Test 8

2.5 Tensile Impact Test 12

2.6 Additional Impact Tests 14

2.6.1 Split Hopkinson Pressure bar 14

2.7 Instrumented Impact test 16

2.7.1 Load cell calibration 18

2.7.2 Dynamic signal control 19

2.7.3 Data Reduction and Evaluation 21

2.8 Determination of Data Collection Parameters 22

2.9 Instrumented Dart Impact 24

2.10 Energy Absorbed During Impact Testing 24

2.11 Energy absorbing mechanism in fibre-reinforced composites 26

2.11.1 Fibre 27

2.11.2 Matrix 27

2.11.3 Interphase 28

2.11.4 Fibre Stacking Sequence 29

2.11.5 Geometry 29

2.12 Analysis of Impact Stresses in Composite Materials..... 31

2.12.1 Introduction..... 31

2.12.2 The Hertz model..... 32

2.12.3 General case of impact between two nonisotropic bodies..... 36

2.12.4 Impact response of a flexible target..... 39

2.12.5 Mathematical models which model the composite media as a periodic material..... 39

2.12.6 Theory of bending of plates..... 39

2.12.7 Finite Element Analysis..... 40

2.13 Evaluation of Damage in composite material..... 41

2.13.1 Introduction..... 41

2.13.2 Non-destructive Test Techniques (NDT)..... 41

2.13.3 Ultrasonic Testing..... 43

2.13.4 Residual tensile and compressive strength measurement..... 45

2.13.5 Prediction of Residual Strength of composites after impact..... 51

2.14 Sheet Moulding Compound (SMC)..... 54

2.14.1 Manufacture Of SMC..... 57

2.14.2 Mechanical Properties of SMC..... 58

Chapter 3 Experimental Procedure and Mechanical Characterisation of SMC and SMC with a layer of Stainless Steel..... 59

3.1 Manufacture of Test Materials and Specimens..... 59

3.1.1 Tensile Test..... 61

3.1.2 Flexure test..... 63

3.1.3 Compression test..... 64

3.1.4 Shear test..... 66

3.1.5 Short Beam Shear Test..... 70

3.1.6 Charpy Impact..... 70

3.1.7 Lap Shear Test..... 72

3.2 Mechanical Properties of Stainless Steel lined - SMC Composites..... 73

3.2.1 Tensile Test..... 73

3.2.2 Flexural Test..... 74

3.3 Impact Testing..... 76

3.3.1 The CEAST Drop Weight Test..... 78

3.3.2 Calibration Of The CEAST Load Cell..... 87

3.3.3 The Low Energy Impact Test Rig..... 91

3.3.4 The Cambridge Impact Test Rig..... 91

3.4 Slow Indentation Tests..... 96

3.5 Residual Tensile and Compressive Strength of Damaged Composites after Impact..... 96

3.6 Damage Detection and Assessment..... 102

3.6.1 Dye Penetrating Technique..... 102

3.6.2 Optical Microscopy..... 102

3.6.3 Scanning Electron Microscope (SEM)..... 103

3.6.4 Ultrasonic C-scan..... 103

Chapter 4 Response of SMC to Low energy impact, high energy impact and Slow test..... 107

4.1 Introduction..... 107

4.2 Response of SMC to Low energy impact..... 107

4.3 Response of SMC to High Energy Impact..... 120

4.4 The effect of thickness and Incident energy on Peak force, Transition load and Absorbed energy..... 121

4.5 Response of SMC to different impact velocities at a constant incident energy 126

4.6 Response of SMC to Slow Indentation Test..... 126

4.7 Prediction of the load-deflection of SMC specimens by the Energy Balance method, Theory of Bending and Finite Element Analysis..... 130

4.7.1 Introduction..... 130

4.7.2 The Energy Balance Method..... 130

4.7.3 Theory of Bending of Plates..... 136

4.7.4 Finite Element Stress Analysis..... 138

4.8 Damage Detection Techniques..... 142

4.8.1 Dye penetrating Technique..... 142

4.8.2 Optical Microscopy..... 143

4.9 Discussion..... 144

4.10 Conclusions..... 157

Chapter 5 Response of SMC with a layer of Stainless steel (SMC+S.S.) to Low energy impact, High energy impact and Slow test. 158

5 Introduction..... 158

5.1 Response of SMC+S.S. to low energy impact..... 158

5.2 Response of SMC+S.S. to High energy impact..... 164

5.3 Determination of the energy absorbed by the layer of stainless steel (s.s.) and SMC in the SMC+S.S. laminate..... 170

5.4 Determination of the energy absorbed by the layer of stainless steel..... 172

5.5 Determination of the energy absorbed by the layer of SMC in the SMC+S.S. specimens..... 180

5.6 The effect of test variables on the amount of energy absorbed by the layer of SMC in the SMC + Stainless steel laminates..... 183

5.6.1 The effect of impact velocity..... 183

5.6.2 The effect of specimen thickness..... 185

5.6.3 The effect of bonding between the layer of SMC and S.S..... 189
5.7 Response of SMC+Stainless steel laminate to slow indentation test..... 191
5.8 Damage detection techniques..... 193
5.9 Analysis of stresses in the SMC + Stainless steel laminate..... 194
5.10 Discussion..... 196
5.11 Conclusions..... 204

Chapter 6 Response of SMC with a layer of Aluminium, SMC with a layer of Ionomer, SMC with a layer of Copper and SMC with a layer of Brass to drop weight impact..... 205

6.1 Response of SMC+Aluminium (grade S1C) to drop weight impact..... 206
6.2 Determination of the energy absorbed by the layer of SMC in the SMC - Aluminium (S1C) specimens..... 207
6.3 Response of SMC+Aluminium (grade L156) to drop weight impact..... 215
6.4 Response of SMC + Ionomer to drop weight impact..... 217
6.5 Response of SMC+Copper to drop weight impact..... 219
6.6 Response of SMC+Brass to drop weight impact..... 221
6.7 Discussion..... 222
6.8 Conclusions..... 230

Chapter 7 Residual tensile and compressive strength of SMC and SMC-Stainless steel laminates after impact..... 231

7.1 Residual tensile strength of SMC after impact..... 231
7.2 Residual tensile strength of SMC+Stainless steel after impact..... 240
7.3 Residual compressive strength of SMC after impact..... 244
7.3.1 Details of compression test..... 244

7.3.2 Results..... 247

7.4 Residual compressive strength of SMC+Stainless steel after impact..... 251

7.5 Discussion..... 256

7.6 Conclusions..... 263

Chapter 8 Summary of the results and conclusions..... 264

8.1 Summary of results..... 264

8.2 Conclusions..... 265

8.3 Future work..... 267

References..... 269

List of Figures

Chapter 2

Figure 2.1 Sketch showing method of loading in charpy and I zod impact tests.. 8

Figure 2.2 Effect of section thickness on transition temperature curves..... 10

Figure 2.3 Tensile impact apparatus : ASTM D1822..... 13

Figure 2.4 Typical configuration of the Hopkinson bar..... 15

Figure 2.5 Typical load-time curves for a) Brittle fracture, b) Brittle / ductile fracture, c) Ductile fracture, d) Repeated fracture (reinforced materials)..... 17

Figure 2.6 The output from three sets of gauges at different positions on an Izod pendulum -after experiments by Server and Ireland..... 19

Figure 2.7 Schematic diagram showing the relationship between specimen, tup, and anvil reactions during Izod impact - after Ireland..... 20

Figure 2.8 Schematic example of impact exhibiting a high inertial load. The initial sharp spike is caused by load required to accelerate the specimen to tup velocity..... 21

Figure 2.9 Examples of incorrect data collection parameters. The load range and test time are insufficient..... 23

Figure 2.10 Location of maximum tensile, compressive and shear stresses are under surface loading..... 35

Figure 2.11 Exploded view of DFVLR anti - Buckling device..... 47

Figure 2.12 Exploded view of ONERA anti - Buckling guide..... 48

Figure 2.13 Assembled view of RAE anti - Buckling guide..... 49

Figure 2.14 NLR anti - Buckling guide..... 50

Figure 2.15 SMC type designates reinforcement configuration used..... 56

Figure 2.16 Combination of fibre configurations..... 56

Figure 2.17 Manufacture of SMC..... 57

Chapter 3

Figure 3.1 The typical dimension of a tensile test specimen..... 62

Figure 3.2 The typical Stress-strain curve for SMC from tensile test experiment. 62

Figure 3.3 Flexural test loading diagram..... 63

Figure 3.4 A typical load-deflection curve for SMC from the three point bend test experiment..... 64

Figure 3.5 IITRI compression specimen and fixture..... 65

Figure 3.6 The typical Stress-strain curve for SMC from compression test experiment..... 66

Figure 3.7 Specimen and apparatus used for two rail shear test..... 67

Figure 3.8 A typical shear stress-shear strain curve for SMC from two rail shear test experiment..... 68

Figure 3.9 Typical failure of two rail shear specimen..... 69

Figure 3.10 Charpy impact test specimen..... 71

Figure 3.11 Typical force-time curve for 4 mm SMC - R30 obtained from charpy test..... 71

Figure 3.12 shear strength specimen..... 72

Figure 3.13 Tensile curves for 4 mm SMC, 0.6 mm stainless steel and 4 mm SMC with a layer of 0.6 mm stainless steel..... 73

Figure 3.14 Flexural curves for SMC and SMC with a layer of stainless steel.... 75

Figure 3.15 Impact test geometry used for all impact test programme..... 77

Figure 3.16 CEAST drop weight impact machine..... 79

Figure 3.17 Schematic drawing of the Instrumented striker..... 80

Figure 3.18 Drop weight test support with an adjustable ' V ' plate..... 80

Figure 3.19 Block diagram of the CEAST data processing software..... 81

Figure 3.20 Method of integration of the force-time by dividing the curve into strips..... 83

Figure 3.21 Method of integration of the force-time by dividing the curve into strips..... 84

Figure 3.22 Typical F-t, V-t, and F-x curves for non- penetrating impact obtained using CEAST, a) force-time, b) energy-time, c) velocity-time, d) displacement-time, e) force-displacement..... 86

Figure 3.23 AFS MK3 fractoscope..... 88

Figure 3.24 The load measuring ring used for calibration of CEAST load cell... 89

Figure 3.25 QMW low energy impact machine..... 92

Figure 3.26 Cambridge test rig..... 93

Figure 3.27 Support used for Cambridge impact machine..... 93

Figure 3.28 Striker designed and used with the Cambridge test rig..... 94

Figure 3.29 Typical force-time curves obtained using Cambridge test rig, a) 1m/s, b) 5m/s..... 95

Figure 3.30a Slow indentation test rig..... 98

Figure 3.30b Indenter, Support, and transducer used in slow test..... 99

Figure 3.31 Schenk TREBEL machine with compression cage used for compression test..... 100

Figure 3.32 Anti buckling frame used in the present work..... 101

Figure 3.33 Physical Acoustics Corporation C scan machine..... 105

Figure 3.34 Aluminium calibration block..... 105

Figure 3.35 Calibration file..... 106

Chapter 4

Figure 4.1 Typical force-time curve for non-penetrating impact a) 4 mm SMC, b) 8 mm SMC..... 109

Figure 4.2 Position of the point of maximum energy on the force-time and displacement curves..... 110

Figure 4.3 Shows that the velocity of the striker is not zero at maximum force.. 111

Figure 4.4 Typical force-deflection for non-penetrating impact for 4 mm SMC.. 112

Figure 4.5 Force-time curves for SMC, thickness 4 mm, for impact at 1, 1.5 and 2 m/s..... 113

Figure 4.6 SMC, thickness 4 mm, after impact at a) 1m/s (9J), b) 1.5 m/s (21J), c) 2 m/s (38J)..... 113

Figure 4.7 Force-deflection curves for SMC, thickness 4 mm, for impact at 1, 1.5 and 2 m/s..... 115

Figure 4.8 Variation of transition energy with incident energy for different thicknesses of SMC. Error bars denote standard deviation..... 115

Figure 4.9 Force-time curve and photograph of specimen for 4 mm SMC when subjected to 0.5 J incident energy..... 116

Figure 4.10 Force-time curve and photograph of damaged specimen for 4 mm SMC when subjected to 1.1 J incident energy..... 117

Figure 4.11 Force-time curve and photograph of damaged specimen for 4 mm SMC when subjected to 1.99 J incident energy..... 118

Figure 4.12 Force-time curve and photograph of damaged specimen for 4 mm SMC when subjected to 9 J incident energy..... 119

Figure 4.13 Force-time curve for SMC, thickness 4 mm, after complete penetration. 122

Figure 4.14 Energy-time curve for SMC, thickness 4 mm, after complete penetration 122

Figure 4.15 Force-deflection curve for SMC, thickness 4 mm, after complete penetration, a) CEAST, b) Cambridge..... 123

Figure 4.16 SMC specimen after complete penetration..... 124

Figure 4.17 Peak force versus incident energy for three different thicknesses of SMC. Error bars denote standard deviation..... 124

Figure 4.18 Peak force when complete penetration takes place as a function of $(\text{thickness})^2$. Error bars denote standard deviation..... 125

Figure 4.19 The variation of transition load as a function of $(\text{thickness})^2$. Error bars denote standard deviation..... 125

Figure 4.20 Absorbed energy versus incident energy for three different thicknesses of SMC..... 127

Figure 4.21 Maximum energy absorbed by SMC specimens as a function of thickness. Error bars denote standard deviation..... 127

Figure 4.22 Force deflection curve for three SMC specimens of common thickness impacted at constant energy but differing velocities..... 128

Figure 4.23 Comparison of the load-displacement curves from a slow indentation test and an impact test for 4 mm SMC..... 129

Figure 4.24 Profile of deflection during slow test for 4 mm SMC specimen..... 129

Figure 4.25 Local and overall deformation of flexible target..... 132

Figure 4.26 Comparison between the load-deflection of the finite element model, energy balance method..... 135

Figure 4.27 Comparison between peak force-incident energy curve of energy balance method and experiment..... 135

Figure 4.28 Uniformly loaded plate over a very small central circular area..... 137

Figure 4.29 Finite element model..... 139

Figure 4.30 The node order and the element order of the finite element model.. 139

Figure 4.31 Distribution of the contact pressure..... 140

Figure 4.32 Contours of stress in 4 mm SMC shows areas of high stresses during impact..... 141

Figure 4.33 Deformed mesh which has been superimposed upon the undeformed mesh..... 141

Figure 4.34 Comparison between the deflection at the back of specimen of slow test and finite element result..... 142

Figure 4.35 Cracks on the periphery of the area of contact of the striker with 4 mm SMC which has been highlighted by dye penetrating method.. 143

Figure 4.36 Micrograph of 4 mm SMC which has been subjected to impact.... 144

Figure 4.37 Optical micrograph of a polished section showing the microstructure of SMC (X 400)..... 147

Figure 4.38 Impact damage on SMC in the form of indentation on the impacted side 149

Figure 4.39 Cracks which are formed during impact on the tensile and compressive sides of the SMC specimens..... 150

Figure 4.40 Scanning electron micrographs of damaged surface of SMC which has been subjected to drop weight impact shows the debonding between the fibre and the matrix..... 151

Figure 4.41 Force-time curves for a 4 mm SMC specimen which has been subjected to a series of low energy impacts, a) first blow b) 5^{th} blow..... 152

Figure 4.42 Force-time curve for 4 mm SMC subjected to a series of blows..... 153

Figure 4.43 Relationship between energy absorbed during through penetration versus thickness multiplied by fibre volume fraction for glass fibre composites. Legend: A - random and woven fibre thermoset resin. B - Random fibre thermoplastic GMT. C - SMC (After Babic et al [135])..... 154

Chapter 5

Figure 5.1 Typical force time curves for SMC stainless steel laminates after non penetrating impact..... 159

Figure 5.2 Typical energy time curve for SMC stainless steel laminates after non penetrating impact..... 159

Figure 5.3 Position of the point maximum energy on the force time and force deflection curves a) energy time b) force time c) deflection-time..... 160

Figure 5.4 Typical force deflection curve for SMC stainless steel laminate after non penetrating impact (low energy impact)..... 161

Figure 5.5 Force time curves for 4 mm SMC with a layer of 0.6 mm thick stainless steel at 1 ms^{-1}, 1.5 ms^{-1} and 2 ms^{-1} after non penetrating impact..... 162

Figure 5.6 The steel surface in SMC stainless steel laminates after non penetrating impact , indicating the dome height..... 163

Figure 5.7 The surface of SMC in SMC stainless steel laminates after non penetrating impact , showing limited microcracking..... 163

Figure 5.8 Force deflection curves for 4 mm SMC with a layer of 0.6 mm stainless steel at 1 ms^{-1} , 1.5 ms^{-1} and 2 ms^{-1} after non penetrating impact..... 164

Figure 5.9 The clamping technique used for clamping the impact specimens.... 165

Figure 5.10 Typical force time curves for SMC stainless steel laminates after complete penetration a) 1 ms^{-1} b) 5 ms^{-1}..... 167

Figure 5.11 Typical force time curves for 0.6 , 1 and 2 mm stainless steel after complete penetration and perforated specimens , top) 0.6 mm ,middle) 1 mm and bottom 2 mm..... 168

Figure 5.12 Relation between maximum load generated during perforation impact as a function of thickness for stainless steel sheet..... 169

Figure 5.13 Maximum energy absorbed by the layer of stainless steel after complete penetration as a function of thickness..... 169

Figure 5.14 Force time curves for 2 , 4 and 6 SMC mm with a layer of 0.6 mm stainless steel with perforated specimens , top) 2 mm , middle) 4 mm and bottom 6 mm..... 171

Figure 5.15 Energy absorbed by 0.6 mm stainless steel sheet vs deflection during impact test and slow test..... 172

Figure 5.16 The profile of deflection of stainless steel sheet on its own during impact and slow test and when it is a component part of SMC+S.S..... 173

Figure 5.17 Force deflection curve for stainless steel sheet used to construct the calibration curve..... 175

Figure 5.18 Energy absorbed by 0.6 mm thick stainless steel sheet as a function of permanent deflection..... 176

Figure 5.19 Energy absorbed by 1 mm thick stainless steel as a function of permanent deflection..... 176

Figure 5.20 Energy absorbed by 2 mm thick stainless steel sheet as a function of permanent deflection..... 177

Figure 5.21 Force deflection curve for SMC+stainless steel laminate after complete penetration by impact..... 179

Figure 5.22 Energy absorbed as a function of incident energy for SMC , steel-SMC macrocomposites and the SMC layer in the macrocomposite (SMC')..182

Figure 5.23 Energy absorbed as a function of incident energy for SMC , steel-SMC macrocomposites and the SMC layer in the macrocomposite (SMC')..182

Figure 5.24 Force deflection curve for 4 mm SMC with a layer of 0.6 mm thick stainless steel after complete penetration at 1 ms^{-1}..... 184

Figure 5.25 Force deflection curve for 4 mm SMC with a layer of 0.6 mm thick stainless steel after complete penetration at 5 ms^{-1}..... 184

Figure 5.26 Comparison of typical force deflection curves for 4 mm SMC with a layer of 0.6 mm stainless steel after complete penetration at 1 ms^{-1} and 5 ms^{-1}. 185

Figure 5.27 Typical force deflection curves for 6 mm SMC with a layer of 0.6 mm stainless steel after complete penetration..... 186

Figure 5.28 Maximum energy absorbed by the laminate for different thicknesses of SMC as a function of stainless steel thickness..... 187

Figure 5.29 Force deflection curves for non penetrating impact for 2 and 4 mm SMC with a layer of 0.6 mm stainless steel at 9 joule incident energy..... 188

Figure 5.30 Energy absorbed by SMC stainless steel laminates as a function of incident energy for 2 , 4 and 6 mm SMC with a layer of 0.6 mm stainless steel..188

Figure 5.31 Force deflection curves for 4 mm SMC with a layer of 0.6 mm stainless steel , 1) supplied material , 2) lubricated , 3) non lubricated , 4) glued... 190

Figure 5.32 Force deflection curves for impact test and slow test..... 192

Figure 5.33 Profile of deflection before and after applying load during slow test... 192

Figure 5.34 Profile of deflection at transition load..... 192

Figure 5.35 Photograph of cross section through specimen for SMC stainless steel laminate after non penetrating impact..... 193

Figure 5.36 Finite element model..... 194

Figure 5.37 contour of shear stress for 4 mm SMC with a layer of 0.6 mm stainless steel..... 195

Figure 5.38 Relationship between energy absorbed during through penetration versus thickness multiplied by fibre volume fraction for glass fibre composites. Legend: A - random and woven fibre thermoset resin. B - Random fibre thermoplastic GMT. C - SMC (After Babic et al [110])..... 196

Figure 5.39 Contours of shear stress and photographs of cross section for 4 mm SMC and 4 mm SMC with a layer of 0.6 mm stainless steel , top) SMC and bottom smc+steel..... 198

Figure 5.40 contour of principal stress for 4 mm SMC with a layer of 0.6 mm stainless steel..... 199

Figure 5.41 contour of principal stress for 4 mm SMC..... 200

Figure 5.42 Maximum energy absorbed as a function of thickness for SMC and SMC as a layer in macrocomposite (SMC') for all thicknesses of steel tested from 0.6 mm to 2 mm..... 202

Figure 5.43 Contour of stress for 6 mm SMC with a layer of 0.6 mm stainless steel 203

Chapter 6

Figure 6.1 Typical non-penetrating impact force-time and energy time curves for 4 mm SMC-Aluminium (grade 5L16) at 1 ms^{-1} a) force-time b) energy-time..... 208

Figure 6.2 Typical complete penetration force-time and energy time curves for 4 mm SMC-Aluminium (grade 5L16) at 4 ms^{-1} a) force-time b) energy-time 209

Figure 6.3 Force-deflection curves for SMC-aluminium (grade 5L16) at 1 ms^{-1} and 3 ms^{-1}..... 210

Figure 6.4 Relation between maximum force generated during impact as a function of impact velocity for 6.6 mm SMC-aluminium (grade 5L16). Error bar denotes standard deviation..... 210

Figure 6.5 Force deflection curve for aluminium sheet (grade 5L16) used to construct the calibration curve..... 211

Figure 6.6 Energy absorbed by 0.6 mm Aluminium sheet as a function of permanent deflection..... 212

Figure 6.7 Force deflection curve for 0.6 mm thick Aluminium (grade 5L16) after complete penetration..... 213

Figure 6.8 The amount of energy absorbed as a function of incident energy for 2 mm SMC in SMC+Aluminium (grade 5L16) and 2 mm SMC specimen... 214

Figure 6.9 Energy absorbed as a function of incident energy for 4 mm SMC in SMC+Aluminium (grade 5L16) and 4 mm SMC..... 214

Figure 6.10 Energy absorbed as a function of incident energy for 6 mm SMC in SMC+Aluminium (grade 5L16) and 6 mm SMC specimen..... 215

Figure 6.11 Energy absorbed by 0.6 mm Aluminium sheet (grade L156) as a function of permanent deflection..... 216

Figure 6.12 Force deflection curve for o.6 mm thick Aluminium (grade L156) after complete penetration..... 216

Figure 6.13 Absorbed energy vs impact energy for SMC in a range of alternative macrocomposite systems based on 4 mm thick SMC..... 217

Figure 6.14 Energy absorbed by 4 mm thick Ionomer as a function of permanent deflection..... 218

Figure 6.15 Force deflection curve for 4 mm Ionomer after complete penetration by impact..... 219

Figure 6.16 Energy absorbed by 0.75 mm copper sheet as a function of permanent deflection..... 220

Figure 6.17 Force deflection curve for 0.75 mm thick copper after complete penetration..... 220

Figure 6.18 Energy absorbed by 0.75 mm thick brass sheet as a function of permanent deflection..... 221

Figure 6.19 Force deflection curve for 0.75 mm thick brass after complete penetration..... 222

Figure 6.20 Contour of principal stress for 2 mm SMC with a layer of 0.6 mm aluminium..... 224

Figure 6.21 Contour of principal stress for 4 mm SMC with a layer of 0.6 mm aluminium..... 225

Figure 6.22 Force deflection curve for 4 mm SMC-aluminium (grade 5L16) after complete penetration..... 227

Figure 6.23 Force deflection curve for 4 mm SMC-aluminium (grade L156) after complete penetration..... 227

Figure 6.24 Force deflection curve for 4 mm SMC after complete penetration..... 228

Figure 6.25 Maximum energy absorbed as a function of thickness for SMC as a layer in macrocomposite (SMC') for all thicknesses of steel tested and aluminium, Ionomer, brass and copper..... 229

Chapter 7

Figure 7.1 Geometry and dimensions of the specimens used for measuring the tensile residual strength after impact a) without hole, b) with a 20 mm diameter hole..... 232

Figure 7.2 Residual tensile strength σ_R / σ_0 against incident energy for 2 mm SMC. 233

Figure 7.3 Residual tensile strength σ_R / σ_0 against incident energy for 4 mm SMC. 234

Figure 7.4 Residual tensile strength σ_R / σ_0 against incident energy for 6 mm SMC. 234

Figure 7.5 Residual tensile strength σ_R / σ_0 for 6 mm SMC (log scale)..... 235

Figure 7.6 Comparison of predicted and experimental residual tensile strength for 4 mm SMC.....238

Figure 7.7 Comparison of predicted and experimental residual tensile strength for 6 mm SMC..... 238

Figure 7.8 Typical fracture of residual tensile specimens at two different incident energies a)38J, b)78J..... 239

Figure 7.9 Typical fracture of tensile specimen with a 20 mm diameter drilled hole. 240

Figure 7.10 Residual tensile strength σ_R / σ_0 against incident energy for 4 mm SMCwith a layer of 0.6 mm stainless steel..... 241

Figure 7.11 Comparison of the residual tensile strength against incident energy for 4 mm SMC with a layer of 0.6 mm stainless steel..... 242

Figure 7.12 Typical tensile failure of SMC in SMC+stainless steel laminates..... 243

Figure 7.13 Photograph of the QMW post impact compression support. 245

Figure 7.14 Schematic representation of C-scan tank..... 245

Figure 7.15 Ultrasonic C-scan of SMC specimens after impact..... 246

Figure 7.16 Damage width as a function of incident energy..... 247

Figure 7.17 Damage area as a function of incident energy..... 248

Figure 7.18 Compression strength after impact as a function of incident energy..... 249

Figure 7.19 Compression strength after impact as a function of damage width.. 249

Figure 7.20 Typical fracture of residual compressive specimens after impact for 4 mm SMC..... 250

Figure 7.21 Typical fracture of compressive specimen with a 20 mm diameter drilled hole..... 250

Figure 7.22 Ultrasonic C-scan of SMC' specimens after impact..... 252

Figure 7.23 Damage width as a function of incident energy for 4 mm SMC with a layer of 0.6 mm stainless steel..... 253

Figure 7.24 Damage area as a function of incident energy for 4 mm SMC with a layer of 0.6 mm stainless steel..... 253

Figure 7.25 Compression strength after impact as a function of incident energy for 4 mm SMC with a layer of 0.6 mm stainless steel..... 254

Figure 7.26 Compression strength after impact as a function of damage width for 4 mm SMC with a layer of 0.6 mm stainless steel..... 254

Figure 7.27 Typical fracture of residual compressive specimens after impact for 4 mm SMC in SMC with a layer of 0.6 mm stainless steel..... 255

Figure 7.28 Compression and tensile strength after impact as a function of incident energy for 4 mm SMC..... 256

Figure 7.29 Schematic diagram of Compression strength after impact as a function of incident energy..... 258

Figure 7.30 Photographs of 2 mm SMC after complete penetration for two level of incident energies a) 21 J, b) 154..... 259

Figure 7.31 Compression strength after impact as a function of damage width for 4 mm SMC and 4 mm SMC with a layer of 0.6 mm stainless steel (SMC')... 260

Figure 7.32 Comparison of predicted and experimental residual compressive strength for 4 mm SMC..... 262

Figure 7.33 Comparison of predicted and experimental residual compressive strength for 4 mm SMC..... 262

List of Tables

Table 2.1 Common test standards adapted for composites..... 11

Table 2.2 Summery of drop weight impact tests courtesy of Wyrick et al (22)..... 12

Table 2.3 Data on traditional impacting test methods..... 14

Table 2.4 Typical values of the energy absorbing capability of various continuous fibre composites for different failure modes courtesy of Cantwell et al (42).... 26

Table 2.5 Ranking of the impact tests according to their analytical usefulness.... 31

Table 2.6 Values of parameters n, r, and s..... 37

Table 2.7 Inorganic radio-opaque penetrants. 42

Table 2.8 Typical mechanical properties of SMC-R50 at room temperature courtesy of Denton (8)..... 58

Table 3.1 Typical properties of Stainless Steel type 304..... 60

Table 3.2 Typical Composition and Properties of Aluminium..... 61

Table 3.3 Tensile properties of SMC-R30..... 63

Table 3.4 Flexural properties of SMC-R30..... 64

Table 3.5 Compression properties of SMC-R30..... 66

Table 3.6 Shear properties in the two rail shear test for SMC-R30..... 70

Table 3.7 Results of Shear strength measured by short beam shear test..... 70

Table 3.8 Charpy impact properties for SMC-R30..... 72

Table 3.9 Tensile properties of SMC, stainless steel and 4 mm SMC with a layer of 0.6 mm stainless steel. Standard deviations in parenthesis..... 74

Table 3.10 Flexural properties of SMC and SMC with a layer of 0.6 mm stainless steel. Standard deviations in parenthesis..... 75

Table 5.1 Deflection at the tensile surface of the 0.6 mm stainless steel sheet in relation with the movement of the plunger..... 174

Chapter 1

Introduction

In the selection of a material for a particular application the possible solution lies between an isotropic material, such as a metal, or a fibre reinforced material. There are many cases where neither material alone offers the optimum solution to the problem. When high specific strength, lightweight and chemical corrosion resistance are necessary, fibre reinforced plastics (FRP)are often preferred. The choice is not always risk free because the fibre reinforced system is more complex, less well understood and there is a belief that performance is more difficult to predict. The consequence is that large safety factors are used to compensate for the projected deterioration of physical and mechanical properties over the life span of the component. By combining a metal skin on the surface of an FRP, the system is able to benefit from the load bearing characteristics of the metal skin and the weight saving resulting from the using the FRP. In this type of composite material, the plastic would not experience environmental ingress and degradation so that design safety factors can be reduced accordingly making more efficient use of the reinforced plastic. Mechanical and creep rupture tests show that interesting load transfer behaviour occurs between the metal skin and the fibre reinforced matrix, allowing the fibre reinforced matrix to perform satisfactorily up to twice its normal failure load under creep rupture conditions (1).

If the exploitation of laminate macrocomposites is to continue then information regarding the mechanical behaviour of such systems under a range of conditions is required, and the link between laminate and constituent properties must be established. In this work a macrocomposite system consisting of thin stainless steel sheet, 0.6 mm bonded to sheet moulding compound (SMC) was studied under impact conditions. Additional tests were

performed on the constituent materials, SMC, stainless steel and the combination of SMC and stainless steel to determine their mechanical properties.

It is now more than 30 years since the first industrial product based on sheet moulding compound (SMC), a cable distribution box, was put onto the market (2). SMC is a composite material which is usually a mixture of chopped 'E' glass fibres, fillers and catalysed polyester resin supplied in sheet form sandwiched between two polyethylene film layers to prevent contamination and adhesion during delivery (3). In use the SMC is cut to the required shape and both layers of polyethylene film are removed. The SMC can then be placed in a heated mould and pressed. Sheet moulding compounds give mouldings with excellent dimensional stability, good mechanical and electrical properties. They can therefore be used with confidence for the speedy and efficient production of high quality compression mouldings, such as automotive body parts, electrical switch-gear housing, furniture and a variety of other products. The use of SMC in the automobile industry and other industrial areas has become more and more popular. In recent years complete truck cabs have been produced from SMC mouldings (4). Current interest in SMC compounds for automotive applications has resulted in extensive research in different aspects of this material and the importance of this material is highlighted by the number of papers which are presented at composite conferences (5-7). One of the problems in using SMC is that under some conditions, it can suffer environmental degradation with resulting loss in mechanical failure. Another problem is that it has low specific stiffness in comparison with most metals and carbon fibre composite materials. These two shortcomings can be overcome by combining SMC with a layer of thin metallic material. SMC clad with a thin stainless steel skin offers a cost effective solution to the problem of deterioration in many situations by virtue of the impermeability of the metal skin. A stainless steel liner also provides a significant contribution to SMC performance under load, in addition to its prime purpose as an impermeable barrier layer. Stiffness and strength properties for the metal lined-SMC composite are higher than for

SMC alone; this is especially noticeable under bending conditions with the stainless steel surface in tension (see chapter 3).

Sheet moulding compounds (SMC) with a layer of stainless steel have found applications in automobile industry and for making water storage tanks (1). Intensive studies have been conducted to investigate the basic mechanical behaviour of SMC under static loading, for example, references (8-10). On the other hand there have been fewer attempts to characterise the response of SMC materials to impact type conditions (11-14) and the impact response of laminated composites with a layer of metallic material, the main concern of this work , has received no attention and no directly related background literature exists.

The aim of this project is two-fold. Firstly to provide an understanding of the behaviour of SMC when subjected to drop weight impact and secondly to investigate the effect of a surface layer of a metallic material on its tensile, flexural and impact behaviour.

In chapter 2 of this thesis the relevant literature is reviewed. Impact tests, in particular instrumented drop-weight tests, finite element and various mathematical models for analysis of stresses and strains, models for prediction the strength reduction and non-destructive techniques which are used to assess the damage in composite materials are discussed. The experimental techniques, the description of the test rigs employed and the mechanical characterisation of SMC and SMC with a layer of stainless steel are described in chapter 3. This is followed in chapter 4 by a description of the results obtained from the non penetrating and penetrating impact of SMC on its own. In chapter 5 the non penetrating and penetrating impact response of SMC-stainless steel laminates is described. The majority of impact tests on laminates were performed with the SMC layer as the impacted face supported by the steel layer. The impact response of SMC with other systems such as aluminium, copper, brass, and an ionomeric polymer is covered in chapter 6. In chapter 7 the effect of damage on the residual tensile and compressive

strengths of SMC after impact are described. The work is summarised and guide-lines for the design of energy absorbing macrocomposites are described in chapter 8. Conclusions and suggestions for further work arising from this project are given in chapter 8.

Chapter 2

Literature review

2 - 1 Introduction

The general objective of this review is to provide the reader with an insight into the subject of impact of composites. In the first six sections some of the impact tests which are widely used for composites are reviewed. The problems involved in using instrumented impact tests are followed in sections 7, 8, and 9. Energy absorbed by the specimen and energy absorbing mechanisms are covered in sections 10 and 11. Some of the techniques which are used for analysis of stresses during impact are reviewed in section 12. Evaluation of damage resistance in composite material is reviewed in section 13. The final section deals with the characteristics of SMC itself.

2 - 2 Impact Test Methods

A very common way to evaluate impact properties is to determine material toughness by measuring the energy required to break a specimen of a particular geometry. There are two types of impact test ; materials tests and product tests. The former measure the impact energy required to fracture a material specimen and are mainly for quality control. In the latter, a component is evaluated under impact conditions similar to those met in service. Neither type of test gives unambiguous information about any fundamental physical property of the material nor do they necessarily indicate how a component might behave under different impact conditions.

In tests of the first type a small specimen is subjected to a controlled impact and, in order to compare results from different laboratories, it is necessary to specify test conditions

carefully. A number of International and National Standards ASTM D256 (15), BS 2782 (16) and ASTM D1822 (17) have been written to cover the main types of impact testing namely flexed beam (15, 16), drop weight tests (16) and tensile impact tests (17). The two most common variants of flexed beam tests are Charpy and Izod which are described in the following section.

2 - 3 Charpy and Izod Tests

Charpy and Izod tests have been used for many years to determine the energy absorption, notch sensitivity, fracture toughness and fracture behaviour of metals and polymers. It is not surprising that the first test methods explored for impact testing of composites were derived from the methods used successfully for these other materials.

The charpy specimen has a square or rectangular cross section and contains a 45 degree V notch, 2 mm deep with a 0.25 mm root radius. The specimen is simply supported as a beam in a horizontal position and loaded behind the notch by impact of a heavy swinging pendulum. The energy of the impact machine shall be such that the energy absorbed in breaking a test specimen is neither less than 10% nor more than 80% of the energy of the blow.

The Izod specimen has either a rectangular or square cross section and contains a V notch near the clamped end. The main difference between the two tests is the method of holding the specimen. In an Izod test it is clamped vertically at one end and in a Charpy test held horizontally but not clamped. BS 2782 for the Izod differs from the ASTM D256 in test piece dimension and the impact velocity. The impact velocity for the British Standard is 2.44 m/s whereas for the American Standard is 3.46 m/s. The difference in loading between the Charpy and Izod tests is shown in figure 2.1.

These tests are very useful for the isotropic materials for which they were developed. In their simplest form the pendulums are not instrumented and datum recorded from each test is the energy absorbed by the specimen. The greater the swing of the pendulum after impact, the smaller the amount of energy absorbed. The fracture energy in both cases is determined by measuring the energy lost by pendulum. It is customary to express results, either in terms of energy absorbed per unit area of fracture, using the relation :

$$\text{Impact Energy} = \frac{E}{W\,(d-c)} \qquad (J / m^2)$$

where :

E = Energy absorbed in breaking specimen (J)

W = Specimen width (m)

d = Specimen depth before notching (m)

c = notch depth (m)

or the energy absorbed per unit width of notch (J / m).

The test can be instrumented in order to record force during the test. The instrumentation of the test is explained in more details in 2-7.

The fracture energy in impact test depends on test specimen geometry, temperature, anisotropy, impact speed, type of blow and the existence of stress raisers such as notches. It follows that impact data from different types of test can not be compared meaningfully, nor is there an accepted framework for using the data in design. BS 4618 (18) discusses in detail the many factors which influence impact strength.

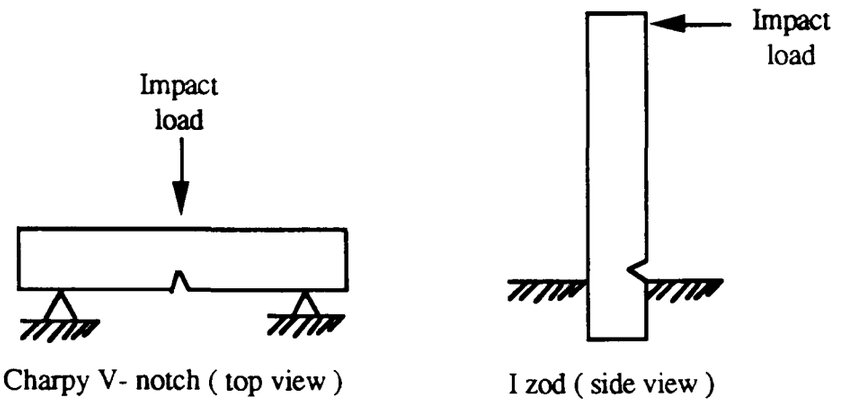

Figure 2.1 - Sketch showing method of loading in charpy and Izod impact tests.

2 - 4 Drop Weight Test

Drop-weight impact tests have become widely used in attempts to reproduce the conditions of impact which are representative of the type of blow which may occur in practical use. Sometimes for the following reasons, Izod and charpy tests can not be used and drop weight is an alternative (18).

1- The material is too thin. In such circumstances, for example, weights may be dropped on clamped samples of the thin material.

2 - The finished article may have a complex shape for which stress analysis is difficult. Dropping it on a hard surface or dropping weights on the moulding may demonstrate weak points in the design or show up the result of poor fabrication technique.

3 - A quality control test may be required for a particular article in a particular application. It might be more convenient to test the whole article rather than to machine out a test specimen.

4 - The surface finish of an article may have an important effect on its impact strength. For some materials this can be studied by means of pendulum tests on un-notched specimens but, for other materials, it may be better to drop weights on samples.

5 - Very high speed impacts may be involved in service, e.g. bullets may be fired at safety screens or raindrops may strike aircraft canopies.

Due to small size of charpy and Izod specimens, they are not always a realistic model of the actual situation. Not only does the small specimen lead to considerable scatter, but these specimens cannot provide the same constraint as would be found in a structure with a much greater thickness. The general situation that can result (for all classes of materials) is shown in figure 2.2. At a particular service temperature a standard charpy specimen may exhibit a high toughness while the same material in a thick-section structure has low toughness (19).

Drop weight tests are more appropriate than flexed beam tests since they permit failure criteria other than ultimate fracture to be specified (20). The impact energy required to produce a certain damage state may be a more suitable impact failure criterion.

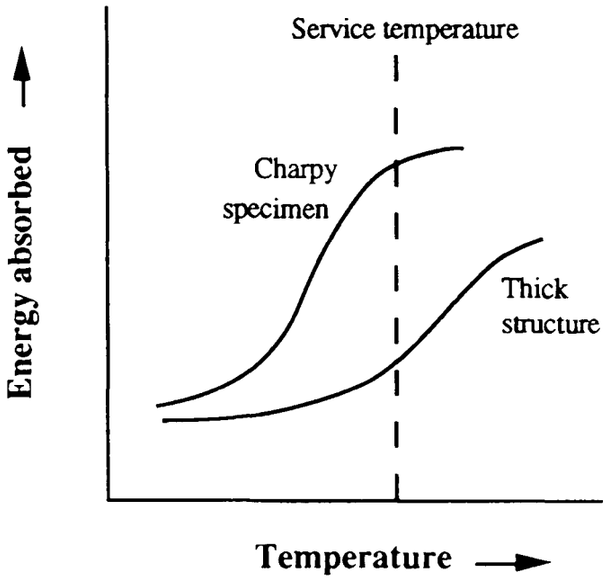

Figure 2.2 - Effect of section thickness on transition temperature curves.

The drop weight test machine consists of a tower frame with a weight capable of being raised and released with a little friction in the vertical direction (see fig. 3.16, chapter 3). In many cases standards developed for plastics have been adopted for use in composites with no modification of geometry or specimen size. In accordance with BS 2782 for plastics the drop weight test specimen can be a disc 57-64 mm in diameter or a piece 57-64 mm square. The specimen support is in the shape of a hollow steel cylinder of internal diameter 50.80 mm, external diameter not less than 57.2 mm and height not less than 25.4 mm. The striker has a hardened hemispherical striking surface 12.7 mm in diameter. According to ISO/DISS 6603/1 (21), the specimen can be either a disc 60 mm diameter or square and the support is a hollow cylinder of internal diameter 40 mm and external diameter 60 mm. The striker has a hardened hemispherical striking surface 20 mm in diameter. Table 2.1 shows the standard tests which were specified for plastics, but commonly used for impact testing of composites.

Table 2.1 - Common test standards adapted for composites.

Method	Impact Velocity	Striker	Support Conditions
BS 2782	3.46 m/s	12.7 mm dia.	50 mm I/D, 57 mm O/D ring (clamped for specimens less than 0.89 mm thick. Specimens 60 mm diameter or square.
ASTM D 3029-FA	3.6 m/s	15.86 mm dia. hemispherical	76 mm I/D clamped specimen
ASTM D 3029-FB	3.6 m/s	12.7 mm dia. hemispherical	38.1 mm I/D ring, clamped specimen
ISO/DIS 6603/2	4.4 m/s	20 mm dia. hemispherical (10 mm option)	40 mm I/D ring, specimens 60 mm dia. or square. clamping optional.

Apart from the standards which have been mentioned in table 2.1, there is a wide range of plate sizes and support dimensions which have been reported by various investigators (22). Drop weight impact machines can be instrumented to yield the useful information, such as peak force, energy to peak force and total energy absorbed by the specimen. The typical force-time, force-deflection and energy-time which have been obtained by an instrumented drop weight impact machine is shown in figure 3.22 in chapter 3.

Table 2.2 - Summery of drop weight impact tests courtesy of Wyrick et al (22).

Impact Plate Dimensions, mm	Plate Support Dimensions and Type of Support	Diameter & Shape Impactor	Investigator
300 x 1000	100 mm dia. ring clamped	12.7 mm hemisphere	Cantwell, et al.
300 x 840	200 x 800 mm clamped	15 & 30 mm hemisphere	Levin
	152 mm apart clamped	20 mm hemisphere	Joshi and Sun
80 x 220	clamped only on 80 mm sides	20 mm hemisphere	Caprino, et al.
152 x 152	127 x 127 mm simply supported	12.7 mm hemisphere	Wardle & Tokarsky Winkle & Adams
150 x 150	140 x 140 mm clamped	9.7 mm flat cylinder	Chaturvedi & Sierakowski
102 x 152	76 x 127 mm not specified	7.9 mm Dart	Hirschbuehler
102 x 152	76 x 127 mm simply supported	15.9 mm sphere	Boll, et al.
25 x 150	28 mm apart simply supported	5.5 mm sphere	Caprino
75 x 75	50 mm dia. ring not specified	12.5 mm hemisphere	Leach & Moore
100 mm dia.	100 mm dia. clamped	25.4 mm cantilever ball	Lal
90 mm dia.	90 mm dia. clamped	25.4 mm cantilever ball	Lal
50 mm dia.	50 mm dia. clamped	25.4 mm cantilever ball	Lal

2 - 5 Tensile Impact Tests

Izod, Charpy and drop weight impact tests which were described in the previous sections, use a flexural mode of deformation. In service a component may be subject to shock loading in a tensile configuration. Tensile impact tests may be performed on machines used for Izod and charpy tests with suitable modification (23). In these tests the specimen conforms to ' dumb-bell ' or ' dog-bone ' shape; one end is clamped to the pendulum head, with the other is held in clamps attached to a striker plate (fig. 2.3). When the pendulum is released from its raised position, it swings down between stop brackets,

trailing the specimen behind. The striker plate is then arrested by the stop brackets as the pendulum head swings on, causing the specimen to be strained rapidly in tension to failure. ASTM D1822 (17) which has been developed to enable data to be gathered from this type of loading, employ a pendulum impact machine and at least five and preferably ten specimens are tested and the results calculated on a unit cross sectional area.

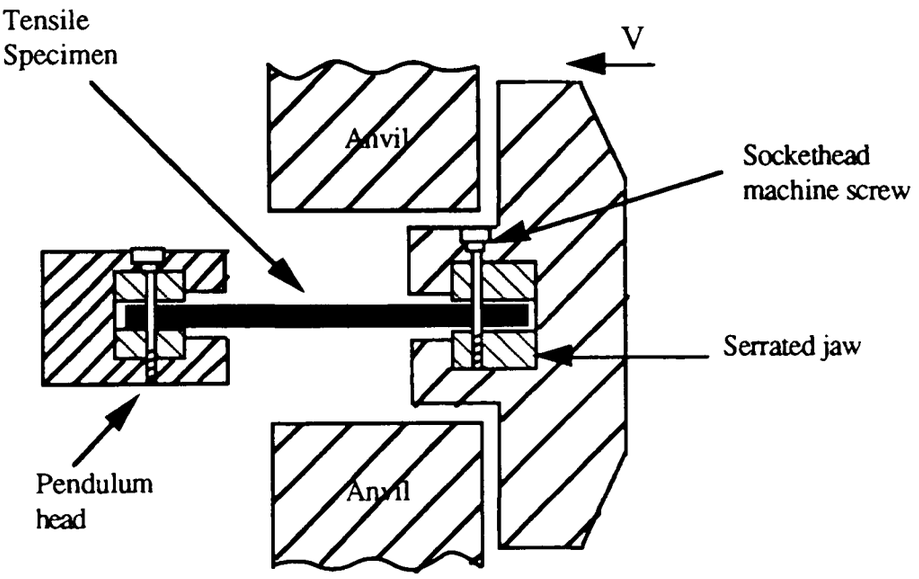

Figure 2.3 - Tensile impact apparatus : ASTM D1822

2 - 6 Additional Impact Tests

Impact tests are usually carried out to investigate the material behaviour at high strain rate. Driscoll (24) has compared the relative advantages and disadvantages of different modes of impact testing (table 2.3) and has indicated that charpy, Izod and drop weight impact tests do not necessarily provide high rate of strain.

Table 2.3 - Data on traditional impacting test methods

Impact Method	Temperature	Rate	Realistic Geometry
Pendulum impact	x	o	o
High rate tensile	x	x	o
Drop weight	x	o	x

Key: x = good; o = poor

Many deformation processes occur at strain rates that are well above those possible with standard mechanical testing procedure. High rate forming operations and impact events on automobile bumpers or the impact of a projectile with an armour plate are examples of high rate deformation processes. Because mechanical properties such as strength and ductility can vary with strain rate, it is often necessary to determine these properties under conditions that closely match the expected deformation rates in service. One of the high strain rate tests which is not actually classified as impact test (23) and may be considered as adjuncts to impact testing is the Split Hopkinson bar.

2 - 6.1 Split Hopkinson Pressure bar

The Hopkinson pressure bar comprises a bar several feet long and about an inch diameter split into two sections (25). The specimen which is in the form of a thin disc, is

sandwiched between the two sections of the bar (fig. 2.4). To one end of the bar is attached a detonator system, the firing of which generates the stress waves. The other end of the bar, known as the free end, is instrumented for measuring the displacement of that end, from which the pressure applied to the specimen may be calculated. The device is usually well instrumented and the load-deformation behaviour of the specimen may be monitored.

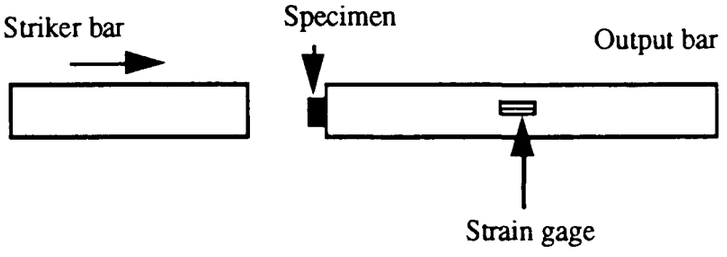

Figure 2.4 - Typical configuration of the Hopkinson bar.

2 - 7 Instrumented Impact test

The conventional impact tests described in sections 2-3 to 2-5 are very useful for a comparative study of different materials, since the only parameter determined by the tests is the impact energy (energy absorbed). A high-strength brittle material and a low strength ductile material may have the same total impact energy, therefore knowing the value of impact energy alone is not sufficient to interpret the fracture behaviour of the material. Broutman et al (26) point out that for the purpose of comparison and quality control the conventional impact tests are quite adequate for studying impact behaviour of isotropic metals or polymers. However, for composites in which the fracture phenomenon is much more complex, conventional impact tests may not be sufficient for providing data of basic physical significance. Reed points out that the widespread use of instrumentation has led to a much greater understanding of impact testing in recent years (27).

Izod, charpy and drop weight tests are instrumented to record the load history during the impact event. Instrumentation does provide more complete information, for example, on whether the failure mode is brittle, ductile, tear, or punched hole fracture (24). Typical load-time curves for brittle fracture, brittle / ductile fracture, ductile fracture and repeated fracture are shown in figure 2.5. Hoover points out (28), whether it be drop weight, charpy impact or Izod impact testing, an instrumented impact testing system consists of three major components, the dynamic load cell, the data display system, and a signal conditioning unit. The dynamic load cell is the tup (or striker) which produces an electrical analogue of the interaction force between the specimen and the machine. The data display system is commonly an oscilloscope or a microcomputer which records the force data as a function of time. The signal conditioning unit facilitates the balancing of the strain-gauge bridge, amplification of the bridge output, filtering of the signal, and a calibration function for determination of the bridge amplification.

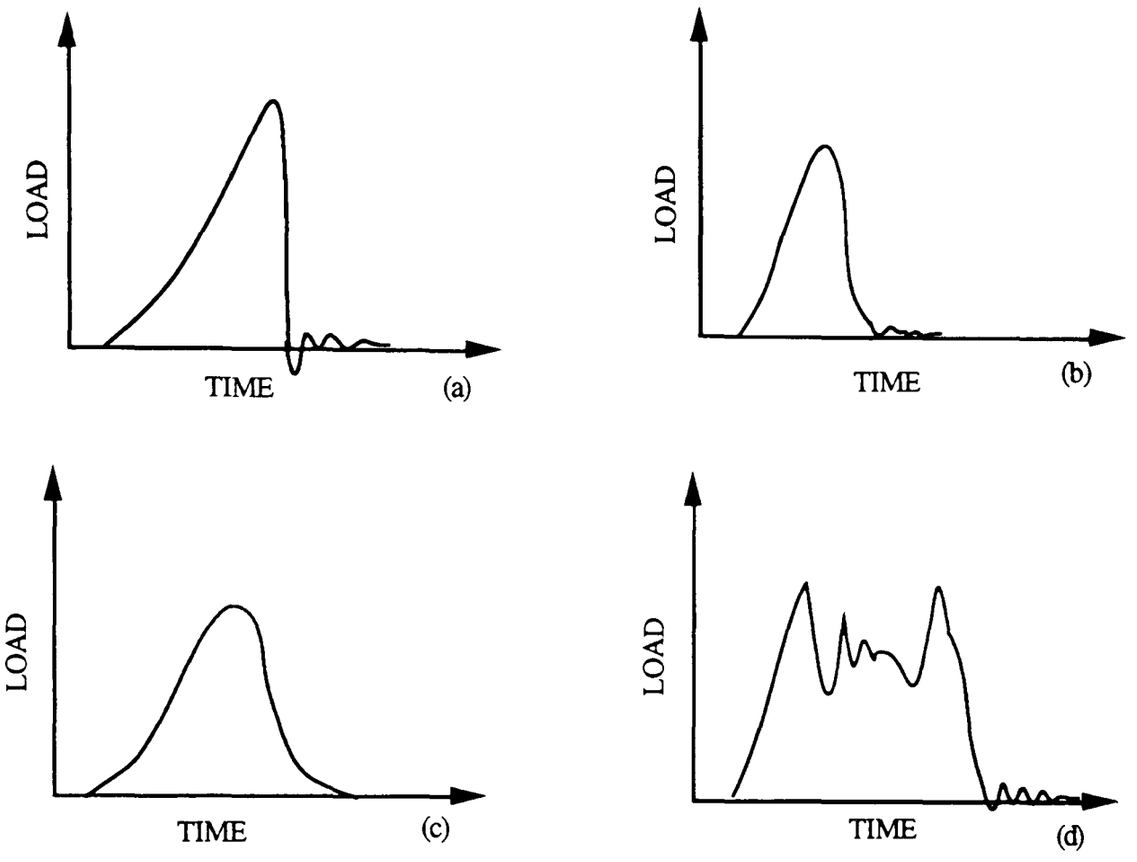

Figure 2.5 - Typical load-time curves for a) Brittle fracture, b) Brittle / ductile fracture, c) Ductile fracture, d) Repeated fracture (reinforced materials).

Ireland (29) points out the three following factors as most important for reliable instrumented impact testing:

(1) Calibration of the dynamic load cell,

(2) Control of the instrumented tup signal, and

(3) data reduction.

2 - 7.1 Load cell calibration

The most commonly used load sensor is that obtained by cementing strain gauges to the striker (30) or specimen supports (31) of the impact machine. The force acting on the striker is measured and it is assumed that the same force is sustained by the specimen. The instrumented tup is a dynamic load cell, and therefore the most applicable calibration procedure should be one utilising dynamic loading techniques. Ireland (29) argues that because load is being equated to the results of strain-gauge signals for elastic strains, and elastic properties are relatively strain-rate independent, static loads and dynamic loads will produce the same strain-gauge signals. However, it is not uncommon to have strain gauges respond differently for dynamic conditions than for static because of variations in the properties of the bonding materials which are holding the gauges on the tup (29).

Dynamic calibration of an instrumented tup can be performed with a low-blow elastic impact test (31), by striking the tup with a known elastic impulse. It is crucial for the strain gauges to produce a signal which is a good analogue of the response of the test specimen. Server and Ireland (31) have used three sets of strain gauges to evaluate three different locations on an Izod tup. These positions sensed three strains: compression (similar to that normally used for the charpy tup), shear, and compression bending. Low-blow tests (totally elastic) were performed by dropping the hammer from the same low height. It was found that compression and shear gauges produce distorted signals and the outputs are less than one third that of the bending gauges figure 2.6. It was also found that the output from the bending gauges is linear with load up to 10000 lb. Therefore, the bending gauges were selected for subsequent use in instrumented Izod testing.

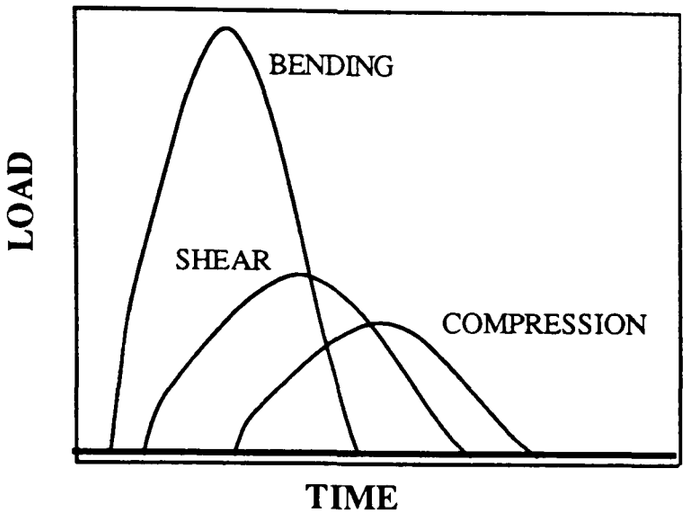

Figure 2.6 - The output from three sets of gauges at different positions on an Izod pendulum -after experiments by Server and Ireland (31).

2 - 7.2 Dynamic signal control

Ireland (29) points out that the force-time signal obtained from strain gauges on a tup during impact is not necessarily indicative of the reaction of the specimen and represents a complex combination of the following components:

1 - The true mechanical response of the specimen

2 - Inertial loading of the tup as a result of acceleration of the specimen from rest.

3 - Low frequency fluctuations caused by stored elastic energy and reflected stress waves.

4 - High frequency noise in the KHz range caused primarily by the amplification system.

The latter is usually minimised through use of high-gain strain gauges (for example, semiconductors) to achieve a relatively large signal-to-noise ratio.

The following techniques have been suggested by Ireland (29) to determine the true mechanical response of a specimen tested by impact:

1 - Monitor the response of strain gauges attached directly to the specimen.

2 - Reduce the amplitude of the oscillations of the tup signal by testing at a reduced velocity.

3 - Electronically filter the tup signal without adversely distorting the signal with respect to the specimen reaction.

For brittle fracture, the reaction of the specimen can be quite different than that of the supports (tup and anvil). Several investigators (32,33,34) have documented these differences through tests with strain gauges appropriately positioned on the tup, anvil, and various locations on the specimen. The relationship of the specimen reaction is schematically shown in figure 2-7.

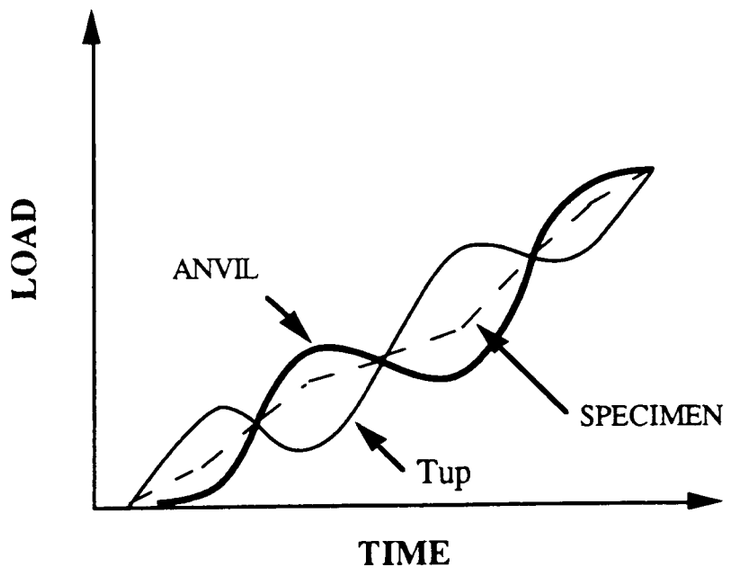

Figure 2.7 - Schematic diagram showing the relationship between specimen, tup, and anvil reactions during Izod impact - after Ireland (29).

2-7.3 Data Reduction and Evaluation

Techniques for reduction of dynamic test data usually vary with the specific goals of the investigators. The instrumented tup signal provides a force-time record from which various loads, energy, and deflection parameters can be determined. The calculations of energy and deflection from load-time records have been described by Ireland (29). The analysis which have been used in this work to provide information about velocity, displacement and energy with time is given in chapter 3.

Cheresh and McMichael (35) point out that the evaluation of data depends on understanding of inertial loads and harmonic oscillations. Inertial load is the load required to accelerate the specimen from zero velocity to the velocity of the striker. Inertial loads are most often characterised by a sharp spike (often followed by a decaying oscillation) at the beginning of the curve (fig. 2.8). A simple diagnostic test to determine whether a given spike is caused by a mechanical specimen response or by inertial loads is to repeat the suspect test using a different (usually lower) impact velocity. The magnitude of an inertial load is essentially proportional to the impact velocity (36), therefore, if the data in question are caused by inertial effects, a lower impact velocity should reduce this load by a proportional amount.

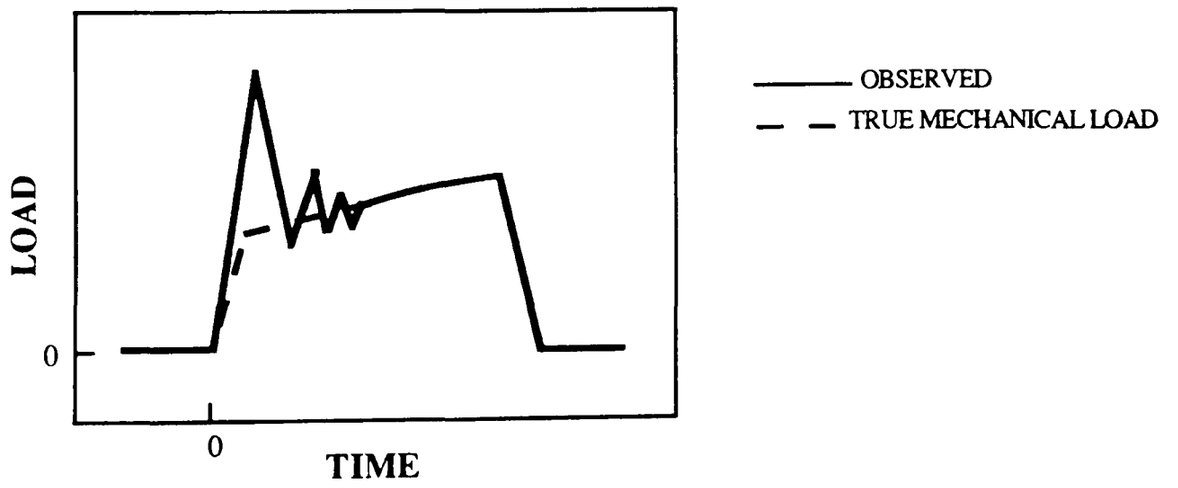

Figure 2.8 - Schematic example of impact exhibiting a high inertial load. The initial sharp spike is caused by load required to accelerate the specimen to tup velocity.

During an impact, the components involved (specimen and tup) react to the impact by oscillating at their natural frequencies (35). Distinguishing between mechanical and oscillatory loads requires that the frequency of oscillation be compared to the natural frequencies of the tup. Cheresh and McMichael (35) suggests the two following techniques for determination of the natural frequency of the tup and the specimen. To determine the natural frequency of the tup, an impact test is carried out on a relatively strong but brittle material. The tup will continue to oscillate at its natural frequency after the specimen has fractured. Plotting the data collected after specimen fracture against time should allow the tup oscillation frequency to be determined. If oscillations are caused by the natural frequency of the specimen itself, several impact tests on specimens of the same materials with different thickness or other parameters such as unsupported span that is known to influence the natural frequency of the specimen are carried out. Once the frequency and the source of the oscillations are known, the effect on the signal can be estimated. The methods which have been suggested by Ireland (29) for reducing the level of oscillations have been described in section 2-7.2.

2 - 8 Determination of Data Collection Parameters

The test time, load ranges, method of triggering and the degree of filtering are important parameters which are required to be determined and set prior to performing an impact test. Incorrect test time and load range results in a load-time curve such as the one shown in figure 2.9. In this case, the test time was too short and the load range too low. Cheresh and McMichael (35) propose the following steps to determine a suitable time range setting and load range setting for a specimen with unknown behaviour. For time setting the deflection that will be required to obtain complete fracture is divided (35) by the impact velocity

$$t = d/v$$

where t=time, d=the expected deflection to complete failure, and v=the impact velocity. For safety the calculated time is increased by a factor of two. To determine the load range for the

test, the highest expected load which can be measured by static testing is calculated and multiplied by a factor of two for safety.

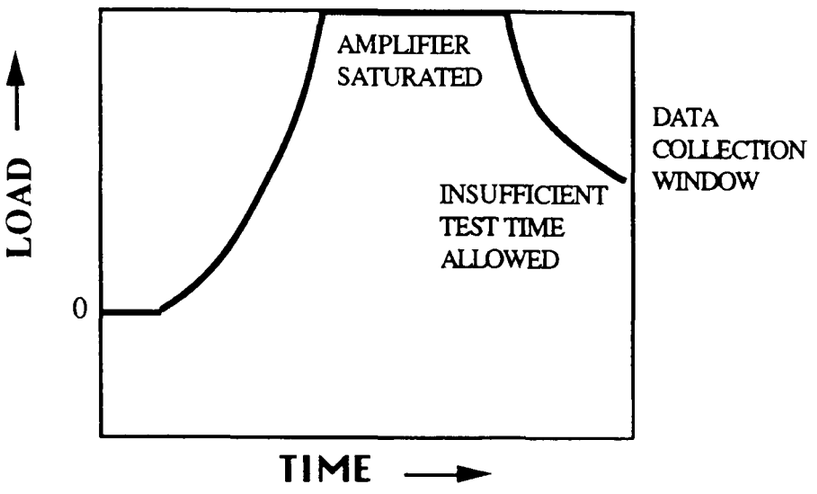

Figure 2.9 - Examples of incorrect data collection parameters. The load range and test time are insufficient.

The trigger level is usually set about 10% of the expected maximum load to ensure that the trigger level is well above any background noise. Also, an adequate number of data points collected prior to the trigger signal must be saved. About 10% of the points as ` pretrigger ' information are saved.

Many data collection systems incorporate filters to reduce noise introduced by specimen and tup vibrations and to eliminate high-frequency noise from other external sources. Although these filters can almost always improve the readability of test data, their use should be restricted to situations in which the source of the removed noise is known and the effect on data is understood (35). There is a growing reluctance to electronically filter the raw data because oscillations on the force-time curve can be associated with the progression of damage and are part of the specimen response. Post-processing of the stored data is becoming more popular and has the advantage that the original data can always be retrieved (27).

2 - 9 Instrumented Dart Impact

Instrumented impact tests such as charpy and Izod have limited use in testing sheets or films. Instrumented dart tests have been developed to overcome these shortcomings (37) and also to produce the conditions of impact which are representative of the type of blow which may occur in practical use. The biaxial loading imposed by a hemispherical dart on a flat plate specimen supported over a circular annulus is a good approximation to typical loading conditions.

The two most common methods for producing the dart impact condition are use of a free falling weight and a servo hydraulic ram. Knakal (38) points out that the latter has a distinct advantage because of its ability to vary the impact velocity over a wider range. Driscoll (24) also points out this problem and states that the limitation on drop-weight testing is the impacting rate unless the laboratory ceiling is unusually high. Most conventional ceiling rooms can not accommodate a drop tower of more than 2.4 to 3.0 m. Consequently, the impacting rate is below 5 m/s, which could miss the critical rate-dependent 'window ' of some polymeric material systems.

As for any other instrumented impact tests, dynamic load cell, data display unit and signal conditioning unit are the three major components of instrumented dart impact. These components together with the setting of the drop weight impact test machine and a servo hydraulic ram machine which were used for this thesis are given in chapter 3.

2 - 10 Energy Absorbed During Impact Testing

The energy absorbed during an impact test (E) is not necessarily the energy absorbed by the specimen alone. Several factors are involved in the absorption of energy (E) during an impact test (29, 39, 40).

$$E = E_I + E_{sd} + E_B + E_{Mv} + E_{ME} + E_{CF}$$

Where :

E_I = increment of energy required to accelerate the specimen from rest to the velocity of the striker .

E_{sd} = the total energy (elastic + plastic) consumed by bending the specimen .

E_B = energy consumed by Brinell - type deformation at the specimen load points .

E_{Mv}= energy absorbed by the impact machine through vibrations after initial contact with the specimen .

E_{ME} = stored elastic energy absorbed by the machine as a result of the interactions at the specimen load points, and

E_{CF} = energy needed to create new surfaces .

The energy which is indicative of the " toughness " of the material is that indicated by factors (E_{sd} (plastic part)) and (E_{CF}) and these should be large to the rest if the test is to be of value. Factors (E_I), (E_{Mv}), and (E_{ME}) are not related to the material " toughness " but are peculiar to the test and should be relatively small in order for the test results to be considered a measure of the material's shock resistance.

2 - 11 Energy absorbing mechanisms in fibre-reinforced composites

A fibre-reinforced composite is composed of three constituents: the fibres, the matrix and the interface between the matrix and the fibre. The manner in which the material deforms and fractures depends upon both the chemical and mechanical properties of these three constituents. Detailed analyses using both optical and scanning electron microscopes have identified a number of failure mechanisms in fibre-reinforced composite materials (41). These include delamination, interlaminar matrix cracking, longitudinal matrix splitting, fibre/matrix debonding, fibre pull-out and fibre fracture (42). The relative energy absorbing capability of these fracture modes depends upon the basic properties of the constituents as well as the loading mode. Typical values measured for a number of continuous fibre composites are given in table 2-4.

Table 2.4 - Typical values of the energy absorbing capability of various continuous fibre composites for different failure modes courtesy of Cantwell et al (42).

Failure mode	Material	Typical fracture energy kJ / m2
Splitting	Type II CF/epoxy	0.1 - 1
	AS4/PEEK	3.8
Delamination	T300/epoxy	0.1
	IM6/PEEK	2.2
Transverse	Treated CF/epoxy	20
	Untreated CF/epoxy	60
fibre fracture	AS4/PEEK	128
Fibre pull-out	CF/polyester	26
Debonding	CF/epoxy	6

The following sections reviews the role of the material constituents independently and examine the influence of varying their properties on the overall impact resistance of the composite.

2 - 11.1 Fibre

The mechanical properties of fibres greatly influence the impact resistance and post-impact properties of fibrous composites (43,44,45,46,47). The strain energy absorbing capacity of the fibres is one of the most important parameters in determining the impact resistance of a composite structure. Fibres that have a large area under the stress/strain curve tend to be better suited to energy absorbing applications. Since in fibre reinforced composites the stored strain energy is dependent on the tensile strength and the Young's modulus, it is probable that a composite manufactured from high strength, low stiffness fibres would offer an improved impact resistance. Greszczuk (48) states that the resistance to damage increases as the fibre strength increases and the fibre modulus decreases. Kevlar fibres, which exhibit large areas under the stress/strain curves, offer excellent impact resistance. The role of the fibre diameter is not completely clear. A simple pull-out model suggests that composites with larger diameter fibres should be inherently tougher. However, current trends are towards smaller diameter fibres offering higher strain to failure. Any reduction in toughness linked to the interface is thereby hidden by the increased energy absorbing capacity of the fibres (42). Coating and surface treatment of fibre also affects the impact properties. Study by Rogers et al. (49) on impact resistance of carbon fibre laminates showed that fibre surface treatment increases the transverse tensile strength of the composite resulting in higher energy thresholds for first damage.

2 - 11.2 Matrix

The polymeric matrix in a fibre-reinforced composite serves to protect, align and stabilise the fibres as well as assure stress transfer from one fibre to another. Many researchers have investigated the effect of matrix properties on the impact response of carbon fibre composites (50,51,52). The use of toughened resins compared to that of the conventional

resin has shown considerable improvements in the impact properties of carbon fibre composites (53,47). Hunston (54) analysed data from three sources in an attempt to identify a link between matrix properties and composite fracture toughness. He identified a definite correlation between the resin Mode I fracture toughness and composite interlaminar fracture energy as measured by the DCB specimen. The higher the resin Mode I fracture toughness the higher composite interlaminar fracture energy. Tougher resins may be produced by modifying a base resin or by a different type of resin such as thermoplastic resins. In recent years considerable interest has been generated by carbon-fibre reinforced PEEK (APC2), a semi-crystalline thermoplastic composite (55,56,57,58). Interlaminar fracture testing and impact loading have shown that this material offers excellent static and dynamic toughness and is capable of absorbing a considerable amount of energy whilst incurring only small amounts of damage (59,60). Another advantage of this material is that its thermoplastic matrix allows rapid repair using fusion techniques such as the hot press technique (61). It should be noted that matrix toughness improves low energy damage development in impact, but does not affect through penetration excess energy impact.

2 - 11.3 Interphase

The strength of the bond between the matrix resin and the fibre reinforcement is a controlling factor in determining the mechanical performance of most polymer composites. The bond between the fibre and the surrounding matrix can be improved with the aid of suitable fibre surface-treatments. Studies have shown that varying the level of surface treatment applied to a carbon fibre composite can change the mode of failure as well as many fundamental mechanical properties (62). Study by Harris et el. (63) on the strength and fracture toughness of carbon fibre composites showed that work of fracture and interlaminar shear strength are both affected by surface treatments of the fibre. During the fracture process the fibres may become separated from the matrix material by cracks running parallel to the fibres (Debonding cracks). This type of cracking occurs when fibres are strong and the interface is weak. If debonding is extensive, a significant increase in the impact energy may be obtained. An increase in impact energy may be observed with a

decrease in interface strength because it promotes extensive debonding or delamination (64).

Values of the work of debonding for a number of materials have been given by Kelly (65) ; they are usually < 500 J/m^2 and of the order of the interface shear strength times the failure strain of the resin.

2 - 11.4 Fibre Stacking Sequence

Considerable work has shown that the impact resistance of composite materials also depends upon the specific order in which the plies are stacked (59,62). For example, unidirectional composites having all their fibres aligned in one direction fail by splitting at very low energies and are therefore highly unsuitable for applications where impact loading might occur. A detailed study by Hong and Liu (66) showed that increasing the angle θ in a $(0°_5, \theta°, 0°_5)$ laminate resulted in greater delamination type damage for a given incident energy. Increasing θ in this way also had the effect of reducing the first damage threshold energy. Hyung Yun Choi (67) et al. showed that the change of stacking sequence significantly influences the impact damage and its effect is much more than the change of thickness.

2 - 11.5 Geometry

Geometry is a fundamental parameter in determining the impact response of a composite component (68, 69, 59). Broutman and Rotem (26) showed that increasing the size of a GFRP beam increases its energy absorbing capability under low velocity impact conditions. However, doubling the size of the beam did not result in an equivalent increase in energy absorption. High velocity impact tests on CFRP indicated that the areal geometry of the target is less important at high rates of strain (70). Ultrasonic C-scans of impacted specimens showed that the level of damage in a small 50 mm long beam was the same as that in a 150 mm coupon. This suggests that high velocity impact loading by a light

projectile induces a localised form of target response in which much of the incident energy of the projectile is dissipated over a small zone immediate to the point of impact.

2 - 12 Analysis of Impact Stresses in Composite Materials

2 - 12.1 Introduction

A realistic analysis of impact stresses in composite materials is an enormously complicated task. A large number of parameters, for example, mass, shape, velocity, and material response of both the projectile and the target must be considered (71). Greszczuk (48) points out that although the response of composite materials to particle or foreign -body impact could be studied using empirical or semi-empirical approaches, this appears undesirable because of the large and costly efforts that would be required to cover the various combinations of constituent materials, lay-ups, stacking sequence, and construction.
Some of the impact tests are easier to analyse. In table 2.5 some of the well-known impact tests have been ranked according to their analytical usefulness (72).

Table 2.5 - Ranking of the impact tests according to their analytical usefulness.

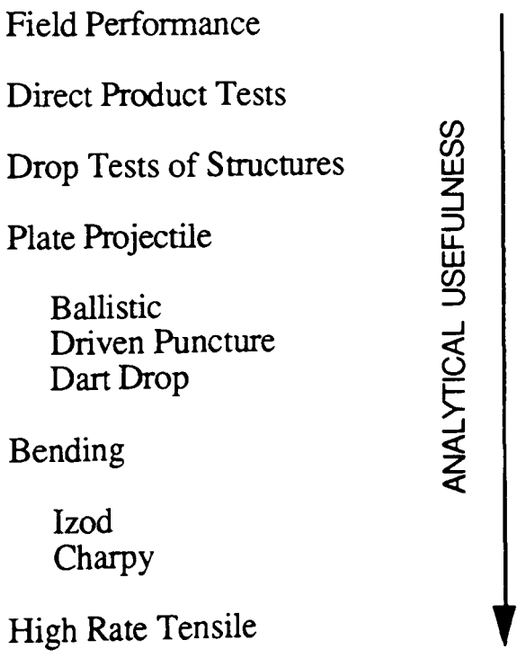

Zukas (73) points out that the study of impact phenomena involves a variety of classical disciplines. In the low velocity regime (< 250 m/s) many problems fall in the area of structural dynamics. Local indentations or penetrations are strongly coupled to the overall deformation of the structure. As the striking velocity increases (0.5-2 Km/s) the response of the structure becomes secondary to the behaviour of the material within a small zone of the impact area. A wave description of the phenomena is appropriate and the influence of velocity, geometry, material constitution, strain rate, localised plastic flow, and failure are manifest at various stages of the impact process. Still further increases in impact velocity (2-3 Km/s) result in localised pressure that may exceed the strength of the material by an order of magnitude. In effect, the colliding solids can be treated as fluids in the early stages of impact. At ultra-high velocities (> 12 Km/s) energy transfer occurs at such a high rate that an explosive vaporisation of colliding materials results. Analytical models may be useful in making predictions, provided care is taken not to violate the simplifying assumptions introduced in their derivations or exceed the data base from which their empirical constants are derived (74). A variety of mathematical models which assume the target and projectile to be isotropic and elastic have been proposed of which the most widely used has been the Hertz model.

2 - 12.2 The Hertz model

The classical Hertz impact model which has been widely used for studying impact of elastic bodies (75) assumes that the dynamic impact problem can be represented by the quasi-static elastic analysis of indentation. The force acting on a target due to the impact of a spherical projectile is given by the following equation (76)

$$F = n \cdot x^{3/2}$$

where

x = displacement (indentation depth), mm

$$n = \frac{4}{3}\sqrt{R}\ \left[\frac{1-\mu^2}{E} + \frac{1-\mu_p^2}{E_p}\right]^{-1}$$

where

E_p = Young's modulus of the projectile, N/mm^2

E = Young's modulus of the target, N/mm^2

μ_p = Poisson's ratio of the projectile

μ = Poisson's ratio of the target

R = Projectile radius, mm

The normal stress distribution is hemispherical over the contact circle and is greatest at the centre (76) where the surface pressure is maximum (q_{max}).

For the case of the Hertzian contact problem involving a sphere of mass m and velocity (V_0) colliding onto a flat surface, the relationship between the contact force (P) and a, the radius of the area of contact with impact velocity (V_0) is (48)

$$P = \frac{4\,R^{\frac{1}{5}}\left(\frac{15}{16}\pi\, m\, V_o^2\right)^{\frac{3}{5}}}{3\pi\left(\frac{1-\mu_p^2}{\pi . E_p} + \frac{1-\mu^2}{\pi . E}\right)^{\frac{2}{5}}}$$

$$a = R^{\frac{2}{5}}\left[\frac{15\pi\left(\frac{1-\mu_p^2}{E_p} + \frac{1-\mu^2}{E}\right) m V_o^2}{16}\right]^{\frac{1}{5}}$$

The value of the maximum pressure q_{max} is obtained (76) by equating the sum of the pressure over the contact area to the compressive force P. For the hemispherical pressure distribution:

$$q_{max} = \frac{3P}{2\pi a^2}$$

The pressure distribution over the area of contact (48) is:

$$q_{x,y} = q_{max} \left[1 - \frac{x^2}{a^2} - \frac{y^2}{a^2} \right]^{\frac{1}{2}}$$

where q_{max} is the surface pressure at the centre of area of contact, x=y=0. At the boundary of the surface

$$\frac{x^2}{a^2} + \frac{y^2}{a^2} = 1$$

and therefore $q_{x,y} = 0$

The maximum tensile, compressive, and shear stresses (σ_T, σ_C, and σ_S respectively) that occur in the target made of isotropic materials are related to the surface pressure by the following simple equations (48)

$$\sigma_T = -\left(\frac{1 - 2\mu}{3} \right) q_{max}$$

$$\sigma_C = q_{max}$$

$$\sigma_S = \left[\frac{1 - 2\mu}{4} + \frac{\sqrt{2(1+\mu)^3}}{9} \right] q_{max}$$

The location of the maximum tensile, compressive and shear stresses are noted in figure 2.10.

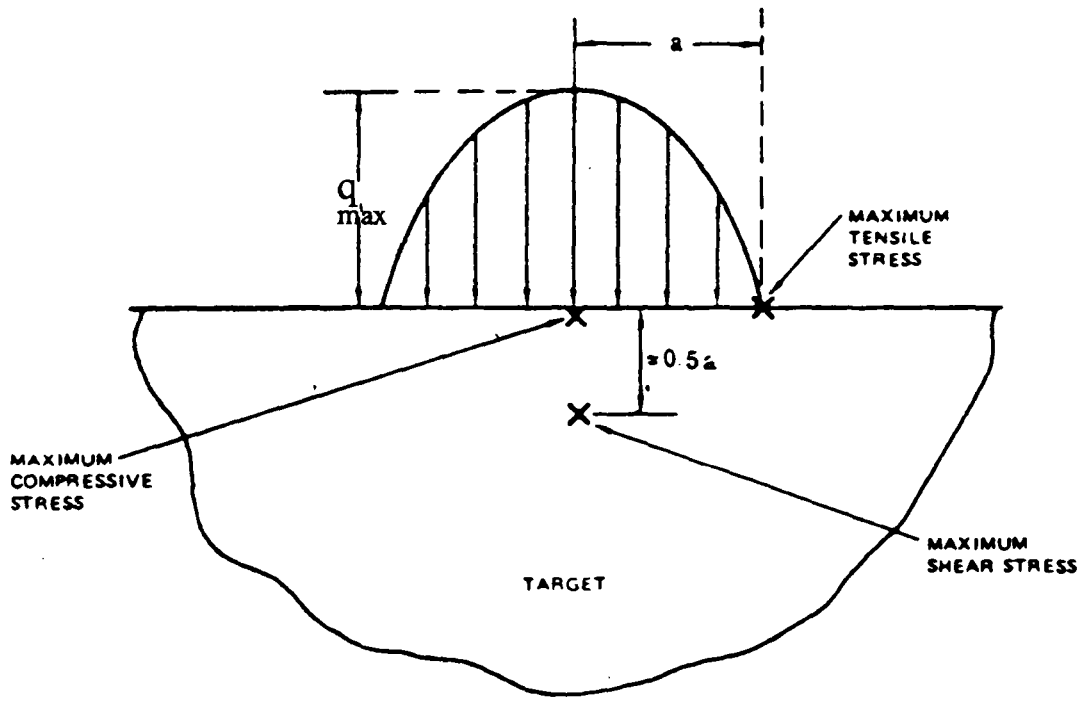

Figure 2.10 - Location of maximum tensile, compressive and shear stresses are under surface loading.

A modified contact law with

$$n = \left(4/3\right)(R)^{1/2}\left[\left(1-\mu_p{}^2\right)/E_P + 1/E_2\right]^{-1}$$

was employed by Yang and Sun (77) for a study on impact of laminated composites. In the above equation, E_p, μ_p, and R are the Young's modulus, the Poisson's ratio and the radius of the isotropic sphere respectively, while E_2 is the modulus of elasticity transverse to the fibre direction in the fibre reinforced composite.

2 - 12.3 General case of impact between two nonisotropic bodies

The solution to the more general contact problem can be found in the paper by Greszczuk (127). The same approach as described in the preceding section can be used for the general case of impact between two bodies made of transversely isotropic and orthotropic materials, including targets made of laminated composites. If a solid (or impactor designated by subscript 1) having, at the point of contact, principal radii of curvature R_{1m} and R_{1M} is pressed by a force P into a target having principal radii of curvature R_{2m} and R_{2M}, the area of contact will be elliptical with major and minor axes of ellipse being

$$a = n \left[\frac{3\pi}{2} P \left(K'_1 + K'_2\right) C_R\right]^{\frac{1}{3}}$$

$$b = r \left[\frac{3\pi}{2} P \left(K'_1 + K'_2\right) C_R\right]^{\frac{1}{3}}$$

where C_R is a term that takes into account the curvature effect

$$C_R^{-1} = \frac{1}{R_{1m}} + \frac{1}{R_{2m}} + \frac{1}{R_{1M}} + \frac{1}{R_{2M}}$$

K'_1 and K'_2 are still to be defined parameters that take into account the elastic properties of the impactor and the target; and n, r, and s are parameters that are a function of R_{1m}, R_{2m}, R_{1M}, and R_{2M} and are given in table 2.6 as a function of θ where

$$\theta = \arccos \left\{ C_R \left[\left(\frac{1}{R_{1m}} - \frac{1}{R_{1M}}\right)^2 + \left(\frac{1}{R_{2m}} - \frac{1}{R_{2M}}\right)^2 + 2 \left(\frac{1}{R_{1m}} - \frac{1}{R_{1M}}\right) \left(\frac{1}{R_{2m}} - \frac{1}{R_{2M}}\right) \cos 2\phi \right]^{\frac{1}{2}} \right\}$$

Table 2.6 - Values of parameters n, r, and s

θ	0°	10°	20°	30°	40°	50°	60°	70°	80°	90°
n	∞	6.612	3.778	2.731	2.136	1.754	1.486	1.284	1.128	1.00
r	0	0.319	0.408	0.493	0.567	0.641	0.717	0.802	0.893	1.00
s	-	0.851	1.220	1.453	1.637	1.772	1.875	1.994	1.985	2.00

and ϕ is the angle between normal planes containing curvatures $1/R_{1m}$ and $1/R_{2m}$.

The relationship between the contact force P and the combined deformation of both solids at the point of contact can be expressed in terms of similar parameters (127) and is

$$\alpha = s \left[\frac{9\pi^2 P^2 (K_1' + K_2')^2}{256 C_R} \right]^{\frac{1}{3}}$$

The above relationship can be expressed in the form similar to Hertz law

$$P = n'. \alpha^{3/2}$$

where now

$$n' = \left(\frac{16}{3\pi (K_1' + K_2')} \right) \left(\frac{C_R}{S^3} \right)^{\frac{1}{2}}$$

If the target is made of transversely isotropic material the following expression has been derived (127) for K'_2

$$K'_2 = \frac{\sqrt{A_{22}}\left\{ \left(\sqrt{A_{11}A_{22}} + G_{zr}\right)^2 - \left(A_{12} + G_{zr}\right)^2 \right\}^{\frac{1}{2}}}{2\pi\sqrt{G_{zr}}\left(A_{11}A_{22} - A_{12}^2\right)}$$

where

$$A_{11} = E_z\left(1 - \mu_r\right)\beta$$

$$A_{22} = \frac{E_r\,\beta\left(1 - \mu_{zr}^2\delta\right)}{1 + \mu_r}$$

$$A_{12} = E_r\,\mu_{zr}\,\beta$$

$$\beta = \frac{1}{1 - \mu_r - 2\mu_{zr}^2\,\delta}$$

$$\delta = \frac{E_r}{E_z}$$

and E, G, and μ are the Young's modulus, shear modulus, and Poisson's ratio of the target, while subscripts r and z denote the radial and thickness directions, respectively, z being in the direction of impact. For a planar isotropic material, the properties in the r plane are independent of the orientation.

If the impactor is also made of transversely isotropic material, the expression for K'_1 will be similar to K'_2 except that the various elastic constants appearing in these equations will be those of the impactor material. Greszczuk (127) states that an approximate numerical solution for K'_2 of generally orthotropic solids shows K'_2 to be relatively insensitive to the in-plane fibre orientation.

Although Hertz indentation law is very simple to use and displays good correlation with the experimental results (127), its use is limited to elastic and non-flexible targets. For a flexible target the bending deformation of the target should also be considered.

2 - 12.4 Impact response of a flexible target

For a flexible, plate-type target, the surface pressure, area of contact, and impact duration will be functions of the parameters which have been mentioned in the above section as well as plate bending stiffness and boundary conditions. For a given impact velocity the magnitude of the dynamic force P will decrease as the target flexibility increases (or target thickness decreases). Increase in target flexibility will also increase contact duration and decrease area of contact. An approximate solution for a flexible plate is described later in chapter 4.

2 - 12.5 Mathematical models which model the composite media as a periodic material

A variety of mathematical models have been proposed which approximately model the composite media as a periodic material. These theories generally treat the composite material as a homogeneous continuum with a complicated mathematical structure (78).

2 - 12.6 Theory of bending of plates

Basically, drop weight impact testing is the bending of a plate which is supported on a circular annulus and loaded at the centre. There are many bending theories, some of which use fairly simple concepts whilst others involve more complex mathematical analysis. The simple theories assume that : 1 - the plate is flat, of uniform thickness, and homogeneous isotropic material ; 2 - the maximum deflection is not more than about half the thickness ; 3 - the plate is nowhere stressed beyond the elastic limit (79). The equations for a plate of thickness t, simply supported on a ring of radius a, and loaded uniformly over a very small central circular area of radius r, are presented in chapter 4.

These equations are limited to small deflections and perfectly elastic material In drop weight impact testing, the deflection is usually large and therefore other analysis have to be investigated. Finite element techniques seem to offer the greatest potential in this respect.

2 - 12.7 Finite Element Analysis

Finite element analysis (FEA) is a relatively new and powerful technique of stress analysis that permits structural engineers to solve problems of design with speed, accuracy, and economy. Turner, Clough, Martin and Topp introduced the finite element concepts in 1956 (80). During the nineteen- sixties, the finite element method became widely accepted and many books have been written on this subject (81). The finite element method has now been widely accepted for all kinds of structural engineering applications in aerospace, aeronautics, naval architecture, nuclear - powered electrical generating stations, etc.

In an actual finite element analysis of a structure, the engineer must first provide a model. The object under analysis is divided into a finite numbers of elements of known stress and deformation characteristics. The elements are then attached at points, called nodal points. The nodal points are chosen at locations where the engineer wishes to determine the stress and deformations, where external loads are applied, where boundaries and discontinuities exist, and the points necessary to define element shapes. The engineer then defines material properties, specifies boundary restraints, and applies load to the model. A digital computer, properly programmed, generates the results.

The accuracy of results obtained with the finite element method depends on the accuracy of the input data on material properties, mechanical and thermal loading, and boundary restraints.

2 - 13 Evaluation of Damage in composite materials

2 - 13.1 Introduction

Due to the complex nature of damage in composite materials subjected to impact, a combination of non-destructive (NDT) and destructive techniques may be required to characterise the damage. Non-destructive testing (NDT) techniques, optical and scanning electron microscope and measurement of residual tensile and compressive strength after impact have been extensively used by many investigators (82-85). Non-destructive tests and residual strength are discussed in the following sections and the use of optical microscope which has been the main tool in investigation of damage in the present work is discussed in chapter 3 and 4.

2 - 13.2 Non-destructive Test Techniques (NDT)

A variety of non-destructive techniques (NDT) are used for evaluating the damage-zone shape and size in composite materials. Among the well-developed NDT techniques, penetrants, eddy current, radiography, acoustic emission, holography, and ultrasonics have all received attention. A comprehensive description of the NDT techniques applied to composites can be found in the literature (3 day course) published by the Centre for Composite Materials at Imperial College (86). The application of NDT techniques for composite materials have been extensive and many papers have been published in ASTM STP 696 (87).

Ultrasonic analysis has been widely used for flaw detection and characterisation in composite materials (88-90). In ultrasonic inspection, material inhomogeneity and anisotropy severely limit the capability for characterising discrete defects. As a result, necessary size, shape, and position information on defects is obtained with much less

accuracy than in homogeneous materials (91) and particular types of defects are classified with much less certainty.

X-ray radiography is also a widely used method for inspecting composite laminates (92,93). Since most composite materials have low density and are inhomogeneous, conventional X-ray radiography can not be applied satisfactorily. Scott in his paper (91) points out that using radiography with conventional X-ray procedures results in poor flaw contrast. This problem has been overcome by using radio-opaque penetrants. Some of the inorganic radio-opaque penetrants (94) which are used for composite materials are shown in table 2-7.

Table 2.7 - Inorganic radio-opaque penetrants.

Inorganic Chemical Compounds	Radiographic Opacity
Zinc Iodide	High
Silver Nitrate	Medium
Lead Nitrate	Low
Barium Sulphate	Very Low

A wide range of halogenated hydrocarbons such as Diiodomethane and Tetrachloroethylene which are used as a radio-opaque penetrants have been listed by Clarke (94).

Acoustic emission and C-scan like X-ray radiography are widely used (95,96). Acoustic emission is based on the phenomenon that the sudden release of energy inside a material

results in emission of acoustic pulses. The acoustic signals are detected by piezoelectric transducers in contact with the specimen. Ultrasonic testing is described in more detail in the following section.

2 - 13.3 Ultrasonic Testing

Ultrasonic testing comprises a range of methods which make use of mechanical oscillations at frequencies above 20 KHz. These waves behave in a similar manner to light: they obey the laws of reflection and refraction. Ultrasound is used both to find imperfections in a component and to measure mechanical moduli. In flaw detection, pulses of ultrasound are reflected from boundaries to build up a picture of the interior of a component. These pulses are produced and received by transducers which are normally piezoelectric crystals. Once the reflected pulse is received from the flaw, it must be displayed to the operator in a convenient form. The method of achieving this are called scans and three most common are termed A, B and C (97). An ultrasonic A-scan refers to data presented as ultrasonic intensity amplitude on the y - axis against time on the x - axis. In a B - scan the position of defects is shown on a cross - sectional plane normal to the surface of the specimen and containing the axis of the pulse of the transducer in a single line scan. C scan gives a map-view of the component showing flawed areas but gives no information on depth of the flaw. C-scan is probably the most used non-destructive test method for composite materials. It is most effective in detecting delaminations (98, 99, 100) porosity (101) and inclusions in these materials. It is also useful for laboratory studies of damage initiation and progression. Ultrasonic C-scanning has also been used to study damage initiation and development in composite materials as a result of mechanical loading (102, 103).

There are two main test techniques for ultrasonic testing. The first is the pulse echo technique where the ultrasonic pulse is passed through one surface of the test specimen and the echo from the opposite surface or any defects is received by the same or another transducer. The time difference between the initial pulse and the echo is represented by a

horizontal trace on the oscilloscope whereas any defects are represented by the position and amplitude of the echoes.

Secondly, the through transmission technique, uses two transducers, one for transmitting and one for receiving the pulse. These are placed directly above and below the specimen and the pulse is sent from the transmitter to the receiver. The amplitude of the transmitted beam is reduced when it encounters a defect or a flaw. An alternative method to through transmission is double through transmission where the transmitter also acts as the receiver. This transducer is placed above the specimen while below the specimen is a glass reflector plate which bounces the transmitted pulse through the specimen and back up to the receiver. This method was used in the inspection of SMC specimens for this thesis.

The use and assessment of ultrasonic C-scan, X-ray radiography and a crack enhancement method for SMC materials has been discussed in reference (12, 104). Raghunath (12), has studied the impact damage in panels made of SMC using radiographic, ultrasonic and crack enhancement techniques and has concluded that the crack enhancement method provides separate measurements for both the front and the rear side of a damaged panel, whereas a single measurement taken across the panel thickness is obtained from the radiographic or the ultrasonic method. He (12) also concludes that the X-ray radiography is not a reliable method for assessing the damage in SMC panels at low impact speeds because, at these impact speeds, the internal cracks are generally not connected and consequently, sufficient radio-opaque penetrants can not be absorbed by panel to produce good radiographs. His (12) conclusion about the ultrasonic C-scan method is that C-scan identifies only part of the damage zone in SMC panels because a portion of the impact damage is masked by the attenuation of the ultrasonic waves due to the material nonhomogeneity. The impact damage modes, for SMC materials include local indentation, lateral and axial cracking, cracks on the front and back surfaces and internal fibre-matrix interface cracks, therefore, an individual technique can provide at best information on

only some of the damage characteristics and a combination of NDT techniques is desirable to obtain an overall picture of the damage state.

2 - 13.4 Residual tensile and compressive strength measurement

Impact damage may not be visually detectable on the surface of the structure but can cause considerable internal damage which may lead to failure at loads considerably less than the structural undamaged strength. Therefore evaluation of composite materials for impact damage resistance and damage tolerance will certainly need some other characteristic measurements besides the damage-zone size and shape. For structural integrity, knowledge about retained mechanical properties of the material after impact is very important. Residual strength can be a useful measure of damage in a composite as well as a means of screening materials for potential application in structures subjected to impact load such as turbine engine fan blades (105).

Compression testing of composites is one of the most difficult types of testing because of the tendency for premature failure due to crushing or buckling. Dorey (106) states that the specimens for tensile and compression tests after impact need to be large enough to contain the damage in the gauge section, and therefore for subsequent compression testing the specimens have to be stabilised against buckling. At the present time there is no standard anti-buckling device and each laboratory has developed its own as required. The only documented procedure for compression after impact tests are those that have been developed by the Aerospace companies, Boeing and Airbus and the recommended methods of SACMA and CRAG. A selection of anti-buckling devices are shown in figures 2.11 to 2.14. The high cost of producing specimens for full size Boeing / SACMA / Airbus has prompted interest from many laboratories in producing a miniaturised version of the test (107). Sjobolom et al (107) estimated that the cost for one data point (average of five tests) was $ 5000 when the NASA test (108) was used. A miniaturised version of

Boeing specimen has been developed by Hogg and co workers at Queen Mary and Westfield College in London (109). The QMW test specimen consists of a plate specimen 89 mm by 55 mm, which is 2 mm thick(109). The impacted plates are supported during compression using a variable fixture that resembled the larger Boeing fixture with the exception that instead of knife edge supports, the plates are supported by slotted side bars. A similar specimen has been examined in Japan (50 mm x 80 mm) and included as part of a round robin study for the test method. The results of both QMW studies and the Japanese programme indicate a high degree of correlation between the miniaturised test specimens and the full scale Boeing tests (109-110). The effect of anti-buckling devices is not very well understood. Compression tests on fully supported specimens and specimens with short unsupported gauge length yield similar data, except in the case of 0^0 specimens, when they give consistently lower values. This may be due to some premature buckling despite lateral support (111). Matondang et al (112) investigated the influence of anti-buckling guides on the compression fatigue behaviour of CFRP laminates. They maintain that holehedral type anti-buckling guides can produce misleading results if the support restricts local buckling which delays the spread of delamination. Since composite materials might be subjected to tensile and compressive load after impact, there has been some attempts to predict their strength.

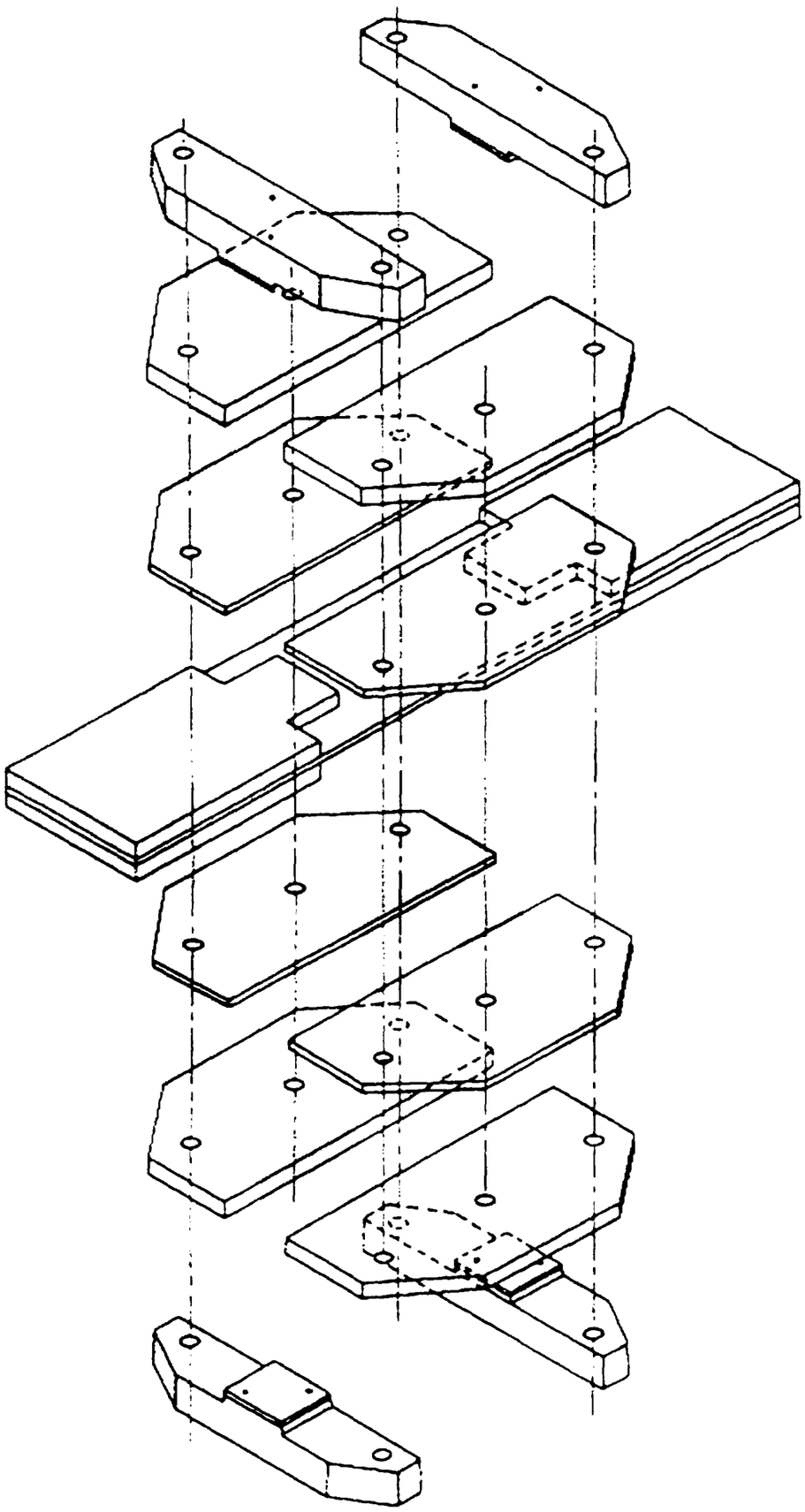

Figure 2.11 - Exploded view of DFVLR anti - Buckling device (113).

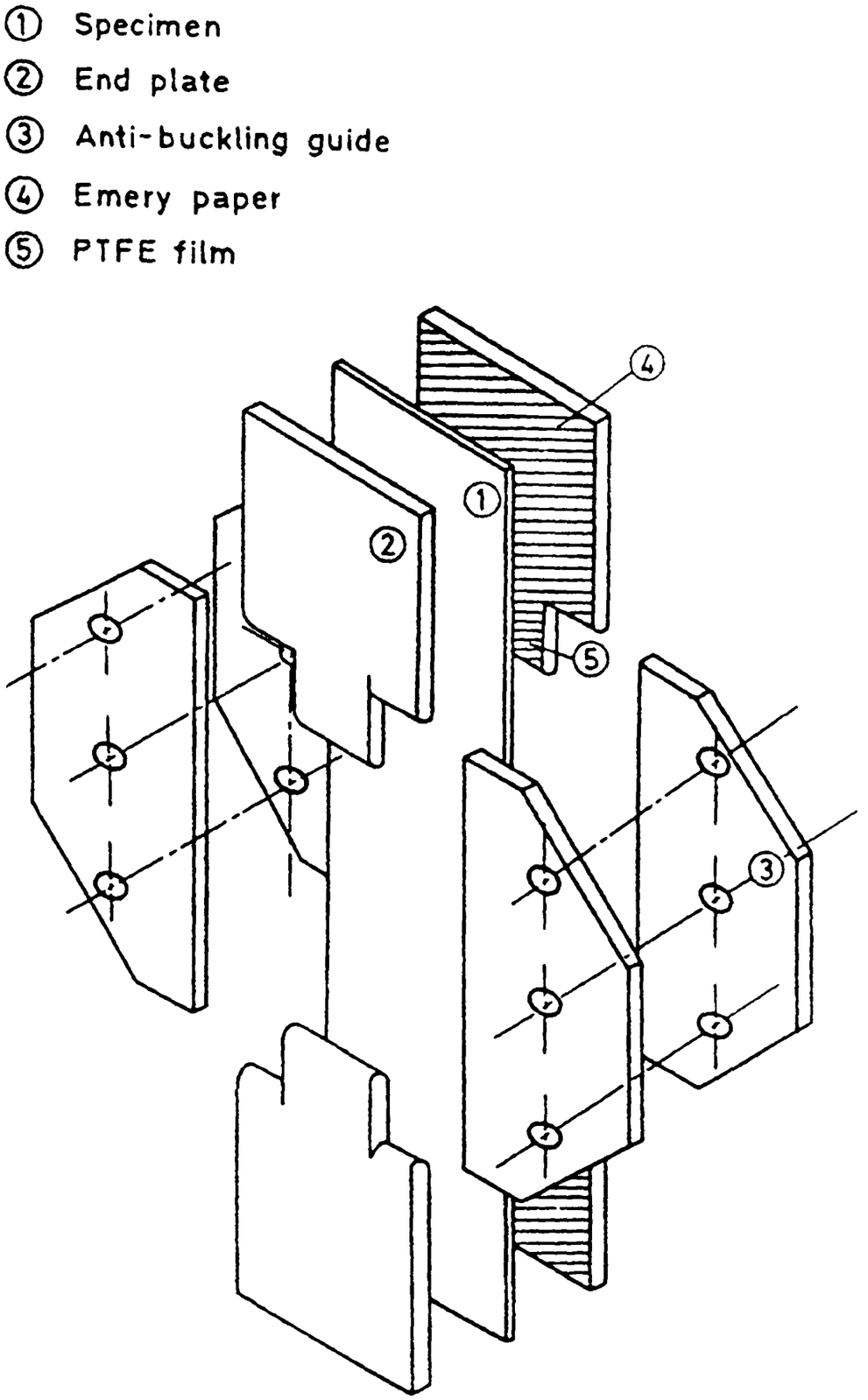

Figure 2.12 - Exploded view of ONERA anti - Buckling guide (113).

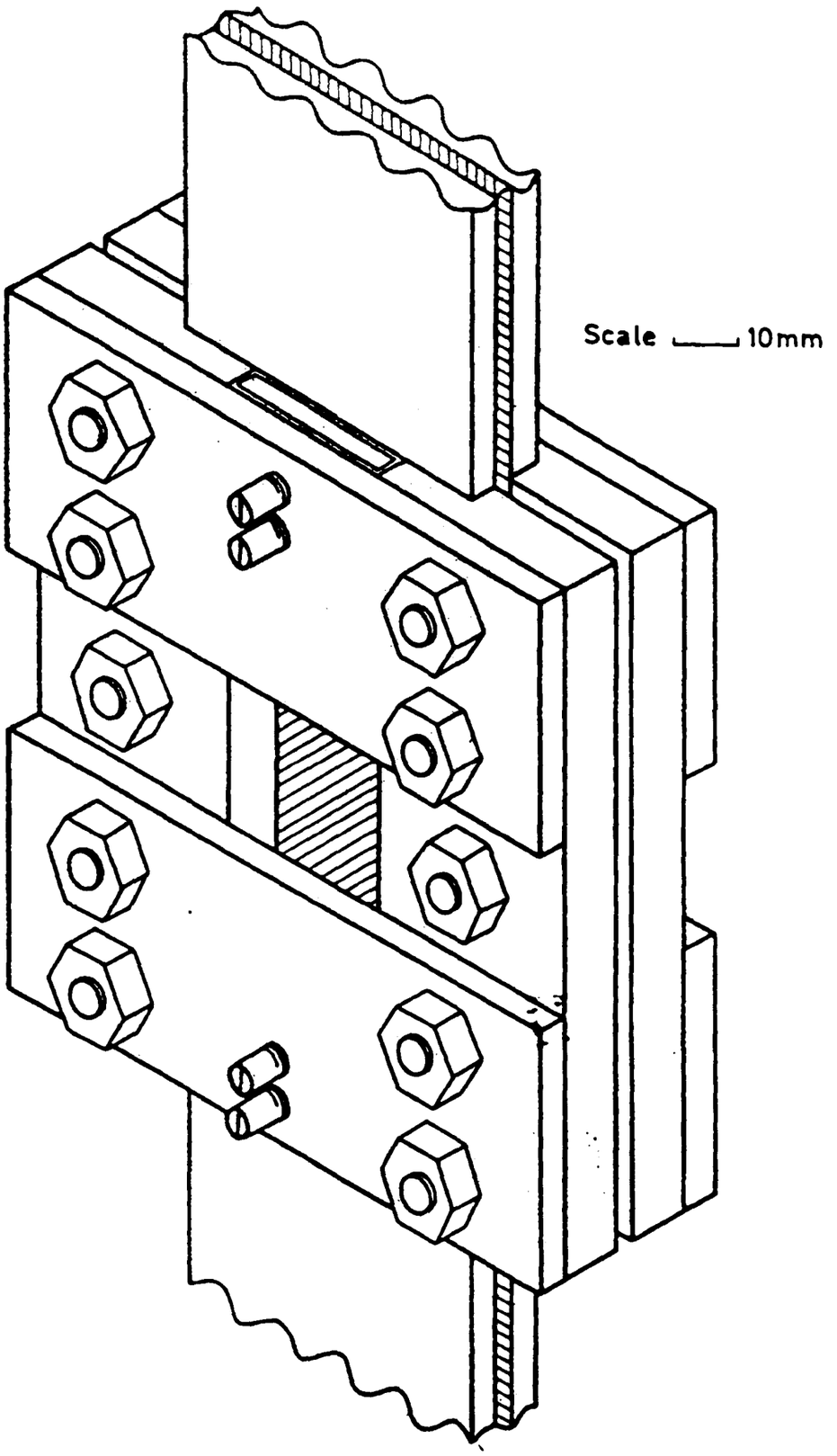

Figure 2.13 - Assembled view of RAE anti - Buckling guide (113).

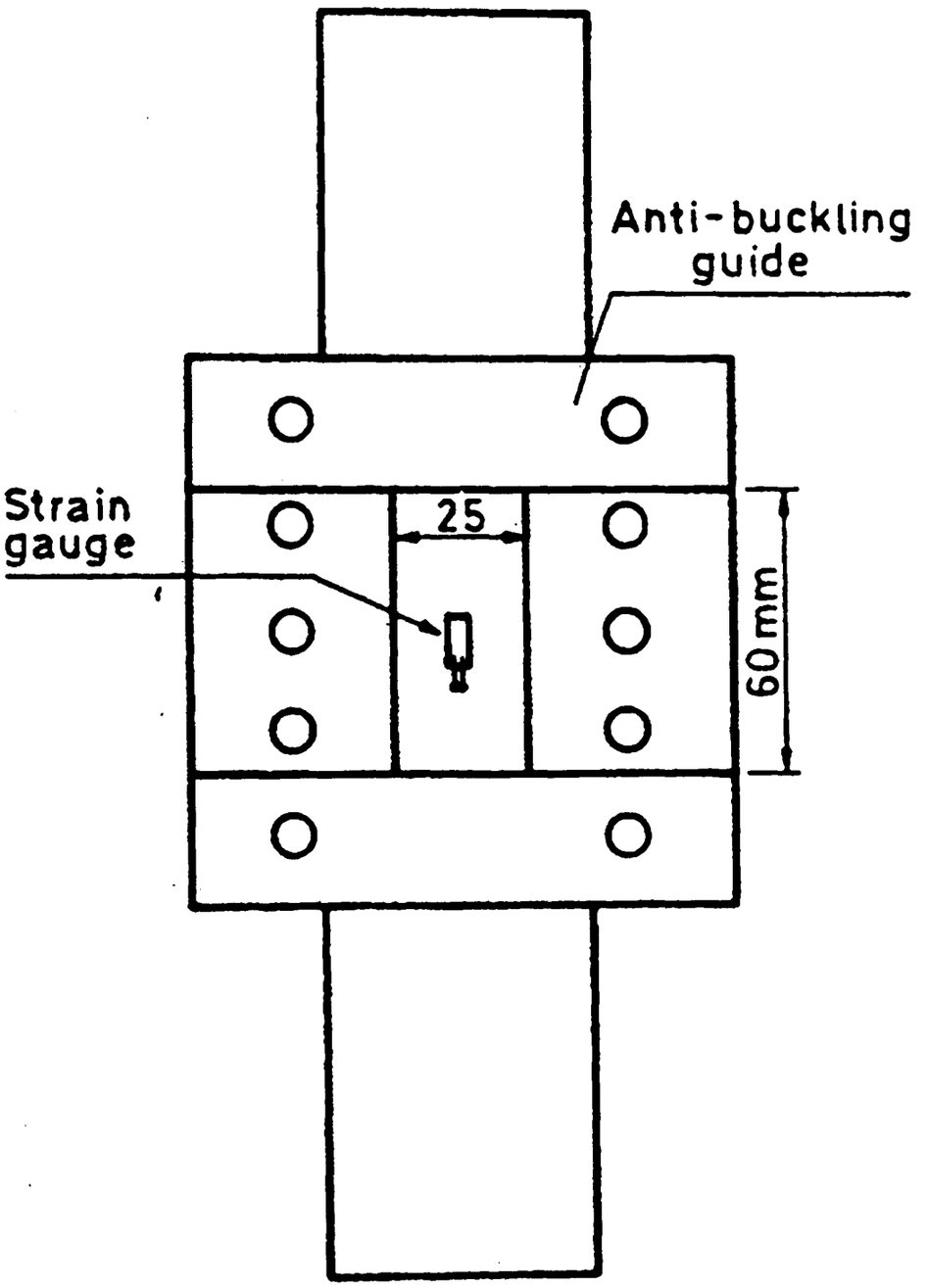

Figure 2.14 - NLR anti - Buckling guide (113).

2 - 13.5 Prediction of Residual Strength of composites after impact.

In most of the mathematical models for predicting the failure of fibrous composite materials, the global response of the composite is considered and the effects due to local material inhomogeneity are ignored.

Waddoups et al (114) proposed a fracture model, in which the notched and unnotched strength of the composites, σ_r and σ_0, are related to the crack length by the relationship

$$\frac{\sigma_r}{\sigma_0} = \sqrt{\frac{C_0}{C + C_0}}$$

where

σ_r = Residual strength

σ_0 = Undamaged strength

C_0 = Inherent crack length

C = Half-crack length

Husman et al (105) derived an analogy, in terms of residual strength, between the local damage inflicted by a small hard-particle impact and damage inflicted by implanting a crack of known dimensions in a static tensile coupon. They assumed that the difference between the energy density required to break an undamaged specimen and the energy density required to break an impacted specimen is directly proportional to the kinetic energy imparted to the specimen. It was further assumed that the kinetic energy is dissipated over some characteristic surface area, A_e, which is independent of the kinetic energy of the impact. The resulting relationship for residual strength in terms of the impact kinetic energy is:

$$\sigma_R = \sigma_0 \sqrt{\frac{W_S - K W_{KE}}{W_S}}$$

where

σ_R = Residual strength

σ_0 = Undamaged strength

W_S = Work / unit volume required to break undamaged specimen

W_{KE} = Kinetic energy imparted to experimental specimen

K = Effective damage area, $K = k/A_e$

k = Damage constant

A_e = Effective surface area

According to the above equation, the residual strength can be predicted as a function of kinetic energy of impact by executing two experiments, a static tension test on unflawed specimens and a static tension test on a coupon previously subjected to a single point impact. If the specimen is sufficiently wide so that the impact damage is reasonably well localised the K factor should be independent of specimen geometry. The value of K may however, depend on laminate stacking sequence and boundary conditions of the experiment (for example, cantilever specimen versus both ends clamped).

Caprino (115) points out that the variation of residual strength, as foreseen by Husman et al ' model (105) seems to be quite different if compared with the experimental results available in the literature. Caprino (115) proposed a model by which residual tensile and compressive strength of a laminate can be calculated as a function of the kinetic energy of the impacting body. The proposed model relies on a formula for residual strength prediction of notched laminates which has been based on linear elastic fracture mechanics concepts (116).

$$\frac{\sigma_r}{\sigma_0} = \left(\frac{C_0}{C}\right)^m \qquad (1)$$

In equation 1, σ_0 represents the strength of unnotched material, C_0 the dimension of a characteristic defect of the material and C the dimension of the notch. The parameter m, together with C_0 must be experimentally determined and depends uniquely on the examined material. Equation 1 is only valid for $C > C_0$. If the relation between C and U can be expressed by a power law, then

$$C = KU^n \qquad (2)$$

U = Impact energy

Because of the increase of C with the increase of U, it must be of course $n>0$

By substituting equation 2 into equation 1:

$$\frac{\sigma_r}{\sigma_0} = \left(\frac{U_0}{U}\right)^\alpha \qquad (3)$$

where

$$\alpha = mn \qquad (4)$$

and U_0, given by:

$$C_0 = KU_0^n \qquad (5)$$

is the energy producing a damage corresponding to an equivalent notch of dimension C_0; therefore, it represents the maximum energy level the material can support without any strength degradation.

Equation 3 gives a model for predicting residual strength as a function of impact energy, provided U_0 and α are experimentally determined. Caprino's model has been employed in the present work and will be discussed further in chapter 7. Equation 3 foresees a continuous reduction in strength with increasing impact energy because of the cumulative damage law assumed in equation 2. In fact, it is natural to infer that the proposed model will fail for kinetic energies higher than the complete penetration threshold. Beyond this limit, a constant residual strength can be expected, except for velocities so high that the fracture modes of the material are changed. In this last case, it has been shown (105) that residual strength undergoes a recovery, approaching the value resulting from a drilled hole having the same diameter as the impacting tup (105). The model proposed by Caprino (115) seems to be effective in predicting not only residual tensile strength but also residual compressive strength of composite laminates.

It is important to recognise that all these 'models' are only curve fitting procedure that use u_0 and α to force fit a curve to experiment and do not model the behaviour in any fundamental way using knowledge of fracture and materials properties.

2 - 14 Sheet Moulding Compound (SMC)

Sheet moulding compound (SMC) may be defined as a moulding compound in sheet form, which is composed of a thermoset resin, fibrous reinforcement, filler and additives required for processing or specific product performance. Historically, SMC has usually contained polyester resin and glass fibre reinforcement. However, other resin types, such as vinyl ester and epoxy, are finding increased use in SMC.

A typical formulation for a sheet moulding compound is given below:

Polyester resin	100
t-Butyl peroxybenzoate (95%)	2-3
Zinc stearate (release agent)	3-4
Magnesium oxide (thickening agent)	2-3
Pigment dispersion	5-8
Filler	140-180
Thermoplastic additive	5-20
CSM or chopped rovings	50-100

The resins formulated for SMC production should have low initial viscosity to ensure thorough wetting of the glass reinforcement. However, once the glass has been wetted the resin must thicken so that a relatively tack-free easy to handle sheet of moulding material is produced. This thickening is usually brought about by the addition of a thickeninig agent such as calcium oxide or magnesium oxide to the resin (117). The filler is added to reduce the amount of resin required per moulding and hence to reduce cost.

A system of nomenclature has been devised to describe the fibre configuration and content in SMC. SMC- R is defined as random fibre SMC. It contains discrete fibres oriented randomly within the plane of the sheet as shown in figure 2.15. Although the random fibres may be of any length, usually they are cut to specific lengths from 12 mm to 50 mm. SMC - C contains unidirectional continuous fibres. SMC - D contains unidirectional fibres of discrete length, usually from 100 mm to 200 mm. A number following the R, C or D designates the weight percent of fibres in the SMC. For example SMC - R50, contains 50 % by weight chopped glass fibres randomly oriented in the plane of sheet (8). Combination of continuous and random (SMC - C/R) or directional and random fibres (SMC - D/R) as illustrated in figure 2.16 can be produced in a single SMC sheet.

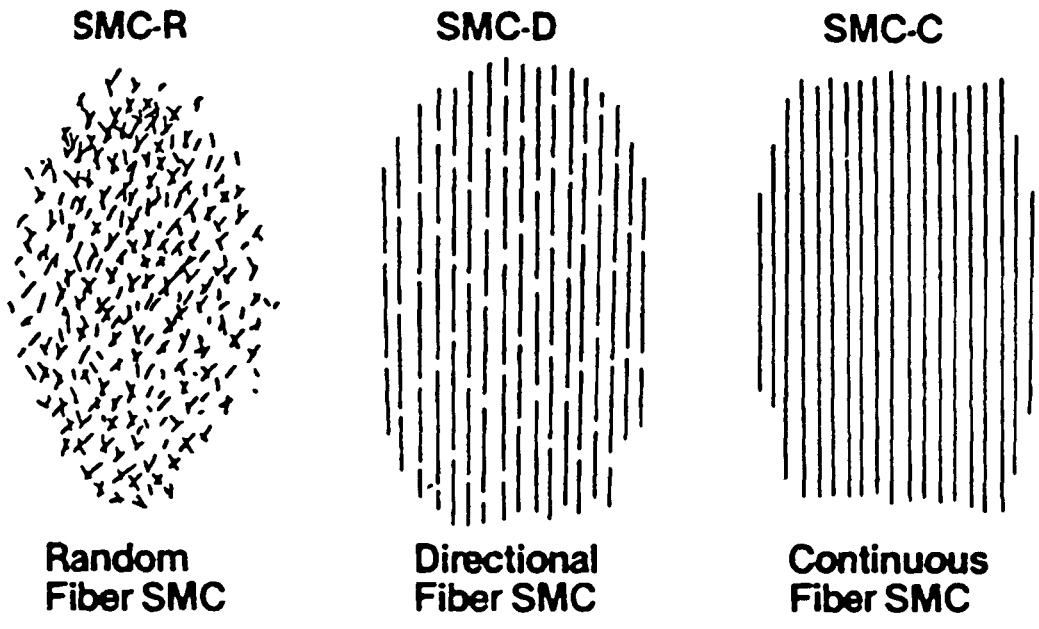

Figure 2.15 - SMC type designates reinforcement configuration used.

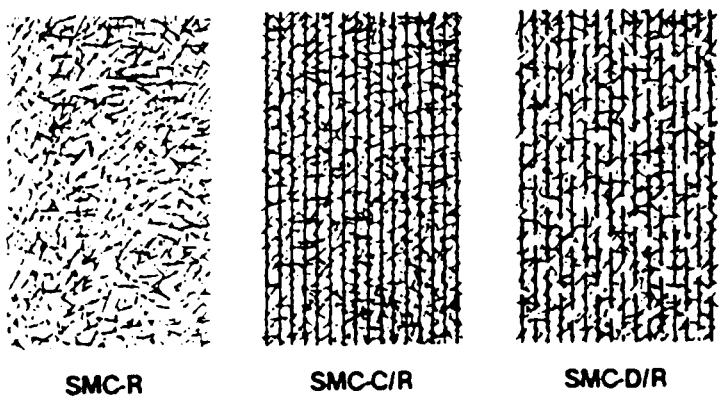

Figure 2.16 - Combination of fibre configurations

2 - 14.1 Manufacture Of SMC

A continuous polyethylene or cellophane film is coated with a suitably formulated polyester resin system into which is deposited a layer of either chopped strand mat or chopped rovings. A second layer of polyethylene film, similarly coated with resin system, is placed over the reinforcement and the sandwich thus formed is passed through a series of rollers to press the glass fibres into the resin and ensure thorough wetting of the reinforcement by the resin. The sandwich is then wound into a roll and allowed to stand while the resin thickens (fig. 2.17). In use the SMC is cut to required shape and both layers of polyethylene film are removed. Then the required number of layers sandwiched together, placed in the mould and pressed under pressure and temperature (117). Pressure, temperature and cure time depend on the particular resin formulation used and component thickness. The moulding temperature for 30% glass content is 150 °C and the pressure is 3 - 7 MPa. Cure time for a typical polyester sheet moulding compound is around one minute per millimetre of wall thickness.

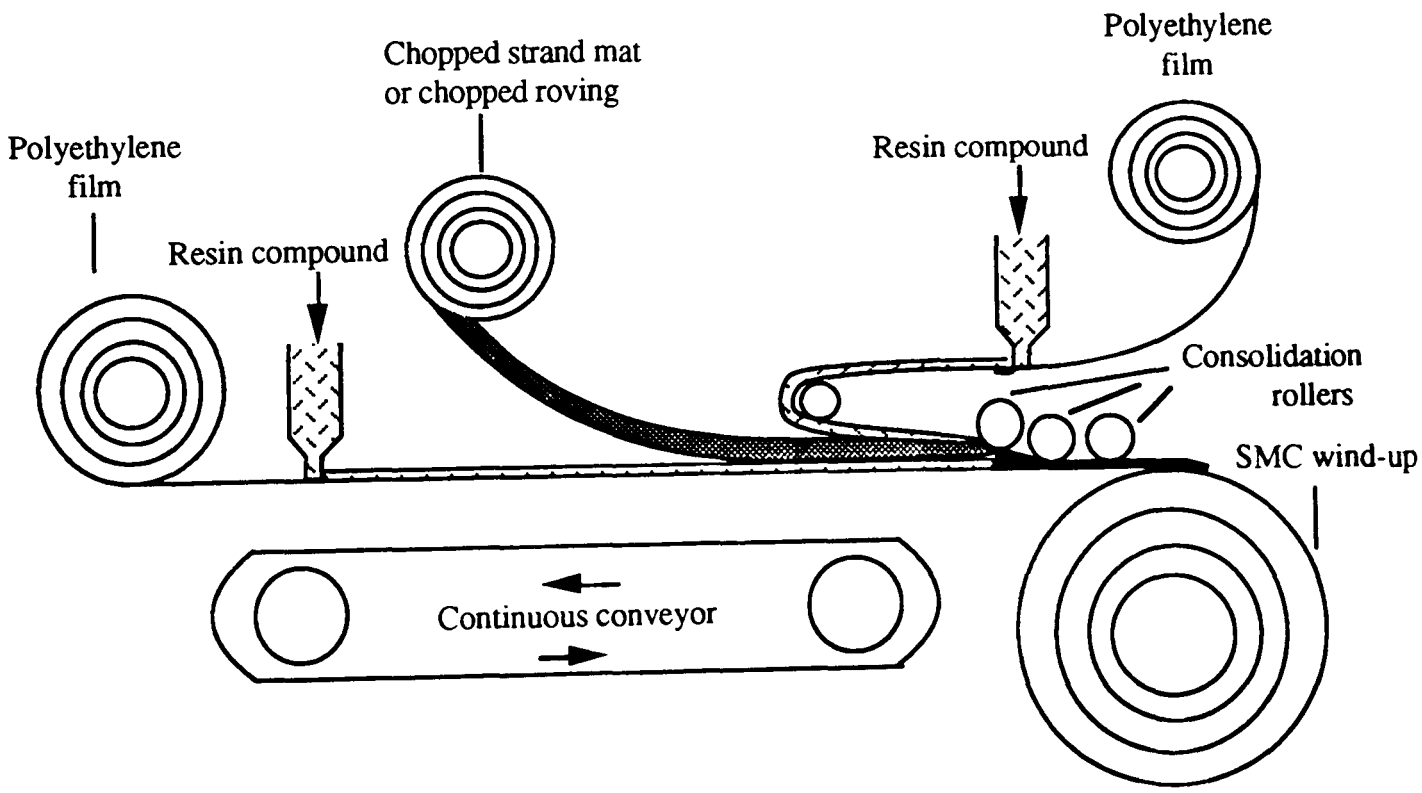

Figure 2.17- Manufacture of SMC.

2 - 14.2 Mechanical Properties Of SMC

Mechanical properties of SMC is mostly depends on the level of glass fibre, filler content and the level of voids and flaws. It has been reported that this material has a scatter in its mechanical properties as large as 40% (118). The main cause of variability in the mechanical properties of SMC is flow during moulding. The initial 'charge' may only fill two thirds of the mould, flowing into the remainder as pressure is applied. Thus considerable flow may take place in some regions of the mould which affects the initial random fibre distribution. The typical mechanical properties of SMC-R50 is listed in table 2.8.

Table 2.8 - Typical mechanical properties of SMC-R50 at room temperature courtesy of Denton (8).

Tensile Modulus in GPa	15.6 ± 0.2
Tensile Strength in MPa	164 ± 3
Elongation at failure in percent	1.73 ± 0.04
Fatigue Limit in MPa	65
Creep, 1000 hrs at 50% ultimate stress, in percent strain	0.85
Compressive Modulus in GPa	15.9 ± 0.4
Compressive Strength in MPa	225 ± 7
Flexural Modulus in GPa	14.0 ± 0.2
Flexural Strength in MPa	314 ± 5
Shear Modulus in GPa	5.9 ± 0.2
Shear Strength in MPa	62 ± 3
Short Beam Shear Strength in MPa	24.7 ± 0.6
Izod Impact Strength	
Notched in KJ / m	1.04 ± 0.03
Unnotched in KJ / m	1.54 ± 0.05

Chapter 3

Experimental Procedure and Mechanical Characterisation of SMC and SMC with a layer of Stainless Steel

3 - 1 Manufacture of Test Materials and Specimens

The materials used in this study consisted of a compression moulded SMC, stainless steel, aluminium, copper, brass and Ionomer. The SMC was supplied ready moulded in plaques 102 mm by 264 mm with a nominal wall thickness of 2, 4, 6 and 8 mm. The resin system was Scott Bader Crystic D4029 and the nominal glass content was 30 % by weight, as the material was designated SMC-R30.

The steel sheet was a nickel-chrome type 304 stainless steel, with thicknesses ranging from 0.6 mm to 2 mm. The aluminium sheets were grade 5L16 and L156, thickness 0.6 mm. The SMC-steel laminates and SMC-aluminium laminates were prepared by directly moulding the SMC onto the steel sheet and aluminium sheet which had been primed by the application of Scott Bader primer, Crestomer 1163. By varying the charge of SMC with a constant thickness of steel and aluminium, laminates 102 mm by 264 mm were prepared with a range of wall thicknesses ranging from 2.6 to 10 mm. All moulding was performed by Scott Bader Ltd. Some additional laminates consisting of single sheets of stainless steel or aluminium bonded to pre-moulded SMC sheet by a Permabond adhesive type F241 were manufactured at QMW.

All specimens used for impact and slow tests were 6 cm squares which were cut from the moulded plaques using a fine band saw. Since heat may affect the mechanical properties of the material, special care was taken to avoid excess heating during cutting out the specimens.

The glass contents of different batches of SMC were measured using the test specification developed by General Motors Technical Centre (119). In this technique the SMC sample is weighed in air and then burned at about 650 ℃ for about one hour. After burning off the resin and dissolving the filler in diluted hydrochloric acid(2.33 M HCl) for 20 minutes the remainder was filtered using ashless filter paper. The filtered sample and the paper is then placed in an oven heated at 480 ℃ which removes the excessive water and burns off the filter paper leaving behind the glass content. Knowing the weight of SMC sample (W_{SMC}) and the weight of glass fibre (W_G), the weight percent of glass can be calculated from :

$$\text{Weight percent of glass} = 100 \times W_G / W_{SMC}$$

The variation from batch to batch was less than 3% and the nominal glass content was 30% by weight.

The typical composition and mechanical properties of the stainless steel and aluminium as specified in standard data sheets are listed in tables 3.1 to 3.2.

Table 3.1 - Typical properties of Stainless Steel type 304.

Property	Units	
Tensile Strength	MPa	586
Tensile Modulus	GPa	210
0.2 % Yield Strength	MPa	241
Hardness	BHN	150
Elongation in 50 mm	%	55

Table 3.2 - Typical Composition and Properties of Aluminium

Specification	Al%	Cu%	Si%	Fe%	0.2% Proof stress, MPa	UTS MPa	Elongation %
5L16	99	0.1	0.5	0.7	52	110-140	6
L156	93	3.9-5	0.5-0.9	0.5	255	400	28

Since SMC is not a homogeneous material the value of ultimate tensile strength, Young's modulus and the other mechanical properties varies from one specimen to another and from one batch to another. In order to have some idea about the variation of mechanical properties of the SMC materials which have been used in this work a broad range of testing methods were used throughout the experimental programme.

3 - 1.1 Tensile Test

Tensile tests were carried out only in the plate direction on different batches of supplied SMC. Five specimens were machined from moulded plates using the size (fig. 3.1) which has been specified by ASTM D638 (120). Tensile specimens were pulled at a constant crosshead speed of 5 mm/min. Strain was measured over a distance of 50 mm in the centre of the gauge area with an extensometer. All data was collected on an x-y plotter provided with the testing machine. Modulus measurements were based on the initial straight line portion of the stress-strain curves. A typical stress-strain curve obtained from the tensile test is shown in figure 3.2. The curve can be described as having two linear regions with a short non-linear transition phase in between. It has been well recognised (8,121) that a knee-point in the curve (fig. 3.2) corresponds to the initiation of a significant number of matrix cracks at relatively low strains. Beyond this stress level the matrix cracks lengthen and multiply and thus the modulus is reduced.

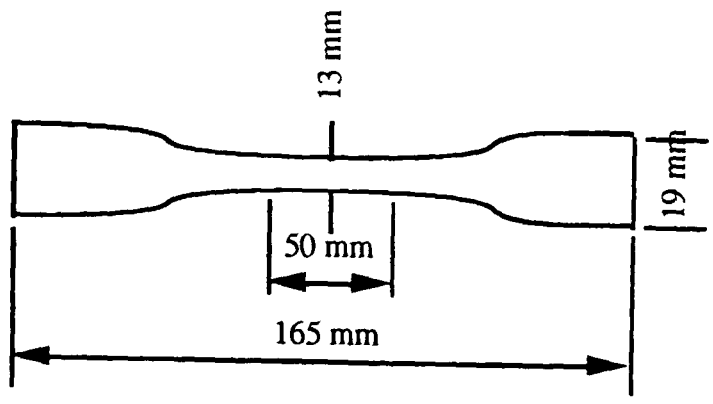

Figure 3.1 - The typical dimension of a tensile test specimen.

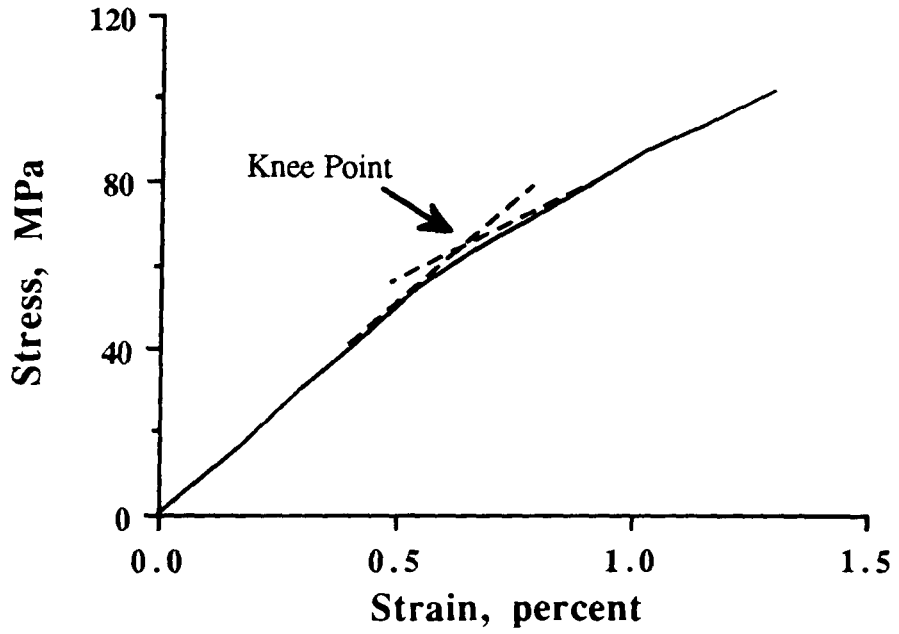

Figure 3.2 - The typical Stress-strain curve for SMC from tensile test experiment.

Tabulation of the means and other basic statistics for the tensile strength, modulus and strain at failure is shown in table 3.3.

Table 3.3 - Tensile properties of SMC-R30

Property	Units	Mean	Standard Deviation	%Coefficient of variation
Ultimate Tensile Strength	MPa	104	8.82	8.4
Tensile Modulus	GPa	13.7	0.53	3.9
Strain at failure	%	1.26	0.02	1.5

3.1.2 - Flexure test

Flexural properties of SMC -R30 were determined using Method I (three point bending) of ASTM D790 (122). The flexural test specimens were 80 mm long and 10 mm wide (fig. 3.3). The tests were conducted with a constant crosshead speed of 1.7 mm / min and a span to thickness ratio of 16:1. A typical load-deflection curve obtained during the three point bend of SMC-R30 is shown in figure 3.4. The tabulated flexural strength and modulus values which are the results of five tests are shown in table 3.4.

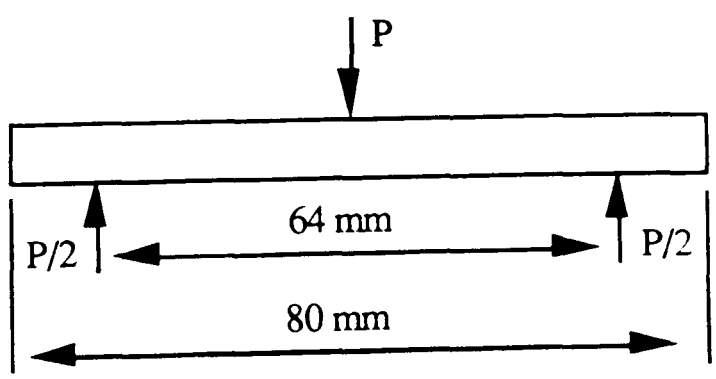

Figure 3.3 - Flexural test loading diagram.

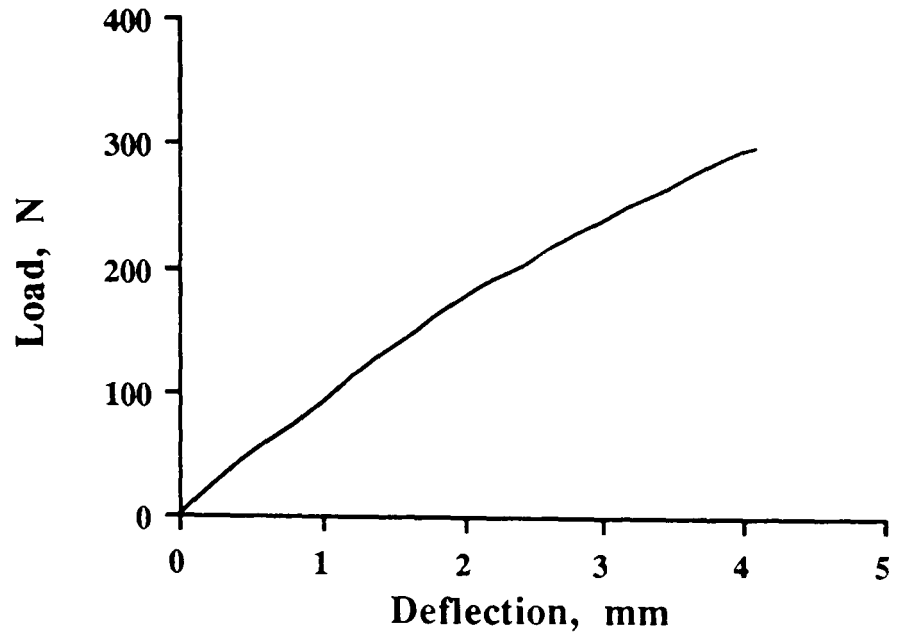

Figure 3.4 - A typical load-deflection curve for SMC from the three point bend test experiment.

Table 3.4 - Flexural properties of SMC-R30

Property	Units	Mean	Standard Deviation	%Coefficient of variation
Flexural Strength	MPa	176	21.29	12
Flexural Modulus	GPa	12.9	1.15	8.9

3.1.3 - Compression test

Compression properties of untabbed SMC-R30 were determined using procedure B of ASTM D3410 (123). The compression test specimens were 140 mm long, 6.3 mm wide with a very short unsupported gauge length of 12.7 mm. The specimen, grips, and IITRI loading fixture assembly which was employed in this work is illustrated in figure 3.5. Strain values were measured by employing two strain gauges glued to specimens in

0^0 and 90^0 direction. By dividing strain in the 0^0 and 90^0 directions the value of poisson's ratio can be determined. The speed of test was 1.2 mm/min. Compressive load and strain were recorded over the full range of the test and a typical stress-strain curve for SMC from a compression test experiment is shown in figure 3.6.

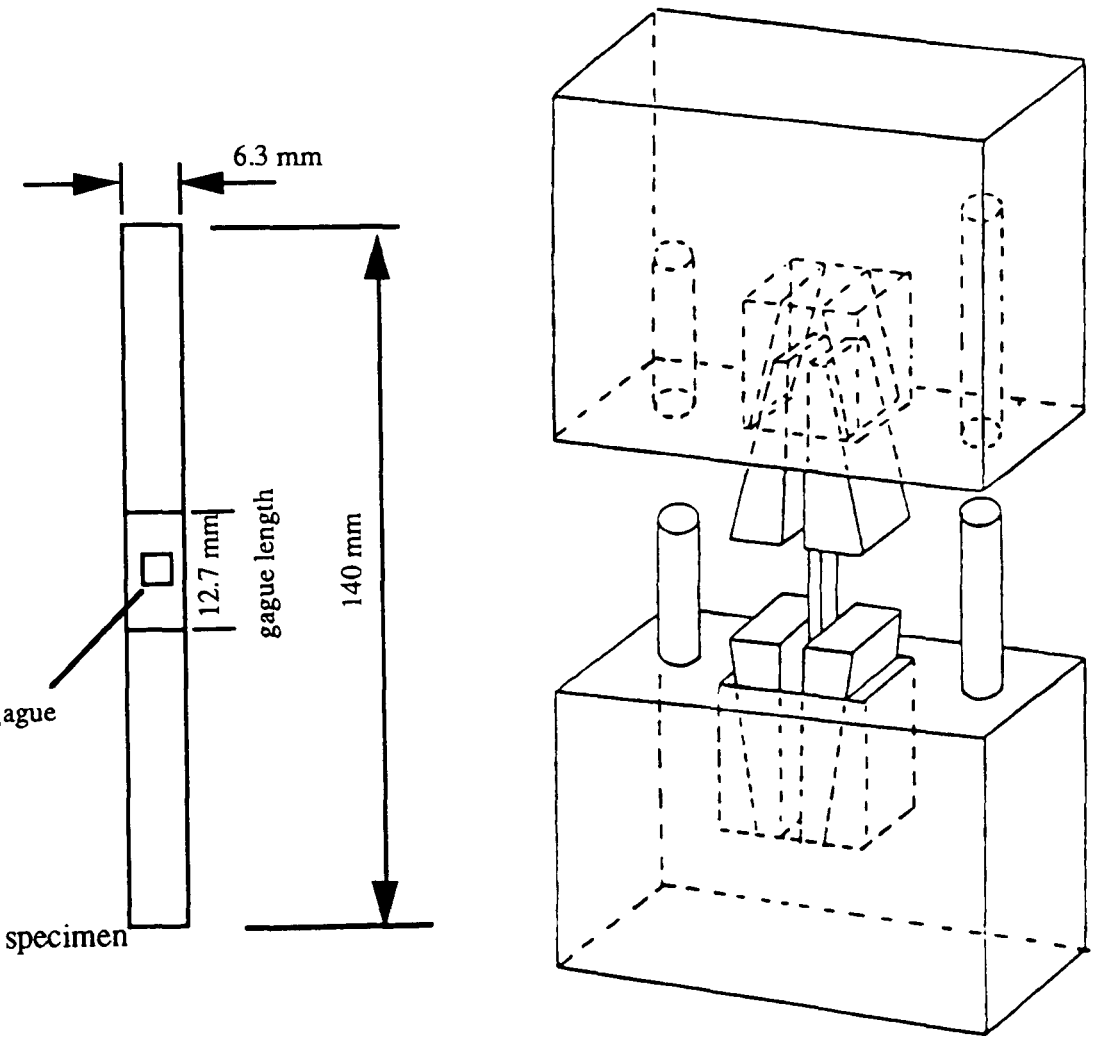

Figure 3.5 - IITRI compression specimen and fixture.

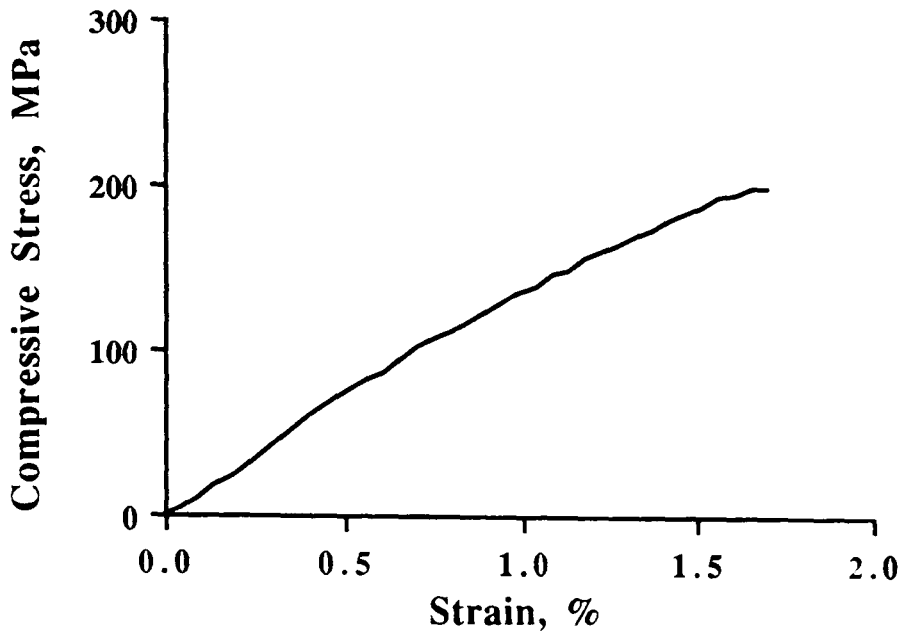

Figure 3.6 - A typical stress-strain curve for SMC in compression.

The mean compressive strength and modulus for five specimens are presented in table 3.5.

Table 3.5 - Compression properties of SMC-R30

Property	Units	Mean	Standard Deviation	%Coefficient of variation
Compression Strength	MPa	192	14.1	7.3
Compression Modulus	GPa	13.4	1.02	7.5

3.1.4 - Shear test

The inplane shear modulus and the inplane shear strength were determined using the two rail shear test method proposed by ASTM D4255 (124). Schematics of the two rail test fixture and two rail specimen is shown in figure 3.7. Strain gauges were glued to each specimen to provide measurements required for the calculation of shear modulus. Some

of the specimens slipped in the fixture when the material was tested to failure. This allowed specimens to come into contact with the bolts, which could act as local stress risers. Figure 3.9 shows the specimen which failed at a bolt holes.

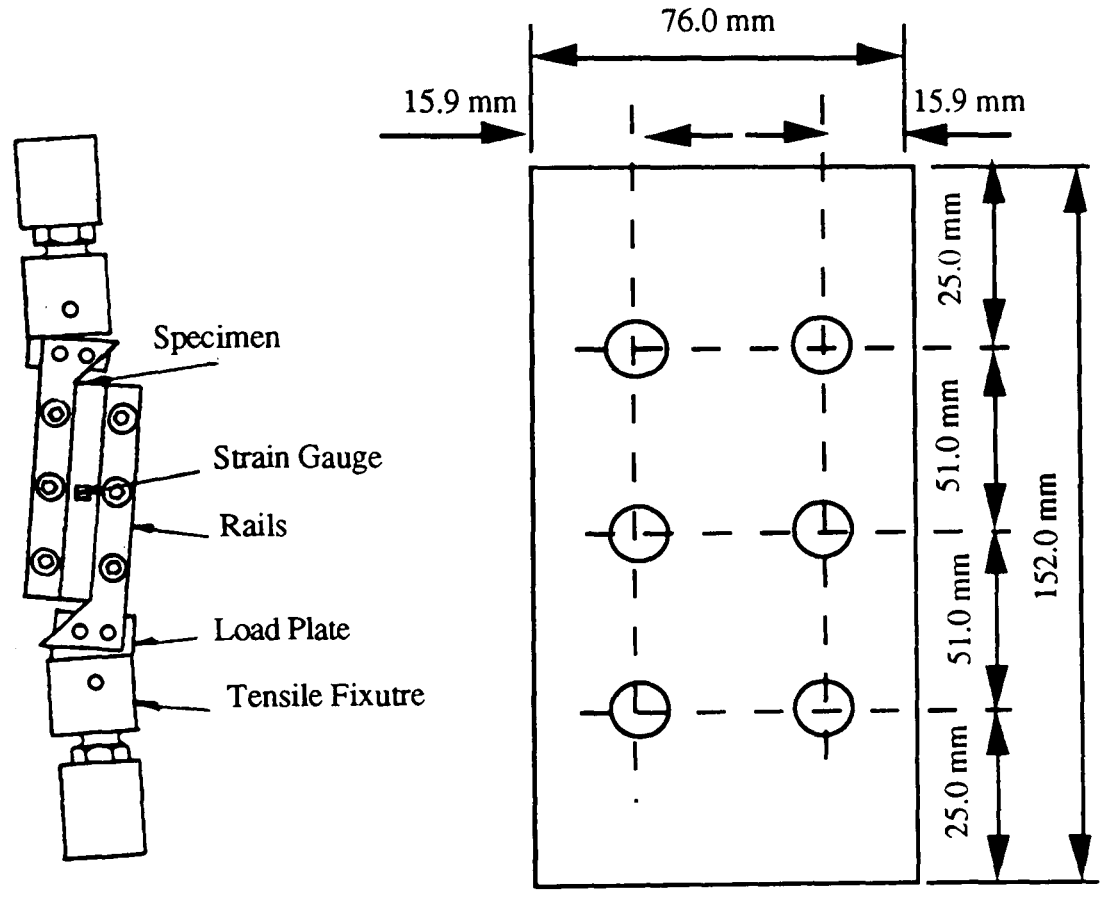

Figure 3.7 - Specimen and apparatus used for two rail shear test.

A typical shear stress - shear strain relationship for SMC-R30 which was obtained using two rail shear test method is shown in figure 3.8.

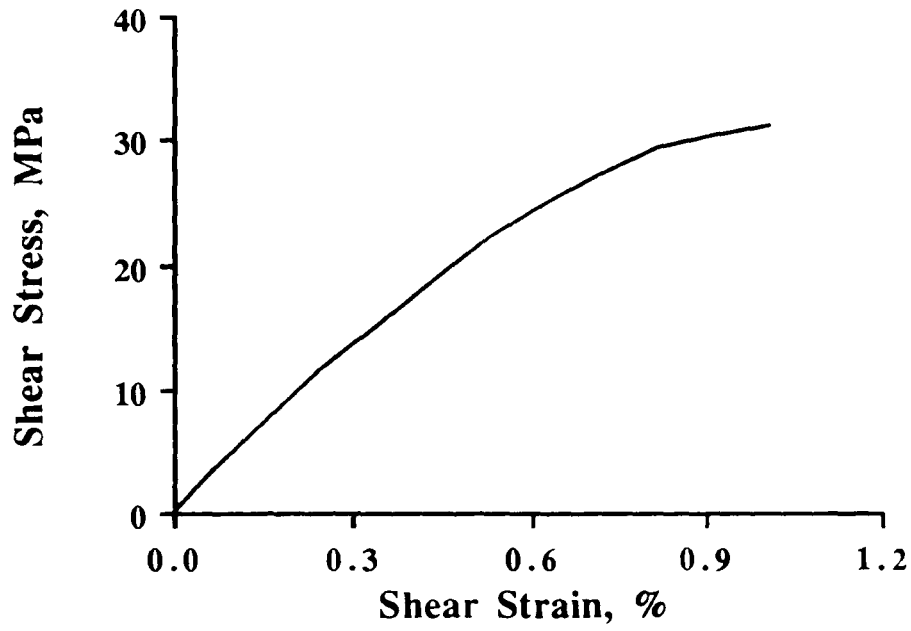

Figure 3.8 - A typical shear stress-shear strain curve for SMC from the two rail shear test experiment.

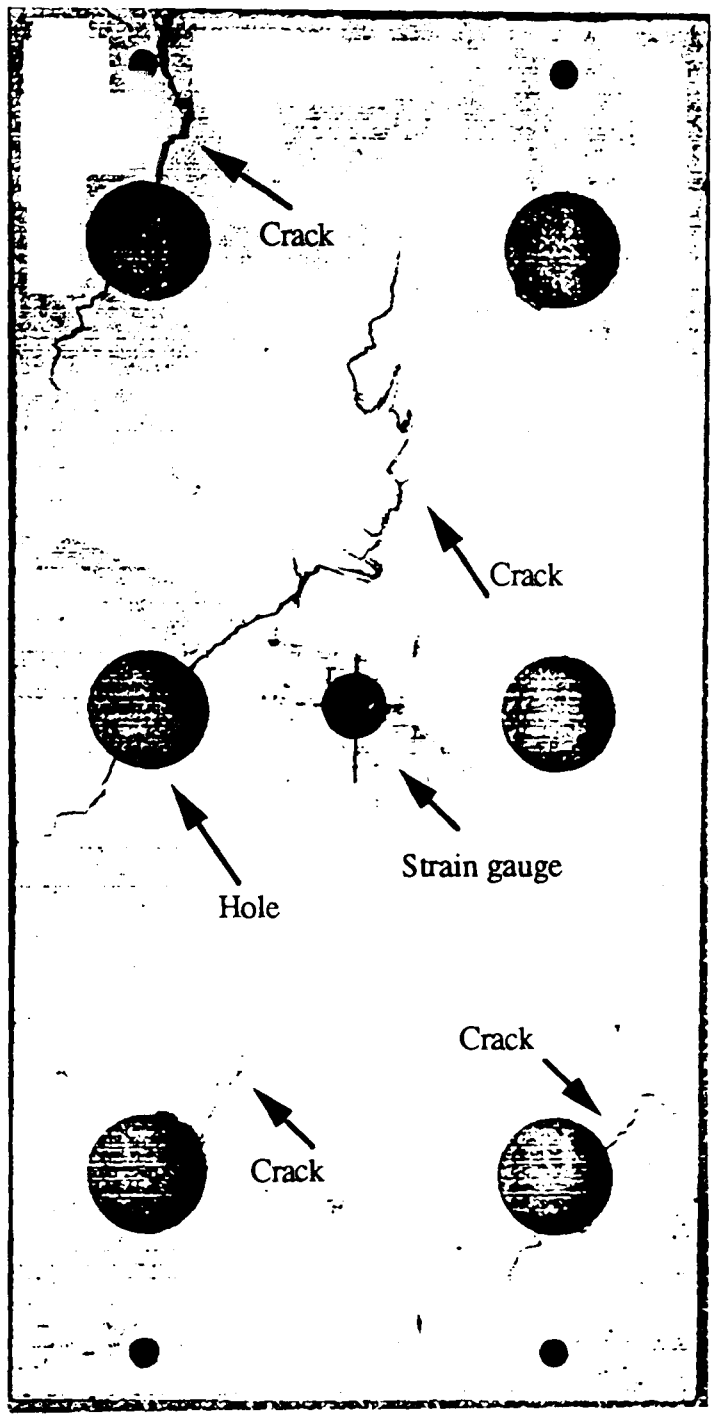

Figure 3.9 - Typical failure of two rail shear specimens.

The tabulated shear strength and modulus values for five specimens which did not fail from the bolt holes are shown in table 3.6.

Table 3.6 - Shear properties in the two rail shear test for SMC-R30

Property	Units	Mean	Standard Deviation	%Coefficient of variation
Shear Strength	MPa	36	5.7	10
Shear Modulus	GPa	4.6	0.24	5.3

3.1.5 - Short Beam Shear Test

Short beam shear tests were performed in accordance with ASTM D 2344 (125). Close examination of the specimens showed cracks across the bottom surface of the specimens which was an indication that some of the specimens did not fail in shear. The short beam shear test does not appear to give reliable interlaminar shear strength results for SMC, however, the values presented in table 3.7 which are the results of five tests do present a lower bound on the interlaminar shear strength.

Table 3.7 - Results of Shear strength measured by short beam shear test.

Property	Units	Mean	Standard Deviation	%Coefficient of variation
Shear Strength	MPa	25.9	3.0	11.5

3.1.6 - Charpy Impact

The charpy impact behaviour of SMC -R30 was measured according to ASTM D256 (15). The charpy impact test specimen which was used in this work is shown in figure 3.10.

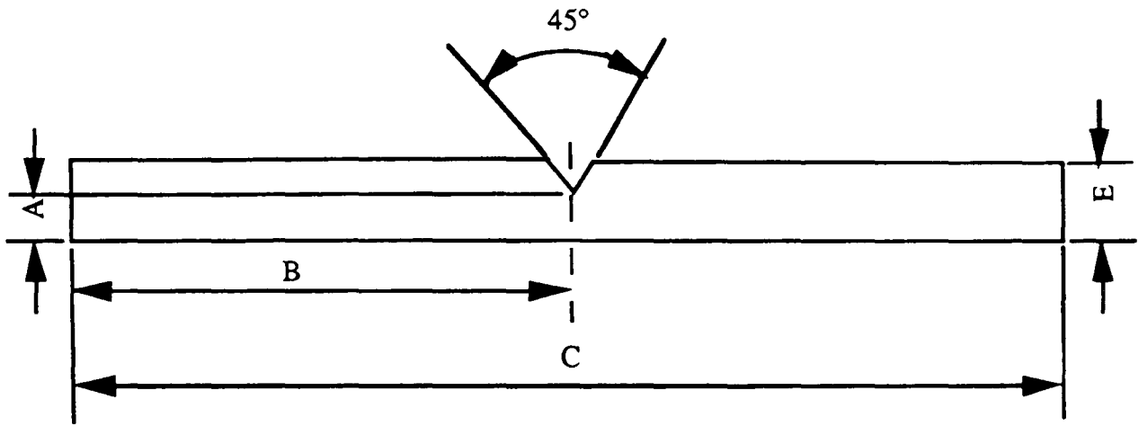

mm

A 10.16 ± 0.05
B 63.50 max
61.00 min
C 127.00 max
124.50 min
E 12.70 ± 0.15

Figure 3.10 - Charpy impact test specimen.

The charpy impact test machine was instrumented and the force-time of the SMC specimen was obtained during the test. Five specimens were tested and the typical force-time which has been obtained during the charpy test is shown in figure 3.11.

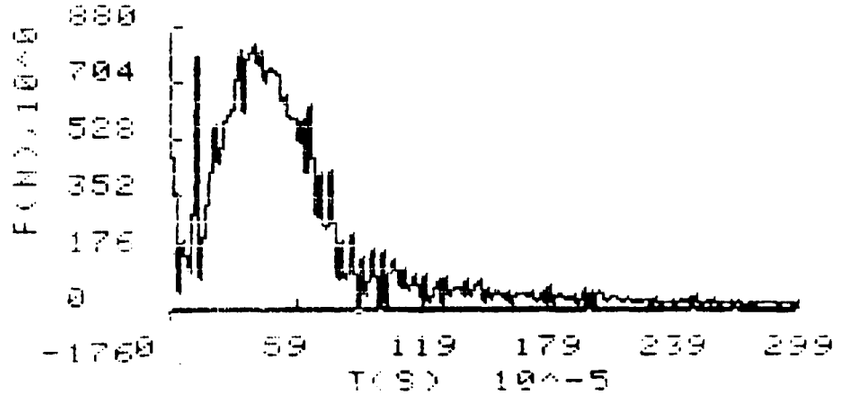

Figure 3.11 - Typical force-time curve for 4 mm SMC - R30 obtained from charpy the test.

The tabulated results of maximum load and energy absorbed by SMC during charpy impact test are shown in table 3.8.

Table 3.8 - Charpy impact properties for SMC-R30.

Property	Units	Mean	Standard Deviation	%Coefficient of variation
Max Load	N	910	30.19	3.3
Absorbed Energy	KJ/m^2	42	4.45	10

3.1.7 - Lap Shear Test

At the start of the experiment it was believed that the bond strength between the stainless steel layer and SMC might affect the impact behaviour of SMC. To investigate this possibility, the values of the bond strength are required. In order to measure the bond strength, 25 mm wide, 100 mm long specimens (fig. 3.12) were cut from the supplied SMC+S.S. laminates and were subjected to lap shear test. The values obtained were in the range of 2.99-3.88 MPa.

A series of lap shear tests were also performed on the SMC bonded to stainless steel by a Permabond adhesive type F241 using the lap shear strength specimens shown in figure 3.12. The lap shear strength measured was found to be 3.47-4.6 MPa.

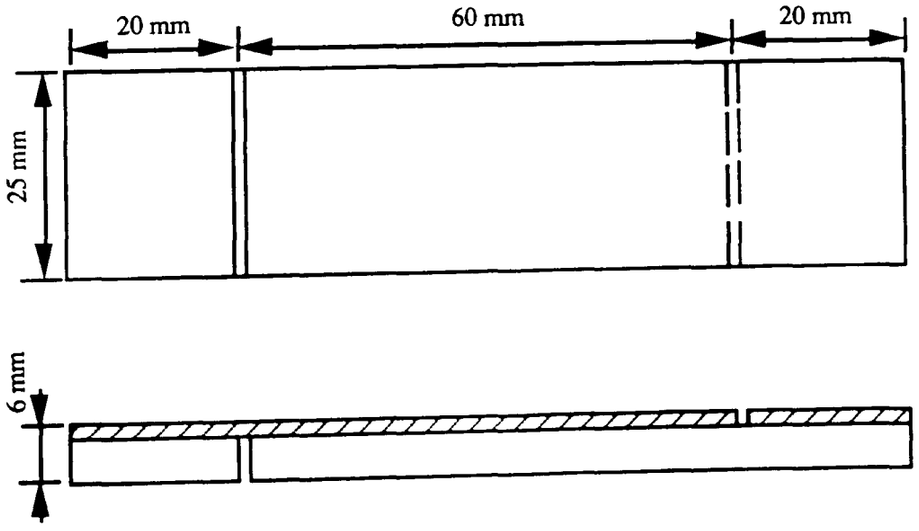

Figure 3.12 - Lap shear strength specimen.

3 - 2 Mechanical Properties of Stainless Steel lined - SMC Composites

In order to find out the effect of a thin layer of stainless steel on the load carrying capacity of SMC, tensile and flexural tests were carried out on stainless steel, SMC and SMC-stainless steel. The following sections explains the methods at which the tests were carried out and also the results from these tests.

3.2.1 - Tensile Test

Tensile tests were carried out on 4 mm SMC, 0.6 mm stainless steel and 4 mm SMC with a layer of 0.6 mm stainless steel. Tensile tests specimens were 250 mm long and 25 mm wide. Five specimens were tested in each case at the crosshead speed of 5 mm / min. The typical stress strain curves for 4 mm SMC, 0.6 mm stainless steel and 4 mm SMC with a layer of 0.6 mm stainless steel are shown in figure 3.13.

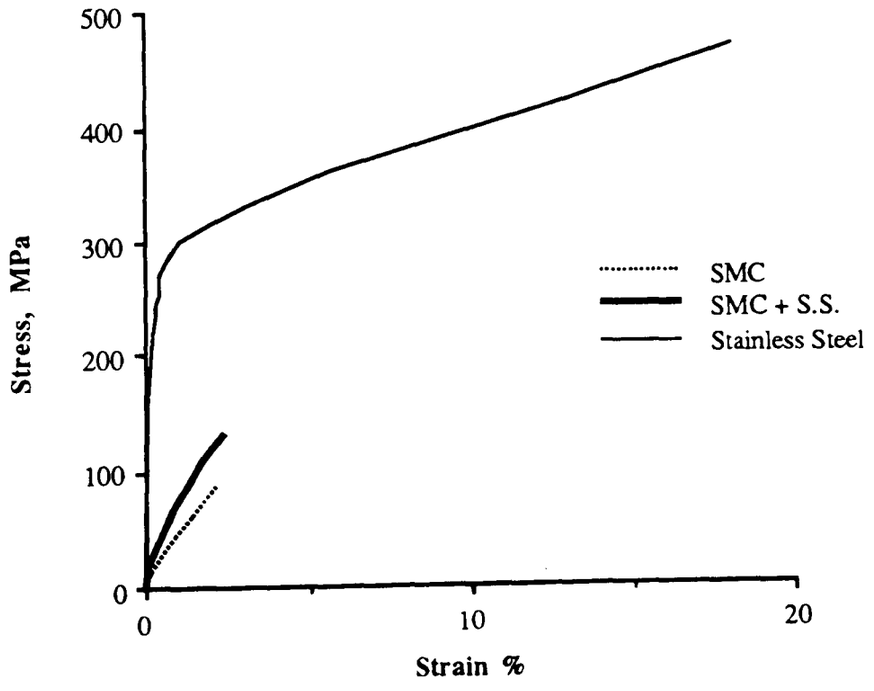

Figure 3.13 - Tensile curves for 4 mm SMC, 0.6 mm stainless steel and 4 mm SMC with a layer of 0.6 mm stainless steel.

Strain was measured over a distance of 50 mm in the centre of the gauge area with an extensometer. All data was collected on an x-y plotter provided with the testing machine. Modulus measurements were based on the initial straight line portion of the stress-strain curves (fig. 3.13). The tensile properties for SMC with a layer of stainless steel together with the data for SMC and stainless steel is shown in table 3.9. The prediction for tensile modulus for 4 mm SMC with a layer of 0.6 mm stainless steel, using rule of mixtures is 38 GPa.

Table 3.9 - Tensile properties of SMC, stainless steel and 4 mm SMC with a layer of 0.6 mm stainless steel. Standard deviations in parenthesis.

Material	Tensile Modulus, GPa	Tensile Strength, MPa
Stainless Steel (S.S.)	210 (10.0)	495 (28)
SMC	12.3 (0.6)	94 (7)
SMC with a layer of S.S.	42 (2.4)	132 (8)

Data in table 3.9 shows that the stainless steel layer provides a significant contribution to the composite materials performance under the tensile load. Tensile modulus and tensile strength properties for SMC with a layer of stainless steel are higher than for SMC (table 3.9).

3.2.2 - Flexural Test

Flexural properties of SMC with a layer of 0.6 mm stainless steel with the overall thickness of 4 mm were determined and compared with the flexural data from 4 mm SMC alone. In the case of SMC with a layer of stainless steel two tests were carried out one with the layer of stainless steel in tension and the other with the layer of stainless steel in compression. The flexural test specimens were 80 mm long and 10 mm wide (fig. 3.3). Five specimens were tested in each case at a constant crosshead speed of 1.7

mm/min and a span to thickness ratio of 16:1. Typical load-deflection curves obtained during the three point bend tests for SMC and SMC with a layer of stainless steel are shown in figure 3.14. The tabulated flexural strength and modulus data are shown in table 3.10. The number of specimens which were tested in each case were five.

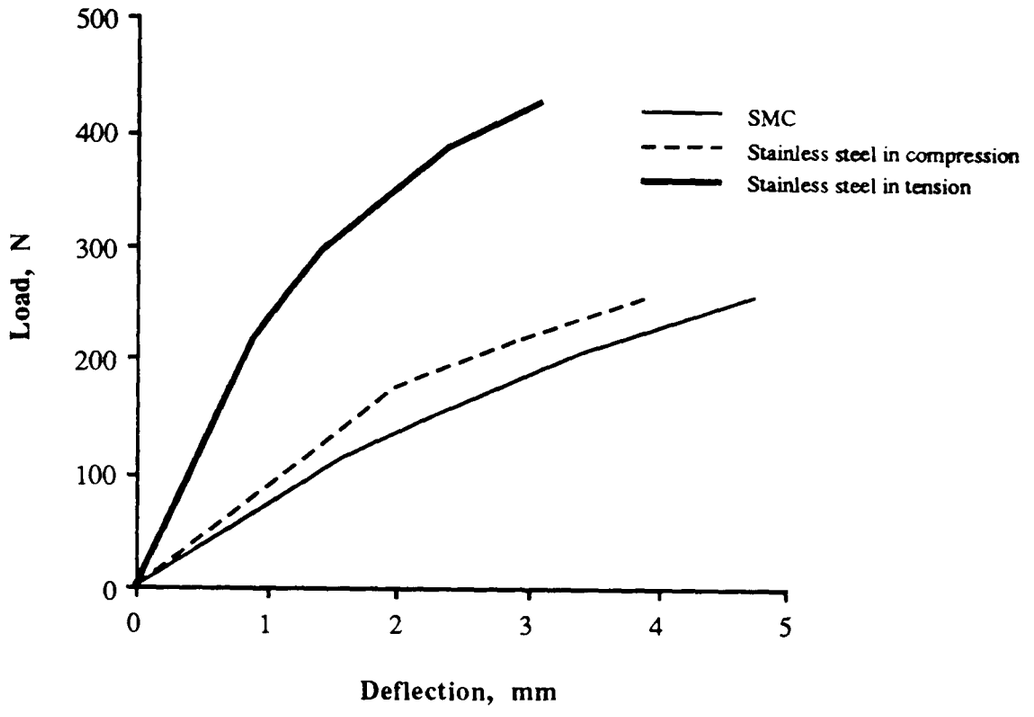

Figure 3.14 - Flexural curves for SMC and SMC with a layer of stainless steel.

Table 3.10 - Flexural properties of SMC and SMC with a layer of 0.6 mm stainless steel. Standard deviations in parenthesis.

Material	Flexural Modulus, GPa	Flexural Strength, MPa
SMC	12.9 (0.39)	176 (21)
Stainless steel surface in tension	22.3 (2.3)	281 (18)
Stainless steel surface in compression	14.8 (1.6)	191 (16)

Flexural modulus and flexural strength are significantly higher for SMC with the layer of stainless steel in tension (table 3.10).

3 - 3 Impact Testing

The impact programme exclusively involved subjecting flat plates to an out of plane impact using a hemispherical striker. Three impact machines were used in the programme, according to the severity of the blow to be applied and the velocity required. The majority of the testing involved a proprietary falling-weight drop tower produced by CEAST of Italy. The limited range of the load cell (max 19.1 KN) fitted to the system meant that where high force, high speed impacts were required, as for total penetration of laminated plates, testing was performed on a high speed servo-hydraulic machine manufactured by Cranfield Institute of Technology (max load 200 KN) and sited at Cambridge University. Where sensitive testing, low energies and low velocities were required, a purpose built, low energy instrumented falling-weight machine produced at QMW (max load 9.55 KN), was employed. The details of the various testing machine including their operating range and data collection systems are described below. All tests employed a common loading geometry as shown in figure 3.15. This consisted of a specimen, dimensions, 60 mm x 60 mm supported by a 40 mm steel ring and impacted centrally by a steel striker with a 20 mm diameter tip. In most instances tests were performed with the specimen simply supported, whereas in certain cases notably testing metal sheet, the specimens were lightly clamped to prevent folding into the support orifice. Where specimens were to be subsequently tested for residual strength one of the principal dimensions was increased from 60 to 100 mm.

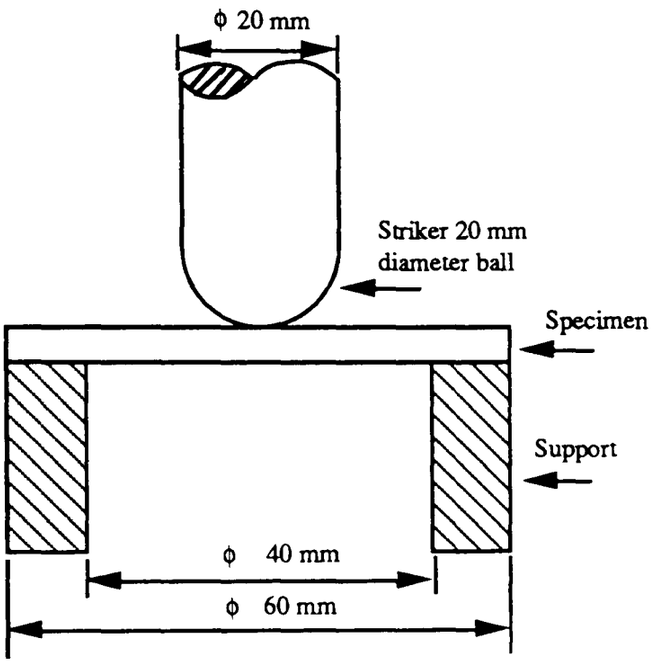

Figure 3.15 - Impact test geometry used for all impact test programme.

A series of tests were also performed in order to assess the effect of metal-composite bond strength on the impact performance of the laminates. To do this a number of specimens were tested into non-standard interfacial conditions, namely:

a) SMC resting on stainless steel, aluminium, Ionomer.

b) SMC resting on lubricated stainless steel.

c) SMC bonded to stainless steel by a Permabond adhesive type F241.

3.3.1 - The CEAST Drop Weight Test.

The majority of the non-penetrating impact tests were performed using an instrumented CEAST drop tower in conjunction with an AFS MK3 fractoscope. The equipment (fig. 3.16), consists of a falling carriage of mass 19.336 Kg which itself includes a striker head (fig. 3.17). The velocity of impact and the incident energy of the striker are simultaneously varied by adjusting the drop height. The maximum falling height of the machine is 2.4 m which yields a velocity of 6.86 ms^{-1}. The velocity immediately prior to impact is measured by an electronic flag device.

In accordance with ISO / DISS 6603/1 the specimens were located onto a 40 mm diameter steel ring and were centrally impacted by a hardened hemispherical tip of 20 mm diameter. By means of an adjustable ' V ' plate (fig. 3.18) accurate and rapid centring of the specimens were ensured. The specimens may be clamped with a second circular annulus positioned above the support. The support assembly is located in an environmental chamber which may operate between - 70 °C and +100 °C . The striking head is interchangeable so that a variety of shapes and sizes may be used. It is screwed onto a small thread at the end of the striker tube (fig. 3.17). This facility was not used during this programme but the details of the fixture itself may have influenced the degree of noise recorded during impact tests.

The signals produced by the load cell after impact are filtered as required, amplified and fed to a transient recorder which may operate at sampling rates between 2 ms and 256 ms, and records 2048 data points in this time. The recorder is triggered by the input signal so that when a pre-set value is reached it records the incoming signal and also recalls a portion of the signal immediately preceding this point, so that no relevant data are lost.

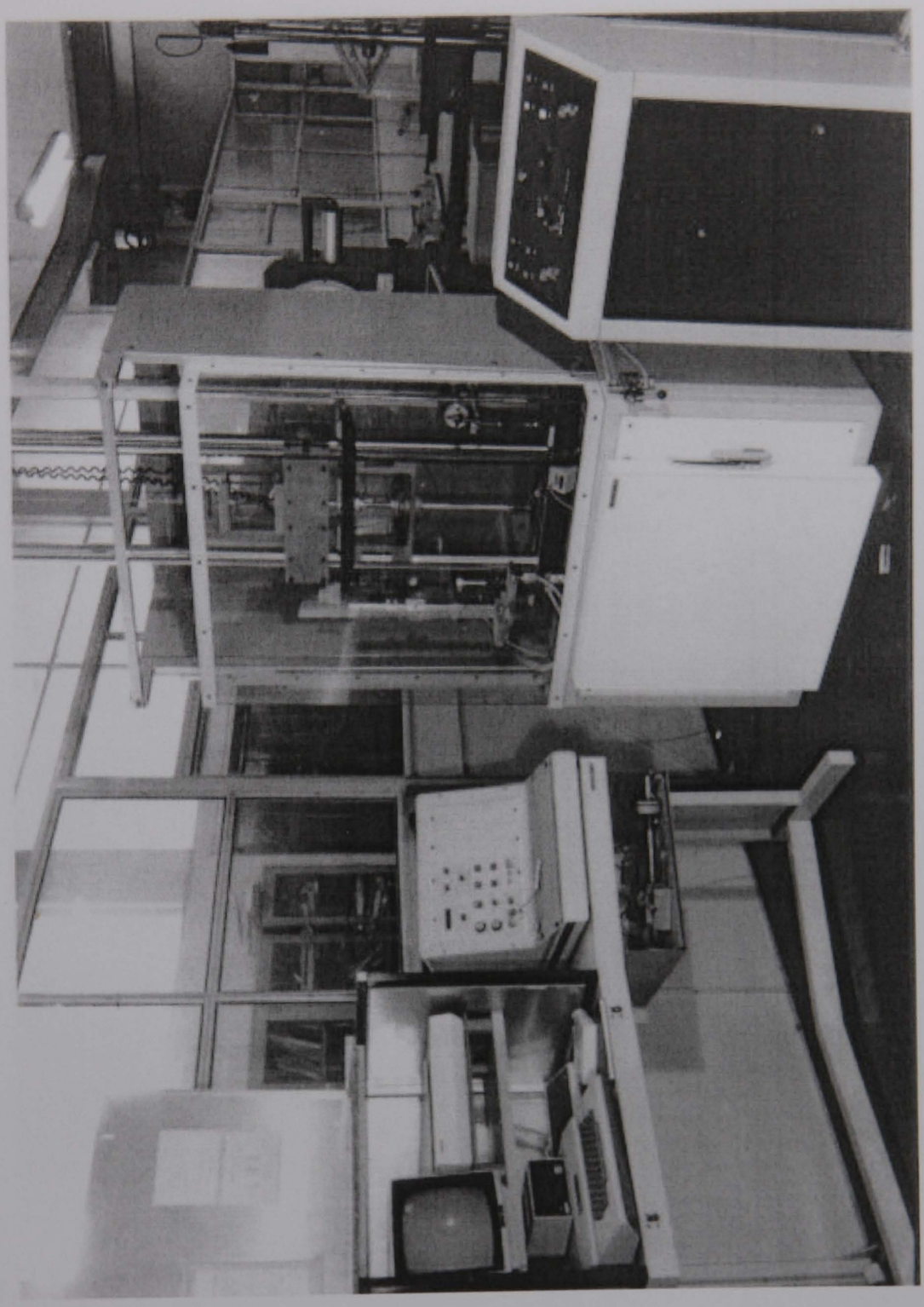

Figure 3.16 - CEAST drop weight impact machine.

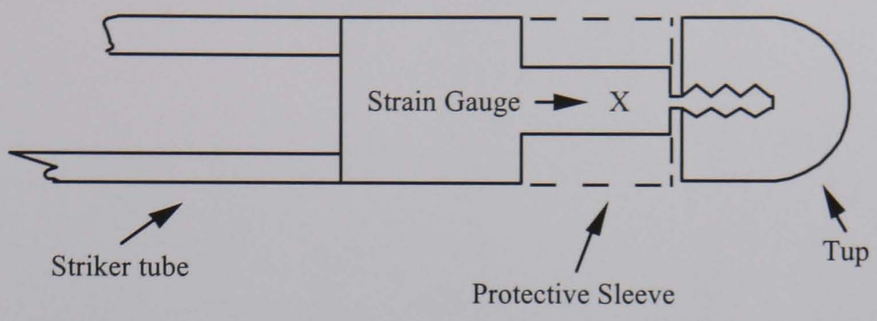

Figure 3.17 - Schematic drawing of the Instrumented striker

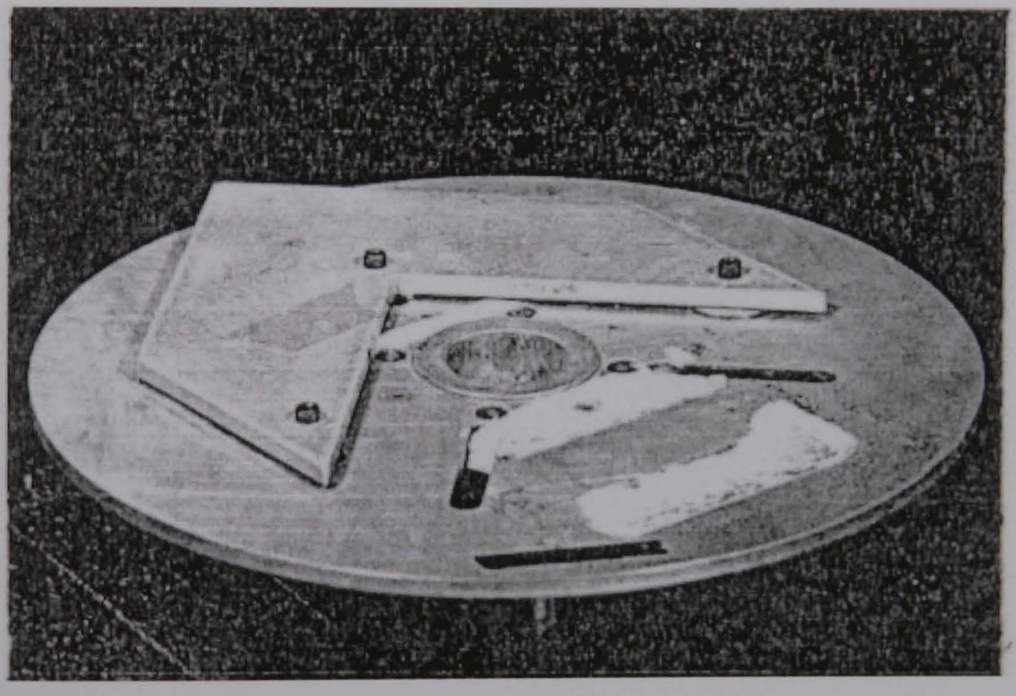

Figure 3.18 - Drop weight test support with an adjustable ' V ' plate.

This stored signal may then be output to a microcomputer which manipulates the data with a program described by the following diagram (fig. 3.19).

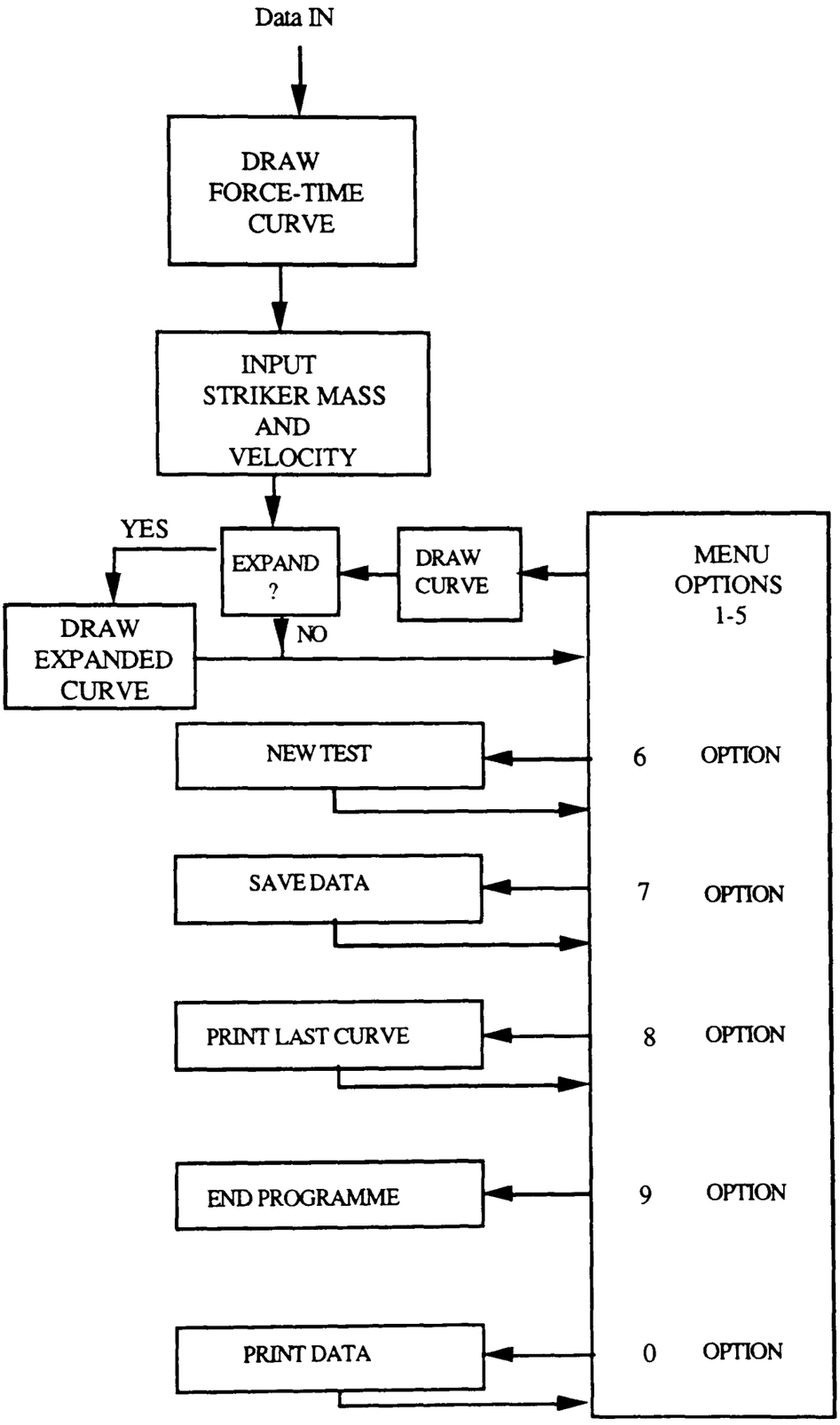

Figure 3.19 - Block diagram of the CEAST data processing software.

The data is input to the computer and the force-time curve is drawn on the screen. The mass and velocity of the striker are then input and access may be given to the menu, which contains a number of options which allows the force-time curve to be integrated and expanded, the data to be re-processed to provide force-time, energy-time, velocity-time, displacement-time, and force-displacement curves, and selected points to be stored and printed as required. If the force during the impact is known, it is possible to calculate the striker velocity and its displacement as well the energy absorbed by the specimen.

$$V = V_0 + gt - \frac{1}{m}\int_0^t F.dt \qquad (1)$$

$$X = V_0 t + \frac{gt^2}{2} - \frac{1}{m}\int_0^t \left(\int_0^t F.dt \right) dt \qquad (2)$$

$$E = V_0 \int_0^t F.dt + g\int_0^t F.t.dt - \frac{1}{2m}\left(\int_0^t F.dt \right)^2 \qquad (3)$$

where:

V_0 = Velocity of the striker just before impact.

m = Mass of the striker.

V = Velocity of the striker at time (t).

X = Displacement of the striker.

E = Energy absorbed by the specimen.

The method of integration of the force-time trace is that the whole graph is divided into many strips (fig. 3.20). The area for each strip is approximately given by :

$$\left[\frac{F_i + F_{i+1}}{2} \right] \times \left[t_{i+1} - t_i \right]$$

Since the strips have the same width, δt, then $[t_{i+1} - t_i]$ must be equal to δt.

Therefore the general expression becomes :

$$\left[\frac{F_i + F_{i+1}}{2} \right] \cdot \delta t$$

The sum of the area of the all strips is equal to the integration of force-time curve, that is :

$$\delta t \sum_{t_0}^{t_n} \left[\frac{F_i + F_{i+1}}{2} \right] \approx \int_{t_0}^{t_n} F.dt$$

One of the problems with the CEAST software is that it assumes the origin of the force-time curve is the same as the origin of the force-time axis, and integration starts from t=0. whereas the actual integration should be between t_0 and t_n (fig. 3.20).

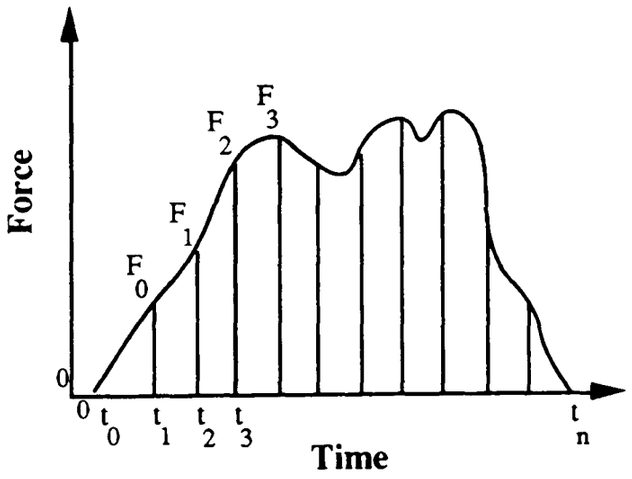

Figure 3.20 - Method of integration of the force-time by dividing the curve into strips.

This technique is only applicable if the force from t=0 to $t=t_0$ zero. However in most cases there is some fluctuation in load before $t=t_0$ (fig. 3.21). A modified version of CEAST (126) software has overcome this problem by using the following subtraction:

$$\int_{t_0}^{t} F.dt = \int_{0}^{t} F.dt - \int_{0}^{t_0} F.dt$$

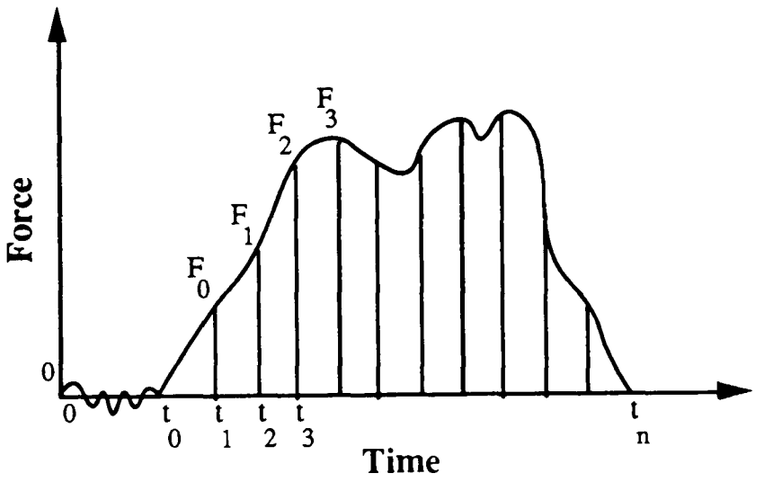

Figure 3.21 - Method of integration of the force-time by dividing the curve into strips.

The modified software was available at the end of the test programme. With the help of a conversion programme it was possible to extract the previous data from the floppy discs and run them with the new software. The values of energy obtained by the two programme showed no significant differences.

Impact testing was performed, on unclamped specimens, at room temperature (16 -20 °C) at a range of velocities and energies. Since the effect of filtering on the data was not very well understood, no filters were used. The trigger level was set at 10% of the expected maximum load to ensure that the trigger level is well above any background noise. Pretrigger level was set at 1/4 and the time base selected as required. At the time of these experiments the equipment was not fitted with an anti-rebound device and consequently for non-penetrating impacts each impact event was in reality a series of blows of decaying magnitude. A series of experiments on low energy impact machine which is described later showed that the subsequent impacts produce no additional damage over and above that caused by the initial blow. The typical force-time, energy-time, velocity-time, displacement-time, and force-displacement curves for non penetrating impact obtained by CEAST are shown in figure 3.22.

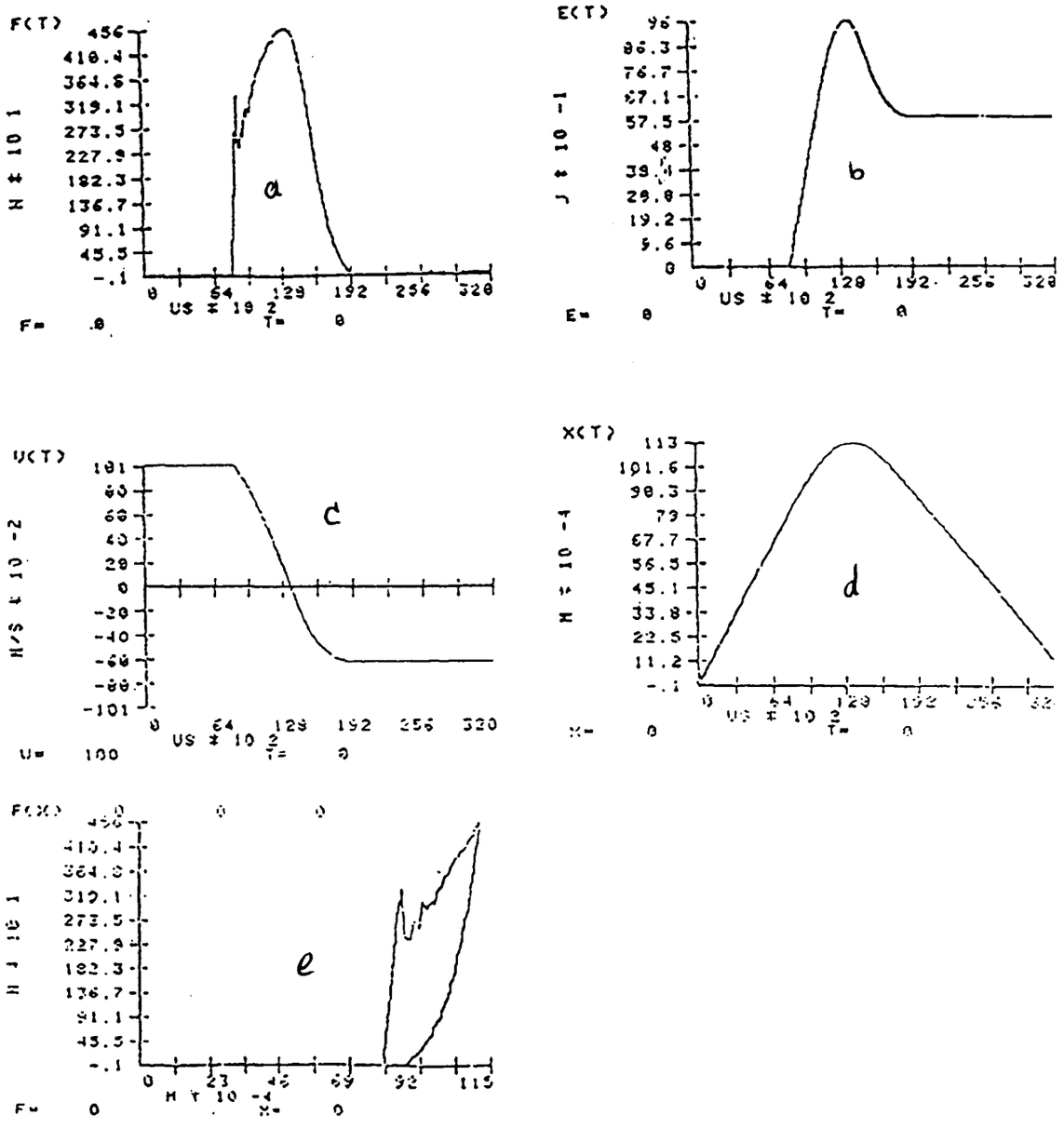

Figure 3.22 - Typical F-t, E-t, V-t, and F-x curves for non- penetrating impact obtained using CEAST, a) force-time, b) energy-time, c) velocity-time, d) displacement-time, e) force-displacement.

3.3.2 - Calibration Of The CEAST Load Cell

It is essential that the instrumented striker signal be a good analog of the time dependent interaction force between the striker and the specimen. The idealised calibration procedure should be one utilising a dynamic technique. Dynamic calibration of an instrumented striker can be performed with the low blow elastic impact test (31). It has been argued (29) that because load is being equated to the results of strain-gauge signals for elastic strains, and elastic properties are relatively strain-rate independent, static loads and dynamic loads will produce the same strain gauge signals. The semiconductor strain gauges used on the CEAST apparatus are small in size and have a high gauge factor compared to the ordinary wire or foil resistance gauges. A primary requirement in dynamic tests is for gauges to exhibit a high signal to noise ratio, therefore such transducers are ideally suitable. The calibration was carried out statically and the procedure was as follows:

1 - The reset key on the panel 65557/002 (fig. 3.23) was switched off and kept off during calibration.

2 - The ' Trigger level ' knob was set to the highest value.

3 - The ' Range ' selector knob was set to desired full scale value.

4 - The striker was loaded by a special calibration device (fig. 3.24) and the load was measured by means of a load measuring ring.

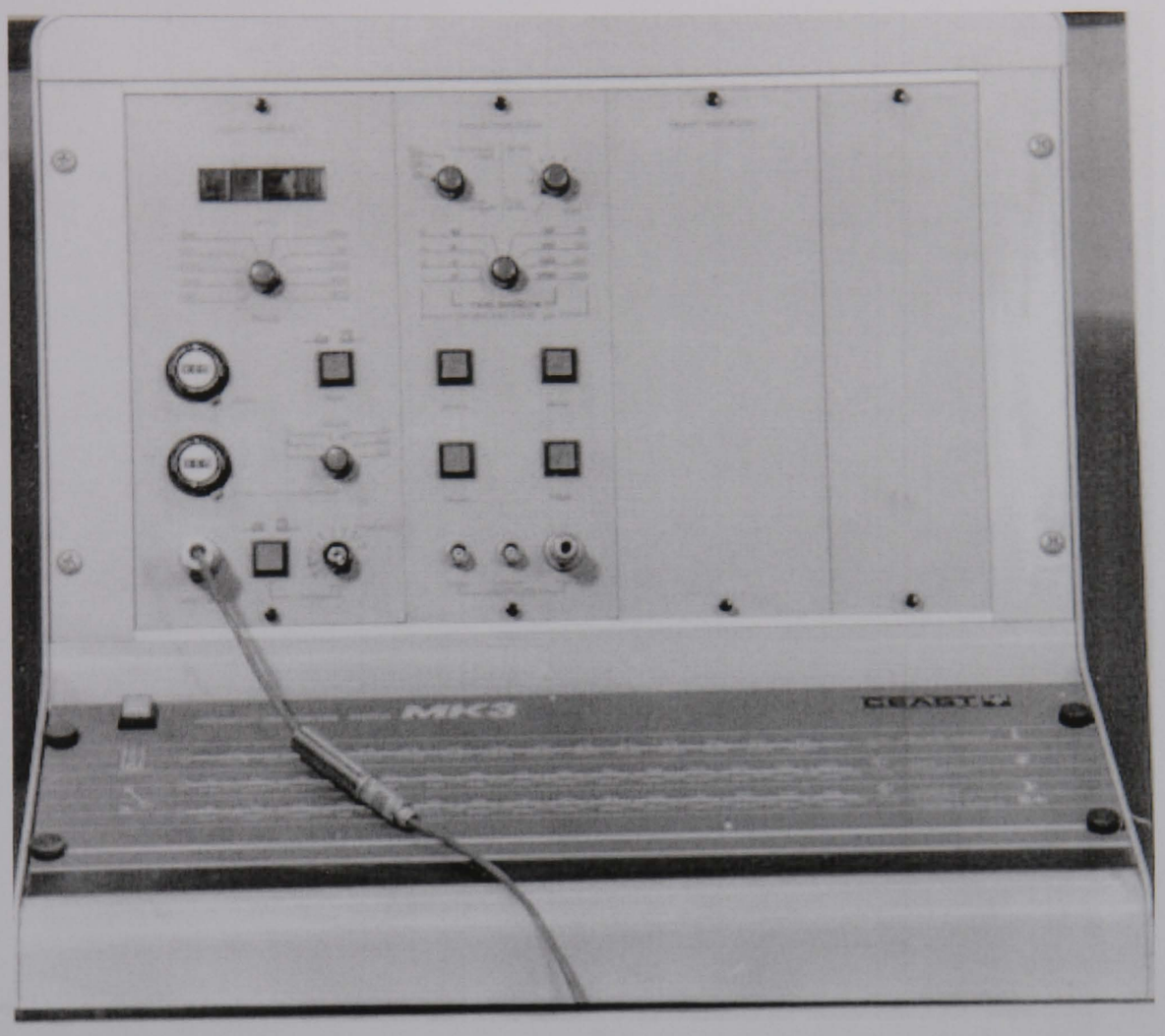

Figure 3.23 - AFS MK3 fractoscope

5 - The ' Gain Steps ' and ' Gain Fine ' knobs on the panel were adjusted to read an display the same value of the load applied on the striker.

6 - ' Gain Steps ' and ' Gain Fine ' values were recorded.

7 - Load was removed and the zero was readjusted by means of the ' zero ' knob.

8 - Steps 4 and 5 were repeated.

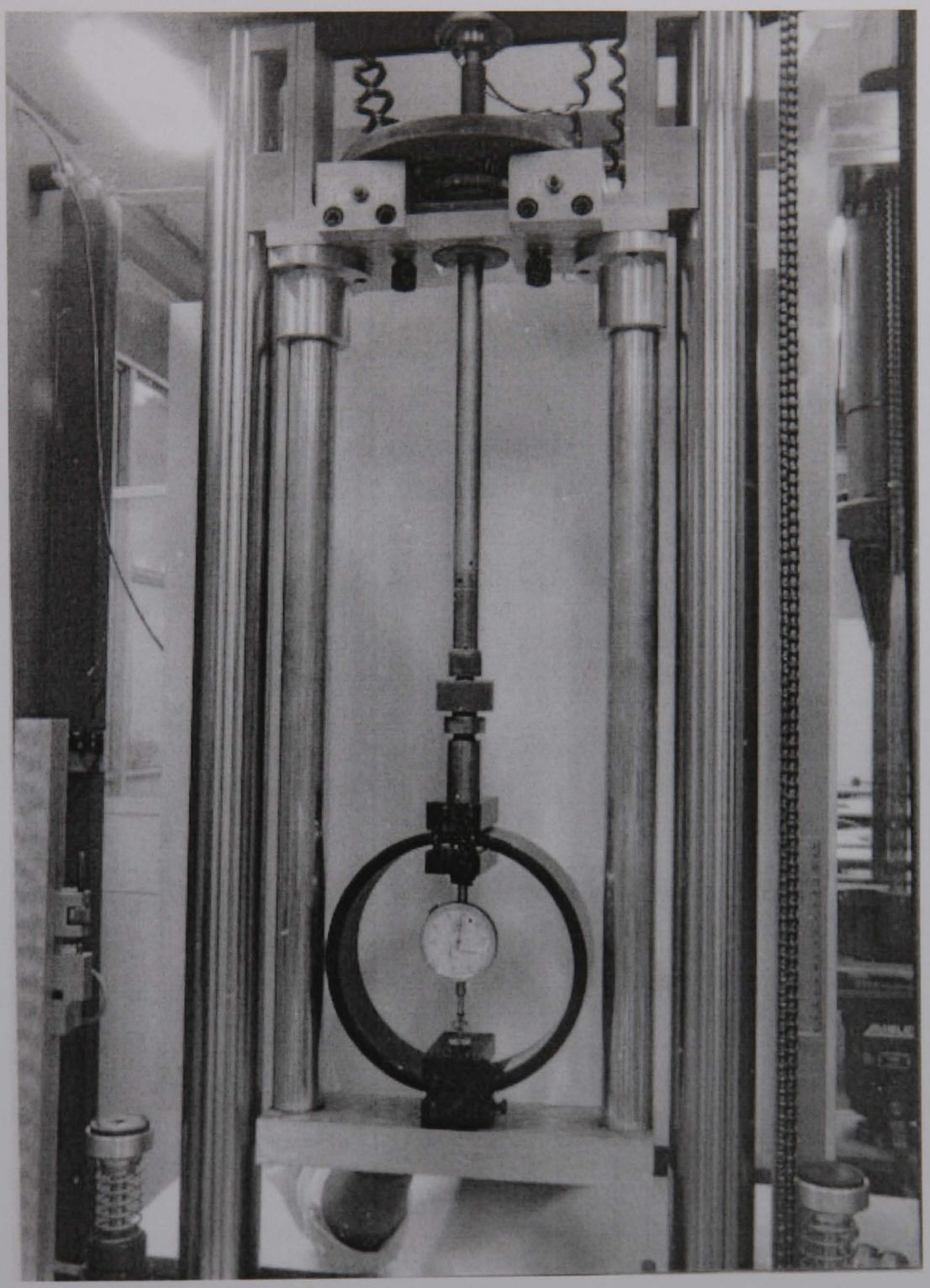

Figure 3.24 - The load measuring ring used for calibration of CEAST load cell.

9 - The load was removed.

10 - If the digital display did not show the zero value, the zero was readjusted by the zero knob, and if it was necessary the steps 4, 5, 6, 7, and 8 were repeated.

11 - Calibration procedure was repeated for different ' Range ' values as needed.

After calibration was completed, the ' Range ' was set to the values which have been obtained during calibration. These values at the time of tests were as follows :

Range (Daq)	1910	955	382	191	95.5
Steps	1	2	5	10	20
Fine	686.8	680.8	692.6	692.6	692.6
Zero	882.6	882.6	879	872.6	876.6

Errors might arise during calibration from the faulty load measuring ring or the operators misreading of the value of deflection of the ring or subsequent reading of the load from the calibration curve of the ring. The load measuring ring might be faulty due to pointers of the dial gage which have been bent or that dirt has increased the friction. In the case of friction the value of load measured is lower than the actual ones. In any case since impact data are used as a comparative base, therefore the source of error in calibration exists in all the impact tests and will not affect the conclusions driven from the impact data.

3.3.3 - The Low Energy Impact Test Rig

The low energy impact machine (fig. 3.25) which was built at Queen Mary and Westfield College is very similar to the CEAST equipment. It employs a lower impacting mass (3.96 Kg) instead of (19.336 Kg) and has a device that captures the impacter if it rebounds from the specimen which therefore is subjected to a single blow. An instrumented striker the same as the one which has been employed by CEAST with lower capacity (9.55 KN instead of 19.1 KN) has been fixed in the low energy impact machine. The same data processing routines as CEAST is used. With the existing tower impact tests with velocities up to 2.7 ms^{-1} can be carried out. The size of the striker head and the support are exactly the same as CEAST.

3.3.4 - The Cambridge Impact Test Rig.

The impact machine which was used at Cambridge was a servo hydraulic testing machine made by the Cranfield Institute of Technology (fig. 3.26). The machine has a hydraulic ram which travels upward at speed of 1 - 5 ms^{-1} and has a load cell at the top with a capacity of 200 KN. Data was recorded using a Gould Os 4035 digital, 2 channel storage oscilloscope.

In order to be able to compare the impact results with the results which were obtained by the CEAST rig, a support with the same size was built and fixed to the moving ram (fig. 3.27) and a striker with the same head size (20 mm) was built and fixed to the stationary load cell. The striker was made in two pieces in order to overcome any alignment problems and to enable various striker heads to be accommodated (fig. 3.28).

Unlike the CEAST impact machine, the energy imparted to the specimen is so high that the impact velocity may be assumed to remain unchanged during the test. Therefore, the impact test is performed at a constant velocity. The oscilloscope can be connected to an X-Y

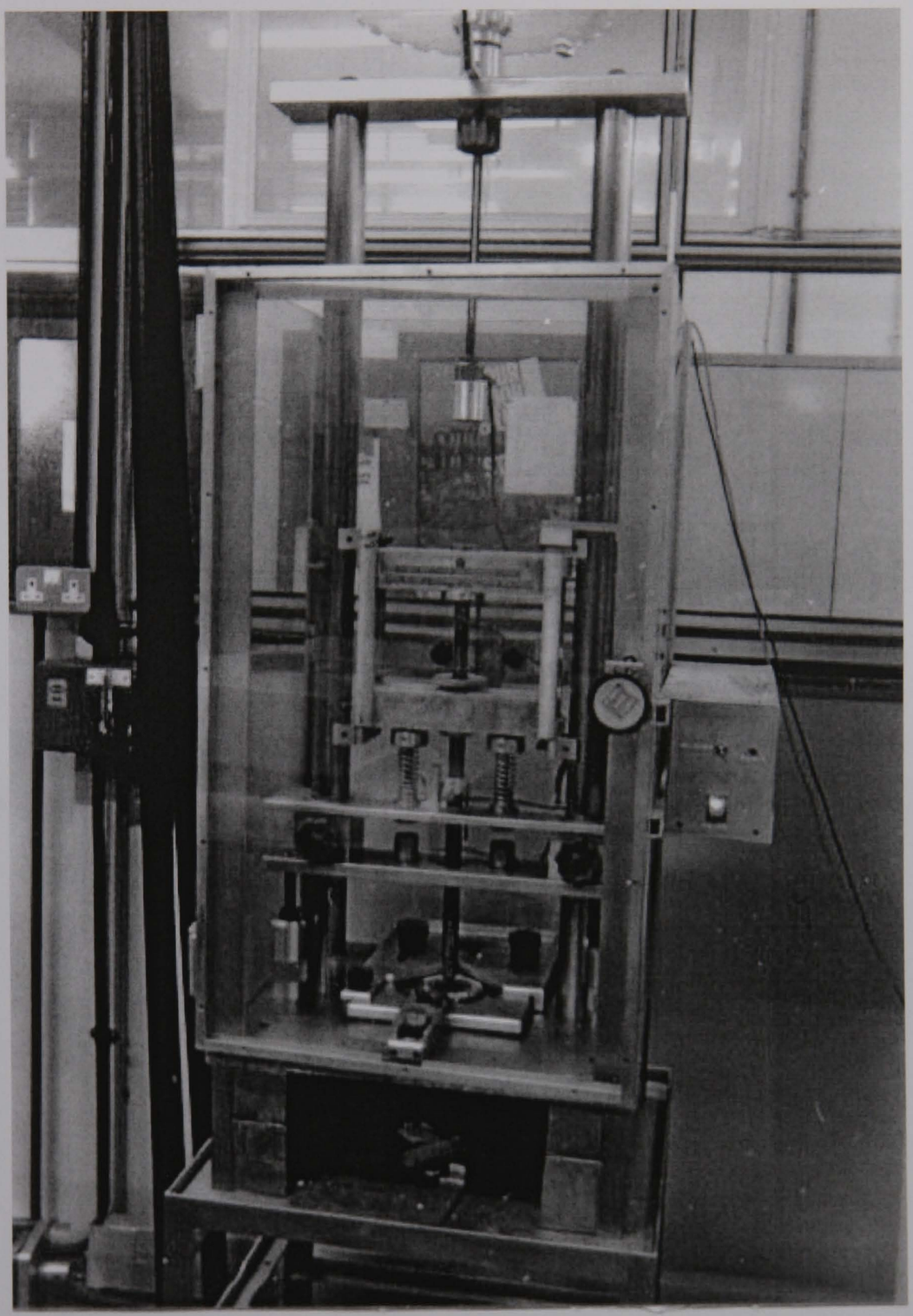

Figure 3.25 - QMW low energy impact machine.

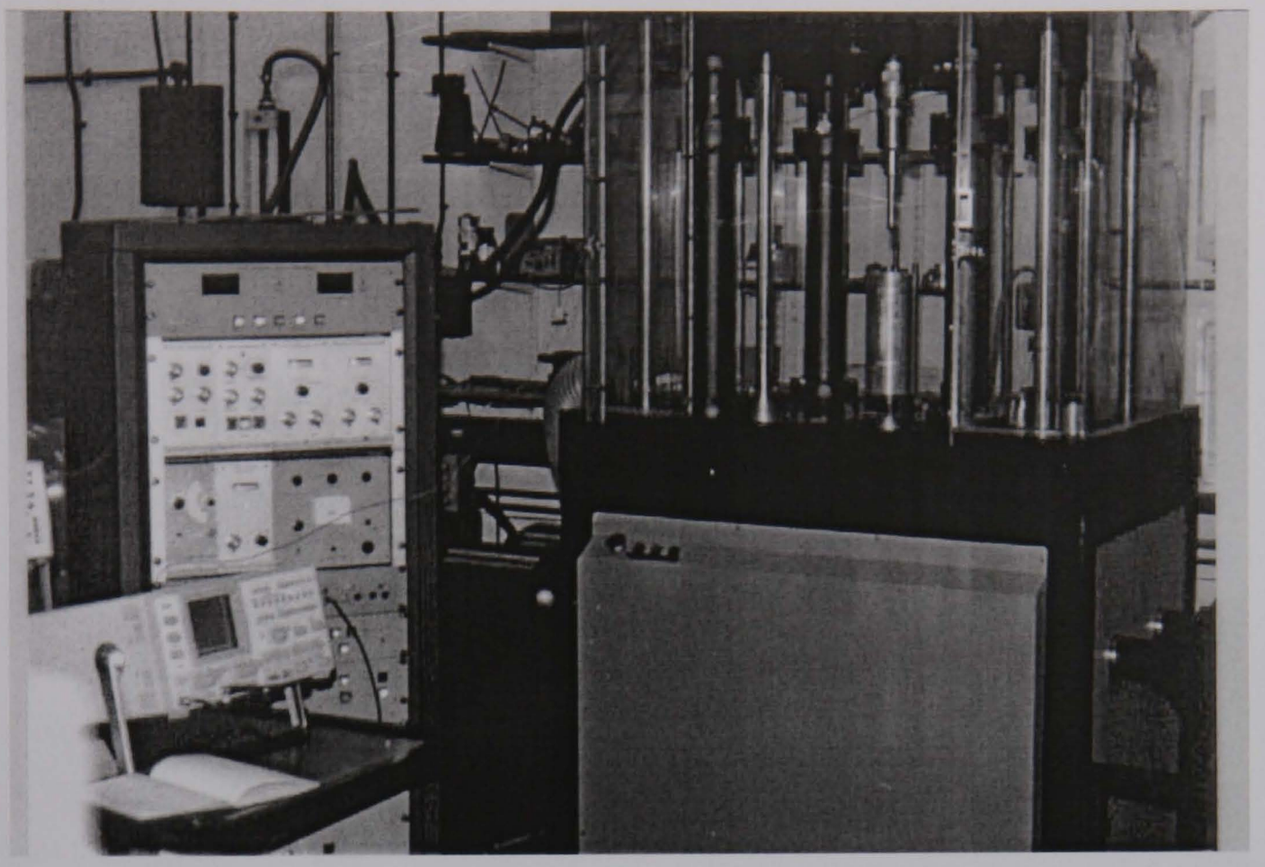

Figure 3.26 - Cambridge test rig.

Figure 3.27 - Support used for Cambridge impact machine.

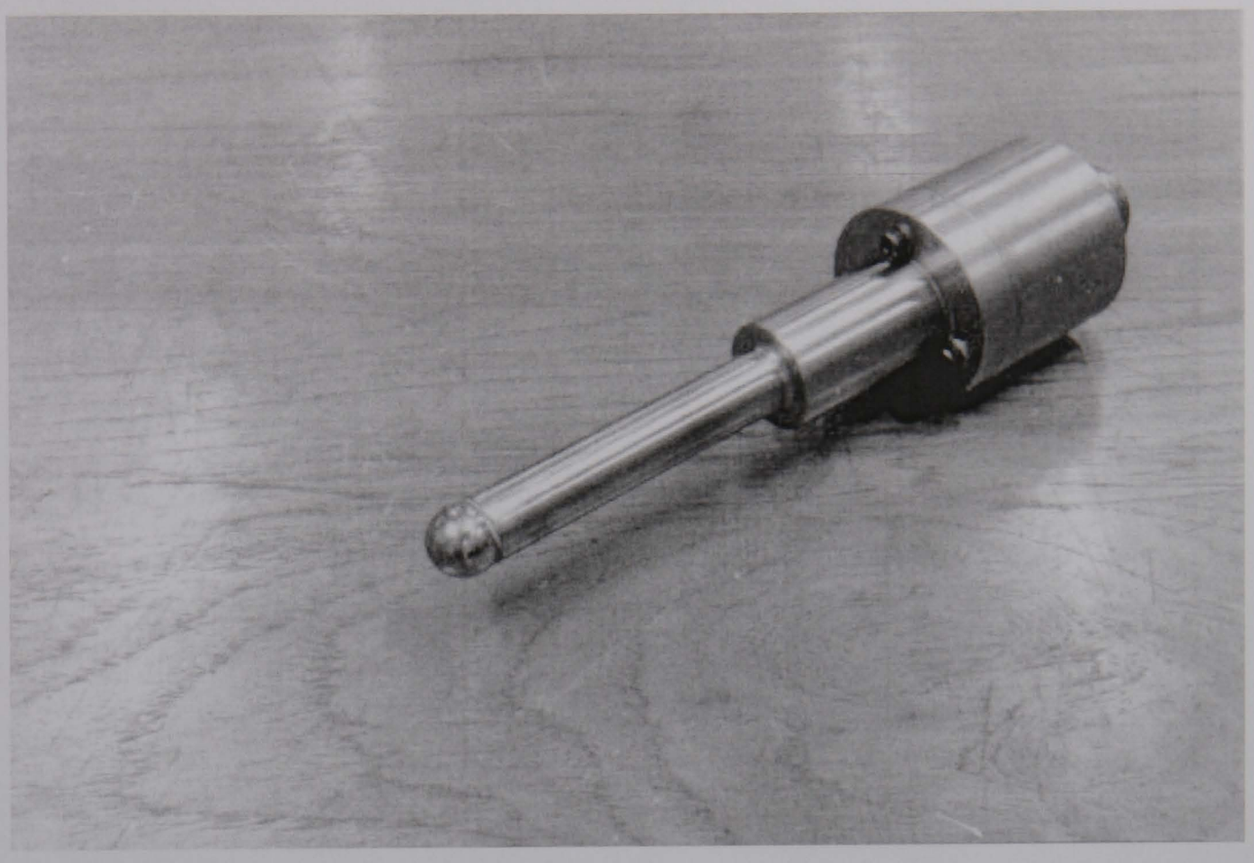

Figure 3.28 - Striker designed and used with the Cambridge test rig.

recorder and the force-displacement may be obtained after the test. One of the problems with the Cambridge test rig is that at high impact velocities (more than 3 ms^{-1}), the background noise is so high that it affects the force displacement curve and makes the reading of the curve more difficult. Figure 3.29 shows a typical force displacement obtained by Cambridge test rig at 1 ms^{-1} and 5 ms^{-1}.

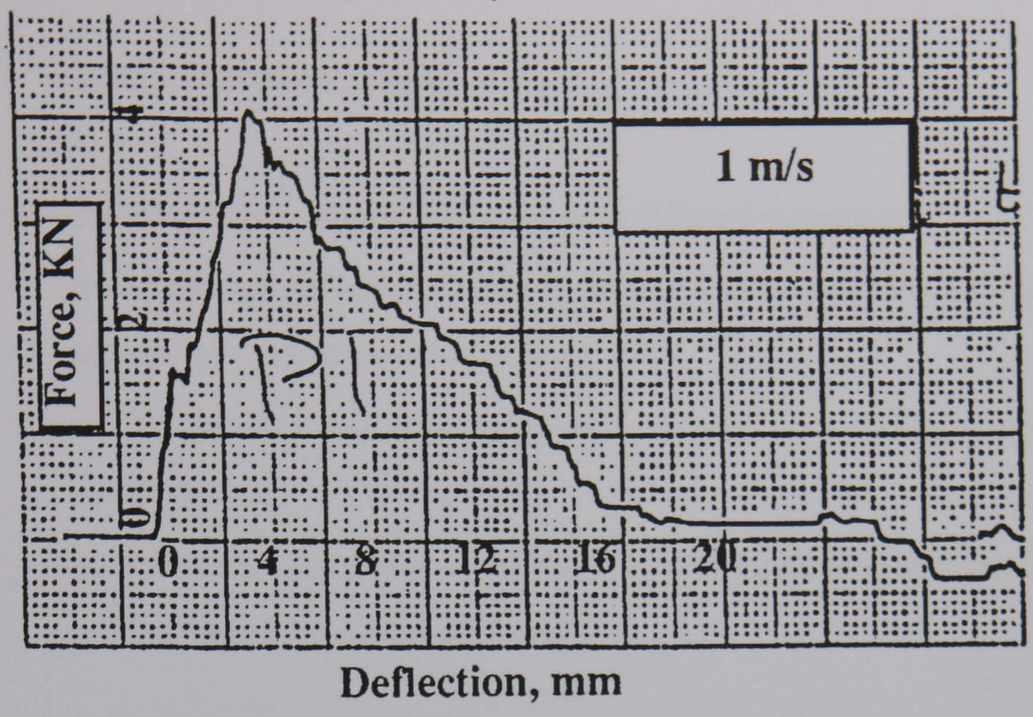

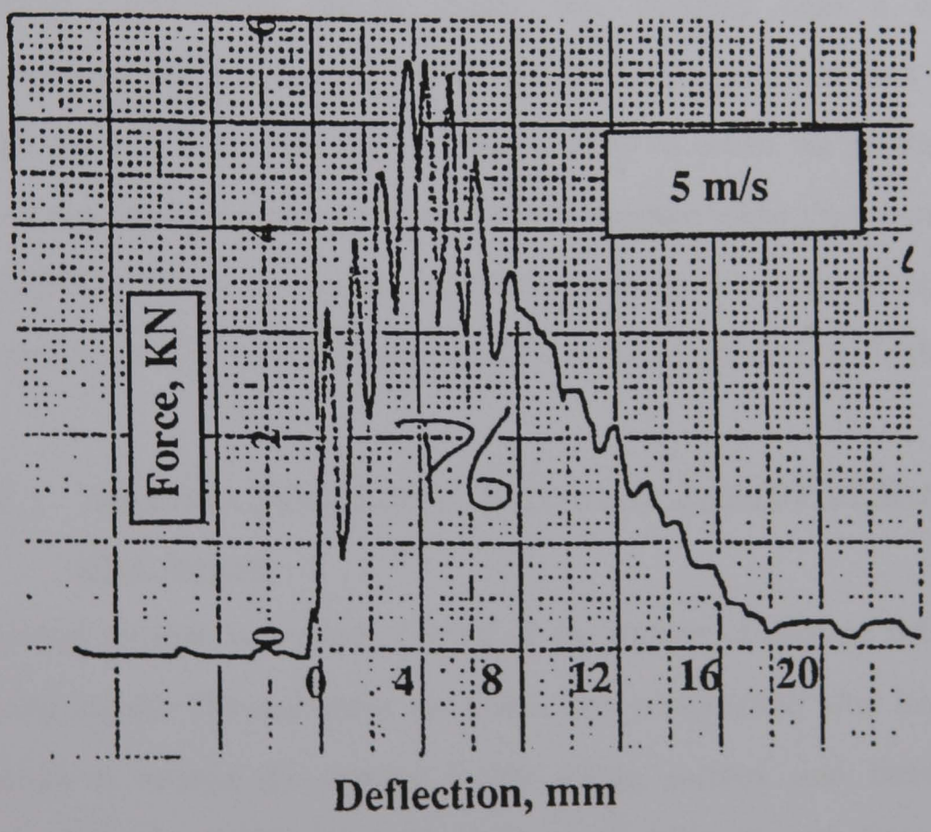

Figure 3.29 - Typical force-deflection curves obtained using Cambridge test rig, a) 1 ms^{-1}, b) 5 ms^{-1}.

3.4 - Slow Indentation Tests

Slow indentation tests were carried out for three different purposes:

1 - To compare the load - deflection curves given by slow tests and impact tests to assess if any rate effects are operative.

2 - To assess the work done in deforming the steel layer in the macrocomposite during impact.

3 - To compare the profile of deflection of slow indentation tests and impact tests.

4 - To determine the onset of damage.

In order to achieve the above purposes an indenter and a support which reproduced the loading configuration during impact was mounted onto a conventional tension-compression test machine (SCHENK TREBEL Machine) and tests performed at a cross head speed of 3 mm/min (fig. 3.30a). In order to obtain the profile of deflection of the specimen during the test, a transducer was mounted under the specimen in the SCHENK TREBEL Machine. By moving the transducer along the radius, the profile of deflection was plotted by an X-Y recorder linked directly to the transducer (fig. 3.30b).

3.5 - Residual Tensile and Compressive Strength of Damaged Composites after Impact

Residual strength is a good criterion of the amount of damage induced in the specimen during impact. The specimens for tensile and compression after impact need to be large enough to contain the damage in the gauge section, and therefore for subsequent compression testing the specimens have to be stabilised against buckling. At the present time there are numerous anti-buckling devices and each laboratory has developed its own as required. The two anti buckling devices which were designed for this work are shown in figures 3.32 and 7.13. The post impact compression tests were performed using plate samples 60 x 100 mm to allow the use of the antibuckling frame (fig. 3.32) and 55 x 89

mm to allow the use of the QMW miniaturised compression after impact test rig. This fixture is a scaled down version of the "Boeing" test fixture which itself the basis of current ASTM, SACMA and Airbus standards. Both residual tensile and compressive strength tests were performed on SCHENK TREBEL Machine at a cross-head speed of 1 mm/min (fig. 3.31).

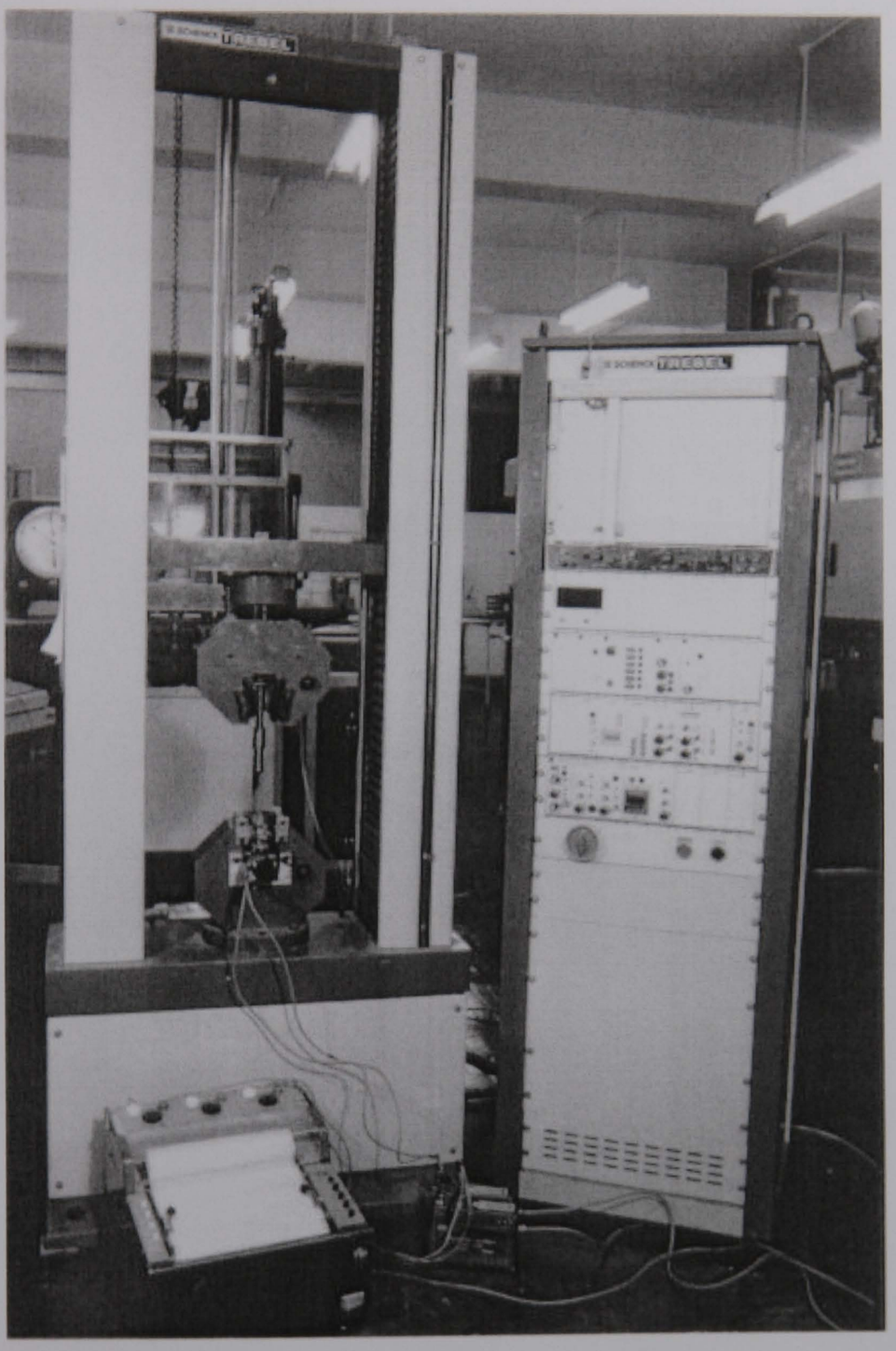

Figure 3.30a - Slow indentation test rig.

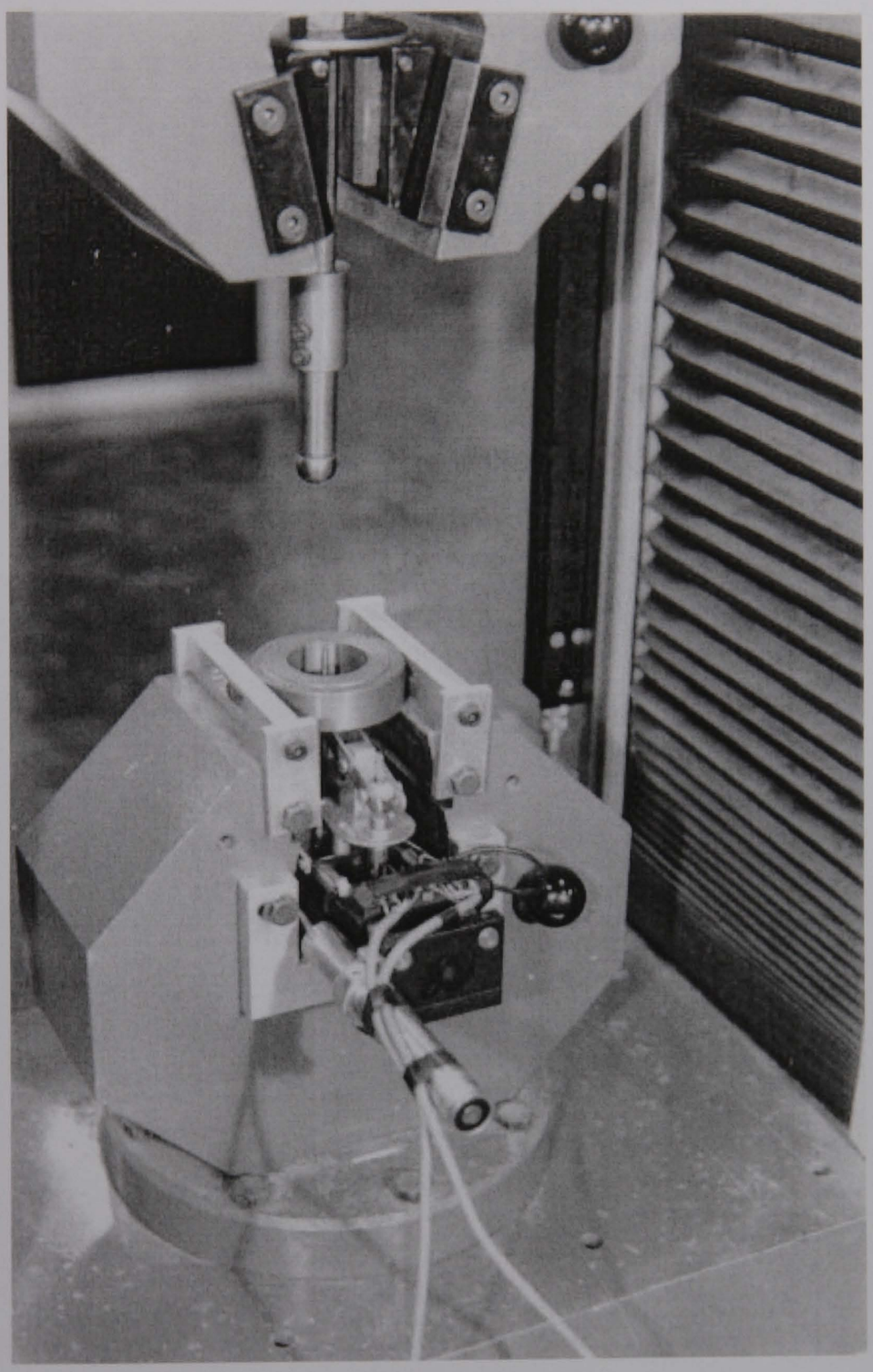

Figure 3.30b - Indenter, Support, and transducer used in slow test.

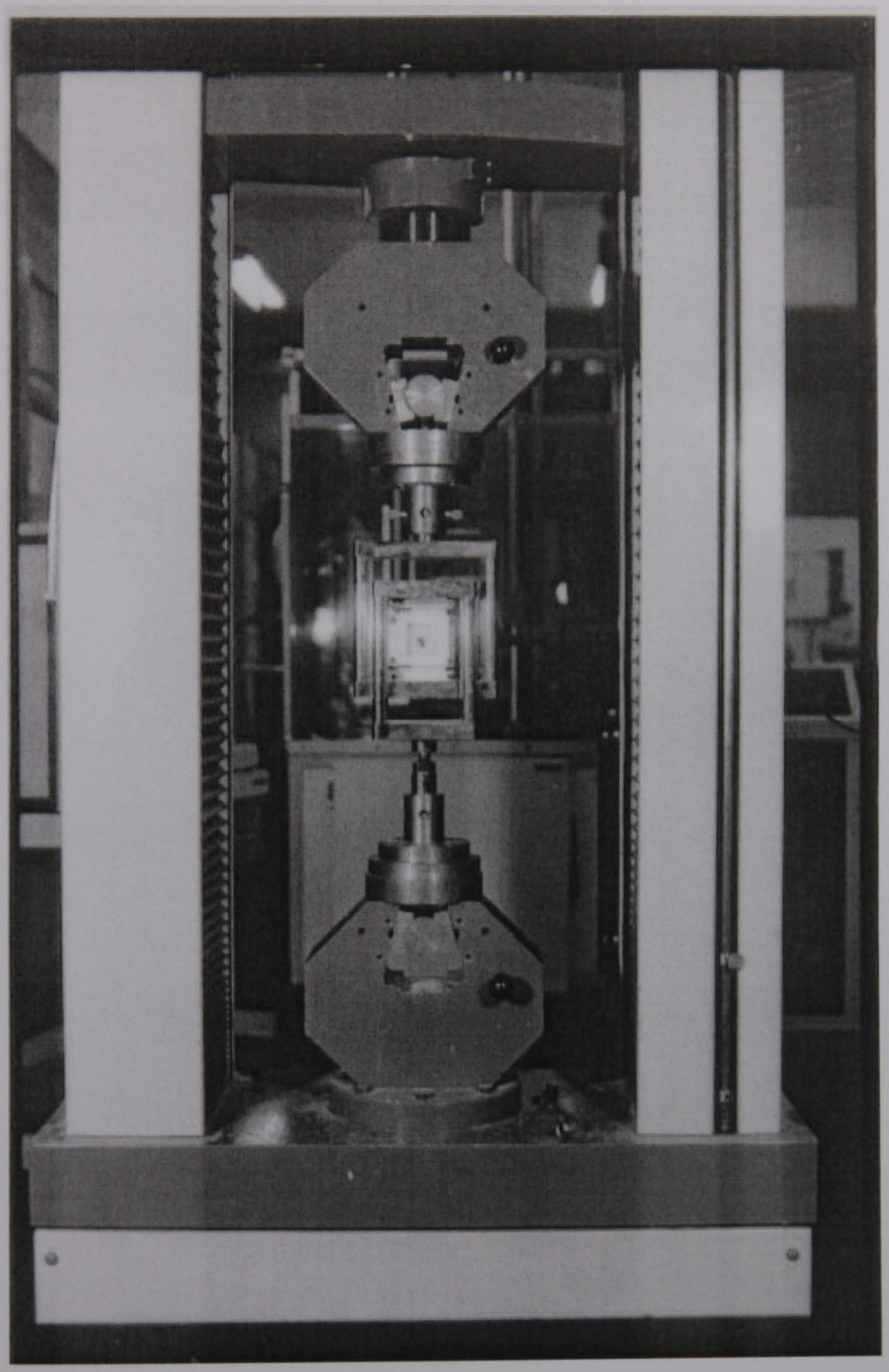

Figure 3.31 - Schenk TREBEL machine with compression cage used for compression test.

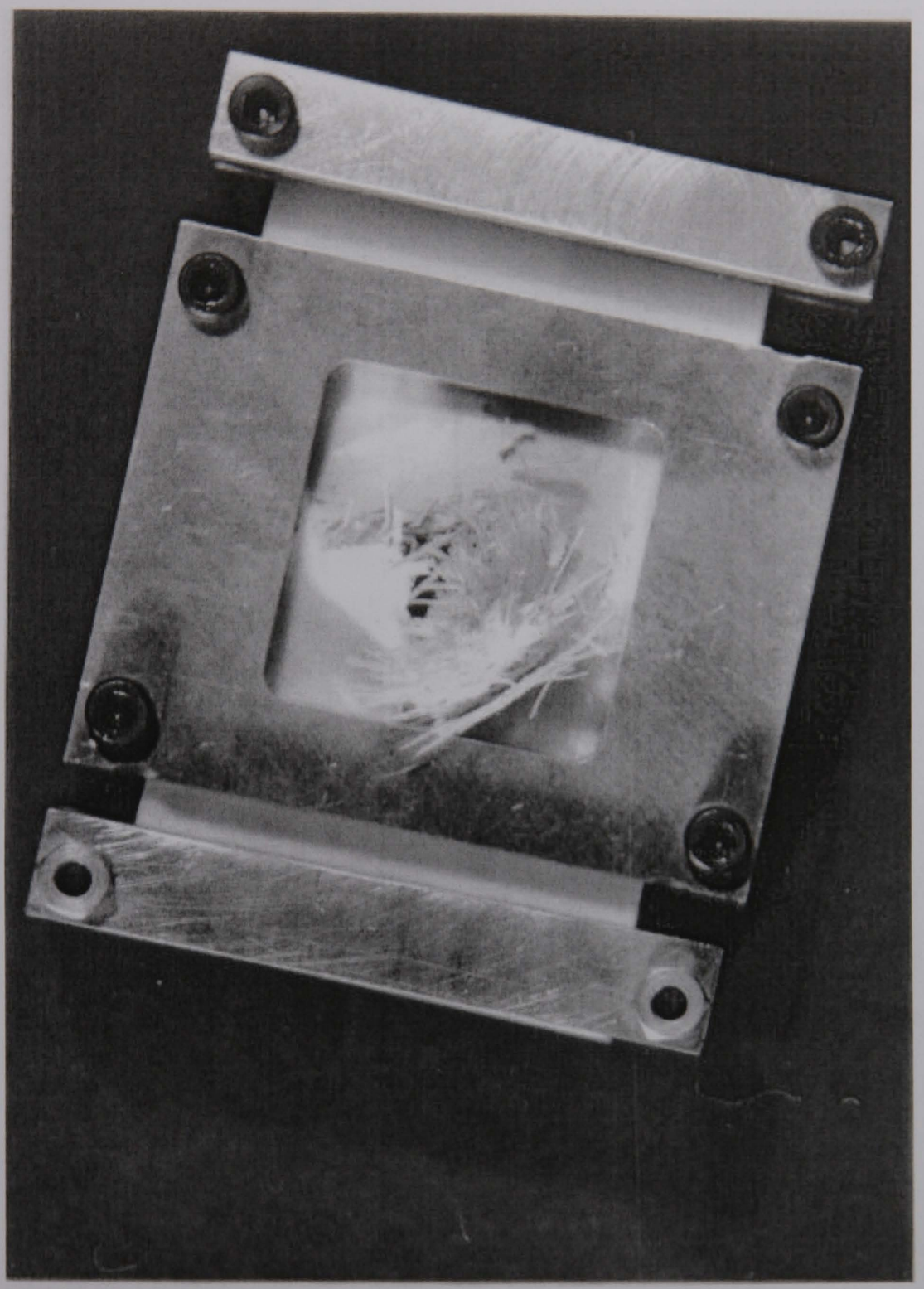

Figure 3.32 - Anti buckling frame used in the present work.

3.6 - Damage Detection and Assessment

Damage in the impacted specimens were monitored by different methods of destructive and non destructive techniques. Dye penetrating, X-ray radiography, scanning electron microscopy and optical microscopy were used during the course of the research programme. These techniques have been described in the following sections.

3.6.1 - Dye Penetrating Technique

After impact, the specimens were sectioned into halves by a hacksaw with a fine blade. The sectioned surfaces were then very carefully polished and cleaned to be free from grease and dust. The penetrant (ARDROX 996P) was sprayed onto the polished surface and left for about 15 minutes, the surplus penetrant was then removed and developer (ARDROX 9D6) sprayed and the cracks were inspected.

3.6.2 - Optical Microscopy

Impact generates larger areas of matrix cracking, fibre fracture and delamination. Optical microscopy is a technique which gives a lot of information about the nature of the damage, and makes it possible to distinguish between the many forms of damage.

In order to examine the specimens under the microscope, the damaged specimens were cut in half and carefully ground and polished with diamond abrasive. The cracking within the composite was subsequently examined with a REICHERT microscope and photographed using an OM-2 Olympus camera.

3.6.3 - Scanning Electron Microscope (SEM)

A scanning electron microscope was used to study the interaction of the cracks, with the individual microstructural elements and the fibres. All specimens were taken from the damaged area and were polished, then coated by carbon sputting. The specimens were then mounted on a solid base and placed on the operating stage of the microscope. All relevant information was recorded on photographic film using the appropriate camera attachment. Although not used extensively in this programme, the SEM is particularly useful for observing fibre pull-out and fibre-matrix debonding, damage mechanisms not readily detected by the other techniques.

3.6.4 - Ultrasonic C-scan

All post impact compression specimens were C-scanned using a Physical Acoustics Corporation machine (fig. 3.33). The machine consisted of a 5 MHz flat transducer which generated the ultrasound waves. Pulse echo testing was used whereby the transducer acts as the pulsar and receiver and the ultrasound waves are reflected off a glass plate at the bottom of the tank. The received signals were then amplified before display on a computer display. The signals received were then accumulated as the transducer passes over the test specimen and the entire image of the test piece displayed. The degree of damage in the specimen, as denoted by any loss in the ultrasound received is shown by a colour band scale. The C-scan machine was calibrated by using a stepped aluminium block with flat bottomed holes drilled in it (fig. 3.34). This was placed in the tank and then scanned by incrementing the rectified gain, attenuation and damping until the image matched that of the manufacture's calibration file (fig. 3.35) which showed the holes and steps at a specific depth and colour intensity and had identical attenuation levels. Acoustics unit had a 5 MHz flat probe which both acted as the transmitter and receiver. The tank was set up for double through transmission where the ultrasound is reflected from a glass plate below the

specimen an received through an electronic gate. this information was passed to a computer storage device which built up the images on a 1 mm spaced grid.

Figure 3.33 - Physical Acoustics Corporation C scan machine.

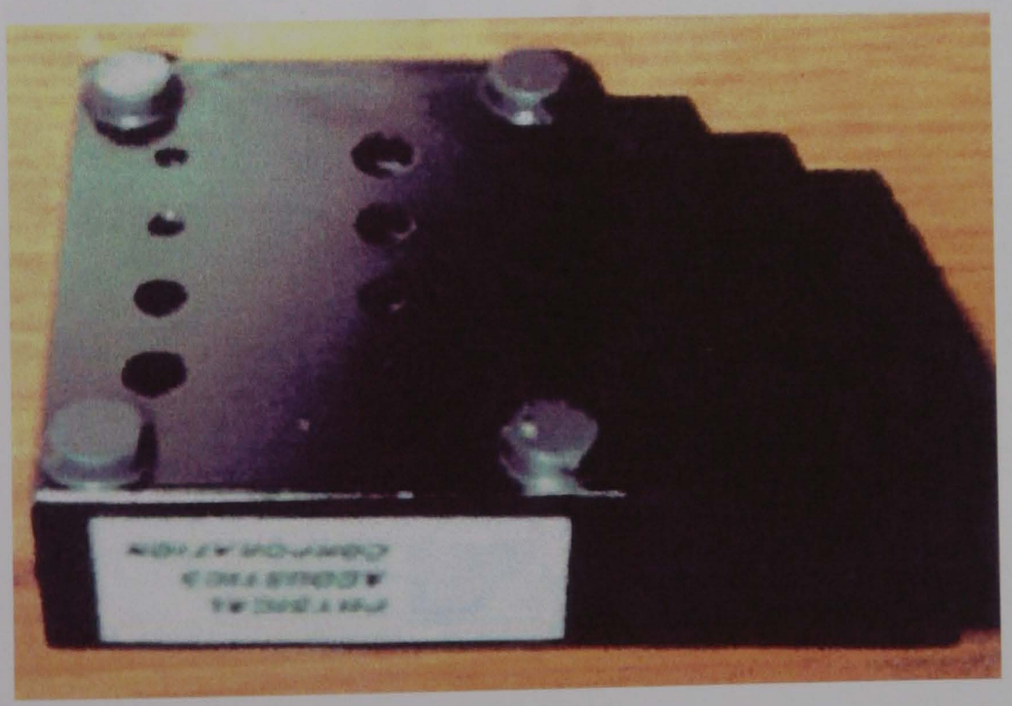

Figure 3.34 - Aluminium calibration block.

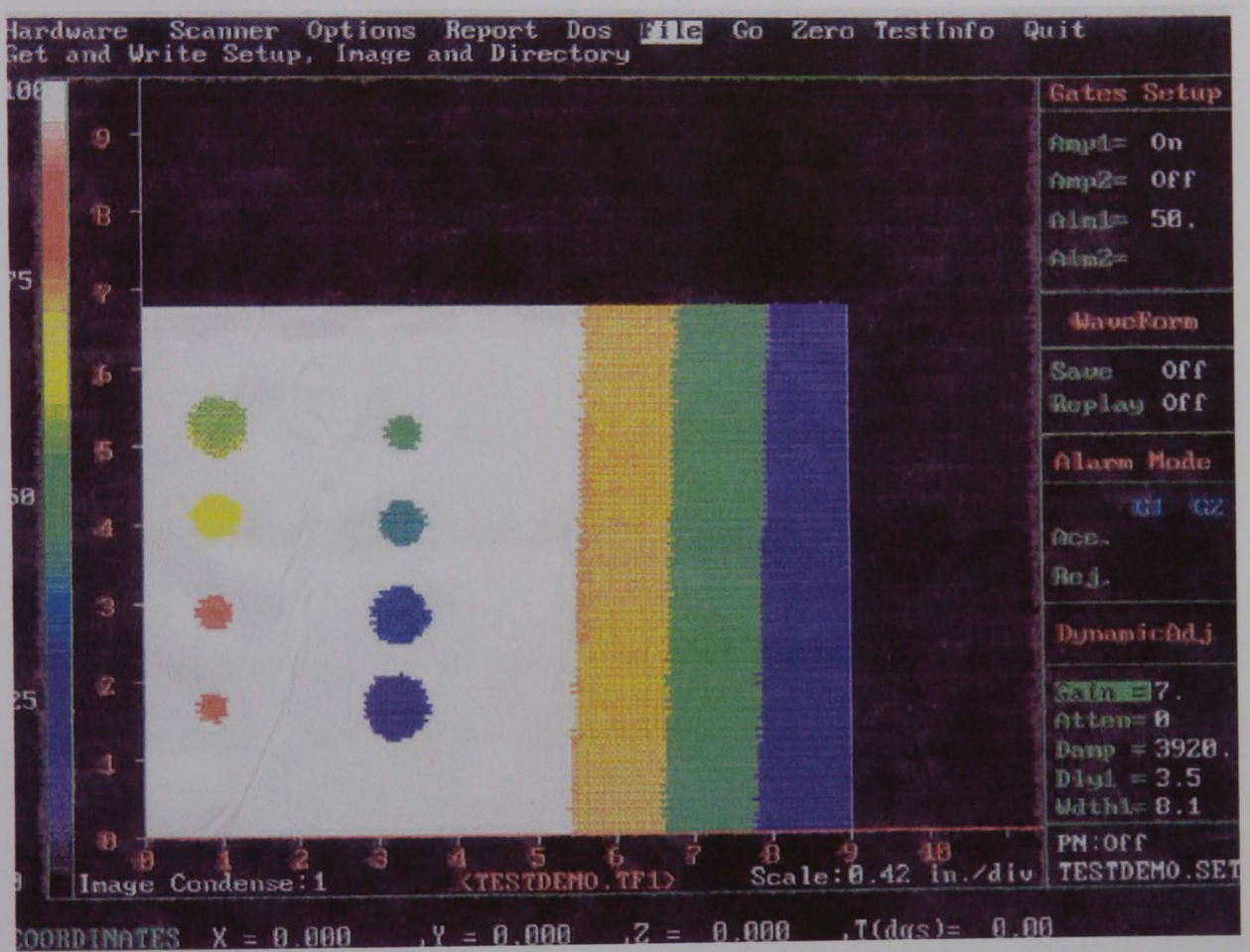

Figure 3.35 - Calibration file.

Chapter 4

Response of SMC to Low energy impact, high energy impact and Slow Indentation test

4 -1 Introduction

This chapter contains the results obtained from testing SMC on its own, both at high and low speed under similar loading regimes to those used subsequently for testing SMC-metal macrocomposites. The objective of the work reported here was to obtain an understanding of the behaviour of SMC as a reference for subsequent interpretation of macrocomposite properties.

4 - 2 Response of SMC to low energy impact

For the purpose of this work, the term low energy impact was defined as the impact tests where the incident energy of the striker was less than that required to penetrate the specimen completely. The impact response of SMC to low energy impact was investigated using both the CEAST and the QMW impact machines. The investigation concentrated on establishing the effects of testing and sample variables on impact behaviour. Factors such as sample thickness, impact velocity and incident energy were considered.

Force time curves for non-penetrating impact had similar forms irrespective of the thickness. Typical force-time (F-t) curves for a non-penetrating impact that was sufficient to cause damage for 4 mm and 8 mm SMC are shown in figure 4.1. The general shape of force-time curves consists of an initial steep rise portion followed by a transition to a curve of lower slope before a maximum is reached.

A typical trace of energy-time (E-t) obtained from such a low energy impact is shown in figure 4.2. The energy rose steadily to a peak value that corresponded to the kinetic energy of the striker (incident energy) immediately prior to impact. The point of maximum energy absorption did not necessarily correspond to the point of maximum force, but always coincided with the maximum deflection as shown in figure 4.2. The reason for this can be explained by the figure 4.3. As it is shown in figure 4.3 the velocity at the maximum force is not zero, therefore there is more energy available to drive the striker into the material which increases the displacement and the energy absorbed by the specimen. After this point specimens exhibited a degree of elastic recovery and the energy absorbed fell somewhat, levelling out at a value equal to the total energy absorbed by the system during the impact event.

A typical force-deflection curve for low energy impact is shown in figure 4.4. The shape of the curve up to the maximum force is similar to the force-time curve except it is followed by a period of unloading and partial elastic recovery with a permanent deflection after unloading. By performing impacts with incident energies above and below the energy absorbed by specimens at the initial peak force (P_i) in figure 4.4, it was determined that the initial peak corresponded to crack initiation on the face of the specimen opposite to the impacted surface. Apart from a slight dent on the impacted surface which is due to very low area of contact at the early stage of loading, no damage was detected in specimens sectioned and examined after loading to a lower level. This initial peak is subsequently referred to as the transition force, indicating the onset of damage in the material.

For specimens of equal thickness, the transition force (P_i) did not change (subject to slight scatter) with increasing impact energy and therefore velocity, but the maximum force did (fig. 4.5). The force-time curves of three SMC specimens of similar thickness (nominally 4 mm) subjected to a range of impact velocities are shown in figure 4.5. The development of damage with increasing impact energy of 4 mm thickness of SMC is shown in figure 4.6. All the damage appeared to be constrained well within the boundaries of the test support ring, indicated by the circular marking on the specimen.

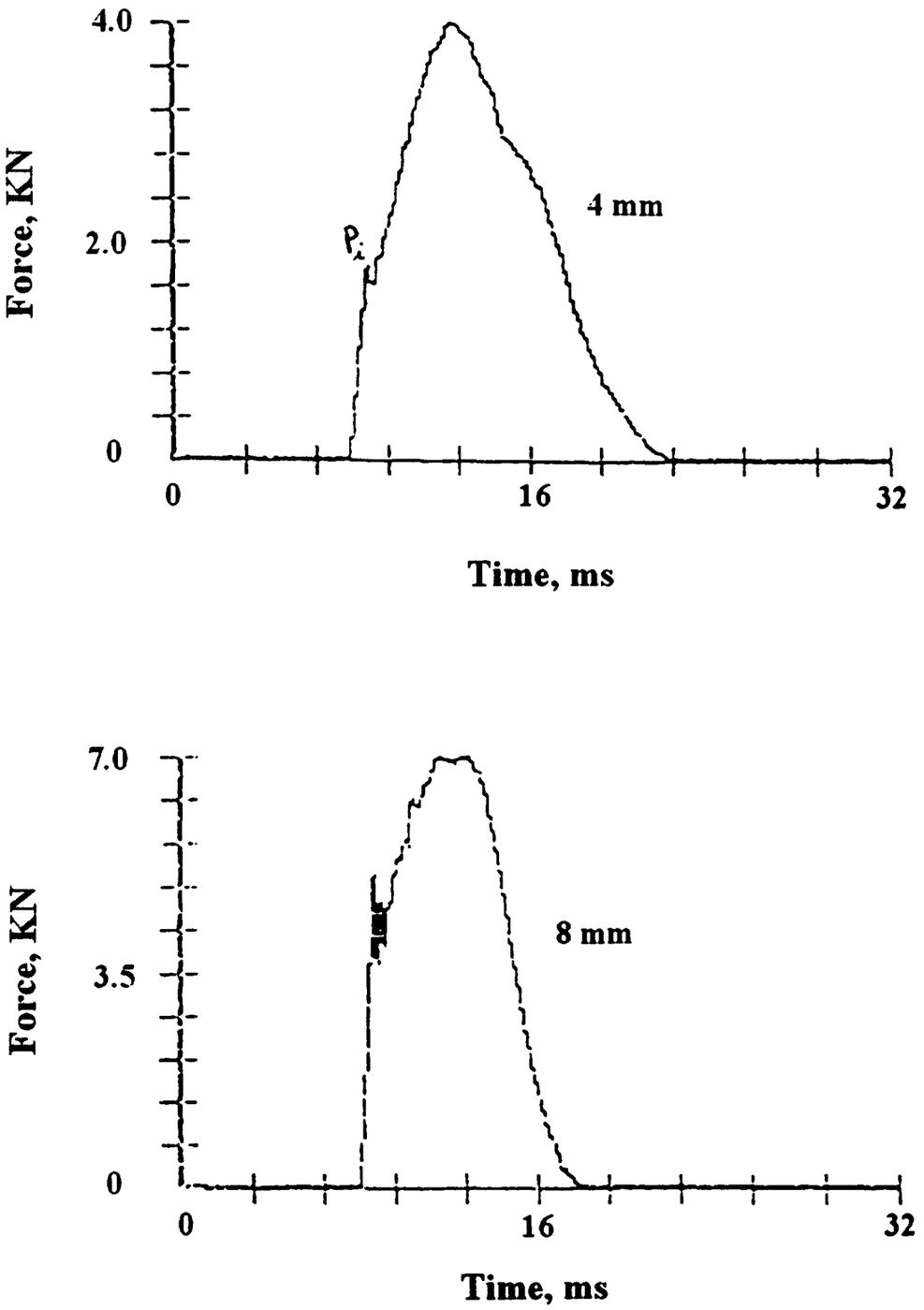

Figure 4.1 - Typical force-time curve for non-penetrating impact a) 4 mm SMC, b) 8 mm SMC.

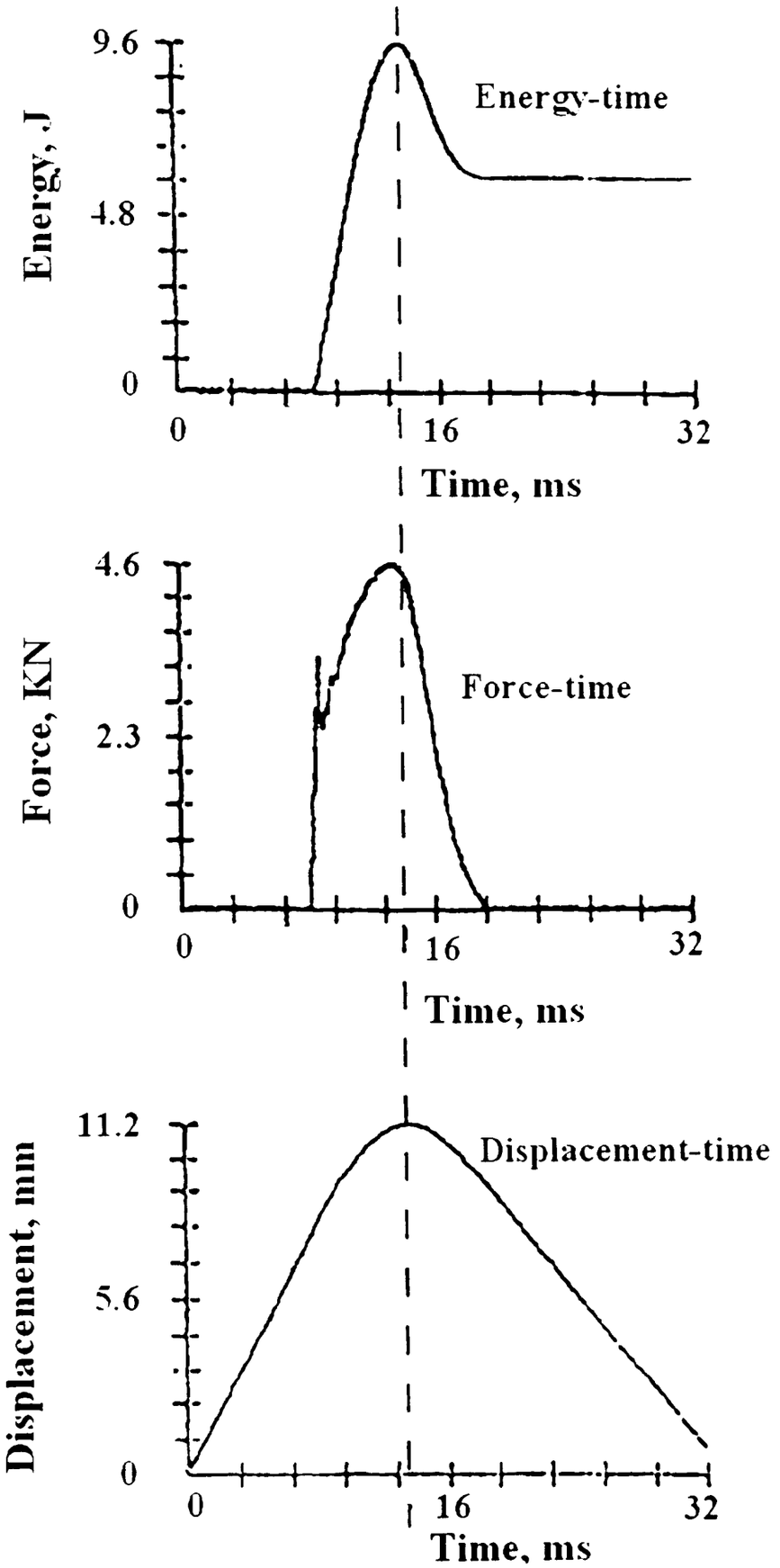

Figure 4.2 - Position of the point of maximum energy on the force-time and displacement curves.

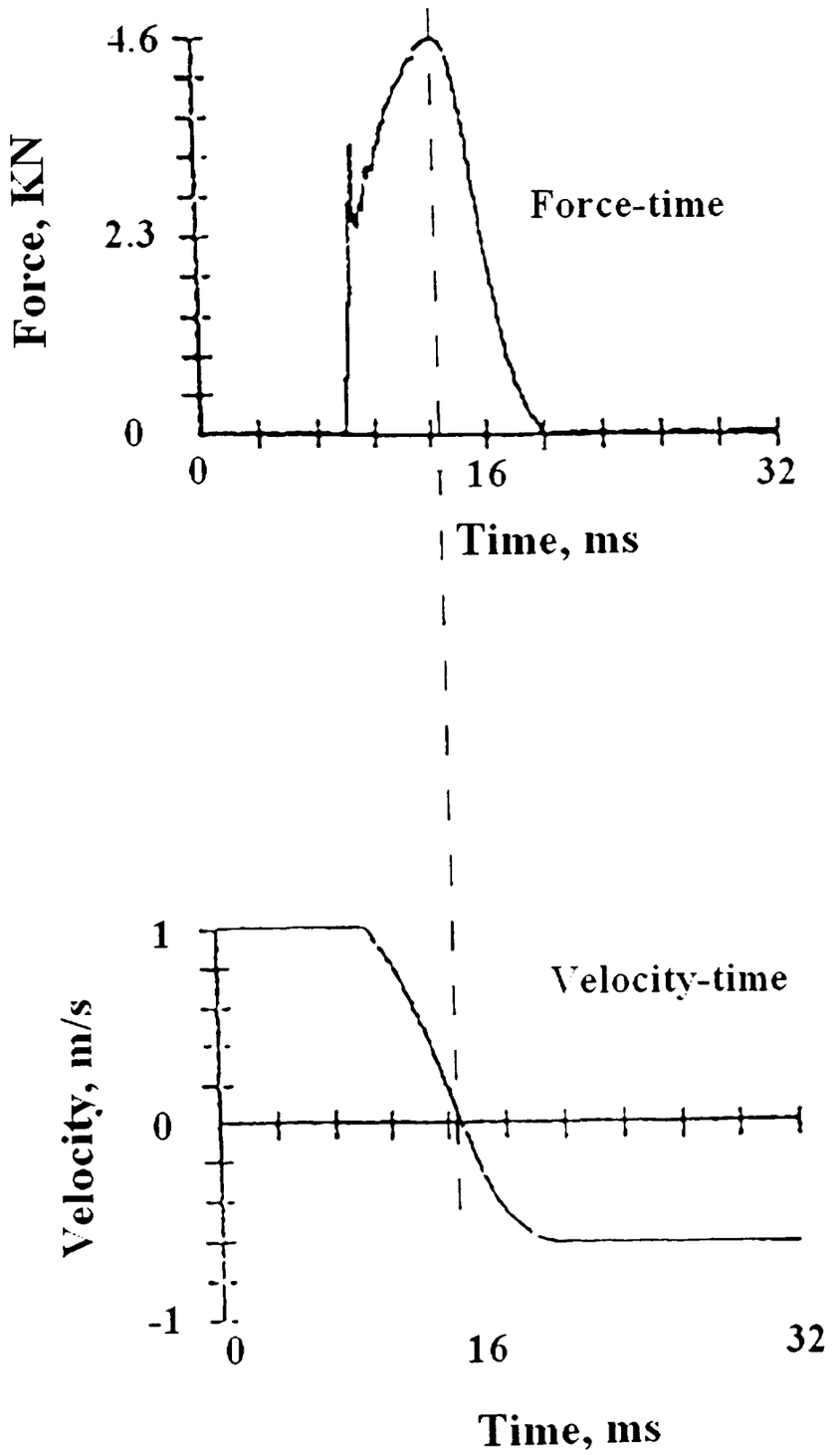

Figure 4.3 - Shows that the velocity of the striker is not zero at maximum force.

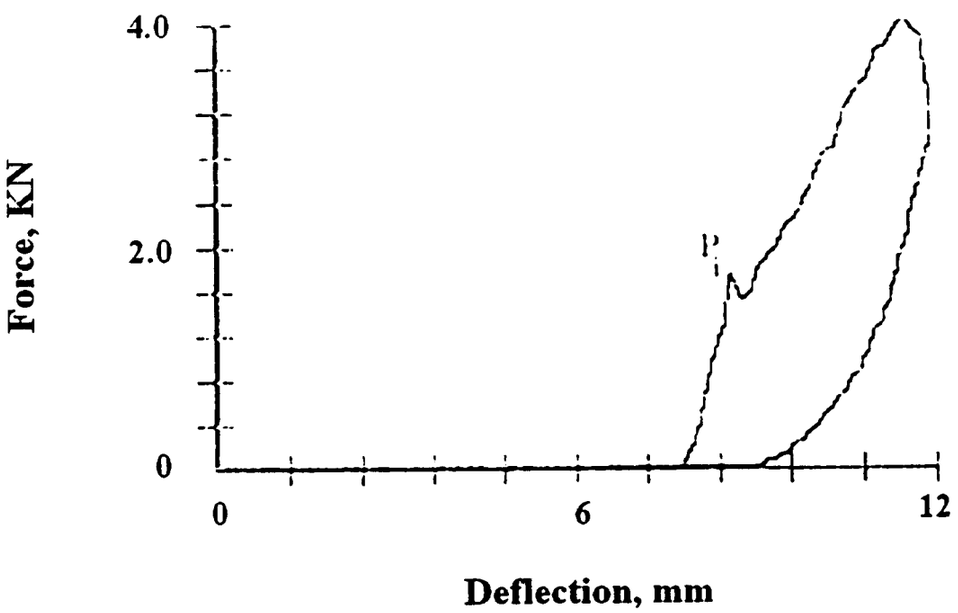

Figure 4.4 - Typical force-deflection for non-penetrating impact for 4 mm SMC

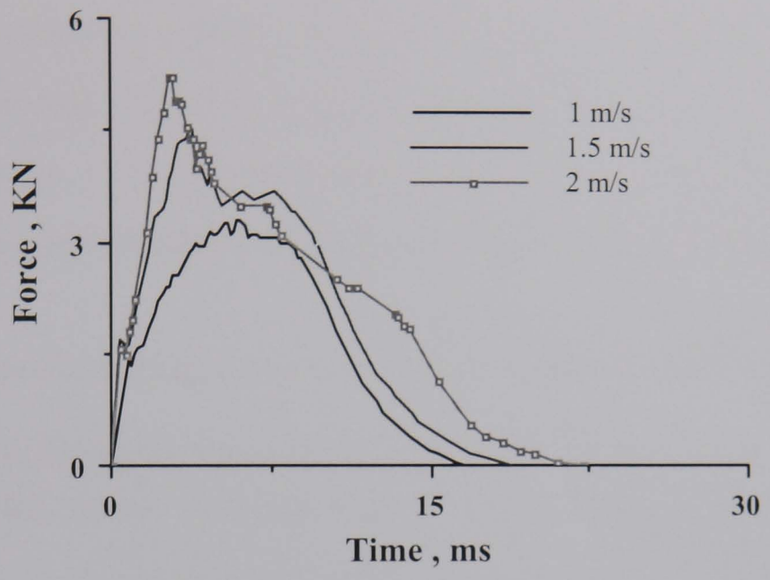

Figure 4.5 - Force-time curves for SMC, thickness 4 mm, for impact at 1, 1.5 and 2 m/s.

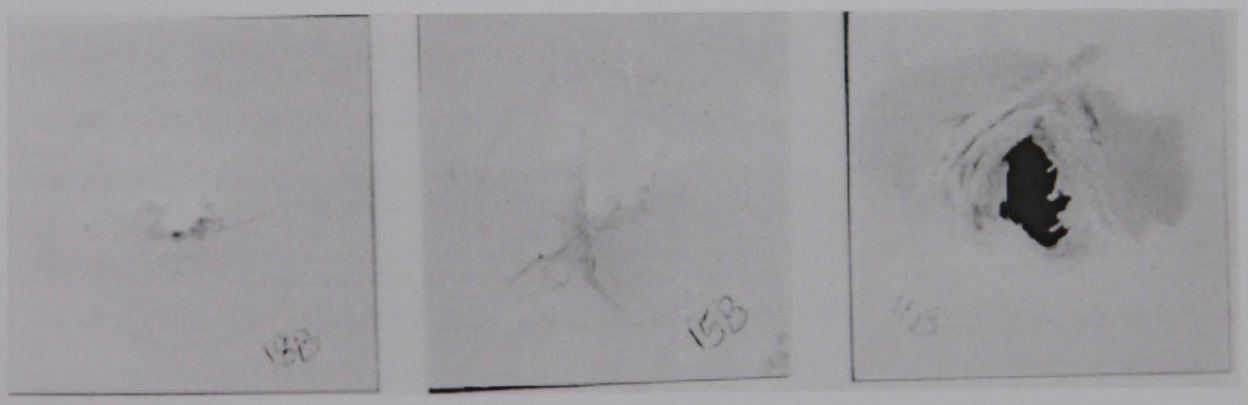

Figure 4.6 - SMC, thickness 4 mm, after impact at a) 1m/s (9J), b) 1.5 m/s (21J), c) 2 m/s (38J).

The force-deflection curves corresponding to the force-time curves shown in 4.5 are shown in figure 4.7. It is apparent that each specimen followed the same loading curve at first. Subsequently however, the individual curves followed different paths as the material underwent a stage where an increase in deflection was accompanied by a decrease in load. The effect of impact speed being to alter the maximum force and the rebound point. As the incident energy increases the separation between the peak force and the rebound point increases which is an indication of more damage in the specimen.

The energy (E_i) corresponding to the transition load (P_i) which is shown in figure 4.4 is very small. This is the energy which is required to initiate damage on the surface opposite to impacted surface. For specimens of equal thickness the transition energy (E_i) is effectively independent of the impact velocities (fig. 4.8). Specimens which were subjected to incident energies less than the transition energy, did not show any sign of damage and the force-time curves were quite symmetric as shown in figure 4.9. When the incident energy reached the level of the transition energy, the force-time was no longer symmetric and damage in the form of very tiny cracks at the surface opposite to the impacted surface was observed. The force-time curve corresponding to the incident energies in the vicinity of the level of the transition energy is shown in figure 4.10. Due to the insufficient incident energy and absorption of most of the incident energy during the damage initiation process the second peak after the transition load is lower than (P_i).

Increasing the level of incident energy caused more damage in the specimen and also increased the value of the second peak which is the maximum load (P_{max}) during impact (figs. 4.11 and 4.12).

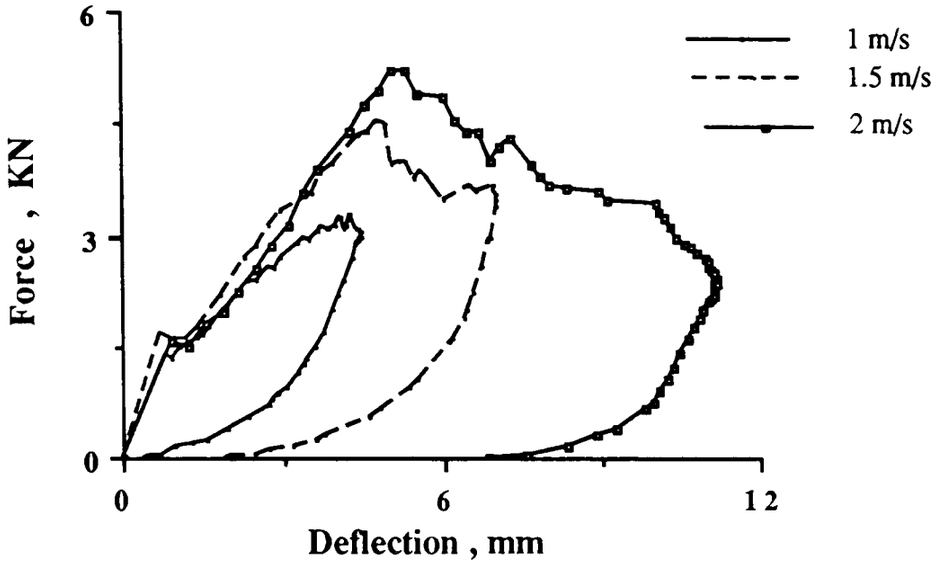

Figure 4.7 - Force-deflection curves for SMC, thickness 4 mm, for impact at 1, 1.5 and 2 m/s.

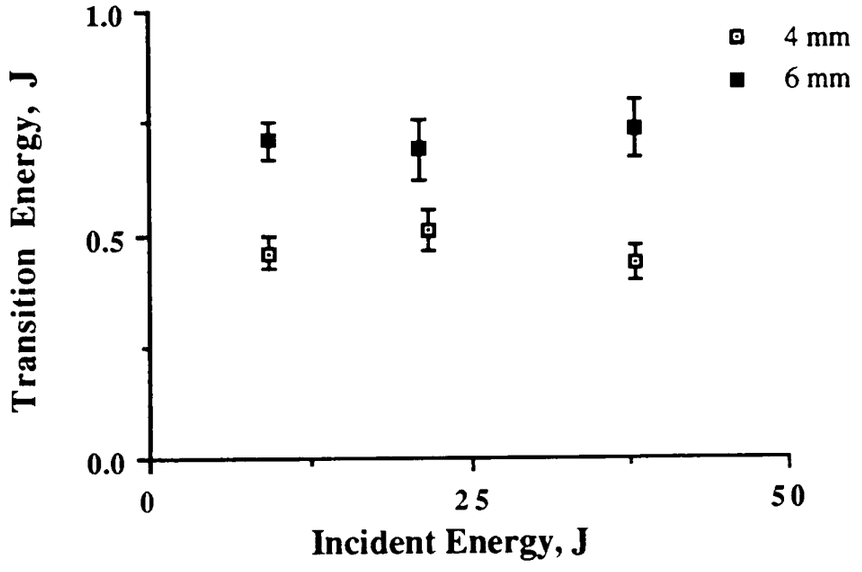

Figure 4.8 - Variation of transition energy with incident energy for different thicknesses of SMC. Error bars denote standard deviation.

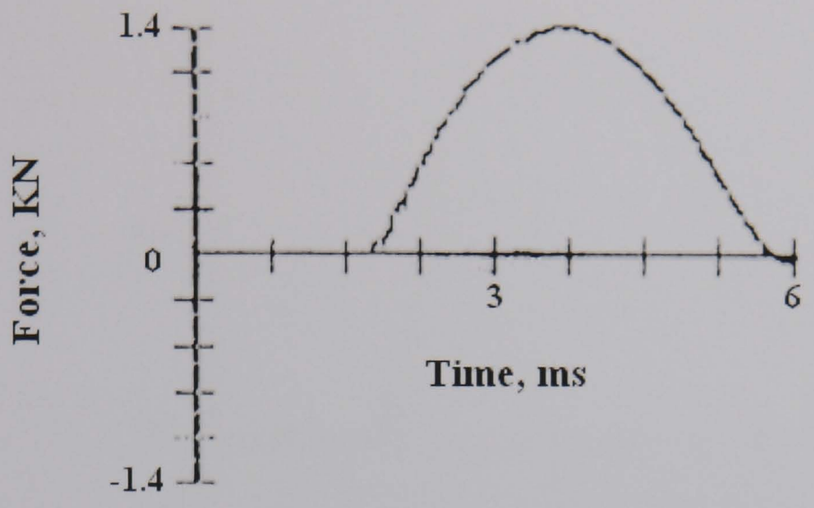

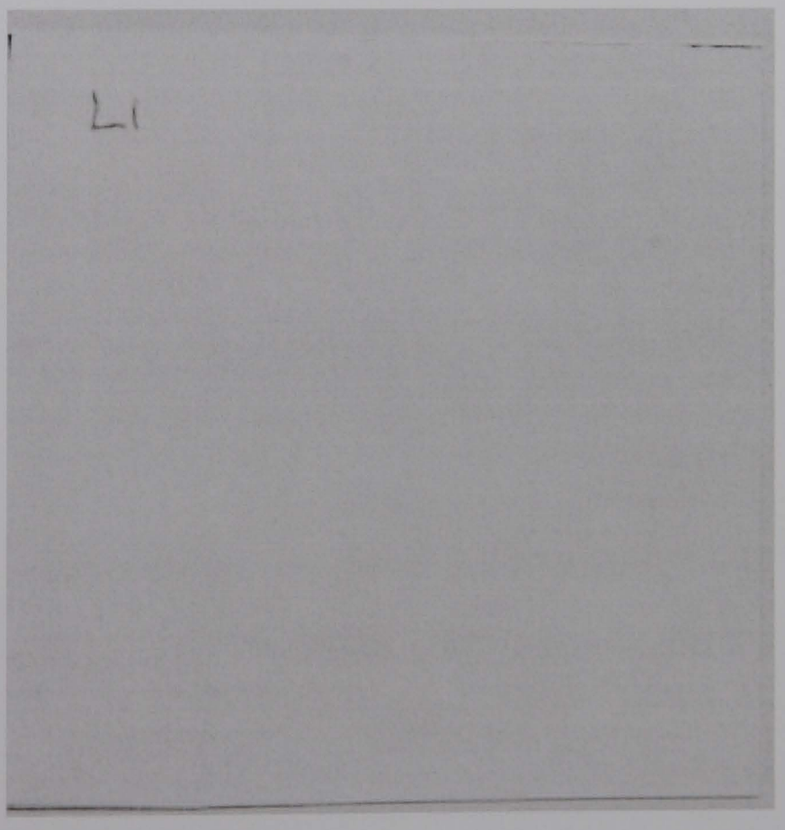

Figure 4.9 - Force-time curve and photograph of specimen for 4 mm SMC when subjected to 0.5 J incident energy.

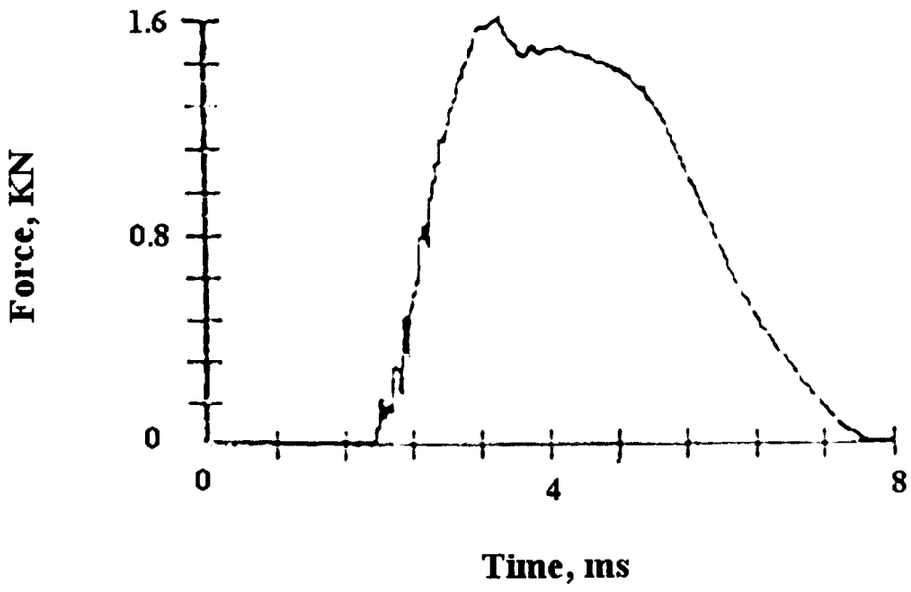

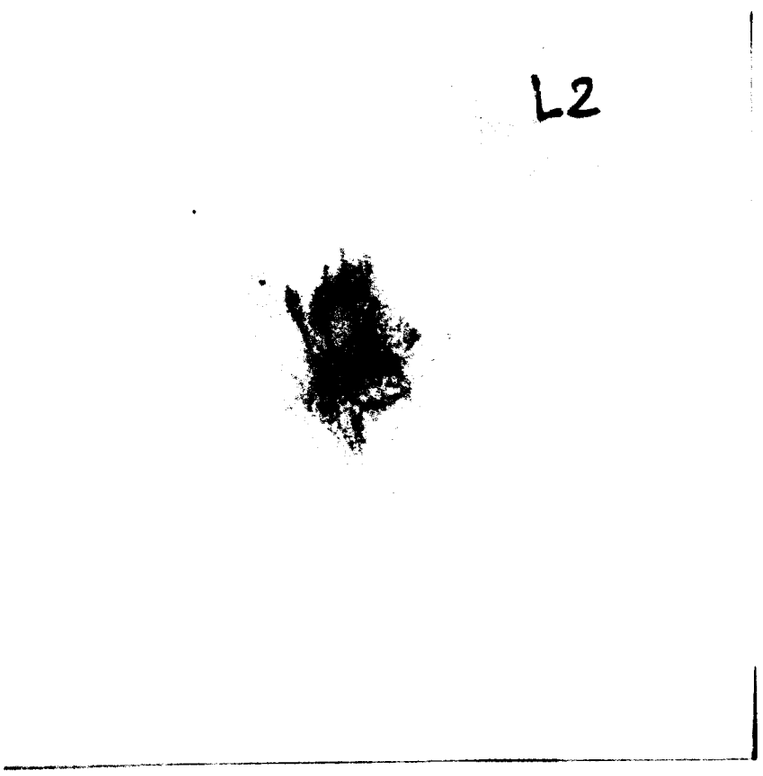

Figure 4.10 - Force-time curve and photograph of damaged specimen for 4 mm SMC when subjected to 1.1 J incident energy.

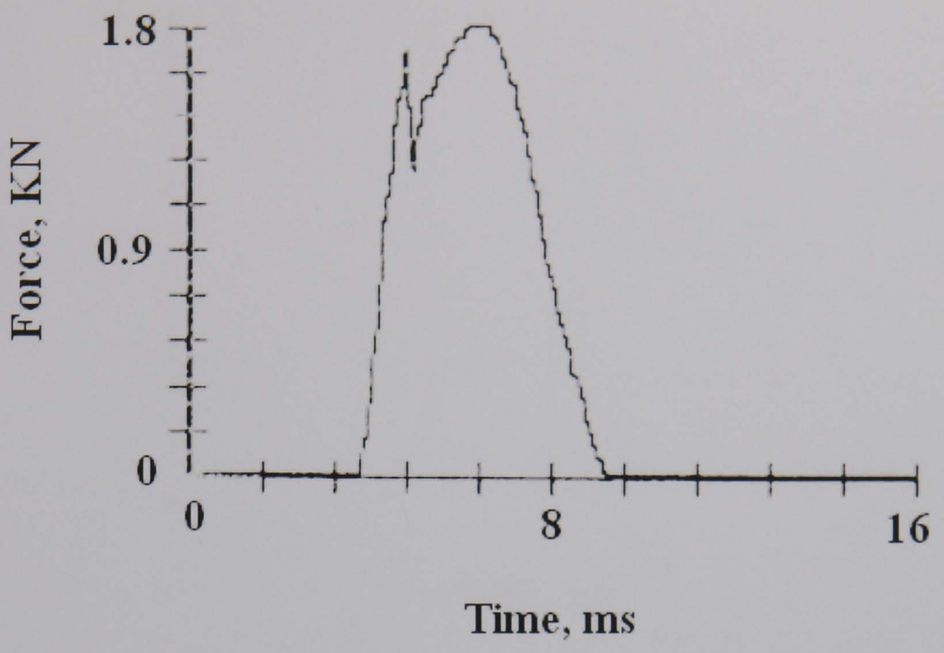

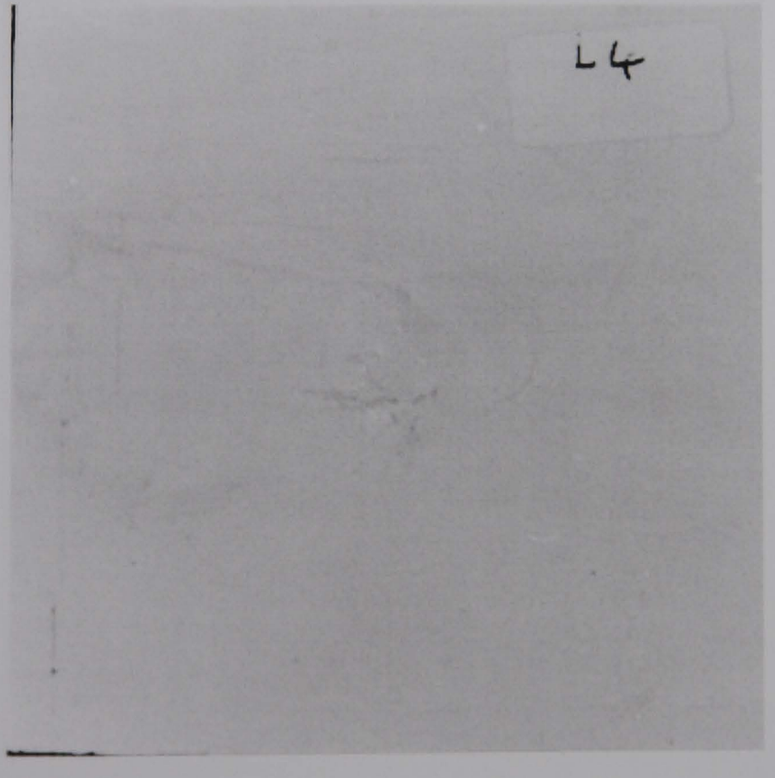

Figure 4.11 - Force-time curve and photograph of damaged specimen for 4 mm SMC when subjected to 1.99 J incident energy.

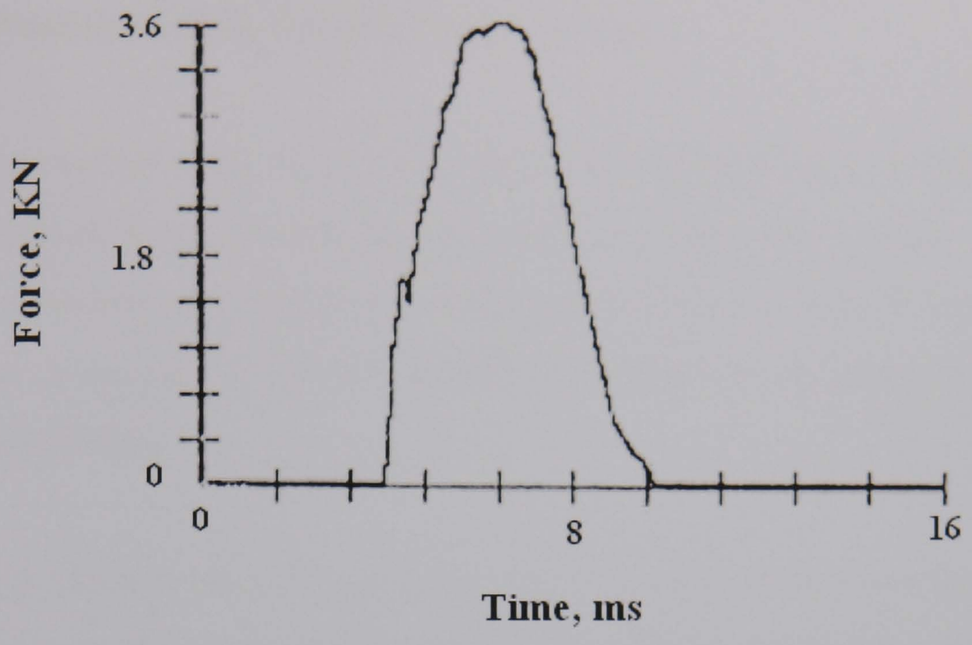

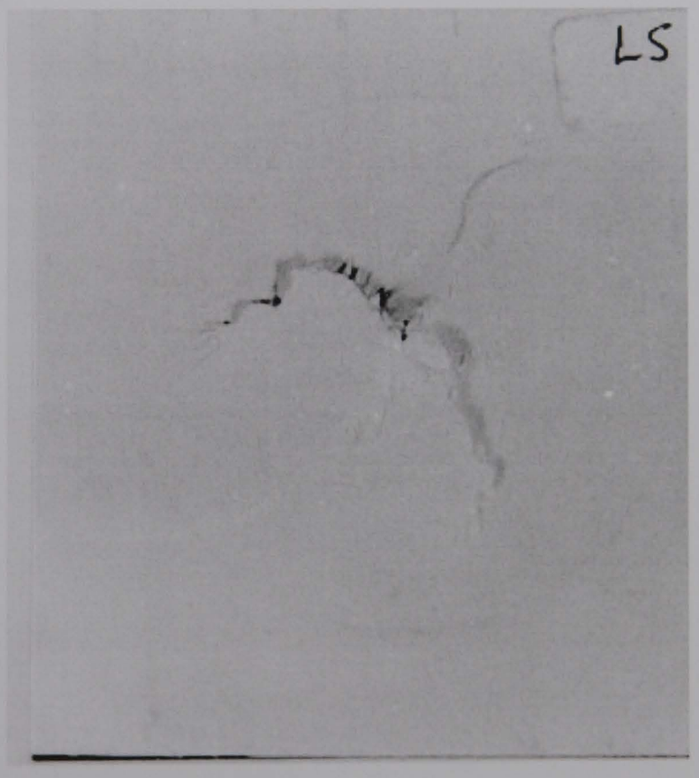

Figure 4.12 - Force-time curve and photograph of damaged specimen for 4 mm SMC when subjected to 9 J incident energy.

4 - 3 Response of SMC to High Energy Impact

For the purpose of this study the term high energy impact was defined as the impact tests where the incident energy of the striker was more than the penetration energy, therefore all the tested specimens were perforated. The impact response of SMC to high energy impact was investigated using both the CEAST machine and the impact machine at Cambridge university.

A typical CEAST force-time (F-t) curve for a penetrating impact is shown in figure 4.13. The general shape of the force-time curve is similar to the one of non-penetrating impact which consists of an initial steep rise portion followed by a transition to a curve of lower slope before a maximum is reached. The energy-time curve for penetrating impact (fig. 4.14) is not similar to the one of non-penetrating impact (fig. 4.2). The energy rose steadily with a gradual decrease in the slope with no fall in the energy absorbed.

The force-deflection curves obtained using CEAST and the impact machine at Cambridge university were the same and were similar to the corresponding force time curves (fig. 4.15). Since penetration took place, there was no rebound point. SMC specimens which were subjected to high energy impact exhibited a common failure mode, irrespective of specimen thickness, figure 4.16. The damaged zone consisted of a central hole surrounded by hinged, triangular flaps of material. All of the damage appeared to be constrained well within the boundaries of the test support ring, indicated by the circular marking on the specimen. The SMC was severely damaged in the vicinity of the hole, exhibiting extensive fibre and resin microcracking and delamination.

4 - 4 The effect of thickness and incident energy on peak force, transition load and absorbed energy.

It was mentioned earlier that, for SMC specimens of equal thickness, peak force increased with incident energy up to the point when through penetration was achieved. After this point was reached an increase in incident energy did not result in any further increase in the peak force (fig. 4.17). Both the transition load and peak load (for perforated specimens) showed a linear relationship with the square of thickness as shown in figures 4.18 and 4.19.

The total energy absorbed by SMC specimens is shown in figure 4.20 as a function of the incident energy. Each thickness exhibited a linear relationship between these energy terms up until reaching a plateau corresponding to total penetration of the specimen by the impactor. The linear portion of the curve did not pass through the origin as a certain finite elastic energy had to be supplied to the material before energy could be permanently absorbed by fracture processes. This elastic energy threshold was very small compared to the total energy that could be absorbed by irreversible fracture processes and increased with specimen thickness. The relation between maximum energy absorbed and thickness is shown in figure 4.21. It is apparent from these results that increasing the impact velocity and incident energy beyond a certain level had no effect on the amount of energy absorbed by the material and no effect on the fracture appearance as shown in figure 7.30, chapter 7. The maximum energies absorbed by SMC were 22 J, 58 J, 98 J, and 152 J for 2, 4, 6, and 8 mm sheet respectively.

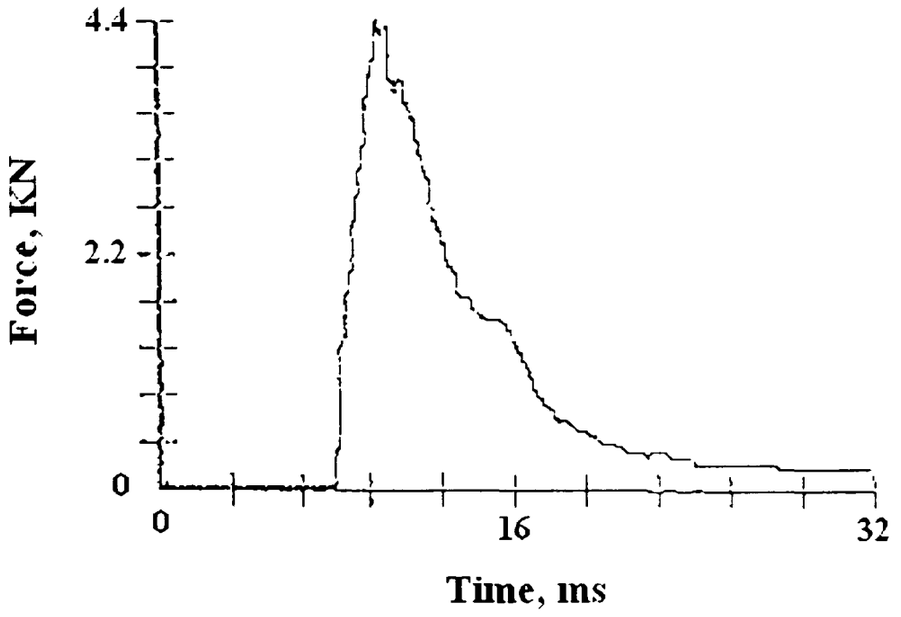

Figure 4.13 - Force-time curve for SMC, thickness 4 mm, after complete penetration.

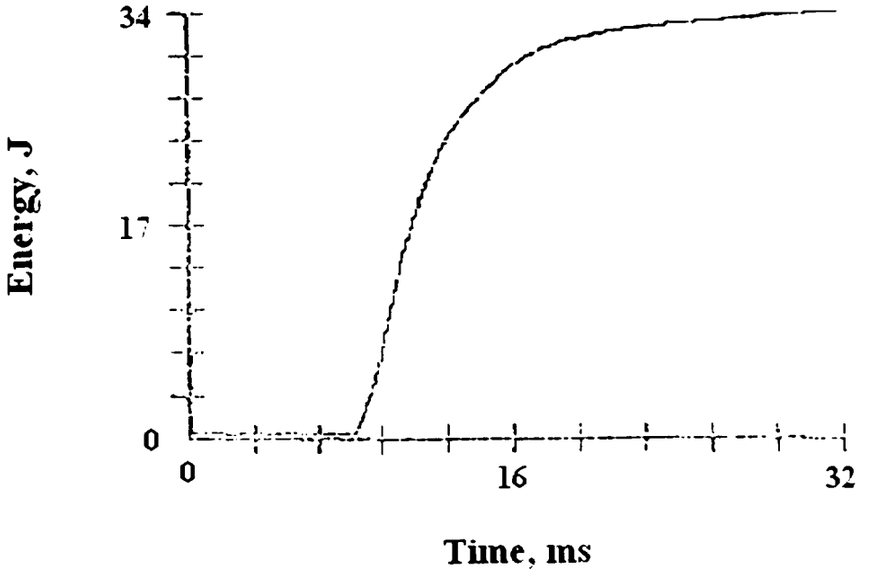

Figure 4.14 - Energy-time curve for SMC, thickness 4 mm, after complete penetration.

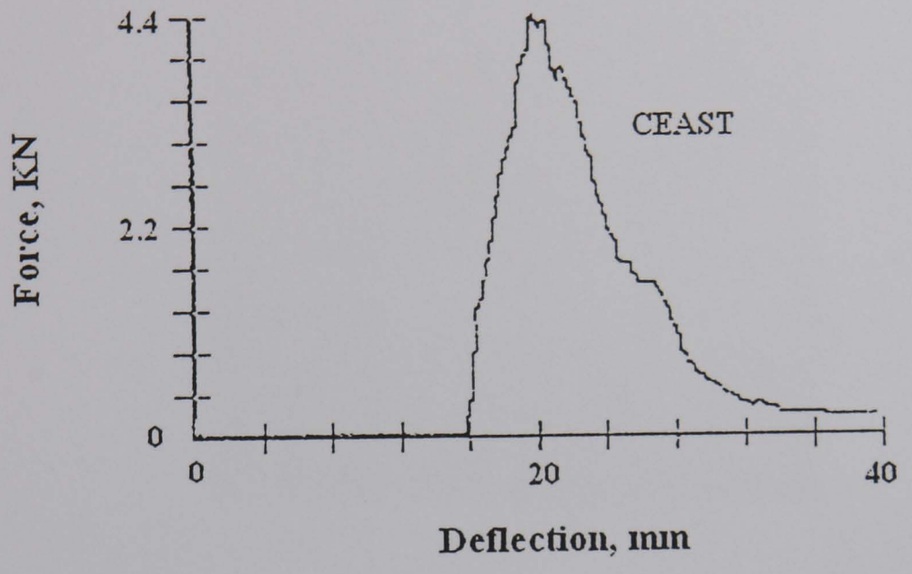

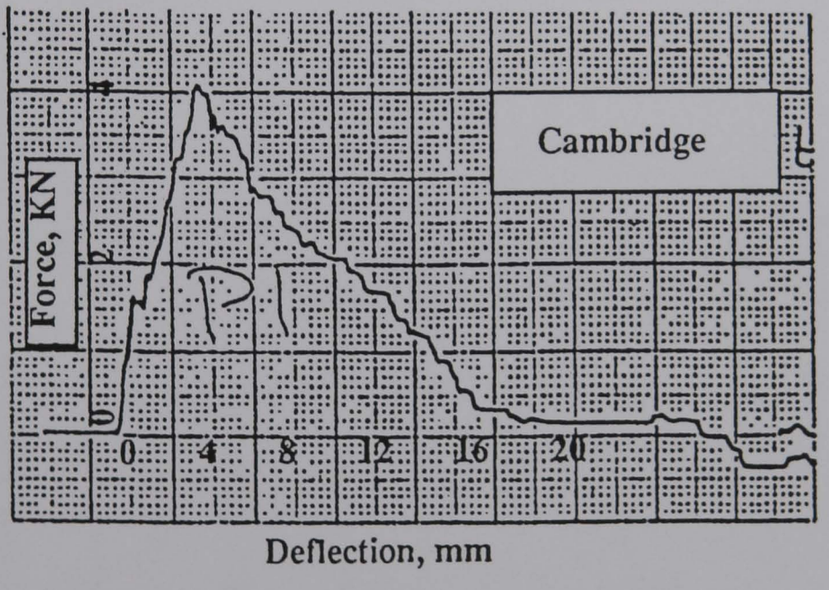

Figure 4.15 - Force-deflection curve for SMC, thickness 4 mm, after complete penetration, top CEAST, bottom Cambridge.

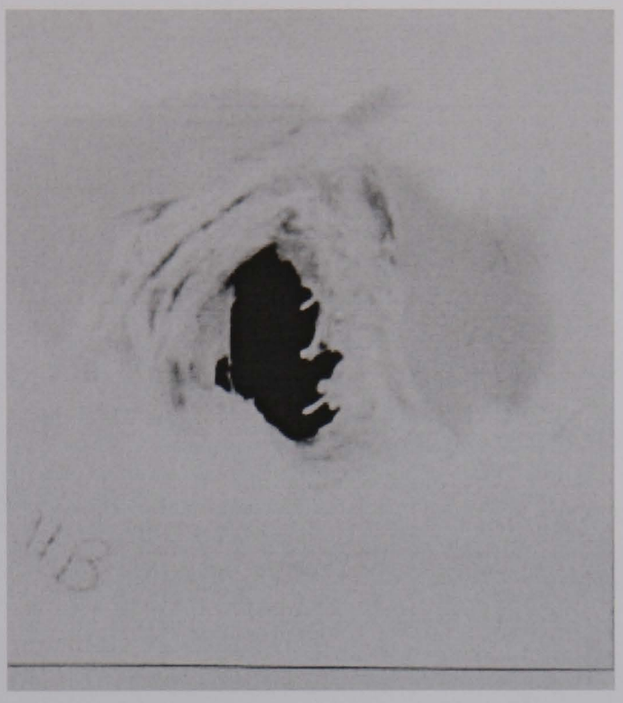

Figure 4.16 - SMC specimen after complete penetration.

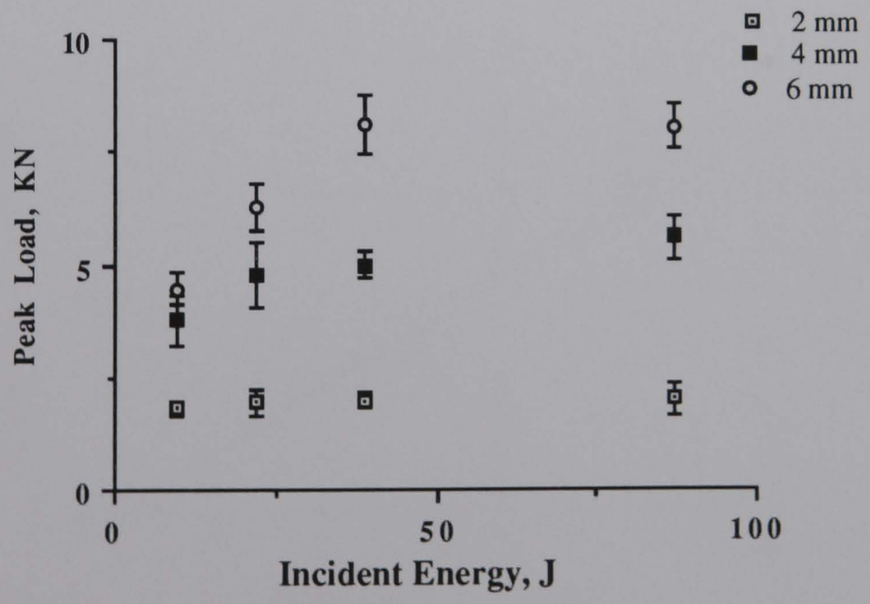

Figure 4.17 - Peak force versus incident energy for three different thicknesses of SMC. Error bars denote standard deviation.

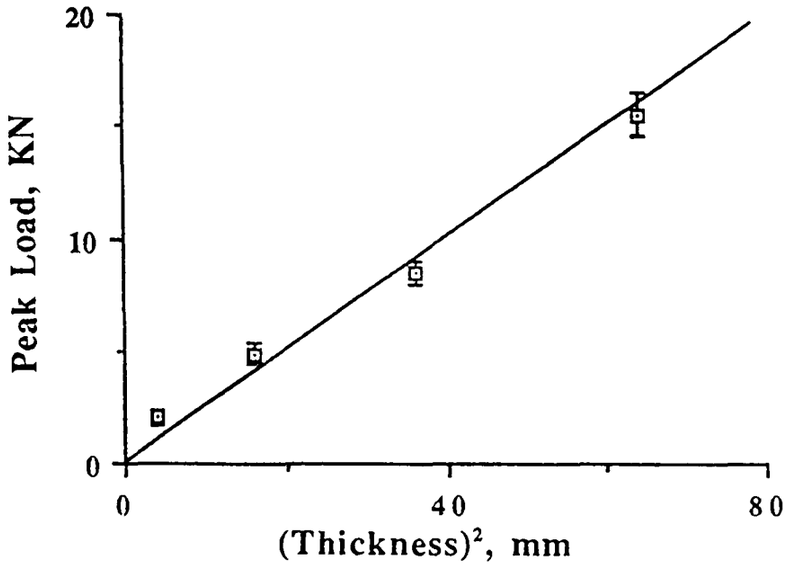

Figure 4.18 - Peak force when complete penetration takes place as a function of (thickness)^2. Error bars denote standard deviation.

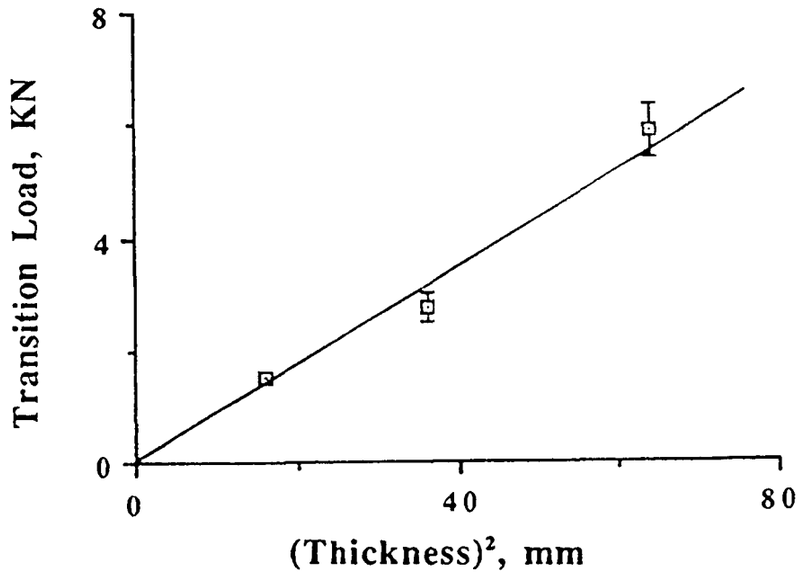

Figure 4.19 - The variation of transition load as a function of (thickness)^2. Error bars denote standard deviation.

4.5 Response of SMC to different impact velocities at a constant incident energy.

In a drop weight test, the incident energy is usually increased by increasing the height at a constant weight. If the weight of the striker is reduced, the same incident energy can be obtained at higher striker height (higher velocities). In order to see whether there is any difference in the behaviour of the SMC specimens subjected to the same value of incident energy but at different impact velocities, 4 mm SMC specimens were subjected to 21.7 joules incident energy at impact velocities of 1.23, 1.5 and 2.57 m/s. The corresponding masses of the strikers were 28.4, 19.32 and 6.57 Kg respectively.

The impact tests at constant incident energy where the weight of the striker was varied as well as the drop height, did not exhibit any differences as is illustrated by figure 4.22.

4 - 6 Response of SMC to Slow Indentation Test

Slow indentation tests on SMC showed that the general shape of the load deflection curves are similar to those of impact (fig. 4.23). The transition loads are identical to those obtained from the impact tests. This indicates a rate-insensitivity of the material. Examination of the slow test specimens loaded below the transition point, showed no visible damage through the thickness and at the tensile surface (fig. 4.9). Cracks were initiated at the tensile surface at the transition point.

Slow indentation tests clearly showed (fig. 4.23) that the peak force and total energy absorbed were less than those obtained during impact.. A typical profile of deflection obtained during slow tests at loads below the transition load is shown in figure 4.24.

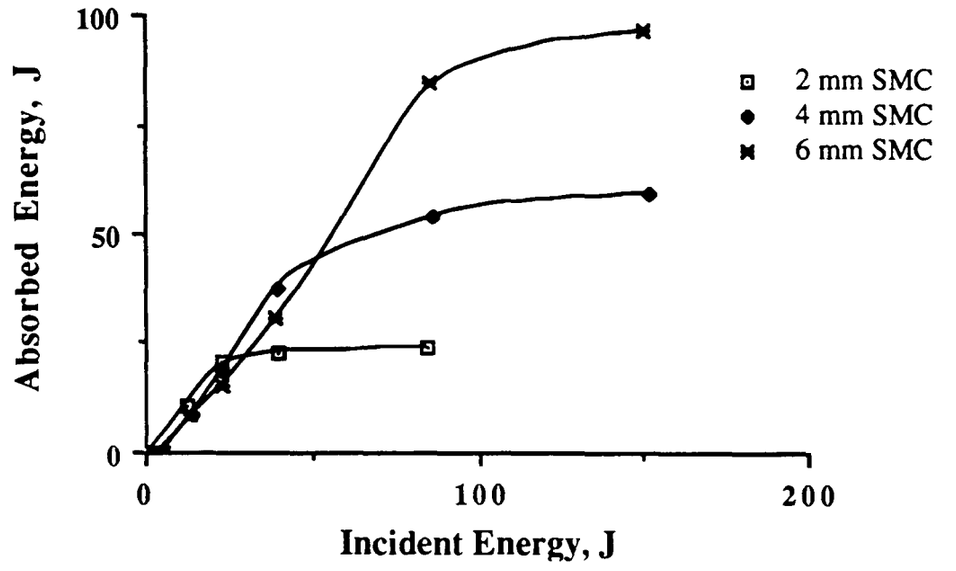

Figure 4.20 - Absorbed energy versus incident energy for three different thicknesses of SMC.

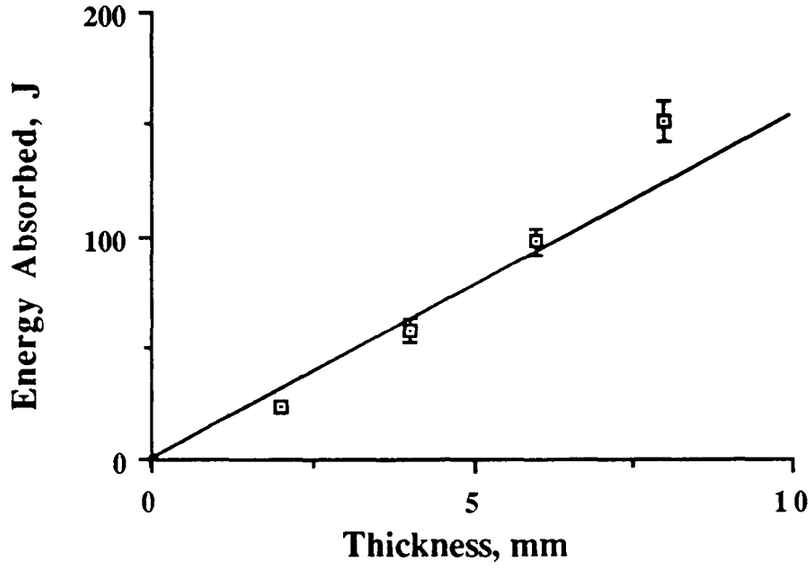

Figure 4.21 - Maximum energy absorbed by SMC specimens as a function of thickness. Error bars denote standard deviation.

The profile is symmetric about the axes passing through the tup. When the specimen was unloaded, the transducer indicated that the specimen had gone back to its original position and there was no deflection.

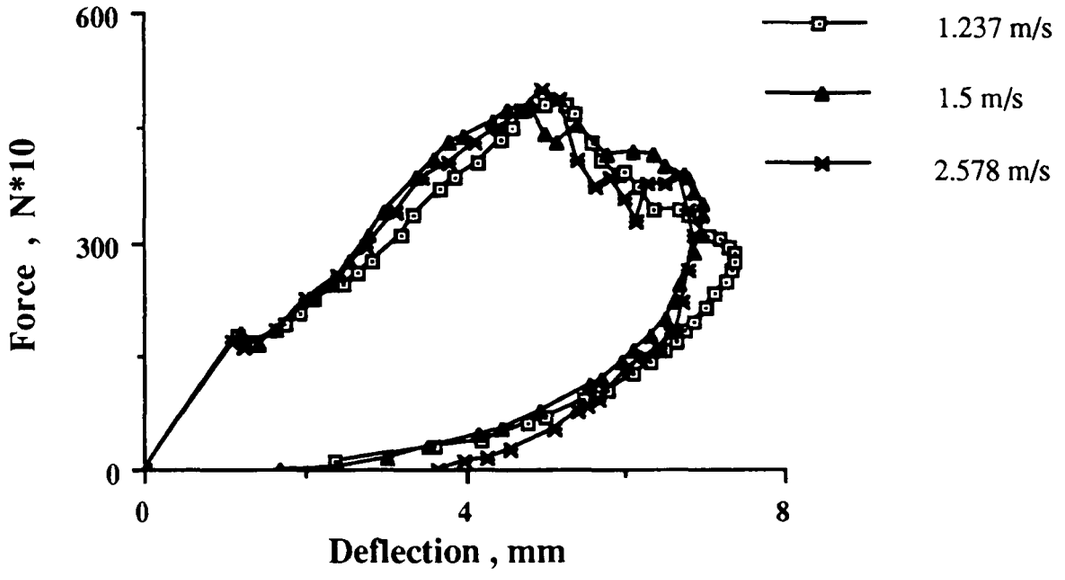

Figure 4.22 - Force deflection curve for three SMC specimens of common thickness impacted at constant energy but differing velocities.

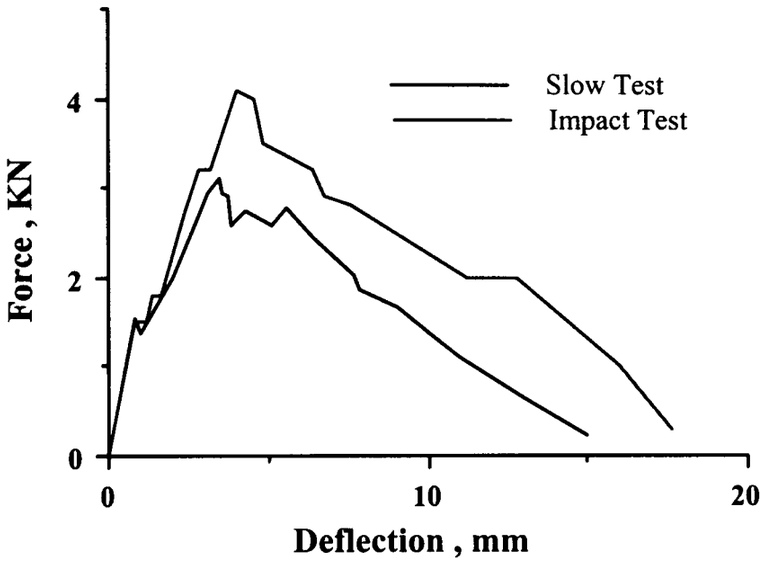

Figure 4.23 - Comparison of the load-displacement curves from a slow indentation test and an impact test for 4 mm SMC.

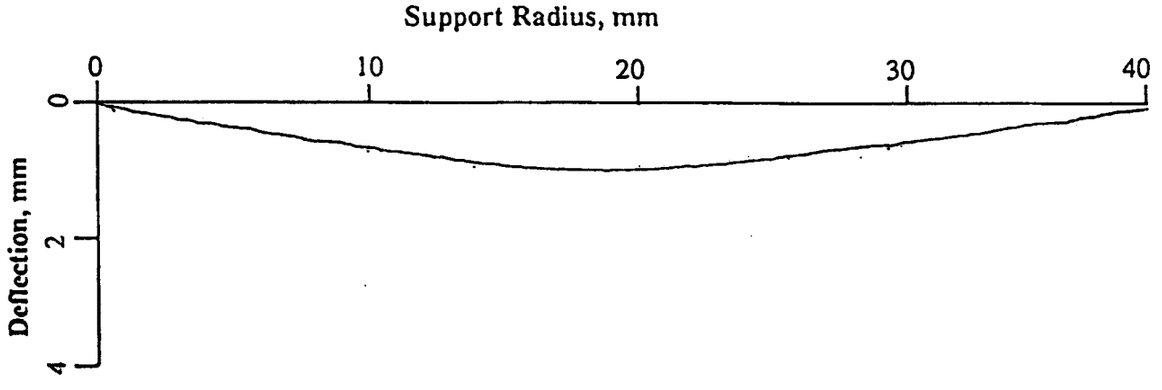

Figure 4.24 - Profile of deflection during slow test for 4 mm SMC specimen which shows the profile is symmetric about the axes passing through the tup.

4 - 7 Prediction of the load - deflection of SMC specimens by the Energy Balance method, Theory of Bending and Finite Element Analysis.

4 - 7.1 Introduction

In designing SMC structures for impact resistance it is necessary to understand the stresses which are generated during impact. Knowing the value and distribution of stresses makes it possible to reinforce the weak points and improve the impact resistance significantly. An analysis of stress in an impacted specimen is also a good tool for explaining the events during impact. For example, finite element analysis was used in this work to explain why more damage is built up in SMC with a layer of stainless steel.

In the following sections some of the techniques which are used for composite materials are employed and particular attention is given to finite element analysis. All of the models used assumed that the material is perfectly elastic and therefore they were valid up to the damage threshold.

4 - 7.2 The Energy Balance Method.

The impact response of SMC specimens was predicted by considering the deformations shown in figure 4.25. The energy of the impacter is accommodated mainly in flexural and contact deformations up to the point of initial fracture. At the point of contact, the plate undergoes the Hertzian contact deformation α, as well as plate bending deformation δ. The Hertezian force-deformation relationship for the contact problem is (76):

$$P_c = n.\alpha^{\frac{3}{2}} \qquad (1)$$

whereas the force-deflection relationship for a plate subjected to a concentrated load will be of the form (127):

$$P_p = K.\delta \qquad (2)$$

where subscripts c and p refer to the contact problem and plate bending respectively and K is the spring constant for the plate.

The energy balance for the system can be written as:

$$\frac{1}{2}mv^2 = \int_0^{\delta} P_p d\delta + \int_0^{\alpha} P_c d\alpha \tag{3}$$

Substitution of 1 and 2 into 3 and evaluation of the integral yields:

$$\frac{1}{2}mv^2 = \frac{1}{2}K\delta^2 + \frac{2}{5}n\alpha^{\frac{5}{2}} \tag{4}$$

Finally combining 1, 2, and 4 and noting $P_c = P_p = P$ we obtain (44):

$$\frac{1}{2}mv^2 = \frac{1}{2}(\frac{P^2}{K}) + \frac{2}{5}(\frac{P^{\frac{5}{3}}}{n^{\frac{2}{3}}}) \tag{5}$$

where:

$$n = \frac{4}{3}\sqrt{R_1}(\frac{1-\mu_1^2}{E_1} + \frac{1-\mu_2^2}{E_2})^{-1} \tag{6}$$

$$K = \frac{4\pi E_2 t^3}{3(1-\mu_2)(3+\mu_2)R_2^2} \tag{7}$$

where:

$P = P_c = P_p$	applied force
α	contact deformation
δ	plate deflection
n and K	constants which can be calculated from equations 6 and 7
m	mass of the striker
v	impact velocity

R_1 radius of the striker head

R_2 radius of the specimen support

t specimen thickness

μ_1, E_1 Poisson's ratio and Young's modulus of the striker head

μ_2, E_2 Poisson's ratio and Young's modulus of the plate material

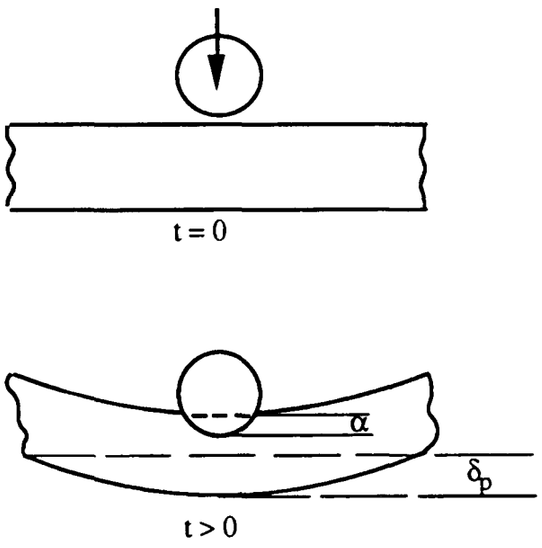

Figure 4.25 - Local and overall deformation of flexible target.

n and K can be calculated from equations 6 and 7 respectively by substituting the values of:

E_1 = 210 GPa, E_2 = 13.7 GPa, μ_1 = 0.3, μ_2 = 0.3, R_1 = 10 mm, R_2 = 20 mm and t = 4 mm (source, experimental results in chapter 3 and standard data sheets).

into equations 6 and 7. Knowing the values of K and n, it is possible to plot force-deflection curve by calculating α and δ from equations 1 and 2. Since the deflection of the impact machine is the deflection of the striker, therefore the sum of α and δ is taken

as the deflection of the specimen. A comparison of the force-deflection curve calculated from equations 1 and 2 and the experimental impact force - deflection curves are shown in figure 4.26.

By using the energy balance outlined in equation 5, assuming no damage, it is possible to estimate the variation of impact force with impact velocity. Calculating a value of n, by substituting the following values in equation 6 and value of K from equation 7, the value

$E_1 = 210$ GPa, $E_2 = 13.7$ GPa, $\mu_1 = 0.3$, $\mu_2 = 0.3$, $R_1 = 10$ mm, $R_2 = 20$ mm and $t = 4$ mm

of impact velocity and incident energy which can generate a given impact force can be determined from equation 5. The relationship between the impact force as a function of impact velocity is shown in figure 4.27. The estimated values are shown as a continuous line. The curve is correct if no damage occurs. Therefore, the plotted line can be used to determine the impact velocity at a given impact force.

Although the energy balance model overestimates the stiffness, its agreement with the experimental data is satisfactory. The deviation of experimental data from theoretical prediction above a transition load is because of inelastic deformation of the specimen. Having the value of force generated during impact, the maximum pressure (q_{max}) and the pressure distribution $q_{x,y}$ can be obtained from the following equations:

$$q_{max} = \frac{3P}{2\pi a^2}$$

$$q_{x,y} = q_{max}\left[1 - \frac{x^2}{a^2} - \frac{y^2}{a^2}\right]^{\frac{1}{2}}$$

The distribution of tensile, compressive and shear stresses in the specimen due to surface pressure can be obtained by the equations developed by Love (128).

The maximum tensile, compressive, and shear stresses (σ_T , σ_C , and σ_S respectively) that occur in the specimen as shown in figure 2.10 can be determined from the following equations:

$$\sigma_T = -\left(\frac{1 - 2\mu}{3}\right) q_{max}$$

$$\sigma_C = q_{max}$$

$$\sigma_S = \left[\frac{1 - 2\mu}{4} + \frac{\sqrt{2(1+\mu)^3}}{9}\right] q_{max}$$

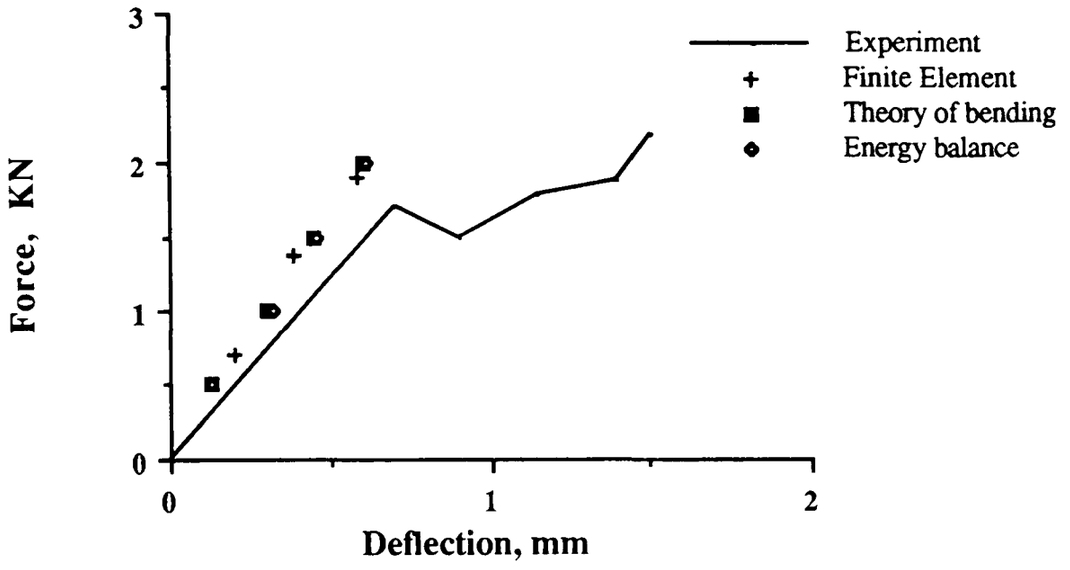

Figure 4.26 - Comparison between the load-deflection of the finite element model, energy balance method

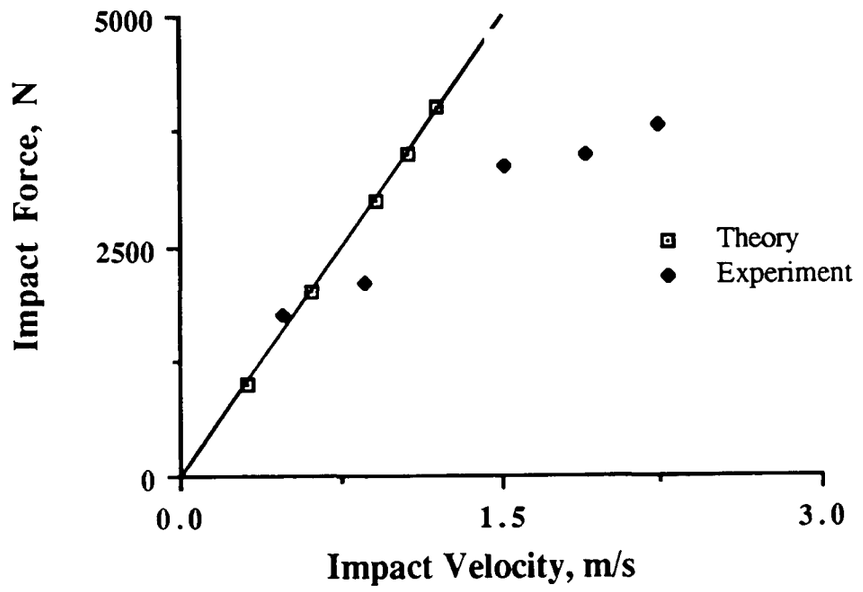

Figure 4.27 - Comparison between peak force-incident energy curve of energy balance method and experiment.

4 - 7.3 Theory of Bending of Plates

Theory of bending of plates was also used to investigate the impact response of SMC. As it was discussed in details in chapter two, drop weight impact testing is basically the bending of a plate which has been supported on a circular annulus and loaded at the centre. For a plate of thickness (t), simply supported on a ring of radius (a) and loaded centrally over a very small central circular area of radius r_o (fig. 4.28), has a deflection (Y) given at any point (r) by the equation (79):

$$Y = \frac{-W}{16\pi D}\left[\frac{3+\mu}{1+\mu}\left(a^2 - r^2\right) - 2r^2 \ln\left(\frac{a}{r}\right)\right]$$

where

$$D = \frac{E.t^3}{12\left(1-\mu^2\right)}$$

W = applied load

E = Young's modulus

μ = Poisson's ratio

Deflection is maximum at the centre of the plate, where r=0. Maximum deflection is calculated from:

$$Y_{max} = \frac{W.a^2}{16\pi D}.\frac{3+\mu}{1+\mu}$$

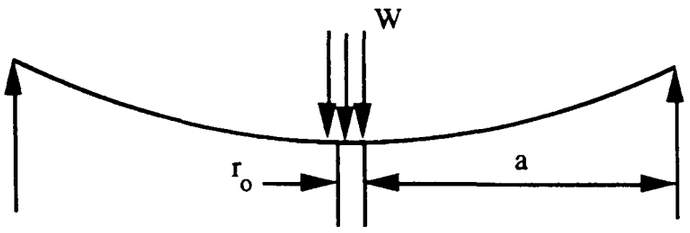

Figure 4.28 - Centrally loaded plate over a very small central circular area.

The simple plate bending theory, assumes that (a) the shear stresses created in the plate upon bending are negligible and (b) that the plate is deflected by a small amount, such that the central deflection is less than half the specimen thickness (79). In this model no consideration is given to possible localised indentation in the region of the striker tip. At r = 0, M_r (radial bending moment) is maximum and its value can be calculated from the following equation (79).

$$M_r = \frac{W}{4\pi}\left[(1+\mu)\ln\frac{a}{r'_\circ}+1\right]$$

$$r'_\circ = \sqrt{1.6r_\circ^2 + t^2} - 0.675t \quad \text{if} \quad r_\circ < 0.5t$$

$$r'_\circ = r_\circ \quad \text{if} \quad r_\circ > 0.5t$$

Radial stress can be found from the moment M_r by the following expression:

$$\sigma = \frac{6M_r}{t^2}$$

Typical results of load-maximum deflection for 4 mm SMC which have been calculated using the theory of bending is shown in figure 4.26. These results are based on the following properties of SMC plate:

$$E = 13.7 \text{ GPa}$$

$$t = 4 \text{ mm}$$

$$a = 20 \text{ mm}$$

The theory of bending is in good agreement with experiment at very small deflections. As the deflection increases the deviation between experiment and theory becomes larger. This is due to the inherent nature of the theory which assumes that the material is perfectly elastic and isotropic.

4 - 7.4 Finite Element Stress Analysis

The LUSAS finite element stress analysis package was used to predict the response of SMC to impact. Impact is a dynamic problem and a dynamic solution should ideally be used. However, as the load deflection curves for slow indentation tests and impact tests are nearly similar, a static stress analysis may be employed with confidence that the results would approximate the real situation. Due to the symmetry of the system it was only necessary to analyse half of the plate. The two dimensional, axisymmetric, finite element model used to analyse the impact test is shown in figure 4.29. The unsupported radius of the specimen was 20 mm and the thickness of the plate was 4 mm, which was divided into eight node, axisymmetric elements (QAX8) and comprised of 208 such elements. Since the stresses are higher at the impact point finer elements were chosen in this area as shown in figure 4.29.

The nodes and elements need to be numbered in as ordered a way as possible so as to simplify data input. Figure 4.30 shows the order that the eight nodes of the QAX8 element has been numbered together with the order of part of the generated mesh.

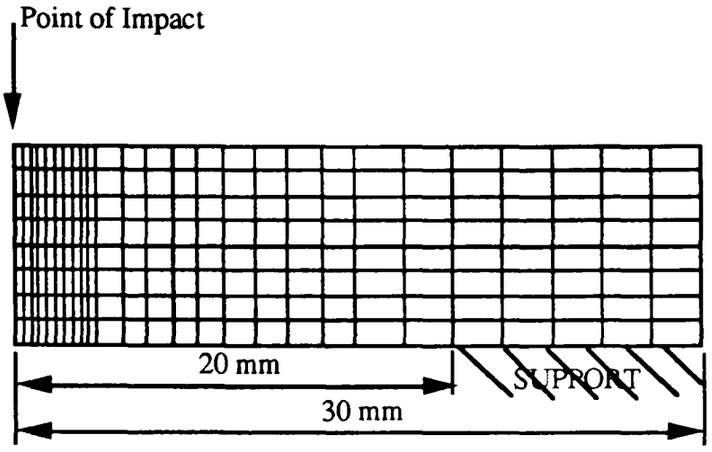

Figure 4.29 - Finite element model.

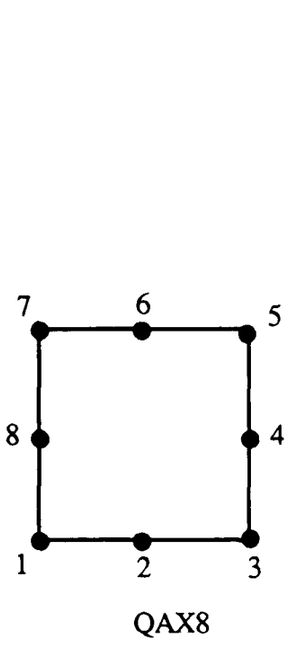

8	16	24	32	40	48	56	64
7	15	23	31	39	47	55	63
6	14	22	30	38	46	54	62
5	13	21	29	37	45	53	61
4	12	20	28	36	44	52	60
3	11	19	27	35	43	51	59
2	10	18	26	34	42	50	58
1	9	17	25	33	41	49	57

Figure 4.30 - The node order and the element order of the finite element model.

Since the indenter has a hemispherical tip, the contact pressure is time dependent and is not uniform over the area of contact (fig. 4.31).

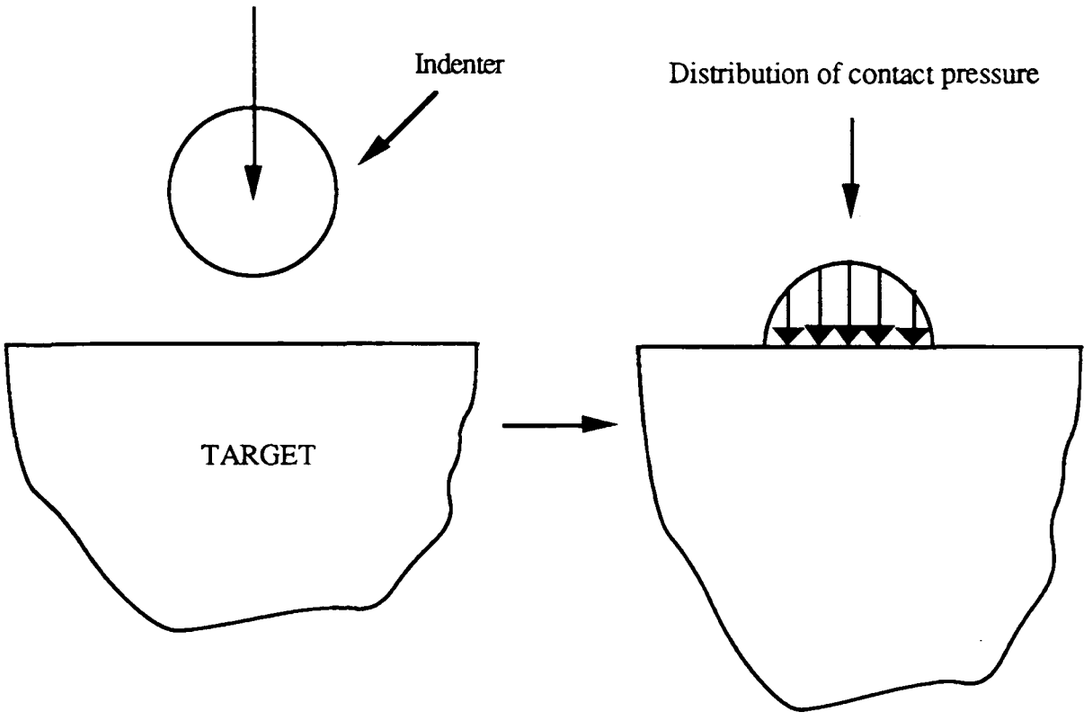

Figure 4.31 - Distribution of the contact pressure.

Therefore concentrated loading was not used and the method of applying load was via prescribed displacement. In this method the displacement of some of the nodes are provided in the data file and the finite element programme calculates the equivalent load which causes this amount of displacement.

For different maximum deflections corresponding loads were calculated. Having the values of load and deflection, a load-deflection curve can be plotted. Figure 4.26 shows the comparison between the load deflection of the finite element model and the experiment. Finite element analysis overestimates the load, but the experimental data is satisfactory up to a transition load. Since the available LUSAS package could only deal with elastic problems and the SMC plate deformed inelastically after the transition load, the deviation between experimental data and finite element prediction became larger. The plotting facilities of LUSAS package made it possible to plot deformed mesh, profile of deflection and contours of stresses and strains. Figure 4.32 shows

region of high stress as defined by the stress contours on the finite element mesh. High stresses are built up at the point of contact with the striker and in the centre of the surface opposite to the impacted surface.

The deformed mesh which has been superimposed upon the undeformed mesh is shown in figure 4.33. The comparison between the profile of deflection obtained with finite element package and slow test is shown in figure 4.34.

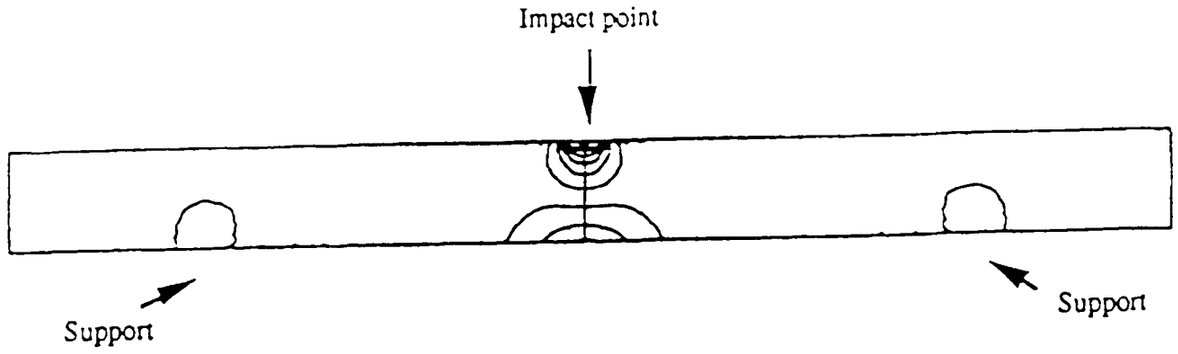

Figure 4.32 - Contours of stress in 4 mm SMC shows areas of high stresses during impact.

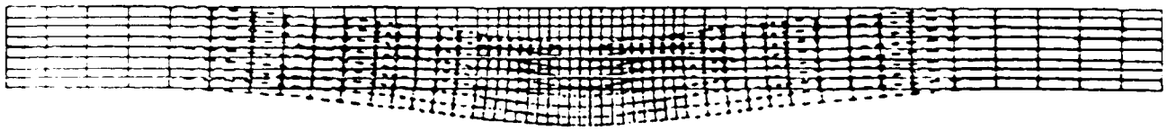

Figure 4.33 - Deformed mesh which has been superimposed upon the undeformed mesh.

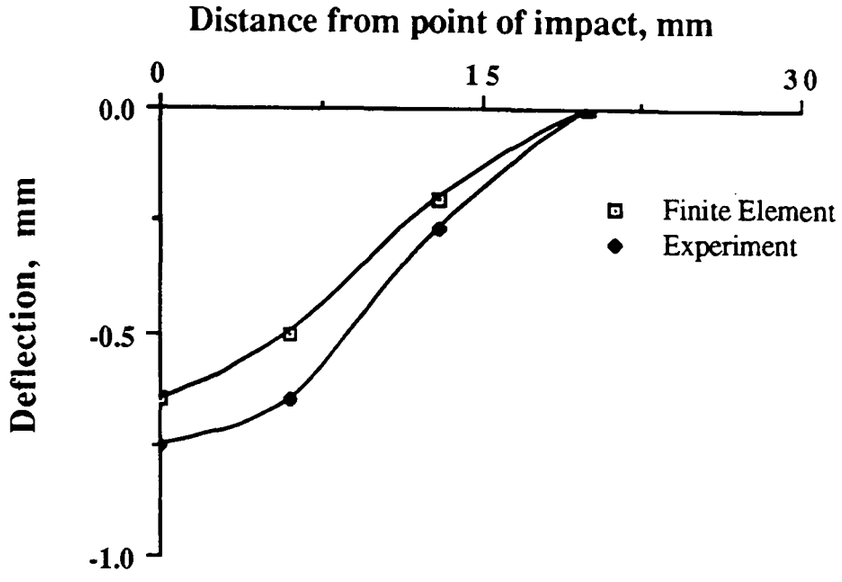

Figure 4.34 - Comparison between the deflection at the back of specimen of slow test and finite element result.

4 - 8 Damage Detection Techniques

4 - 8.1 Dye penetrating Technique

The specimens which were slightly damaged by impact, on which the damage was not clear on either surface (impacted surface and the surface opposite) were sprayed with penetrant and left for about 15 minutes. Surplus penetrant was then removed and developer sprayed. The dye penetrant was also used when the specimens were sectioned into halves and polished. Figure 4.35 shows the very fine cracks which form on the periphery of the area of striker contact with 4 mm SMC which were not visible before applying dye penetrant.

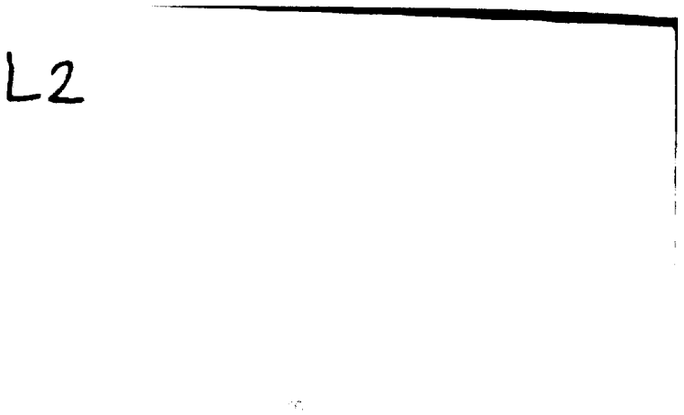

Figure 4.35 - Cracks on the periphery of the area of contact of the striker with 4 mm SMC which has been highlighted by dye penetrating method.

4 - 8.2 Optical Microscopy

Optical microscopy was found to be the best technique which yields a lot of information about the nature of the damage. As fully described in chapter 3, the damaged specimens were cut in half and carefully ground and polished with diamond abrasive and subsequently examined under a REICHERT microscope and photographed using an OM-2 Olympus camera. This technique reveals the delamination cracks and through thickness damage very clearly as shown in figure 4.36.

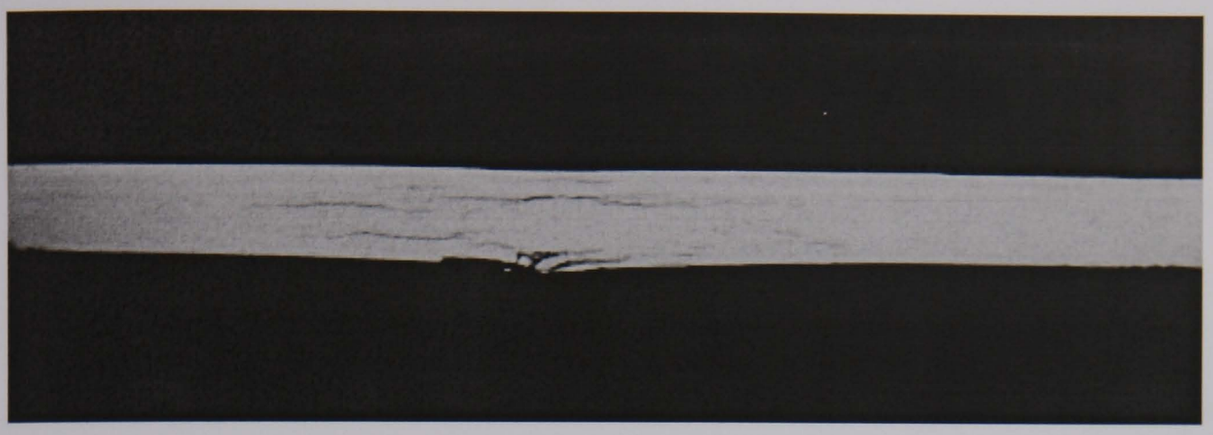

Figure 4.36 - Micrograph of 4 mm SMC which has been subjected to impact.

4 - 9 Discussion

From the experimental results it was found that the failure of SMC occurs in two stages. The first is associated with reverse surface crack initiation and second with tup penetration through the plate. The transition load on the force-time curve (fig. 4.1) is associated with the initiation of cracks on the underside of the impact specimen. Once this occurs the thickness is effectively reduced (compliance is increased) and subsequently events reflect a modified sample geometry. Relating the transition load on the force-time curve obtained during impact to the onset of damage in glass reinforced plastics can also be found in the work of Trubshaw (129) and Detorres (130). SMC is a non-homogeneous material and consists of resin rich and fibre rich areas (fig. 4.37). Examination of the SMC specimens which had been subjected to low energy impact with incident energies corresponding to the transition load suggests that initial failure may be governed in the resin rich surface. This is what one would expect in a flexed plate impact test where a resin rich surface sees the largest biaxial tensile stresses. Detorres (130) states that the first crack is a function of the resin composition only. Therefore it may be suggested that the type of reinforcement in GFRP does not play any role in the initiation of damage during impact and force and energy corresponding to the initiation of damage

is only a function of the resin composition. The continued increase in load after the transition load is associated with the presence of the glass fibres which inhibit catastrophic brittle type failure and the geometry of the tup which impose a stress distribution on the specimen that is both non-uniform and time dependent (fig. 4.31).

The energies associated with crack initiation are very small compared to the total absorbed energies. For example for 4 mm thick SMC the energy required to initiate damage is less than one joule whereas the total energy absorbed by the specimen is 58 joules. This may seriously affect the application of SMC unless it can be shown that the residual properties such as tensile and compressive strength are not affected by the initiation of damage in the specimen and will be sufficient to meet the design requirement.

Fortunately that is the case and the post impact tension and compression tests which are discussed later in chapter 7 shows that the residual tensile and compressive strength remain unchanged when the specimens are subjected to incident energies which are just enough to initiate damage in the specimen. However it should be emphasised that when SMC specimens are subjected to a cyclic load condition (fatigue), the effect of tiny cracks and slight damage should be fully investigated. Cracks associated with initiation of damage do not affect the static properties but under the cyclic load they might grow and reach a critical length which subsequently results in catastrophic failure.

The nature of the cracking pattern in a laminate is to some extent governed by the thickness and therefore stiffness of the specimen. Thin specimens tend to deform extensively under the impactor and cracking initiates as transverse cracks near or at the tensile surface (84). These cracks subsequently connect via a network of delaminations and shear cracks. If the laminate is thick and stiff, then deflection under the impactor is reduced but higher contact stresses are generated and fracture initiates as compressive cracks under the impactor itself (41). Once again, these cracks propagate and connect via

delaminations and shear cracks. The exact thickness required to define a transition point from one mode of failure to another will be dependent on the strengths and stiffness of the material under the specific loading conditions. In composites a single failure mode is not always observed and frequently compressive top surface damage may accompany a failure that is predominantly flexural in its character. SMC within the range of thicknesses tested always failed in flexure with cracks originating at the tensile surface although thicker specimens had more indentation at the impacted surface.

Tests on a conventional tensile test machine (SCHENK) at slower velocities showed that there is very little difference in the mode of failure of SMC at slow speeds (1 mm / min) and impact speeds (typically from 1-5 m/s) and this is reflected in a similar force deflection, at least up until the onset of extensive damage (fig. 4.23). As it is shown in figure 4.23, after the transition point, the load required to produce a certain amount of deflection is higher in an impact test than a slow test. Therefore the specimens tested in impact absorb more energy on complete rupture than specimens tested slowly.

The photograph of the damaged specimens at different impact velocities and therefore energies (fig. 4.6), showed that the damage zone is uniformly spread around the point of impact, however, the shape is not as regular as one might expect. The reason is the inherent inhomogenity of the SMC materials. The damage zone increases non-linearly with impact velocity. Examination of the damaged specimens revealed that the damage is a combination of local indentation (fig. 4.38), cracks on the front and back surface (fig. 4.39), internal fibre-matrix interface cracks (fig. 4.40) and delamination cracks (fig. 4.36). It was generally recognised that due to the presence of several damage modes which were observed on the impacted specimens, a combination of non-destructive techniques and optical microscopy is required to characterise the damage. Dye-penetration and optical microscopy were the most useful technique employed.

All the non-penetrating impacts, which were carried out using the CEAST impact machine, were in reality a series of blows of decaying magnitude. The reason was that at

the time of these experiments the equipment was not fitted with an anti-rebound device.

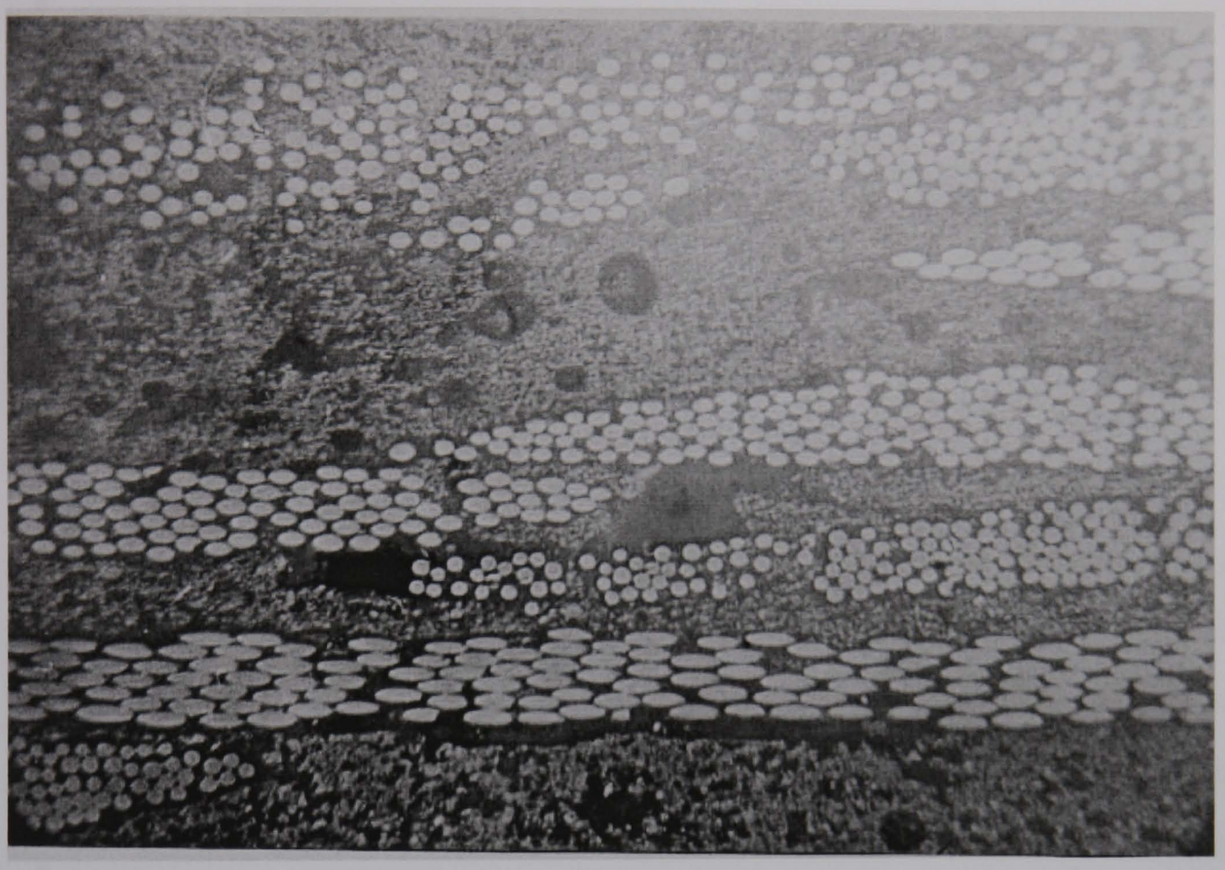

Figure 4.37 - Optical micrograph of a polished section showing the microstructure of SMC (X 400).

The question might be asked as to whether the damage on the specimen is caused by just the initial blow or if the subsequent blows also contribute. The assumption was made that the subsequent impacts produce no additional damage over and above caused by the initial blow. This assumption was later verified in a series of experiments using the QMW impact machine which had been fitted with an anti-rebound device in order to ensure that the specimen was subjected to a single blow. In this experiment SMC specimens (4 mm thick) were subjected to several impacts at particular incident energies and the force-time curve for each blow was obtained. The force-time curves of 4 mm SMC which has been

subjected to incident energy below the damage threshold are shown in figure 4.41. As it is seen, there is no difference between these two force-time curves which is an indication that the specimen has not been changed after the fifth blow. In another experiment 6 mm thick SMC was subjected to impact using CEAST impact machine at incident energy higher than required to initiate damage in the specimen. Since the CEAST machine is not fitted with an anti rebound device the specimen was subjected to a series of blows. The time base was chosen long enough to record the force-time of the second blow (fig. 4.42). The same specimen was impacted for the second time at incident energy corresponding to the energy of the second blow. Then, the specimen was examined visually and no further damage was observed.

Results of the tests using the CEAST and the Cambridge test rig showed that both yield the same force-deflection curves (fig. 4.15). These results may suggest that as long as the test and specimen geometry are the same and calibration of the load cell are correct the dart impact (drop weight, servo hydraulic machines) generate similar data and the results can be compared without any problem. Comparison of the CEAST (unclamped) and Cambridge results (clamped) showed that the clamped and unclamped specimens (fig. 4.15) yield similar results. One would expect that clamped specimens show more brittle behaviour due to material constraint by clamping and the change in the stress field. This would be the case for ductile materials, but SMC is brittle from the outset.

The peak force and the absorbed energy for each thickness of SMC tested, increased with increasing incident energy where the specimens were not ruptured, but level off after the specimens were completely ruptured (figs. 4.17 and 4.20). The load at complete penetration increased with thickness non-linearly with a possible thickness squared dependence in evidence in figure 4.18. The load results seems to agree with the elastic prediction that the bending stresses in a flat plate increase linearly with the ratio of load divided by the square of the thickness (79).

Figure 4.38 - Impact damage on SMC in the form of indentation on the impacted side.

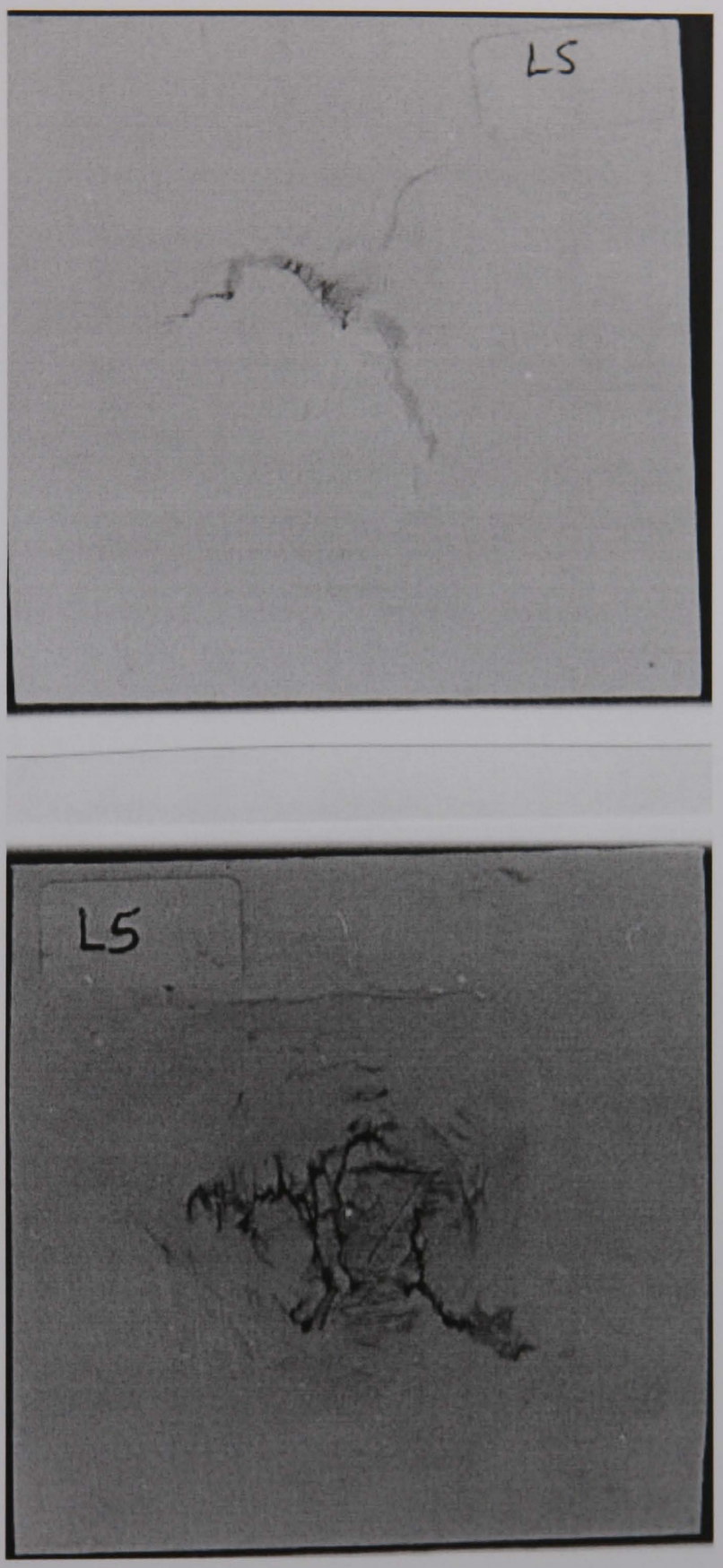

Figure 4.39 - Cracks which are formed during impact on the tensile and compressive sides of the SMC specimens.

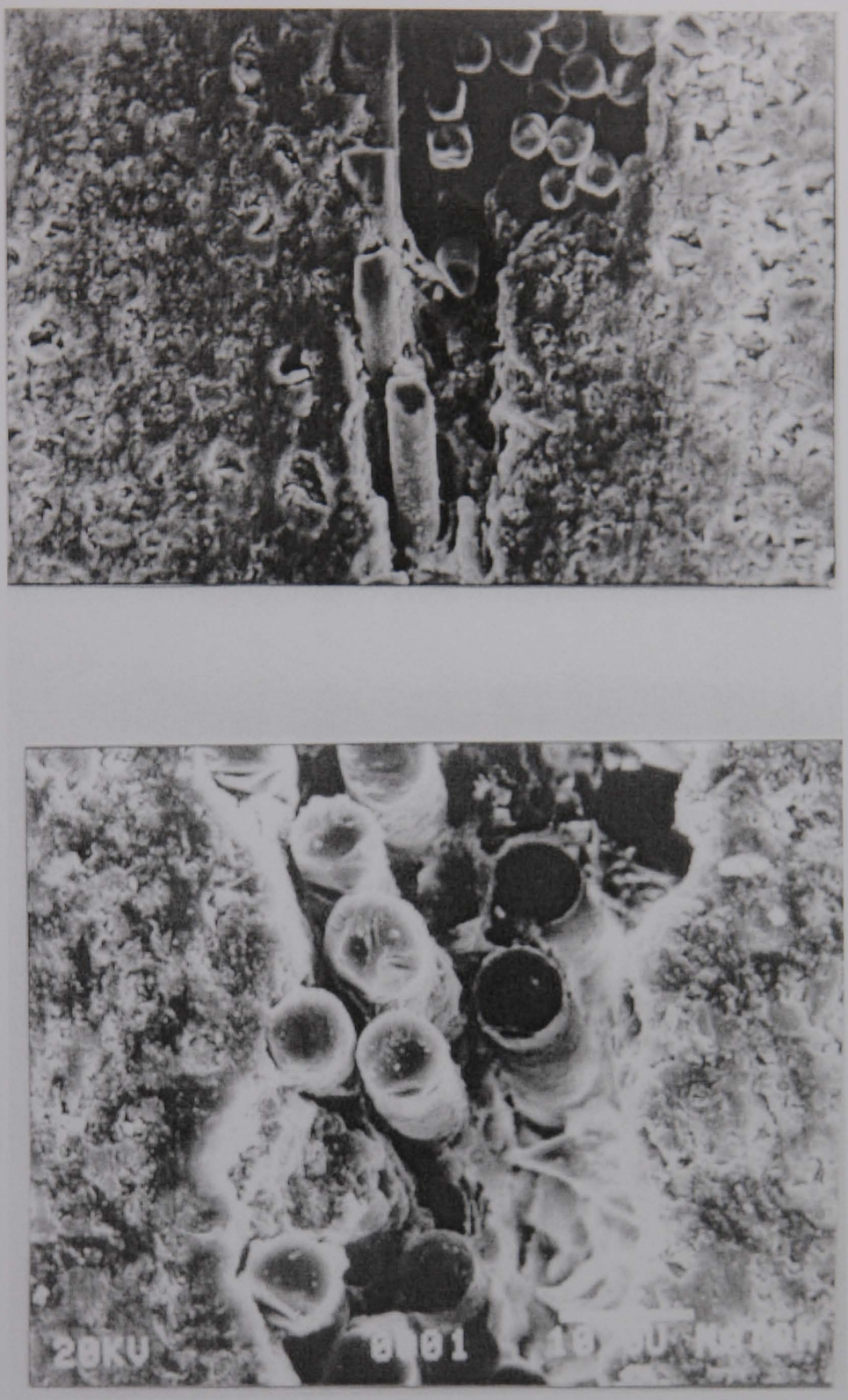

Figure 4.40 - Scanning electron micrographs of damaged surface of SMC which has been subjected to drop weight impact shows the debonding between the fibre and the matrix.

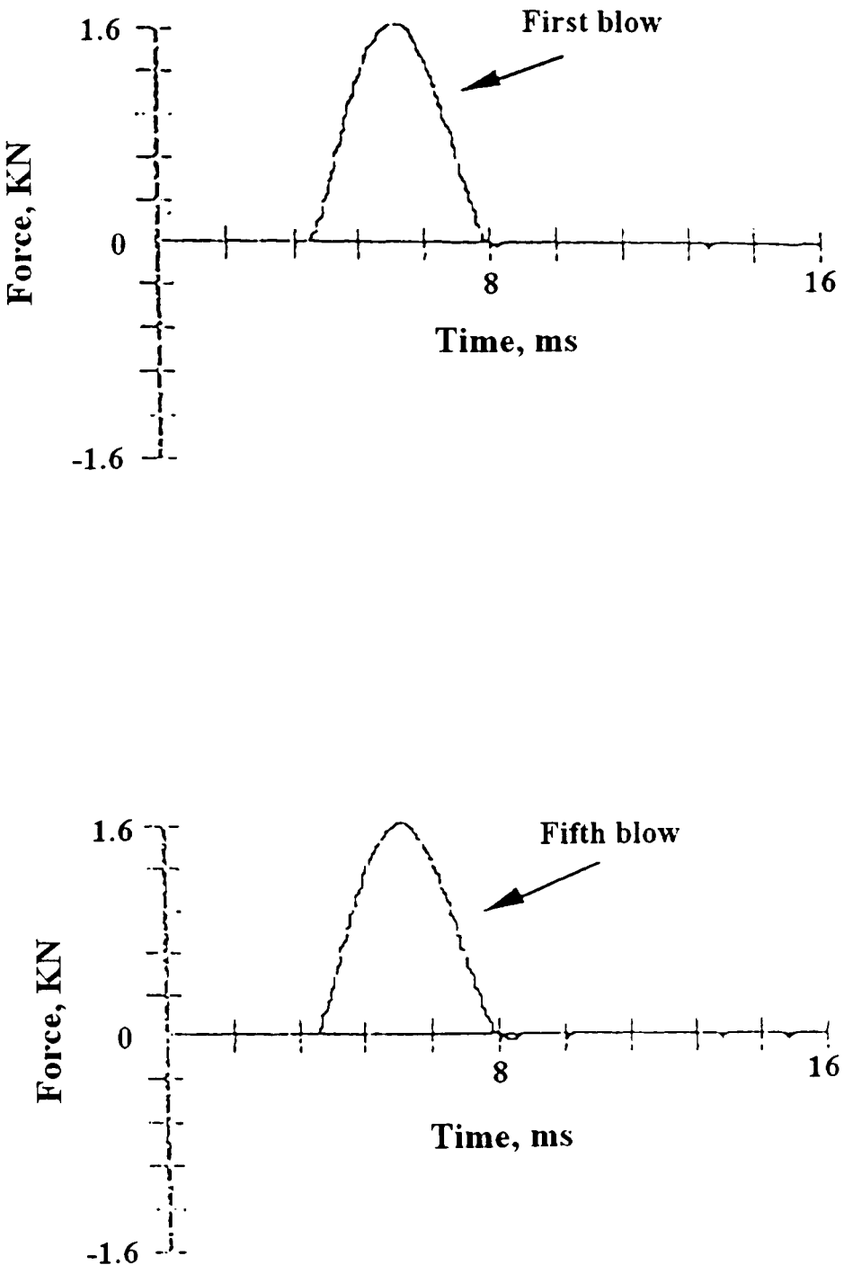

Figure 4.41- Force-time curves for a 4 mm SMC specimen which has been subjected to a series of low energy impacts, a) first blow b) 5^{th} blow.

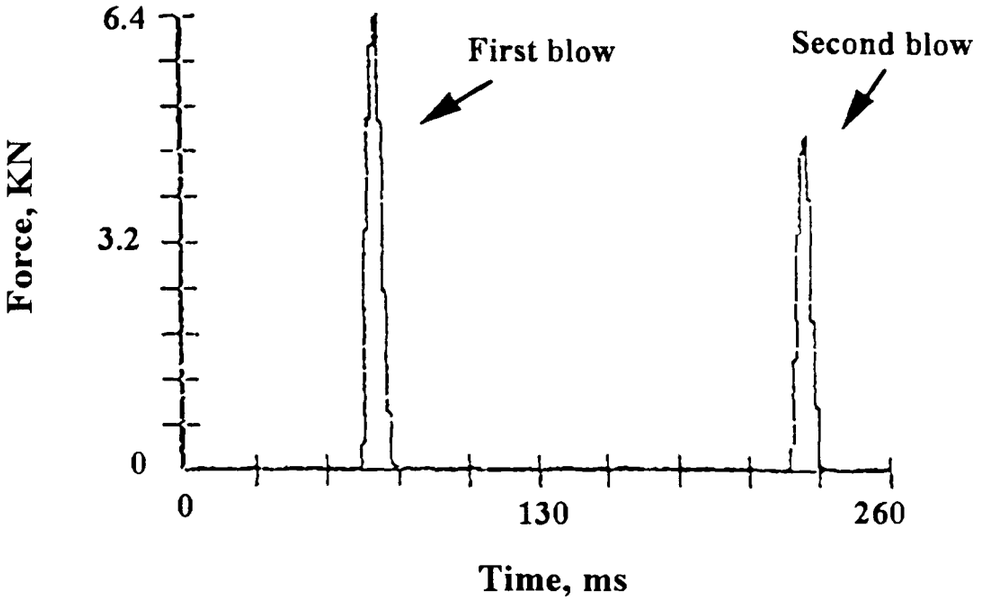

Figure 4.42 - Force-time curve for 4 mm SMC subjected to a series of blows.

Each thickness of SMC absorbed a certain amount of energy when complete penetration took place. The relationship between absorbed energy and thickness was shown in figure 4.21. Obviously the energy absorbed by SMC is a function of its composition and also the test and the specimen geometry. SMC, like most other composites, absorbs energy through delamination, fibre debonding, fibre pull out, matrix cracks etc. Johnson et al (131) stated that increasing the glass content is a very effective method of toughening the SMC. Increasing the glass content increases the number of interfaces between the fibre and the matrix resulting in more fibre matrix debonding and subsequently increasing the energy absorbed by SMC. An extensive amount of work at QMW (132) has shown that for glass fibre composites, where the specimens are of a similar size to those tested in this programme, a master curve can be constructed linking absorbed energy with specimen thickness multiplied by volume fraction. The use of the thickness multiplied by volume fraction comparator allows for those unavoidable variations such as thickness, volume fraction of reinforcement and type of reinforcement which make direct comparisons

difficult. A very wide range of glass fibre composites fall on this master curve, irrespective of matrix type (thermoset, thermoplastic) and reinforcement type (woven fabrics, CSM, UD stacks). It is interesting to know that when the maximum energy value is plotted against thickness x volume fraction, the data fall within the spread of the results of eighteen different GRP constructions (fig. 4.43).

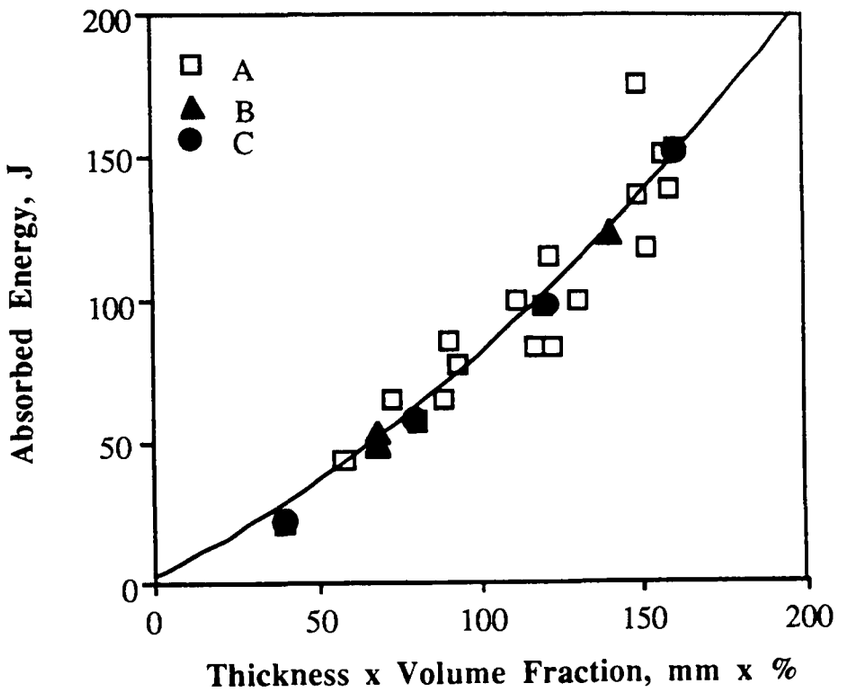

Figure 4.43 - Relationship between energy absorbed during through penetration versus thickness multiplied by fibre volume fraction for glass fibre composites. Legend: A - random and woven fibre reinforced thermoset resins. B - Random fibre thermoplastic GMT. C - SMC (After Babic et al [132]).

This suggests that the volume fraction of fibres and thickness of the specimens are the most important parameters which affect the toughness of GRP and SMC materials. The

energy absorbed for formation of delamination cracks have a great contribution to the total energy absorbed by SMC. Dhasin (133) states that increasing the thickness of the specimen and decreasing the bond strength will promote the delamination cracks and therefore increase the total energy absorbed by SMC. Apart from the glass content, specimen thickness, and bond strength, the test geometry seems to have an effect on the energy absorbed by SMC. Johnson and Lynskey (131) carried out some impact tests using support diameters in the range of 50 mm to 100 mm. They stated that within the limits of the range of their experiment the diameter of the specimen support had little effect upon the energy absorbed by SMC specimens.

Variation of the drop height and weight of the striker at a constant incident energy exhibited similar results (fig. 4.22). This behaviour may be explained by the rate insensitivity and brittle nature of SMC. Cessna et al (72) have reached the same conclusion. They found that the impact strength of those materials which tend to fail in a brittle fashion was relatively independent of drop height or weight variations as long as enough energy was available to cause specimen cracking. Those materials which failed with considerable ductile deformation exhibited a significant reduction in impact strength at higher drop heights (i.e., higher velocities).

To understand the actual mechanism of failure the knowledge of stresses within the specimen is needed. Due to a large number of parameters, for example, mass, shape, velocity, stress wave and material response of both the projectile and the target a realistic analysis of impact stresses in SMC material is an enormously complicated task. The force-time curves, of SMC showed that the initial rise in force from first contact between striker and specimen up to the transition load is linear. This together with the result of slow test suggested that deformation of SMC up to the transition load is elastic which might be described using elastic stress analysis. The behaviour of the material in impact and slow tests were the same up to the transition load (fig. 4.23), therefore static stress

analyses were employed.

Most of the theories such as plate bending theory and the energy balance method, which were employed in the present work account for test variables such as support, span, and specimen thickness but they fail to handle the changes in the contact area of the applied force during impact. Finite element analyses can overcome this deficiency using prescribed displacement. The results obtained with the theory of bending of plates, energy balance method and LUSAS finite element package (fig. 4.26) showed that theses models give good agreement with the experiment up to the transition load. For a given deflection all these theories predict slightly higher loads than the experiment. This is due to the assumption made that the SMC is isotropic. In actual fact SMC is only isotropic in-plane and the Young' s modulus in the thickness direction is about half of the Young' s modulus in the plane of the sheet. Therefore, flexural stiffness of SMC specimens are lower than those calculated by the theories which result in force-deflection with higher slopes than the experiments (fig. 4.26). In addition to the assumed in-plane isotropy, the model does not account for the inhomogeneity of the material due to matrix rich regions, voids, local arrangement of fibre bundles, local differences in the fibre volume fraction, the presence of filler etc. These all contribute to alter the stiffness of the material thus deviating the results from the predicted ones. After the transition point the material is not elastic, damage occurs, and the stiffness of the specimen decreases. The use of theories which assume the material to be perfectly elastic overestimates the load required for a certain amount of deflection and subsequently yields higher contact stresses. In order to have a proper stress analysis, elastic-plastic theories should be used. It seems possible that an elastic-plastic finite element package may be able to predict the impact behaviour after the transition load.

4 - 10 Conclusions

1 - The Impact process in SMC is complex with the incident energy of the striker being dissipated in a variety of elastic and fracture mechanism.

2 - There is a transition load on the force-time curve which is the point at which cracks initiate at the tensile surface of the SMC specimens.

3 - For a given thickness of SMC, increasing the incident energy does not change the maximum energy absorbed by SMC.

4 - Peak force and transition load have a linear relationship with the square of thickness.

5 - SMC does not exhibit any significant rate sensitivity.

6 - Duplicating a high speed test at lower speeds, where the modes of deformation can be conveniently viewed is a valuable technique which can eliminate the need for high speed photography.

7 - Finite element analysis yield similar profile of deflection and load-deflection curve up to the transition load.

Chapter 5

Response of SMC with a layer of Stainless steel (SMC+S.S.) to Low energy impact, High energy impact and Slow indentation test.

5 Introduction

In chapter 4 the response of SMC to drop weight impacts and slow indentation tests was studied. This chapter examines the effect of a layer of stainless steel on the impact behaviour of SMC. The question of whether or not SMC+S.S. absorbs more (or less) energy than the individual constituents will be answered. In the first stage of the impact programme a layer of stainless steel of constant thickness (0.6 mm) with SMC layers nominally 2, 4 and 6 mm thick were investigated. In the next stage the effect of thickness of stainless steel layers 1 and 2 mm on 4, 6 and 8 mm thickness of SMC were assessed.

5-1 Response of SMC+S.S. to low energy impact

The term low energy impact has been defined in chapter 4 . The impact response of SMC+S.S. to low energy impact was investigated using both the CEAST and the QMW impact machine. The test programme was confined to 2, 4 and 6 mm SMC with a layer of 0.6 mm thick stainless steel. Specimens were impacted from SMC side.

A typical force-time curve for non-penetrating impact which was sufficient to cause damage is shown in figure 5.1. The general shape of force-time curves consists of an initial steep rise portion followed by a transition to a curve for lower slope before a maximum is reached.

A typical trace of energy-time curve (E-t) obtained from such a low energy impact is shown in figure 5.2. The energy rose steadily to a peak value that corresponds to the kinetic energy of the striker (incident energy) immediately prior to impact. The point of

maximum energy absorption does not necessarily correspond to the point of maximum force, but always coincides with the maximum deflection as shown in figure 5.3.

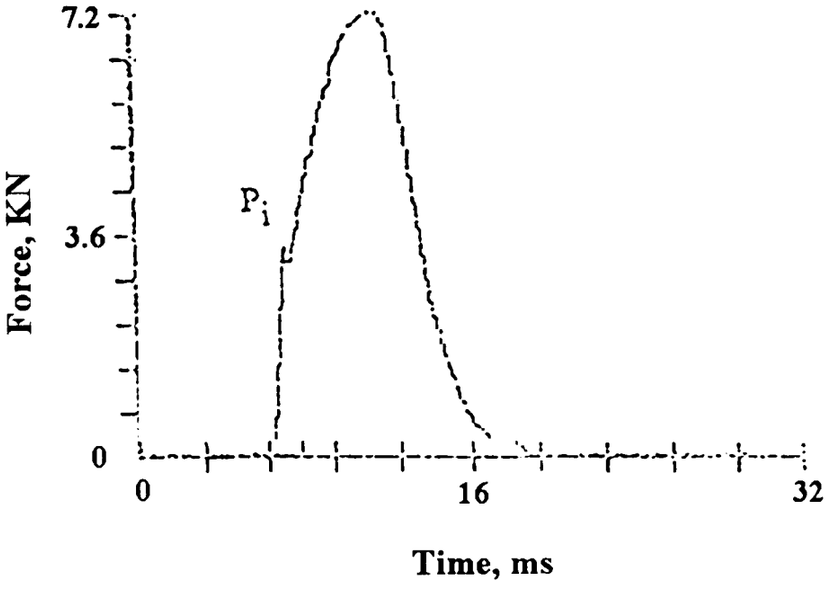

Figure 5.1 - Typical force time curves for SMC stainless steel laminates after non penetrating impact.

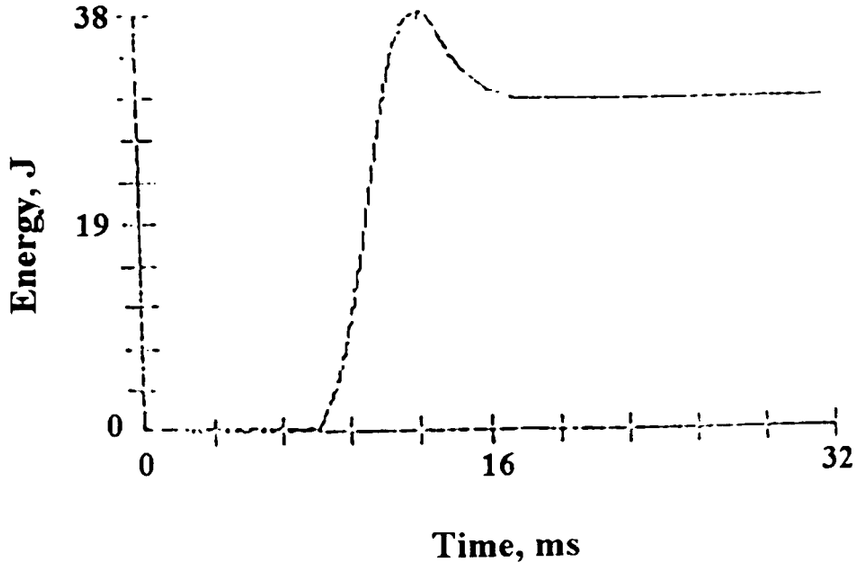

Figure 5.2 - Typical energy time curve for SMC stainless steel laminates after non penetrating impact.

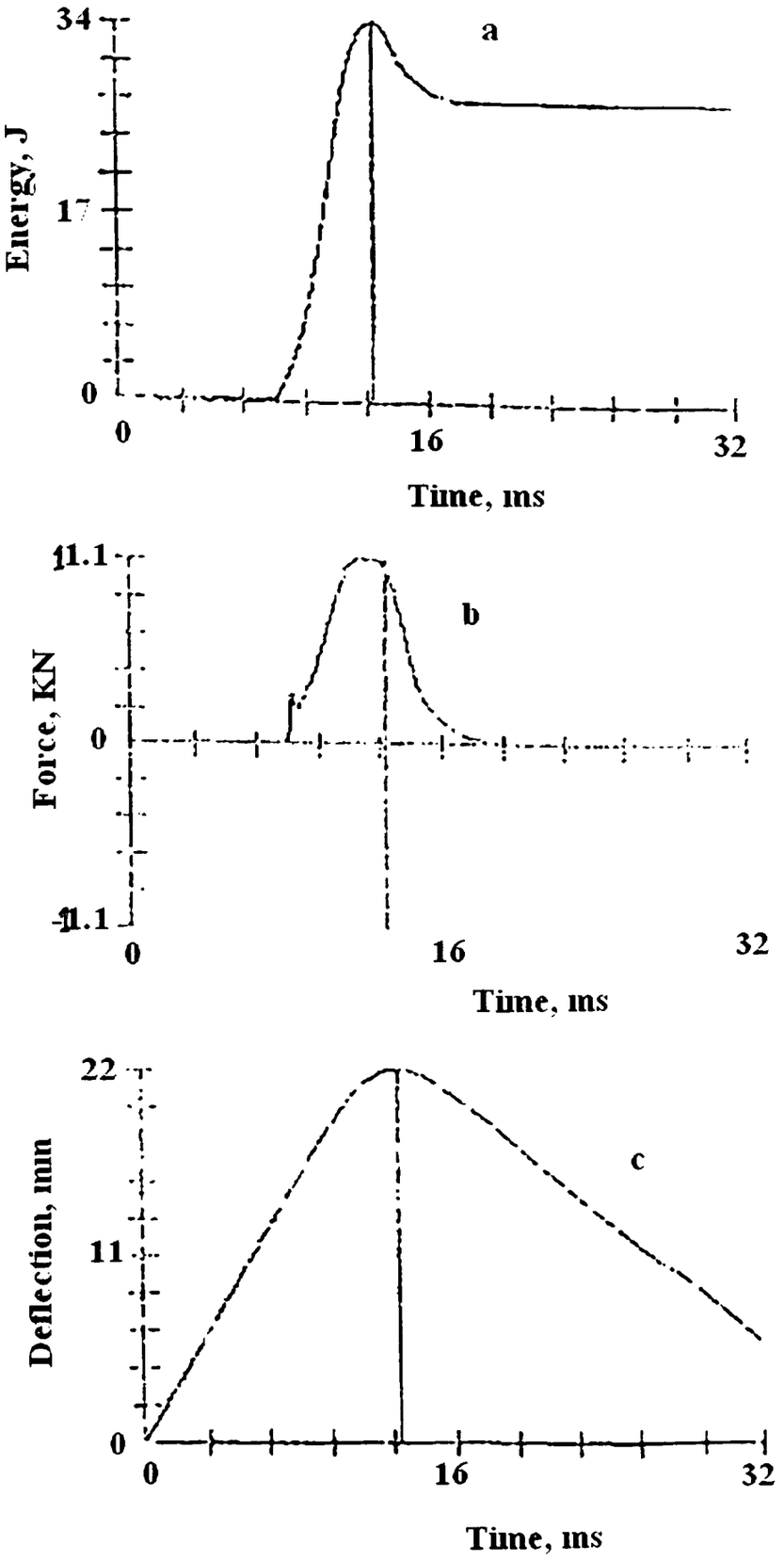

Figure 5.3 - Position of the point maximum energy on the force time and force deflection curves a) energy time b) force time c) deflection-time.

After this point specimens exhibit a degree of elastic recovery and the energy absorbed falls somewhat, levelling out to a value equal to the total energy absorbed by the system during the impact event.

A typical force-deflection curve for low energy impact is shown in figure 5.4. The shape of the curve up to the maximum force is similar to the force-time curve except it is followed by a period of unloading and partial elastic recovery with a permanent deflection after unloading.

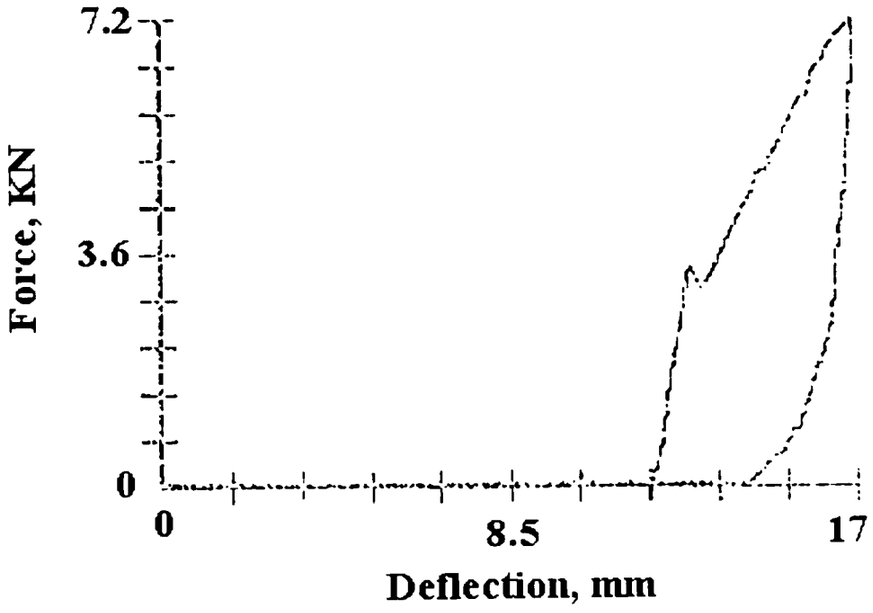

Figure 5.4 - Typical force deflection curve for SMC stainless steel laminate after non penetrating impact (low energy impact).

Impact tests at energies above and below the energy corresponding to the transition load (P_i) and slow indentation tests which are described fully in the following sections showed that the transition load corresponds to the onset of plastic deformation in the stainless steel layer.

For specimens of equal thickness, the transition force (P_i) did not change with an increase in impact energy and therefore velocity, but the maximum force did (fig. 5.5).

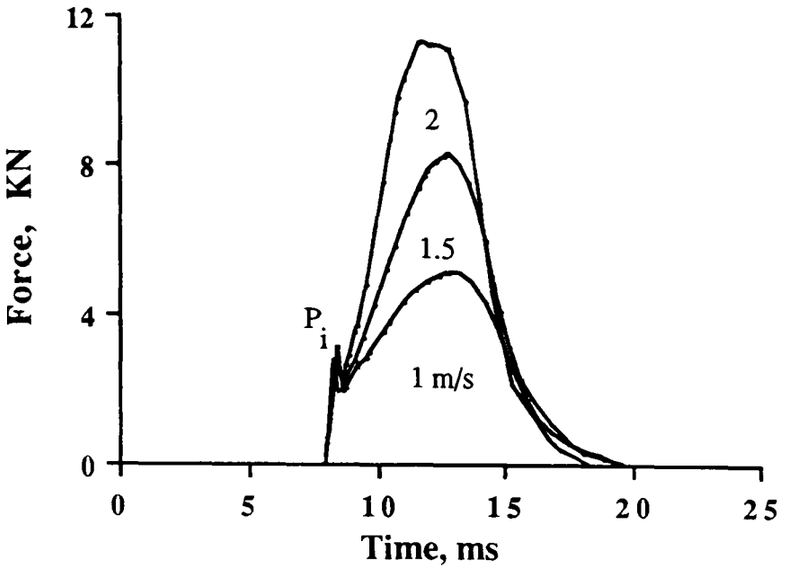

Figure 5.5 - Force time curves for 4 mm SMC with a layer of 0.6 mm thick stainless steel at 1 ms^{-1}, 1.5 ms^{-1} and 2 ms^{-1} after non penetrating impact.

The force-time curves of three SMC+S.S. specimens of similar thickness (nominally 4.6 mm) subjected to a range of impact velocities are shown in figure 5.5. It is apparent that the behaviour of SMC at each testing speed was equivalent up to the point of transition force (P_i). After this point the curves for each test speed appear different and it is important to note that this is not, in itself an indication of any rate effects in the material. The main feature of non-penetrating SMC+S.S. specimens was the large dome formed in the steel sheet as a result of plastic deformation during the impact. The dome region extended as far as the test support ring and the height of the dome, h figure 5.6, was dependent on the incident energy. Microcracking was also evident on the SMC surface as shown in figure 5.7.

Figure 5.6 - The steel surface in SMC stainless steel laminates after non penetrating impact, indicating the dome height.

Figure 5.7 - The surface of SMC in SMC stainless steel laminates after non penetrating impact, showing limited microcracking.

The force-deflection curves corresponding to the force-time curves in figure 5.5 are shown in figure 5.8. It is apparent that each specimen followed the same loading curve, subjected only to inter-specimen scatter, with the effect of varying impact speed being to alter the maximum point.

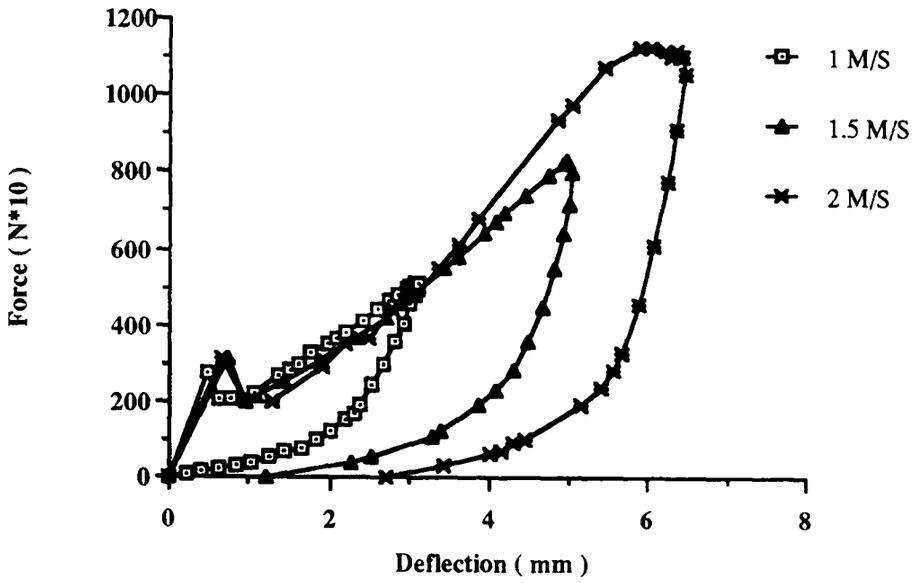

Figure 5.8 - Force deflection curves for 4 mm SMC with a layer of 0.6 mm stainless steel at 1 ms^{-1}, 1.5 ms^{-1} and 2 ms^{-1} after non penetrating impact.

5-2 Response of SMC+S.S. to High energy impact

The high energy impact tests resulted in complete penetration of the SMC+S.S. specimens. Because of the limited range of the load cell (19.9 KN) fitted to the CEAST impact machine, all the high energy impact tests were carried out on a servo hydraulic machine which had been sited at Cambridge University. The specimens and the size of the striker and support, were exactly the same as the CEAST (as described in chapter 3). For each thickness five specimens were tested. The specimens were lightly clamped to prevent

folding of the stainless steel layer into the support orifice, using an steel ring which was bolted to the support, with specimens sandwiched between them (fig. 5.9).

The result of clamped and unclamped SMC specimens in chapter 4 showed that lightly clamped specimen yield the same result of the unclamped specimen (figure 4.15).

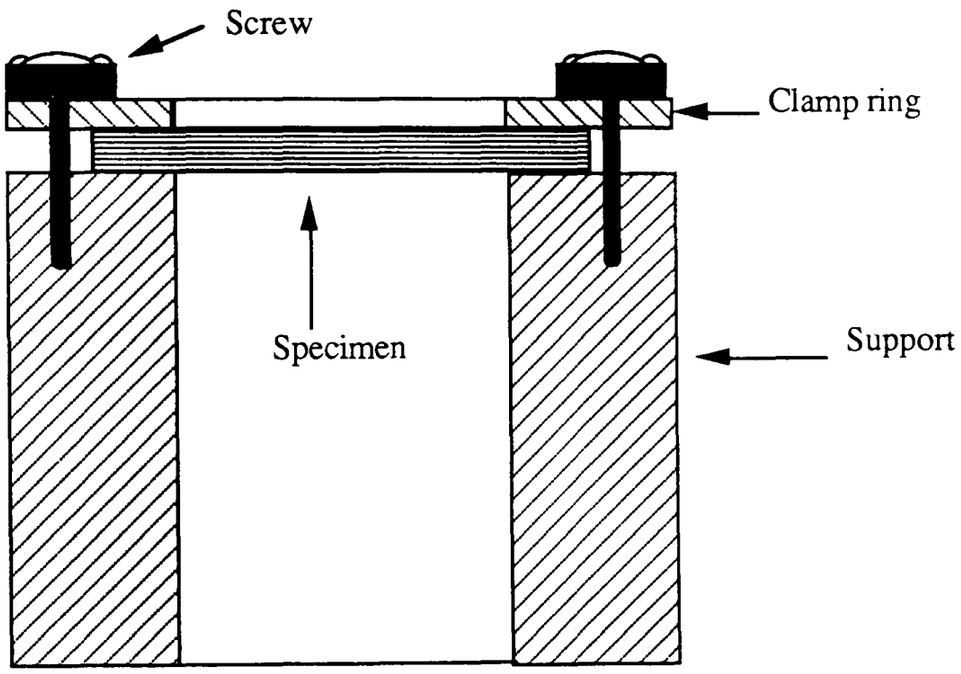

Figure 5.9 - The clamping technique used for clamping the impact specimens.

The specimens which were used in the high energy impact tests were as follows

2, 4, 6 and 8 mm SMC on its own

0.6, 1 and 2 mm Stainless steel.

2, 4 and 6 mm SMC with a layer of 0.6 mm stainless steel.

4, 6 and 8 mm SMC with a layer of 1 mm stainless steel.

6 and 8 mm SMC with a layer of 2 mm stainless steel.

The typical force-deflection curves obtained at 1 ms^{-1} and 5 ms^{-1} from high energy impact are shown in figure 5.10. At 1 ms^{-1} the force-deflection curve is very smooth and there is little evidence of the noise or oscillatory behaviour of the signal. At 5 ms^{-1} the force-deflection curve became very difficult to interpret because the level of noise was high as shown in figure 5.10. However, there were no significant differences in the shapes between the two curves.

The general shape of force-deflection curves consists of an initial steep rise portion followed by a transition to a curve of lower slope before a maximum is reached (figure 5.10a). The moment at which the tip of the striker fully penetrates the specimen and so denotes the end of the impact event is not easily determined. Because the force does not drop to zero at the end of the event as the sides of the central hole in the specimen exert a frictional drag on the striker as it progresses downward. However a satisfactory point may be found, which is an estimate of where the force might have dropped to zero if there were no such frictional drag. This point is visually estimated and therefore will be prone to some random error ; however it was found that small variations in the position of this point had a negligible effect on the value of total energy calculated by measuring the area under the force-deflection curve.

Stainless steel specimens when impacted on their own exhibited a common failure mode, irrespective of specimen thickness. The main feature of perforated stainless steel sheet was a large dome with a circular hole and a 'flap'. force-deflection curves and perforated stainless steel sheets at three different thicknesses (0.6, 1 and 2 mm) are shown in figure 5.11. Peak force and energy required for perforation of stainless steel sheet has a linear relationship with thickness as shown in figure 5.12 and figure 5.13.

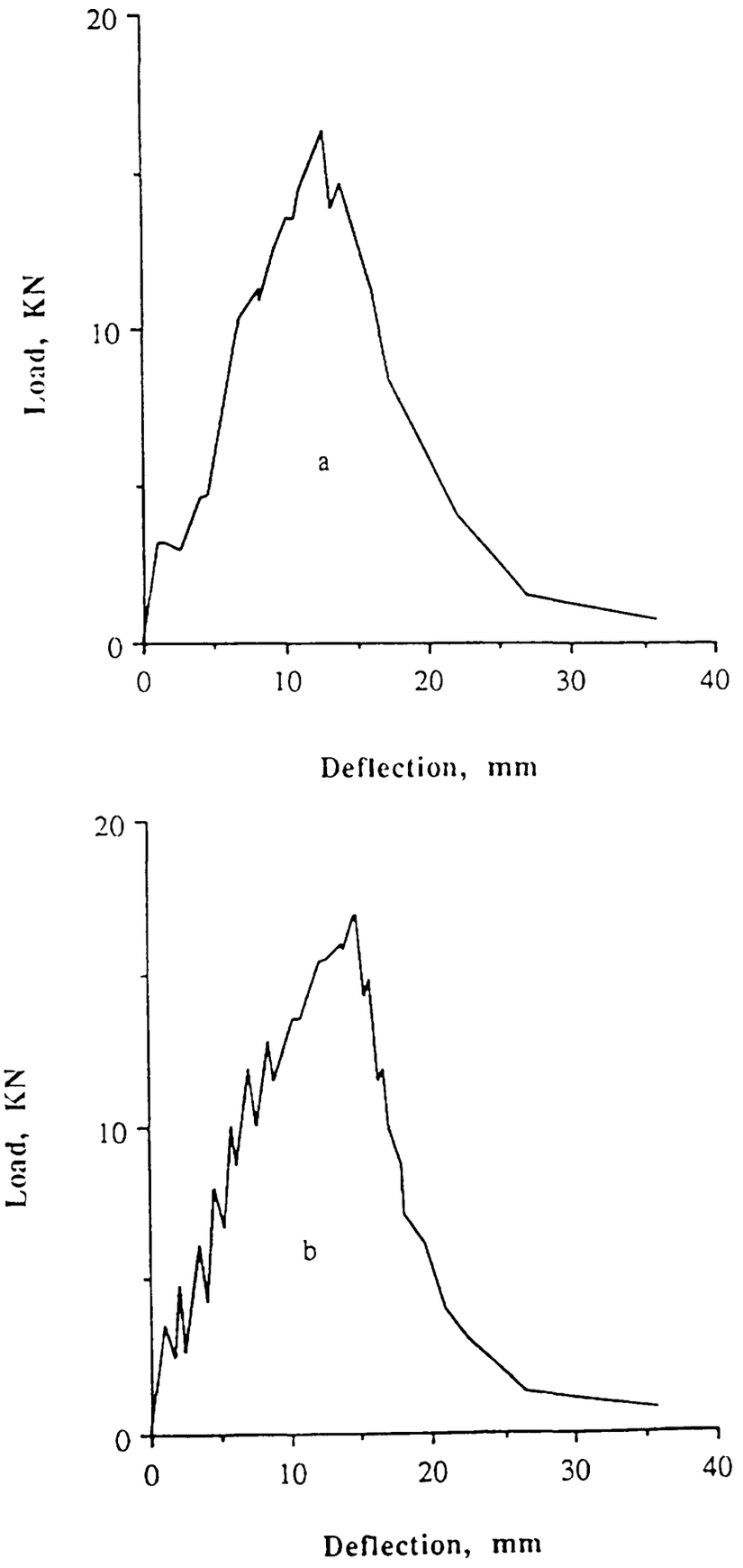

Figure 5.10 - Typical force-deflection curves for SMC stainless steel laminates after complete penetration a) 1 ms^{-1} b) 5 ms^{-1}.

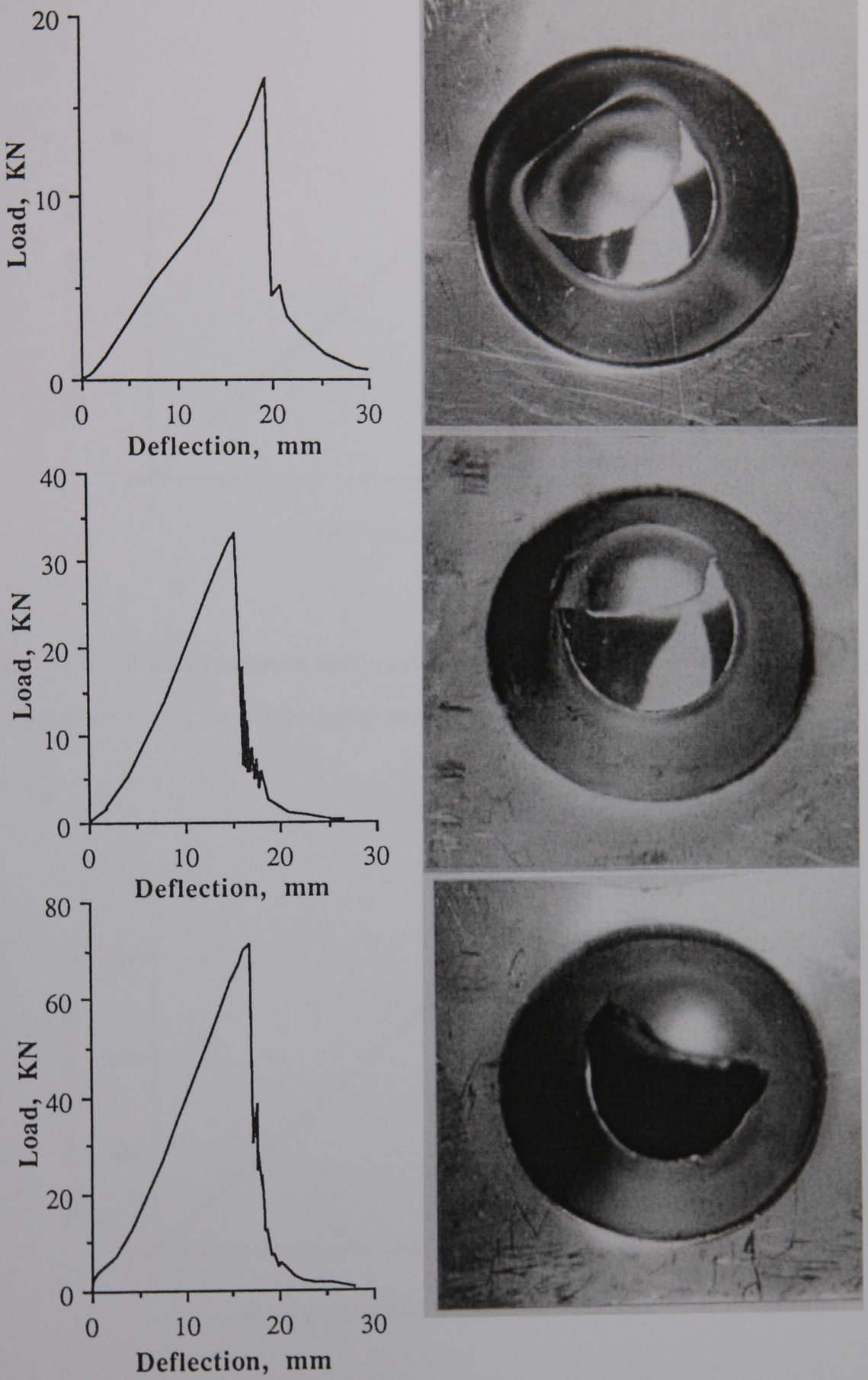

Figure 5.11 - Typical force-deflection curves for 0.6, 1 and 2 mm stainless steel after complete penetration and perforated specimens, top 0.6 mm, middle 1 mm and bottom 2 mm .

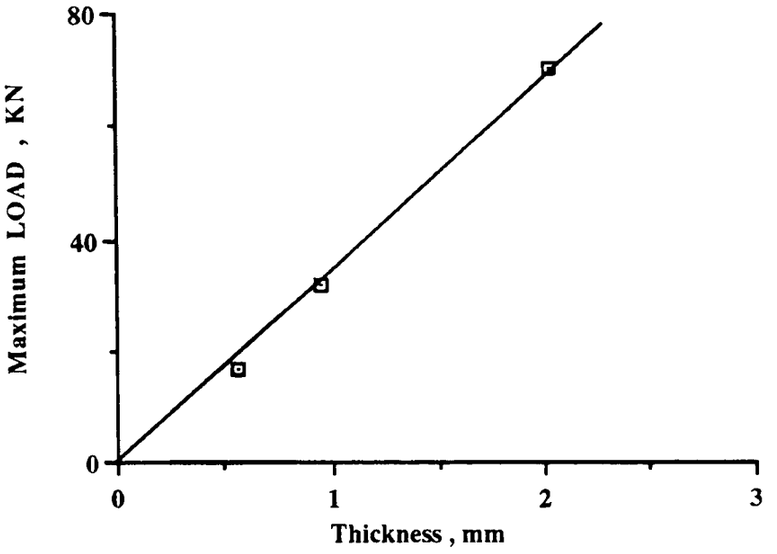

Figure 5.12 - Relation between maximum load generated during perforation impact as a function of thickness for stainless steel sheet.

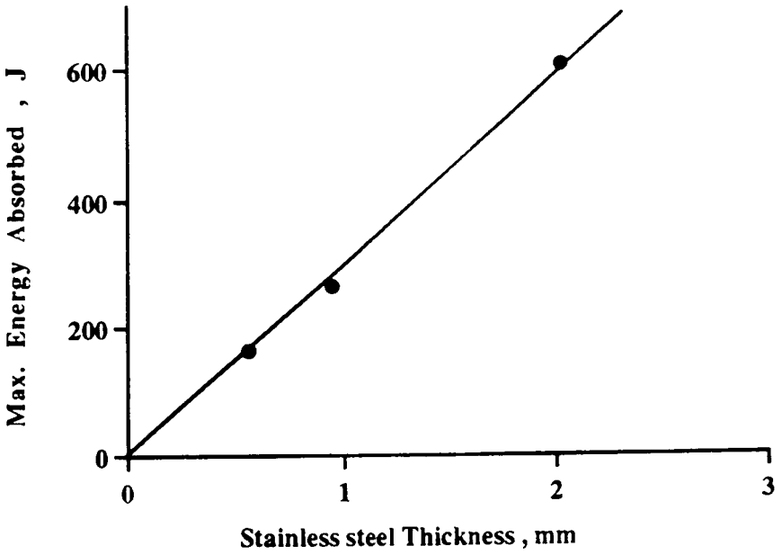

Figure 5.13 - Maximum energy absorbed by the layer of stainless steel after complete penetration as a function of thickness.

SMC+S.S. specimens regardless of the thickness of SMC and stainless steel layers showed a common failure mode. The failure consisted of a circular hole and a main flap which had been divided into two triangular flaps. Figure 5.14 shows the force-deflection and the impacted specimens for 2, 4 and 6 mm SMC with a layer of 0.6 mm thickness of stainless steel.

5-3 Determination of the energy absorbed by the layer of stainless steel (S.S.) and SMC in the SMC+S.S. laminate.

The energy absorbed by SMC+S.S. specimens on impact is the sum of the energy absorbed by the layer of stainless steel sheet and that absorbed by SMC:

$$E_t = E_{smc} + E_{s.s.}$$

Where :

E_t = Energy absorbed by the SMC+S.S. laminate

E_{smc} = Energy absorbed by the SMC layer

$E_{s.s.}$ = Energy absorbed by the S.S. layer

This assumes that the deformation of the steel is unchanged when it forms part of the macrocomposite. The energy absorbed by SMC layer can be calculated once the energy absorbed by stainless steel is known.

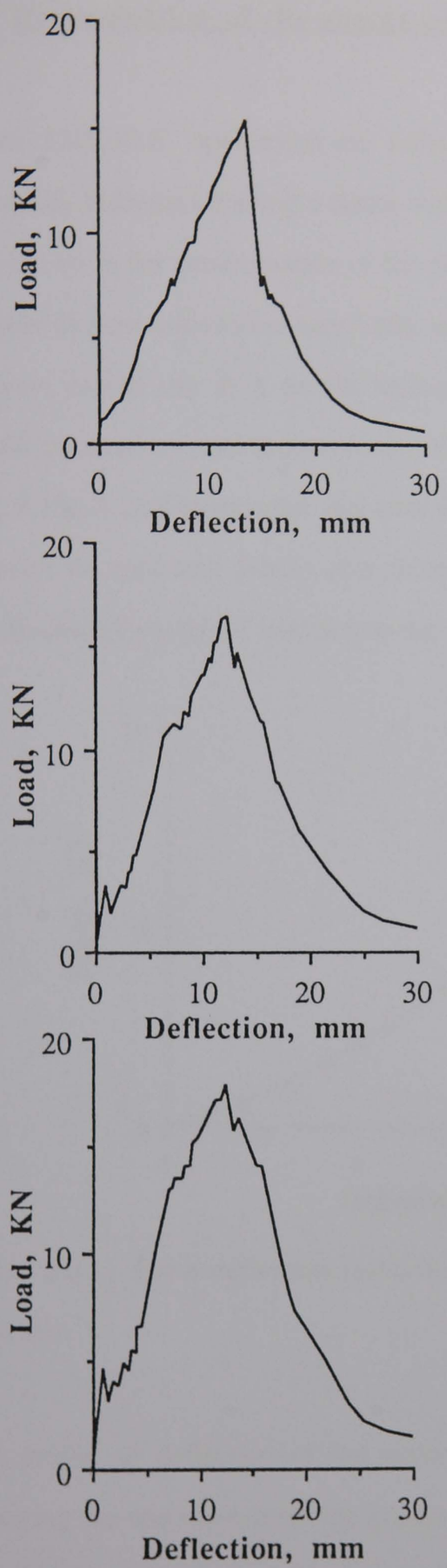

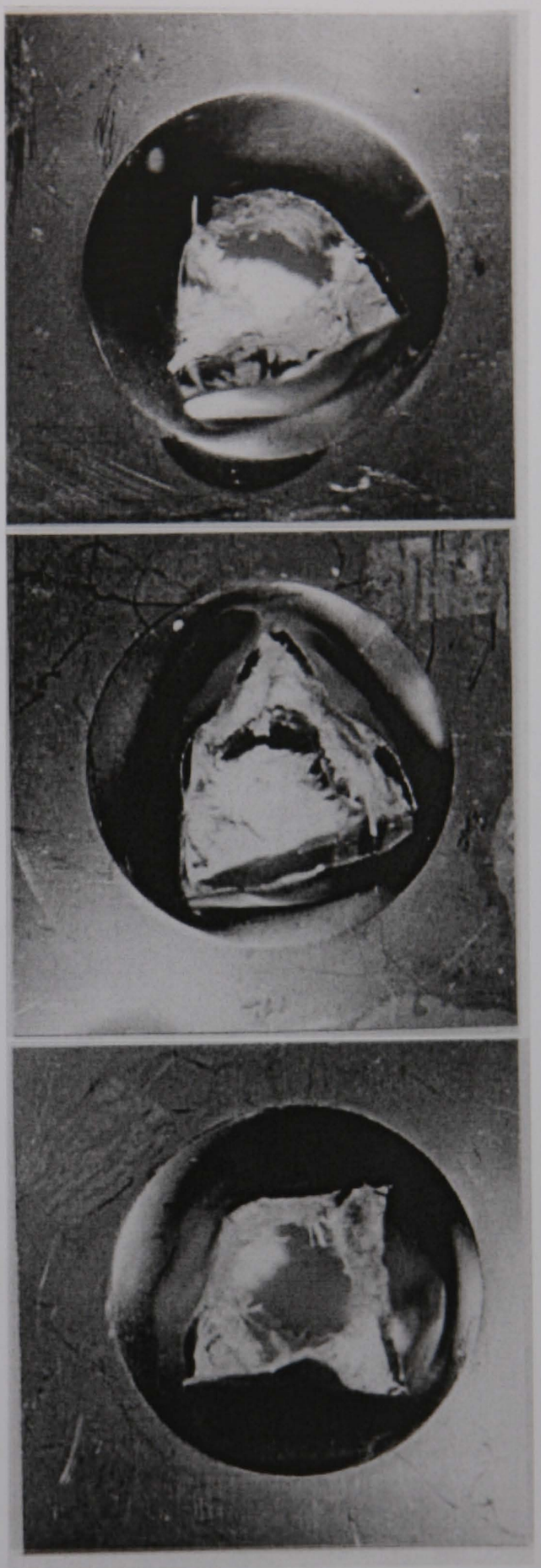

Figure 5.14 - Force-deflection curves for 2, 4 and 6 SMC mm with a layer of 0.6 mm stainless steel with perforated specimens, top 2 mm, middle 4 mm and bottom 6 mm.

5-4 Determination of the energy absorbed by the layer of stainless steel

When SMC+S.S. specimens are subjected to impact, the layer of stainless steel is plastically deformed leaving a dome with height h (fig. 5.6). This permanent deflection was the basis for determination of the energy absorbed by the layer of stainless steel. A number of slow indentation tests under equivalent loading geometry (see page 96, chapter 3) were carried out in a tensile testing machine (SCHENCK). The slow indentation results on stainless steel sheet revealed identical load deflection curves to those of impact (fig. 5.15). A profile recorder was used during the slow indentation test (see chapter 3) to measure the specimen profile after increments of load so that deflection, and hence the distribution of energy or load across the specimen, might be determined.

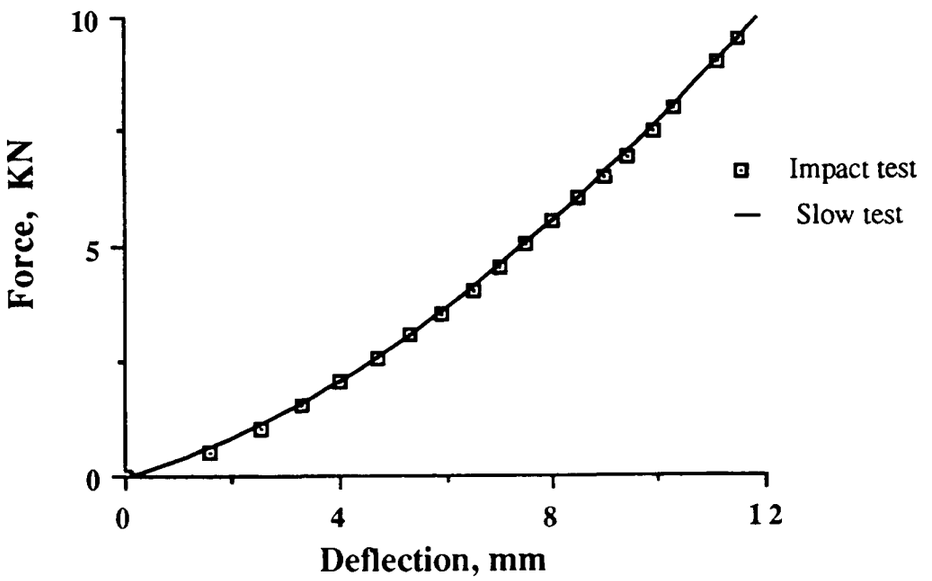

Figure 5.15 - Force-deflection curve for 0.6 mm stainless steel sheet during impact and slow test.

The profile of deflection of the stainless steel sheet after impact was measured by removing the specimen from the impact machine and putting on the support of the slow indentation test in the tensile test machine. The deformation profile of the steel sheet, when subject to indentation and impact was exactly analogous to that observed in the steel when it is a component part of SMC+S.S. laminate (fig. 5.16). Therefore, the energy

required to produce a certain amount of deflection on impact in the layer of stainless steel sheet can be determined by the slow indentation test.

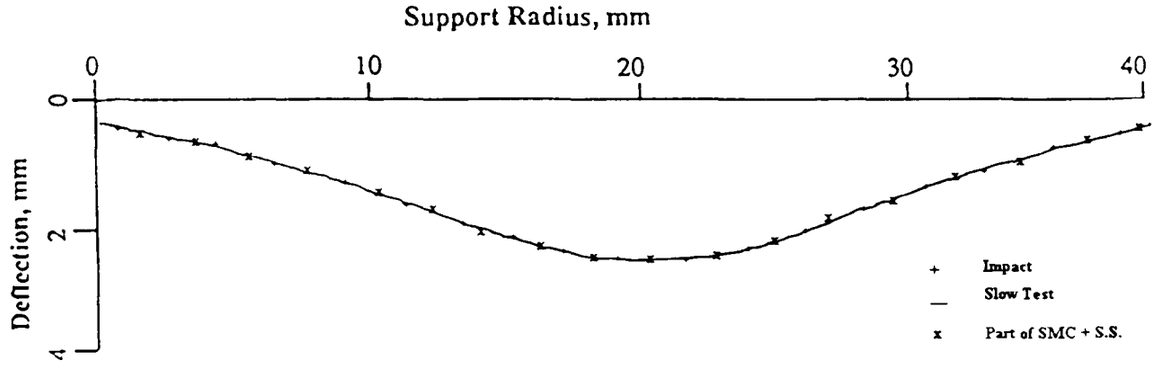

Figure 5.16 - The profile of deflection of stainless steel sheet on its own after impact and slow tests and when it is a component part of SMC+S.S.

Since the load-deflection obtained during the slow test is the load-deflection of the indenter rather than the specimen, a transducer was mounted under the tensile surface of the specimen (see page 98 chapter 3) to measure its maximum deflection (deflection at the centre) during the test. It was found that the deflection at the back of the specimen is similar to the displacement of the indenter (table. 1). Therefore, the total energy (elastic+plastic) required to produce a certain amount of deflection in steel sheet can easily be calculated from the area under the load deflection curve (fig. 5.15). Since the energy

due to elastic deflection is recovered after impact, it is possible to calculate the absorbed (plastic) energy from the slow indentation test curve. In order to do this, at different intervals the specimen was unloaded and the area of the unloaded curve was calculated (fig. 5.17). For example in figure 5.17, the specimen was loaded to 1.05 KN and then unloaded. The deflection before and after unloading was 2.6 mm and 2 mm respectively.

Table 5.1 - Deflection at the tensile surface of the 0.6 mm stainless steel sheet in relation with the movement of the plunger.

Load KN	Deflection at the tensile surface, mm	Displacement of the plunger, mm
0.51	1.5	1.5
1.02	2.35	2.4
1.54	3	3.1
2.02	3.75	3.8
2.54	4.3	4.4
3.01	4.95	5

The dashed area is the energy which has been absorbed to produce 2 mm permanent deflection. By measuring the area under the unloading curves, a calibration curve which is the absorbed energy as a function of permanent deflection produced. Figures 5.18, 5.19 and 5.20 show the calibration curves for 0.6, 1 and 2 mm stainless steel.

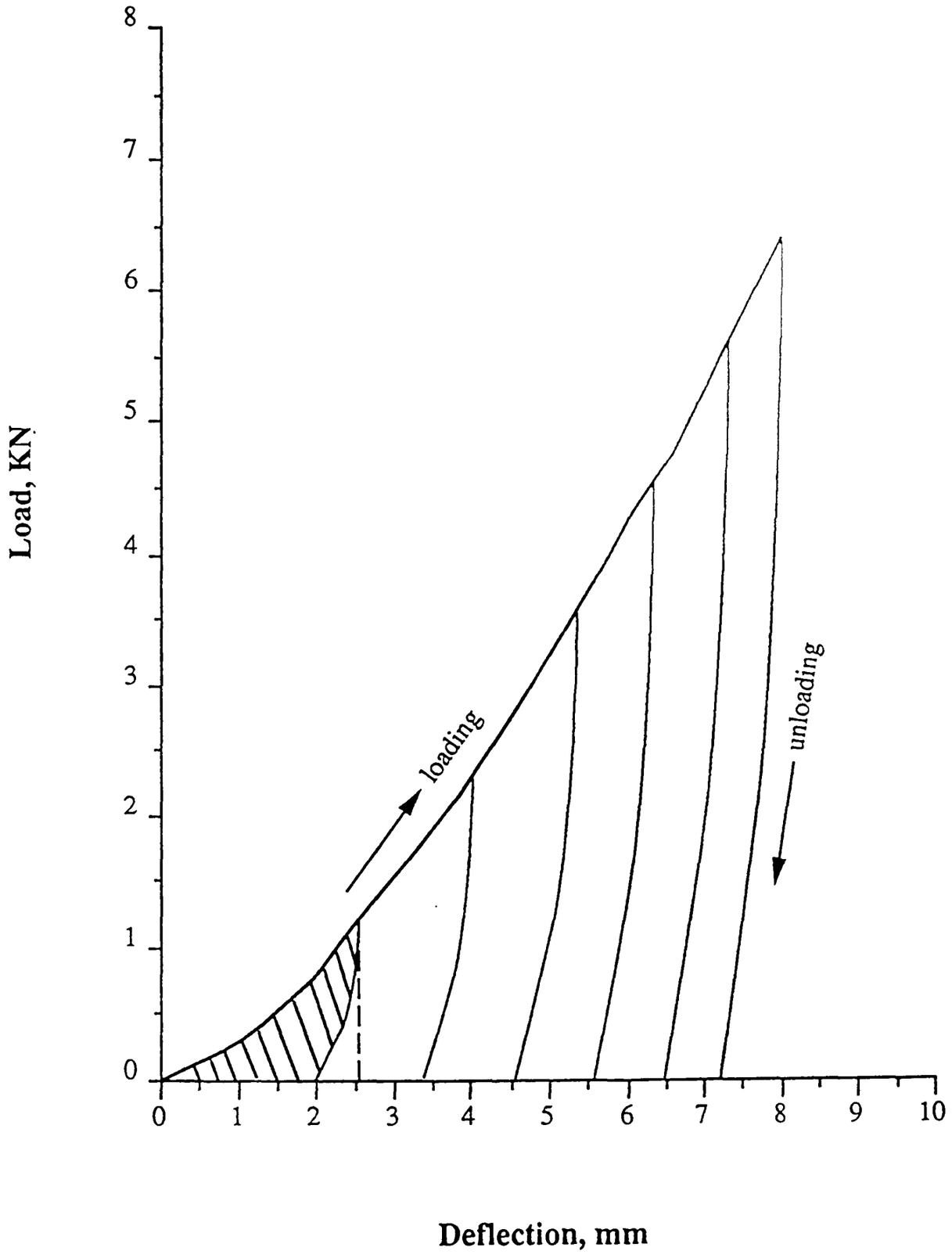

Figure 5.17 - Force deflection curve for stainless steel sheet used to construct the calibration curve.

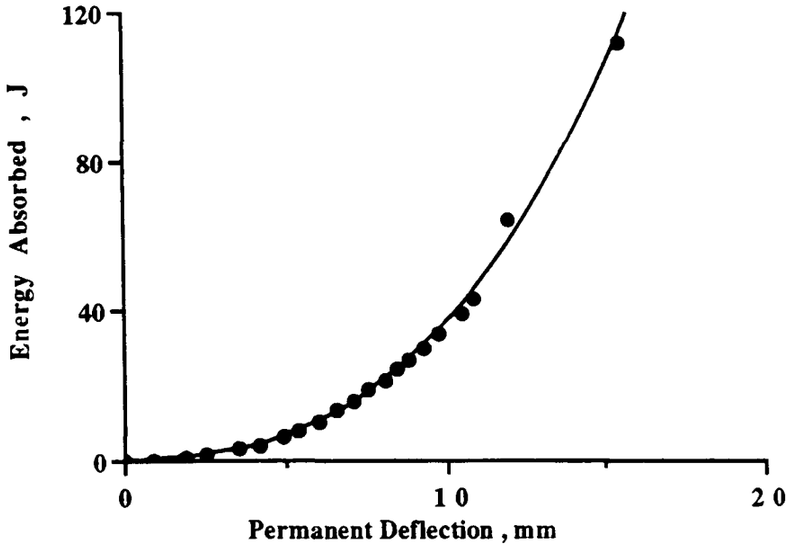

Figure 5.18 - Energy absorbed by 0.6 mm thick stainless steel sheet as a function of permanent deflection.

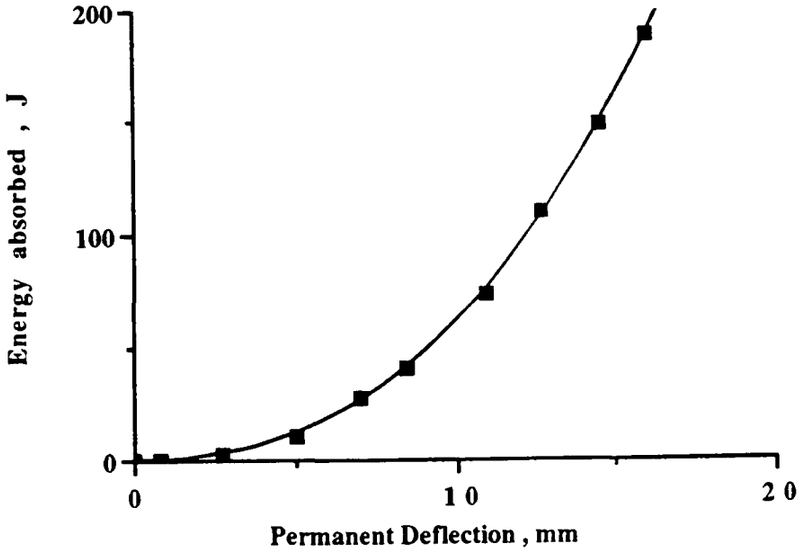

Figure 5.19 - Energy absorbed by 1 mm thick stainless steel as a function of permanent deflection.

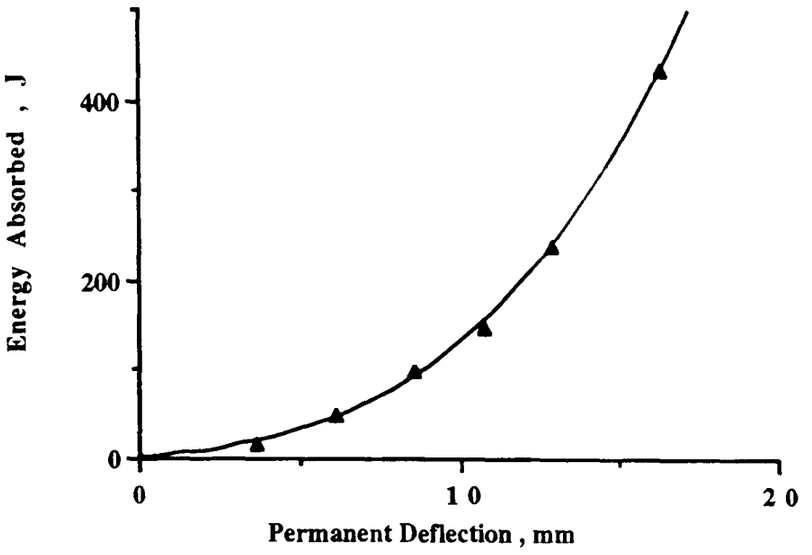

Figure 5.20 - Energy absorbed by 2 mm thick stainless steel sheet as a function of permanent deflection.

Having obtained the calibration curve, it was then straight forward to determine the work done in deforming the steel component of the SMC+S.S. laminate during impact by simply measuring the permanent deflection (dome height) of the steel and reading the relevant value from figure 5.18, 5.19 or 5.20.

The procedure for perforated SMC+S.S. specimens was a bit different. The energy absorbed by the layer of stainless steel was a combination of the energy required to form the dome, nucleate and propagate the crack and deform the main flap into two triangular flaps.

Close examination of the force-deflection curves of the SMC+S.S. specimens which had been perforated using a slow indentation test showed that after maximum force, the load drops in three distinctive stages (AB, BC and CD, fig. 5.21). Slow tests revealed that in stage one (AB) the main flap forms and in stage two (BC) the two triangular flaps are developed. Stage three (CD) is the period during which the tip of the striker fully

penetrates the specimen and is the end of the impact event. Friction between the sides of the striker and the surface of the hole in the specimen does not let the load drop to zero. The energy absorbed by the layer of stainless steel for propagation of crack and formation of flaps (E_p) is equal to the area under the load-deflection curve from point A to C (fig. 5.21). The total energy absorbed by the layer of stainless steel ($E_{s.s.}$) can then be easily calculated. In SMC+S.S. specimens the deflection just before the initiation of crack in the layer of stainless steel is equivalent to the deflection at maximum force on the force-deflection curve (point A, fig. 5.21). Therefore the energy absorbed by the layer of stainless steel before the initiation of crack (E_d) can be easily determined. In order to do so the deflection at maximum force on force-deflection curve is measured. Since deflection at maximum force is the sum of elastic and plastic deflection, the elastic deflection which is 0.6 mm (as shown in figure 5.17) is subtracted from this value and the absorbed energy is read from the relevant calibration curve.

Having the values of energy absorbed for maximum deflection in the steel layer before initiation of crack (E_d) and the energy absorbed during propagation of cracks and formation of flaps (E_p) the total energy absorbed by the stainless steel layer ($E_{s.s.}$) can be calculated:

$$E_{s.s.} = E_d + E_p$$

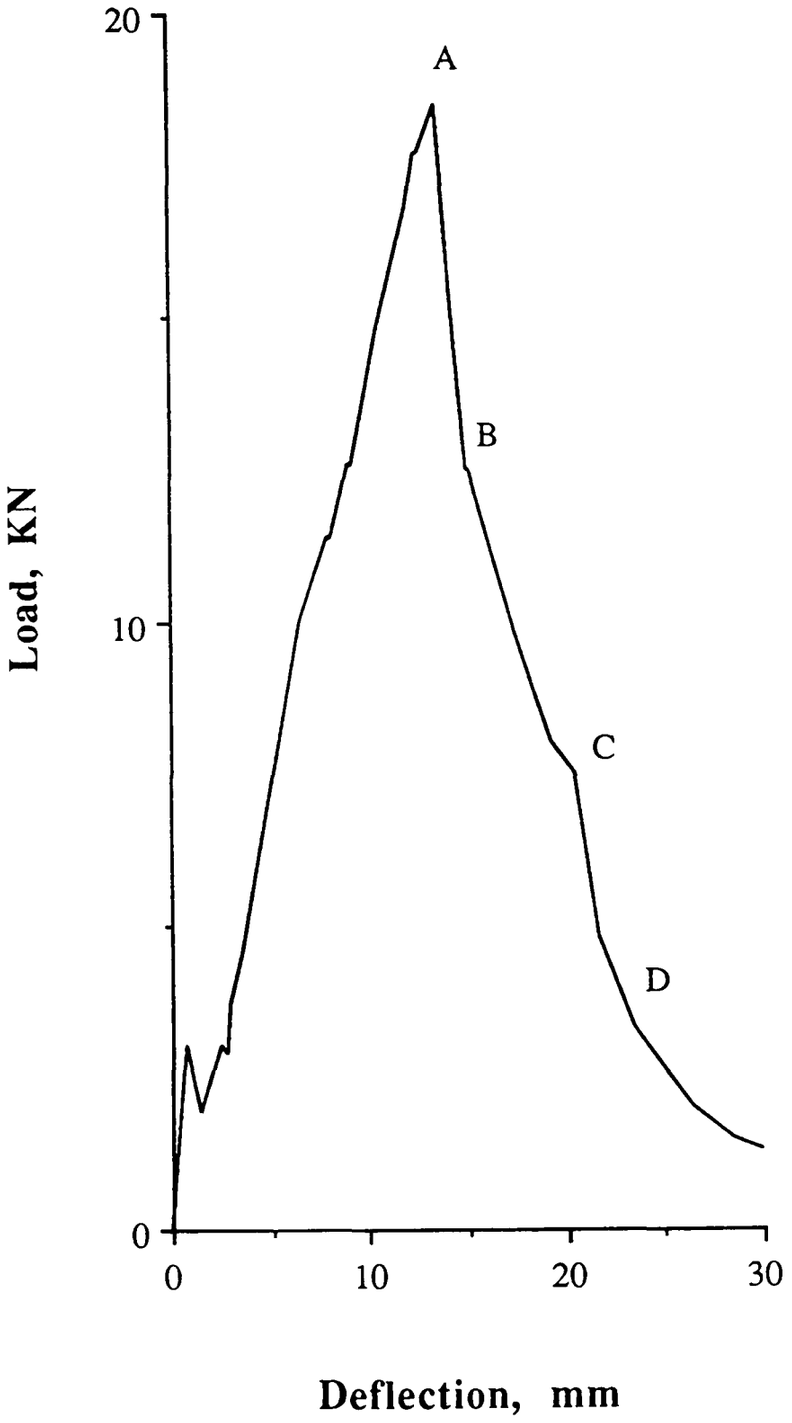

Figure 5.21 - Force deflection curve for SMC+stainless steel laminate after complete penetration by impact

5 - 5 Determination of the energy absorbed by the layer of SMC in the SMC+S.S. specimens

After impact a force-deflection curve is obtained. The area under the force-deflection curve is the amount of energy absorbed by the SMC+S.S. laminate. In the case of non penetrating impact which had been carried out by the CEAST impact machine, energy was calculated by a microcomputer. For perforated SMC+S.S. laminates the area under the load deflection curve was calculated manually by counting squares. When the energy absorbed by the SMC+S.S. laminate is determined, the energy absorbed by the layer of stainless steel ($E_{s.s.}$) is calculated according to the procedure explained in section 5-4 and then the energy absorbed by the layer of SMC in the SMC+S.S. laminate (designated SMC') is calculated from :

$$E_{smc'} = E_t - E_{s.s.}$$

where :

$E_{smc'}$ = Energy absorbed by the layer of SMC in the SMC+S.S. laminate.

E_t = Total energy absorbed by SMC+S.S. laminate.

$E_{s.s.}$ = Energy absorbed by the layer of stainless steel in the SMC+S.S. laminate.

The results of this exercise showed that SMC' absorbs considerably more energy than SMC can when tested in isolation. This very pronounced effect was observed with all combinations of SMC and steel tested. Figure 5.22 shows the energy absorbed by 4.6 mm SMC+S.S. laminate, the energy absorbed just by the SMC layer (designated SMC') and the energy absorbed by a comparable, 4 mm thick SMC sheet tested in isolation. At a given incident energy, the SMC' initially absorbed less energy than the SMC sheet. This was because, at low energies, the elastic energy absorbed by the steel was significant. As the incident energy rose, so the energy absorbed by the SMC' became progressively larger relative to that absorbed by the SMC. The energy absorbed by SMC, SMC' and

SMC+S.S. increased progressively with incident energy until reaching a plateau corresponding to the total penetration of the specimen by the impactor. The 4 mm SMC in SMC+S.S. laminate (SMC') absorbed almost twice the maximum energy that could be absorbed by the 4 mm SMC. The story for different thicknesses of SMC with 0.6 mm stainless steel was the same (fig. 5.23).

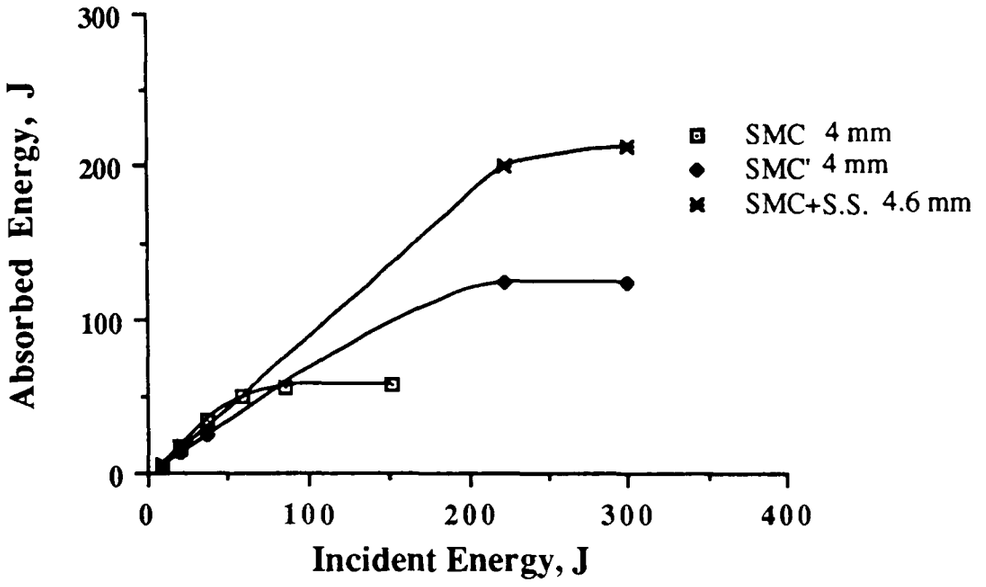

Figure 5.22 - Energy absorbed as a function of incident energy for SMC, steel-SMC macrocomposites and the SMC layer in the macrocomposite (SMC').

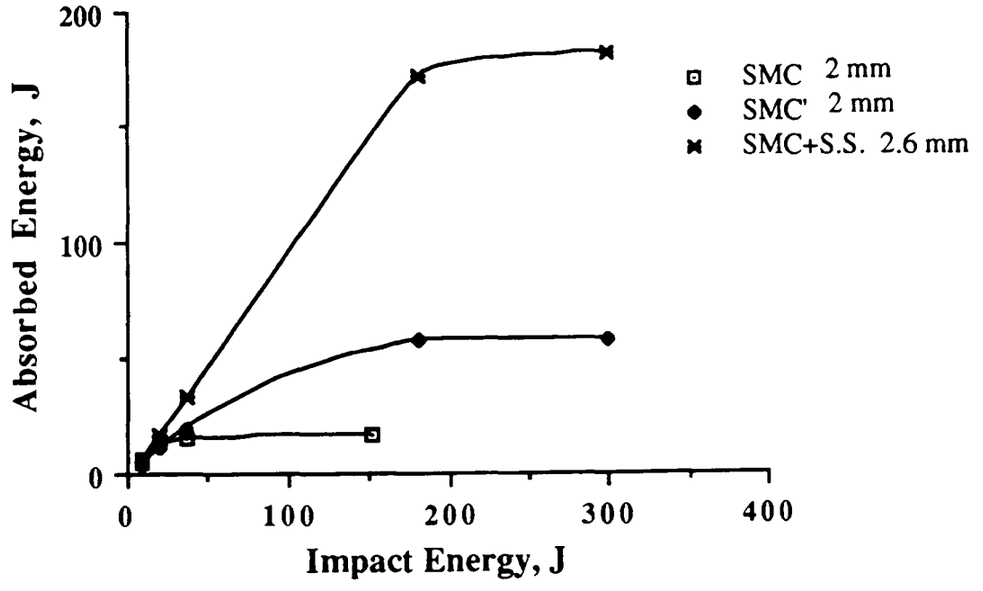

Figure 5.23 - Energy absorbed as a function of incident energy for SMC, steel-SMC macrocomposites and the SMC layer in the macrocomposite (SMC').

5 - 6 The effect of test variables on the amount of energy absorbed by the layer of SMC in the SMC + Stainless steel laminates.

As it was mentioned earlier the area under the force-deflection curve is the amount of energy absorbed by the SMC + Stainless steel laminate. In this section the effect of test variables such as impact velocity and specimen thickness on the force-deflection curve which consequently affect the energy absorbed by the laminate is considered.

5 - 6.1 The effect of impact velocity

For non-penetrating impact, increasing the impact velocity increased the area under the force-deflection curve (fig. 5.8). Therefore the energy absorbed by the laminate increased with impact velocity. In the case of perforated SMC+Stainless steel laminates the impact velocity only affected the level of noise on the force deflection curve and did not affect the area under it. Figures 5.24 and 25 show the force deflection curves for 4 mm SMC with a layer of 0.6 mm stainless steel which had been completely penetrated. At an impact velocity of 1 ms^{-1} the force deflection curve was very smooth (fig. 5.25) and at 5 ms^{-1} it became very noisy (fig. 5.25). The comparison of the force-deflection curves at 1 ms^{-1} and 5 ms^{-1} for 4 mm SMC with a layer of 0.6 mm stainless steel is shown in figure 5.26. It is clearly seen that the two impact velocities (1 ms^{-1} and 5 ms^{-1}) yield similar force-deflection curve and therefore the energy absorbed by the laminate is not affected by the impact velocity.

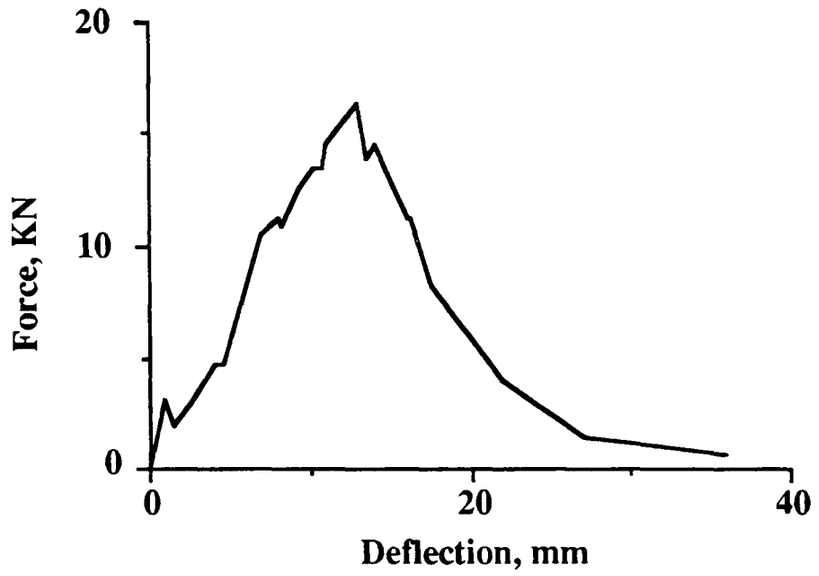

Figure 5.24 - Force deflection curve for 4 mm SMC with a layer of 0.6 mm thick stainless steel after complete penetration at 1 ms^{-1}.

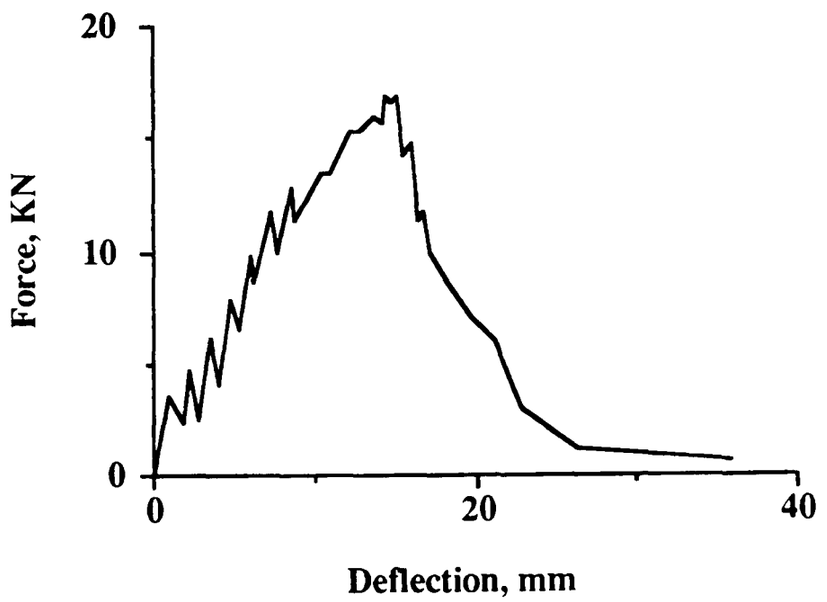

Figure 5.25 - Force deflection curve for 4 mm SMC with a layer of 0.6 mm thick stainless steel after complete penetration at 5 ms^{-1}.

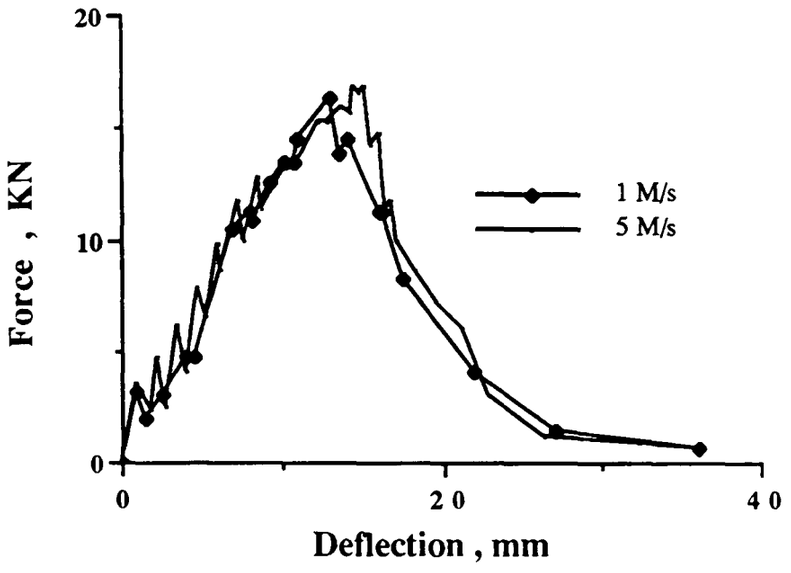

Figure 5.26 - Comparison of typical force deflection curves for 4 mm SMC with a layer of 0.6 mm stainless steel after complete penetration at 1 ms^{-1} and 5 ms^{-1}.

5 - 6.2 The effect of specimen thickness

The thickness of SMC Stainless steel laminates were increased either by increasing the thickness of SMC or stainless steel. The effect of thickness of the laminate depended on whether the specimen was partially or completely penetrated.

When the SMC stainless steel laminates were completely penetrated the energy absorbed by the laminate increased with increasing the thickness of the laminate. The force deflection curves for 6 mm SMC with a layer of 0.6 and 1 mm stainless steel are shown in figure 5.27. The area under the force deflection curve which is representative of

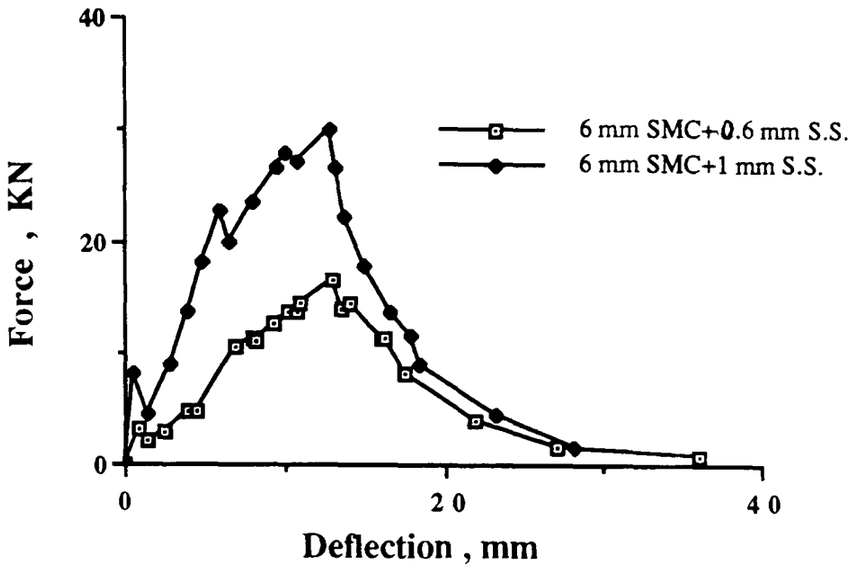

Figure 5.27 - Typical force deflection curves for 6 mm SMC with a layer of 0.6 and 1 mm stainless steel after complete penetration.

the energy absorbed by the laminate is higher for 6 mm SMC with 1 mm thick stainless steel (fig. 5.27). When the thickness of stainless steel was kept constant and the thickness of the laminate was increased by increasing the thickness of SMC, the thicker laminate absorbed more energy on perforation. The relationship between the energy absorbed by the laminate as a function of thickness of stainless steel for different thicknesses of SMC is shown in figure 5.28. For a given thickness of stainless steel the energy absorbed by the laminate increased with increasing the thickness of SMC. The energy absorbed by the laminate for a constant thickness of SMC also increased with increasing the thickness of stainless steel (fig. 5.28).

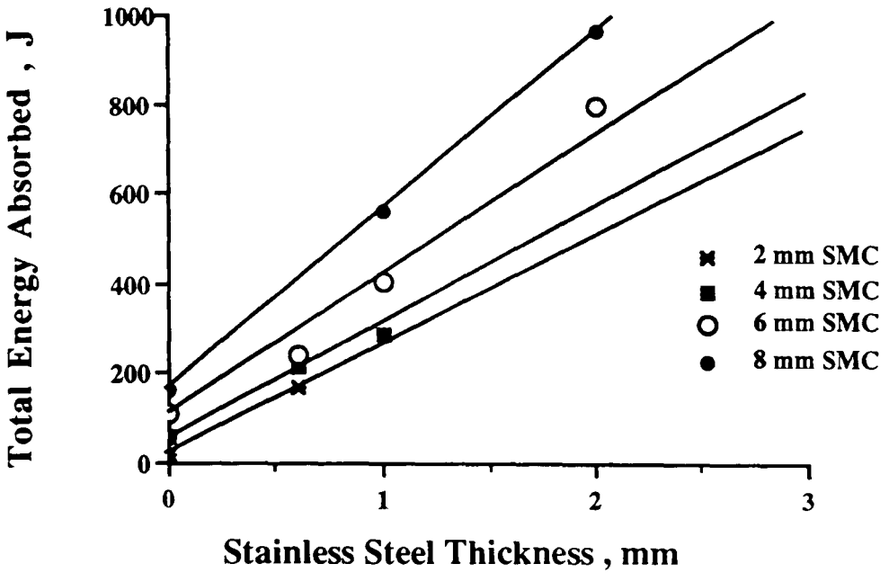

Figure 5.28 - Maximum energy absorbed by the laminate for different thicknesses of SMC as a function of stainless steel thickness.

In the case of non-penetrating impacts for laminates of constant thickness of stainless steel, the area under the force-deflection curve was higher for laminates of lower thickness of SMC. The force deflection curves for 4 mm and 2 mm SMC with a layer of 0.6 mm thick stainless steel produced by a 9 joules incident energy impact is shown in figure 5.29. The area under the force deflection curve for 2 mm SMC with 0.6 mm thick stainless steel is higher than 4 mm SMC with 0.6 mm thick stainless steel (fig. 5.29). The relation between the energy absorbed by the SMC stainless steel laminate as a function of incident energy (impact velocity) for a constant thickness of stainless steel (0.6 mm) with different thicknesses of SMC is shown in figure 5.30. It is clearly shown in figure 5.30 that for non penetrating impact for a given incident energy the laminate with thicker SMC layers absorbed less energy.

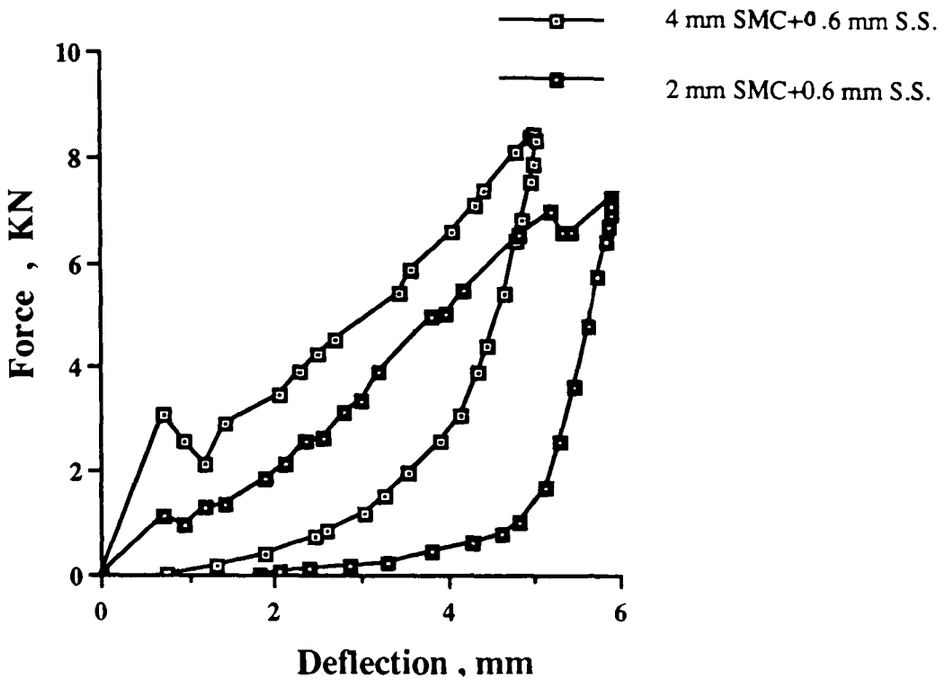

Figure 5.29 - Force deflection curves for non penetrating impact for 2 and 4 mm SMC with a layer of 0.6 mm stainless steel at 9 joule incident energy.

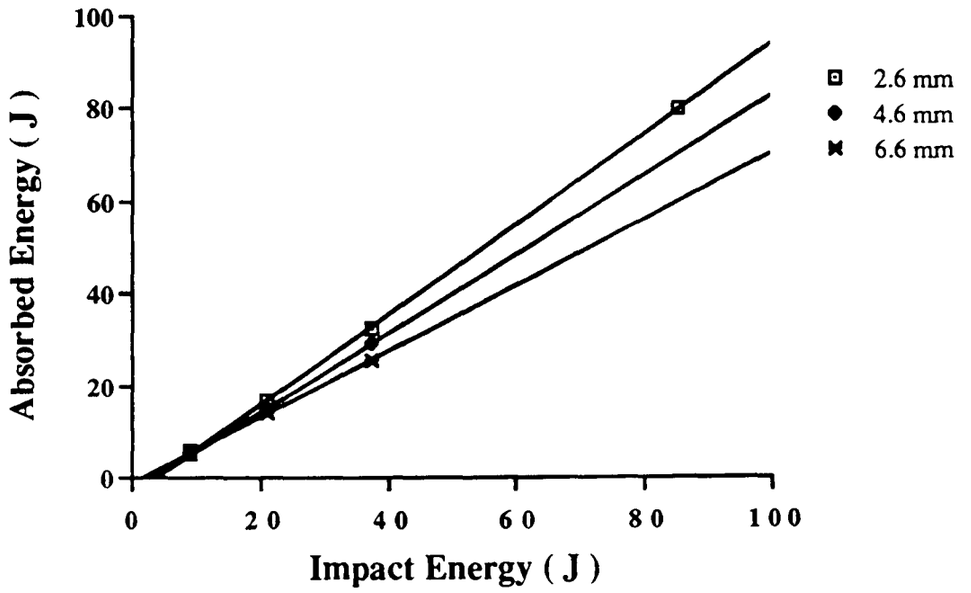

Figure 5.30 - Energy absorbed by SMC stainless steel laminates as a function of incident energy for 2, 4 and 6 mm SMC with a layer of 0.6 mm stainless steel.

5 - 6.3 The effect of bonding between the layer of SMC and S.S.

In order to determine the effect of bonding between the layers of stainless steel and SMC of the composite on its impact behaviour, square specimens of 6x6 cm were cut from the sheets of stainless steel and SMC. Three experiments were carried out. In the first experiment the layer of SMC rested on the layer of stainless steel without any adhesive or lubricant. In the second experiment the contact surface of SMC and stainless steel was lubricated and no adhesive was used. In the third experiment the layer of stainless steel was glued to the layer of SMC by a reasonably strong toughened acrylic adhesive (PERMA BOND Grade F241/F246).

Results of these experiments showed that the impact data for non lubricated, lubricated and as supplied SMC stainless steel laminate (in which SMC was moulded directly onto the steel sheet) were similar, but when the layer of stainless steel was glued to the layer of SMC, the initial peak on the force deflection curve was higher but the energy absorbed by the laminate and the energy absorbed by SMC were similar. Figure 5.31 shows the force-deflection curves for non-lubricated, lubricated, and bonded steel-smc laminates. It is clearly seen in figure 5.31 that apart from the initial peak for glued SMC-stainless steel, the force deflection curves are similar. The result shows that the bonding of the supplied laminates has no significant effect on the impact behaviour of the laminate and therefore the earlier assumption that the energy absorbed by the laminate is the sum of energy absorbed by SMC and stainless steel was correct.

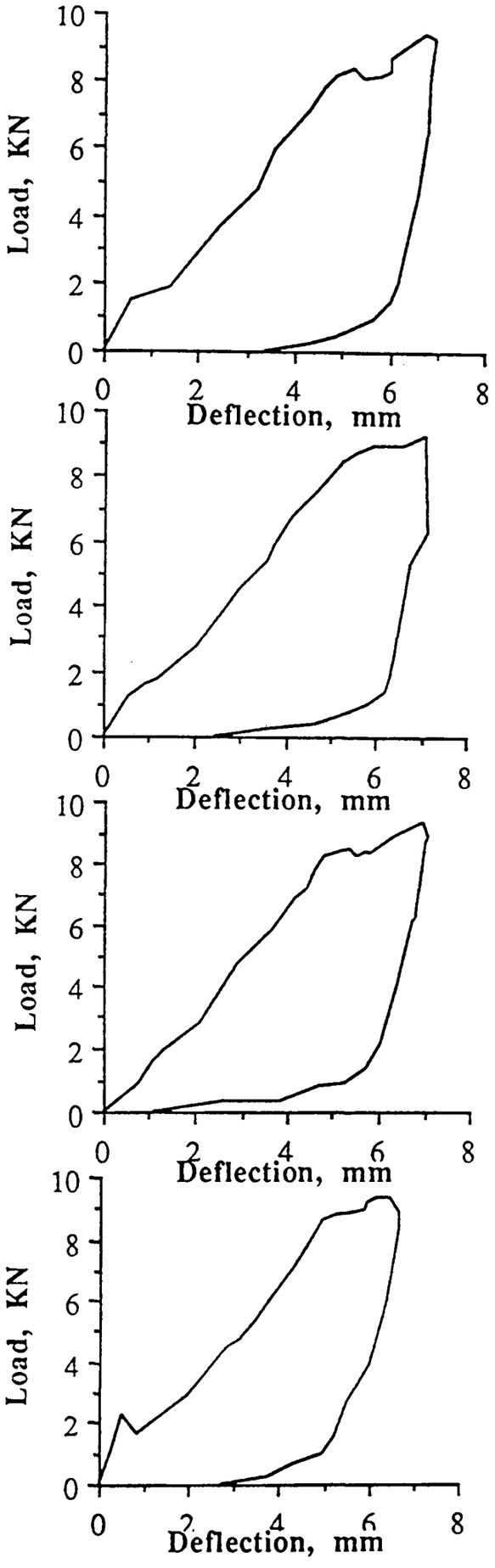

Figure 5.31 - Force deflection curves for 4 mm SMC with a layer of 0.6 mm stainless steel, 1) supplied material, 2) lubricated, 3) non lubricated, 4) glued.

5 - 7 Response of SMC+Stainless steel laminate to slow indentation test

Slow indentation tests (see chapter 3 for details of the test) on SMC+stainless steel specimens showed that the general shape of the load deflection curves are similar to those of impact (fig. 5.32). The transition loads were identical to those obtained from impact tests. Examination of the slow test specimens loaded below the transition point showed that the layer of stainless steel is elastically deformed in this region and after the removal of the load the thickness of the specimen did not change. At transition load the layer of stainless steel yields and after removal of the load at this point a permanent deformation in the form of a dome remains in the specimen. The test procedure to find out when the layer of stainless steel yields was as follows:

Before applying any load the profile recorder was pushed to and fro beneath the specimen, thus drawing the profile of the specimen which in this case was a straight line on the chart (fig. 5.33). This straight line kept as a reference line. Then the cross head of the tensile test machine lowered at the desired rate (1 mm/min) and hence forcing the indenter into the specimen. At loads which were below the transition load the cross head movement was stopped and the profile of the specimen as mentioned earlier was recorded. Then the load was removed and the profile of the specimen recorded. If this profile was a straight line and superimposed upon the reference line then it was concluded that the layer of stainless steel had not been yielded. The load then increased gradually and the above process repeated until the profile of the specimen after removal of the load was not a straight line any more (fig. 5.34). The load at which the layer of stainless steel yielded was the transition load on the force deflection curves.

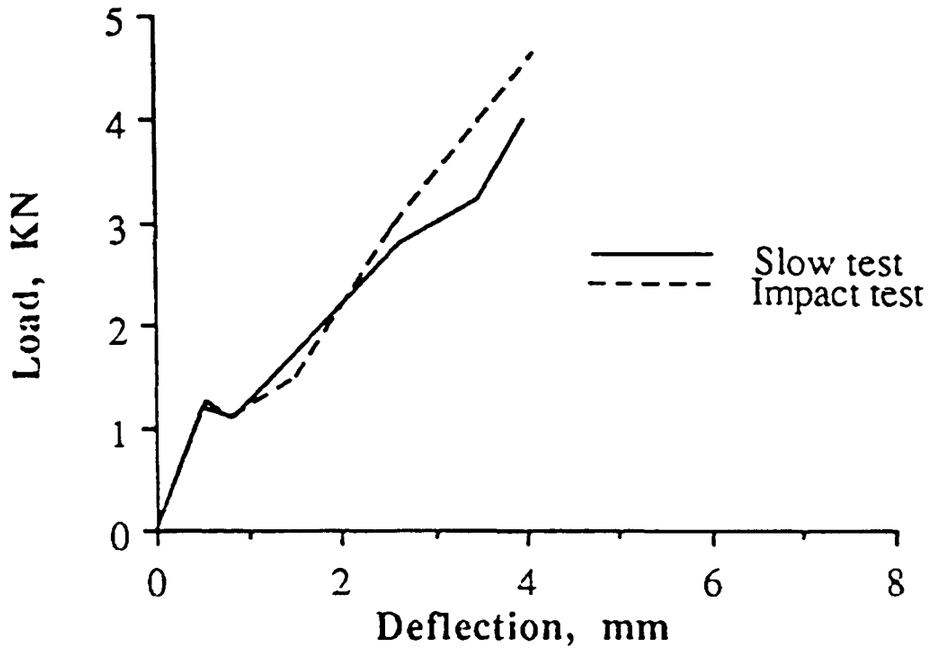

Figure 5.32 - Force deflection curves for impact test and slow test.

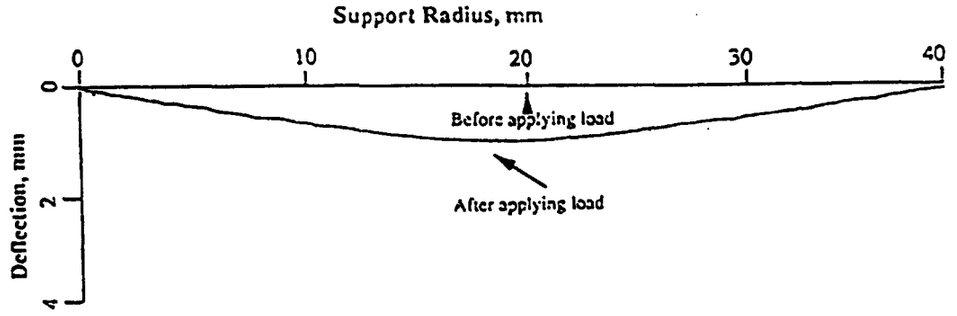

Figure 5.33 - Profile of deflection before and after applying load during slow test.

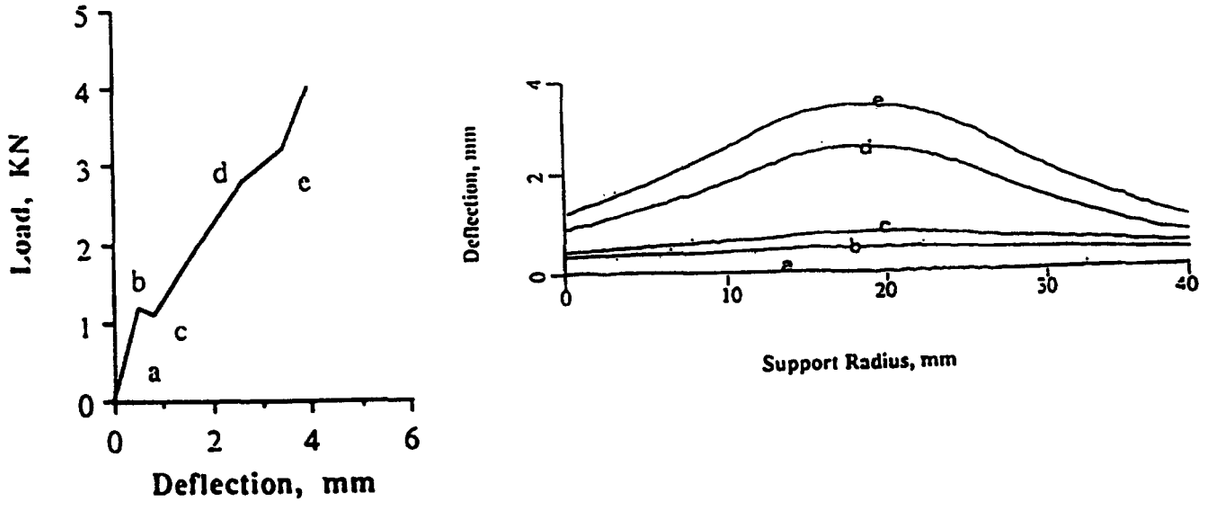

Figure 5.34 - Profile of deflection at transition load.

5 - 8 Damage detection techniques

As it was mentioned in chapter 4, optical microscopy was found to be the best technique to yield information on the nature of the damage. Therefore for SMC stainless steel laminates optical microscopy was used extensively and the other techniques (X-ray radiography, scanning electron microscopy) were used to a lesser extent. The damaged specimens were cut in half and carefully ground and polished with diamond abrasive and subsequently examined under a REICHERT microscope and photographed using an OM-2 Olympus camera. This technique revealed the delamination cracks and through thickness damage very clearly as shown in figure 5.35.

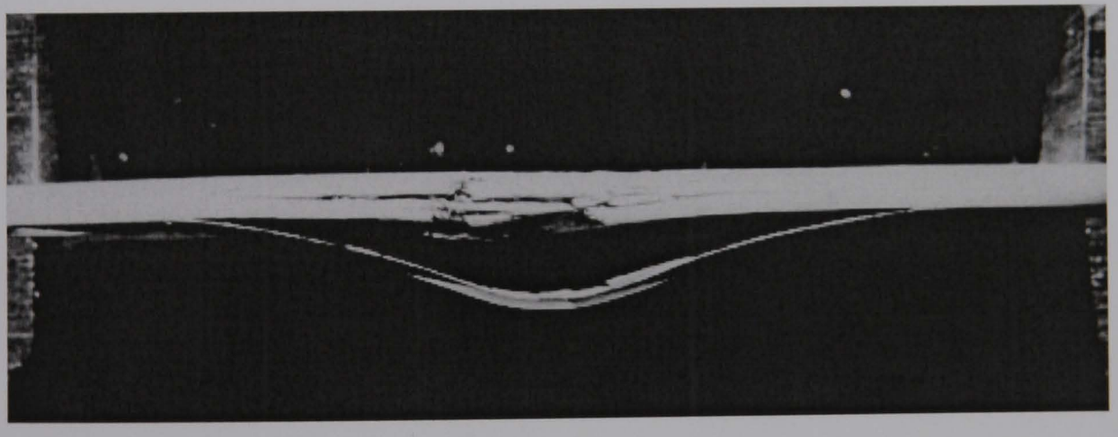

Figure 5.35 - Photograph of cross section through specimen for SMC stainless steel laminate after non penetrating impact.

5 - 9 Analysis of stresses in the SMC + Stainless steel laminate by Finite Element

The Lusas finite element stress analysis package was used to predict the response of SMC+stainless steel laminates to impact. The two dimensional, axisymmetric, finite element model used to analyse the stresses is shown in figure 5.36. The unsupported radius of the specimen was 20 mm and the thickness of the plate was 4 mm, which was divided into eight equal layers. The model used eight node, axisymmetric elements and comprised of 208 such elements. The method of applying load was to prescribe displacement which has been described in chapter 4. The elements in the bottom row of the mesh (fig. 5.36) had the mechanical properties of stainless steel and the other elements had the mechanical properties of SMC.

Contours of stresses were obtained from the Lusas package which were a good means of observing the stress distribution through the thickness of SMC+stainless steel laminates. The typical contours of shear stress for 4 mm SMC with a layer of 0.6 mm stainless steel is shown in figure 5.37. The results of contours of stresses are discussed in more detail in the discussion section.

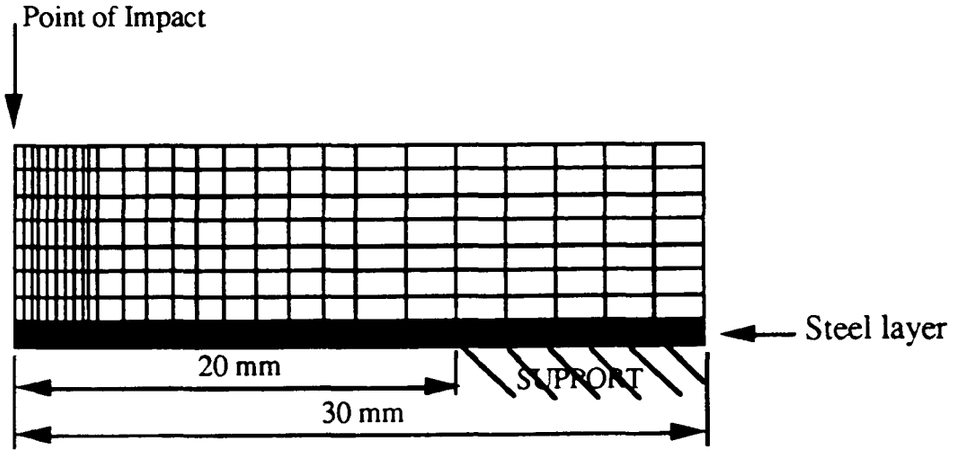

Figure 5.36 - Finite element model.

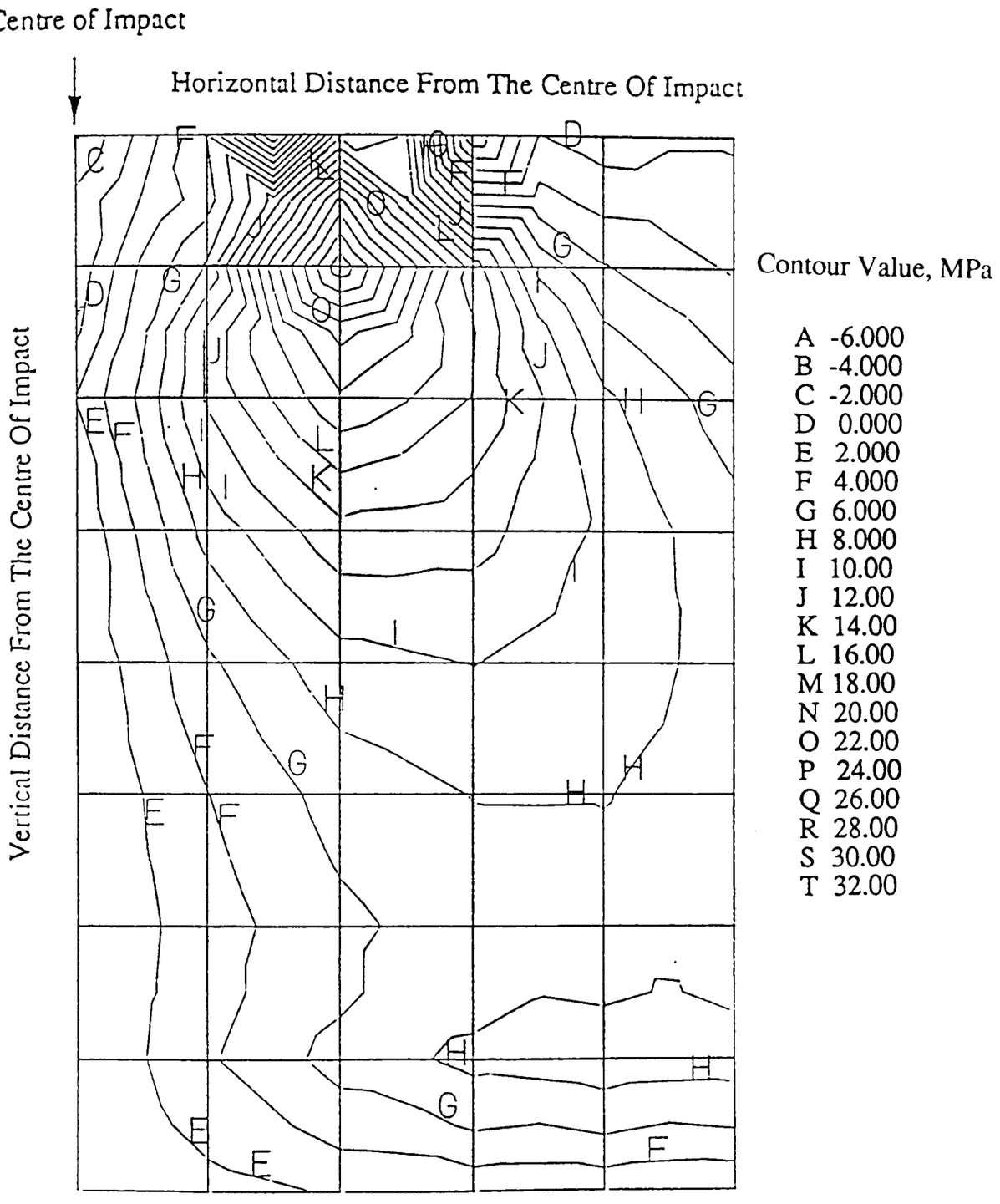

Figure 5.37 - contour of shear stress for 4 mm SMC with a layer of 0.6 mm stainless steel.

5 - 10 Discussion

Experimental results showed that an SMC layer in a SMC-stainless steel laminate absorbs more energy than SMC of a similar thickness can when tested in isolation. The effect of stainless steel layer is better understood, when the maximum absorbed energy value for SMC' is compared with the results of SMC and eighteen different GRP constructions (fig. 5.38). As it can be seen in figure 5.38. the layer of stainless steel has significantly improved the impact properties of SMC.

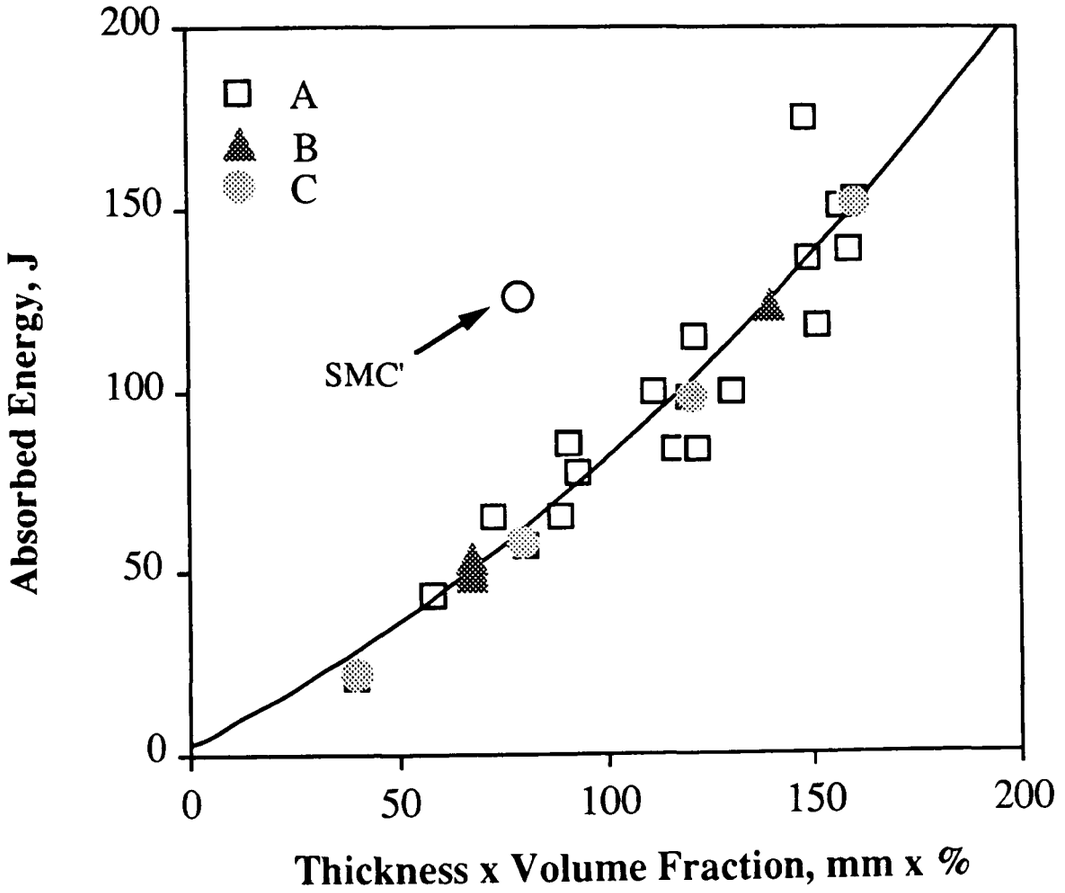

Figure 5.38 - Relationship between energy absorbed during through penetration versus thickness multiplied by fibre volume fraction for glass fibre composites. Legend: A - random and woven fibre thermoset resin. B - Random fibre thermoplastic GMT. C - SMC (After Babic et al [132]).

The increase in the amount of energy absorbed by the layer of SMC in the SMC stainless steel laminate was linked to the stiff steel layer. Stainless steel has a high Young's modulus (210 GPa) which increases the stiffness of the laminate significantly. The increase in stiffness of the laminate builds up stresses in the SMC layer during impact which are higher in magnitude and occupy a larger area in comparison with SMC when impacted on its own. These stresses are responsible for formation of delamination cracks and other kinds of damage which consequently enable the SMC layer to absorb more energy. The better understanding of the effect of stainless steel layer was achieved by analysis of stresses in the laminate. The result of the finite element for SMC stainless steel laminate was described briefly in the analysis section. The comparison between the stress contours for SMC and SMC as a part of SMC stainless steel laminate tells the story inside the laminate very clearly. Figure 5.39 shows the shear stress contours for 4 mm SMC and 4 mm SMC with a layer of 0.6 mm stainless steel together with two photographs of cross section through specimens. Stress contours for SMC stainless steel laminates (fig. 5.40) have higher magnitude and have extended more deeply through the thickness and towards the edge of the support when compared with stress contours of SMC on its own (fig. 5.41). Therefore the damage in the SMC layer in the laminate should be higher. The photographs in figure 5.39 shows that the damage is higher and prediction of the analysis has been correct. The analysis also showed that when 4 mm SMC is combined with a layer of 0.6 mm stainless steel and subjected to impact, the neutral axis shifts toward the interface of SMC stainless steel layers and puts the SMC layer completely in compression. When SMC is impacted on its own the neutral axis lies at approximately half the thickness of the specimen. The position of the neutral axis for both SMC +stainless steel and SMC are shown in figures 5.40 and 5.41. In the case of SMC contour H has zero value and is located approximately in the middle of the thickness. The contours above contour H have negative sign which is the indication that these areas are under compression. The contours I and J have a positive sign and these areas are under tension.

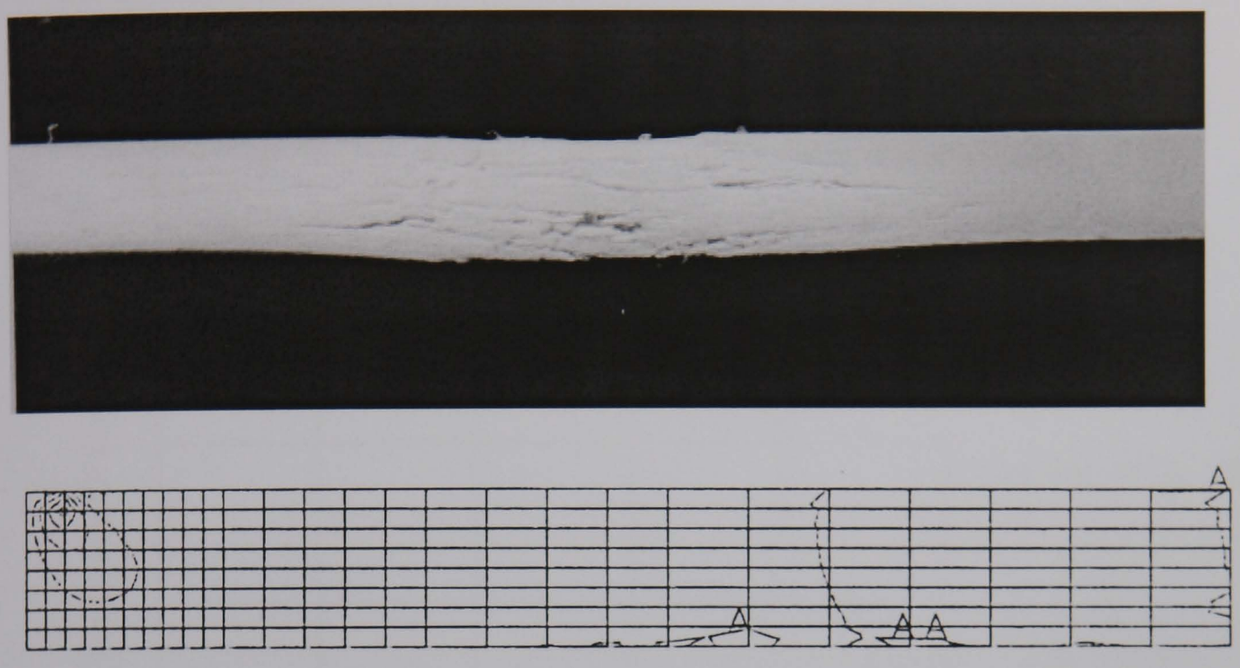

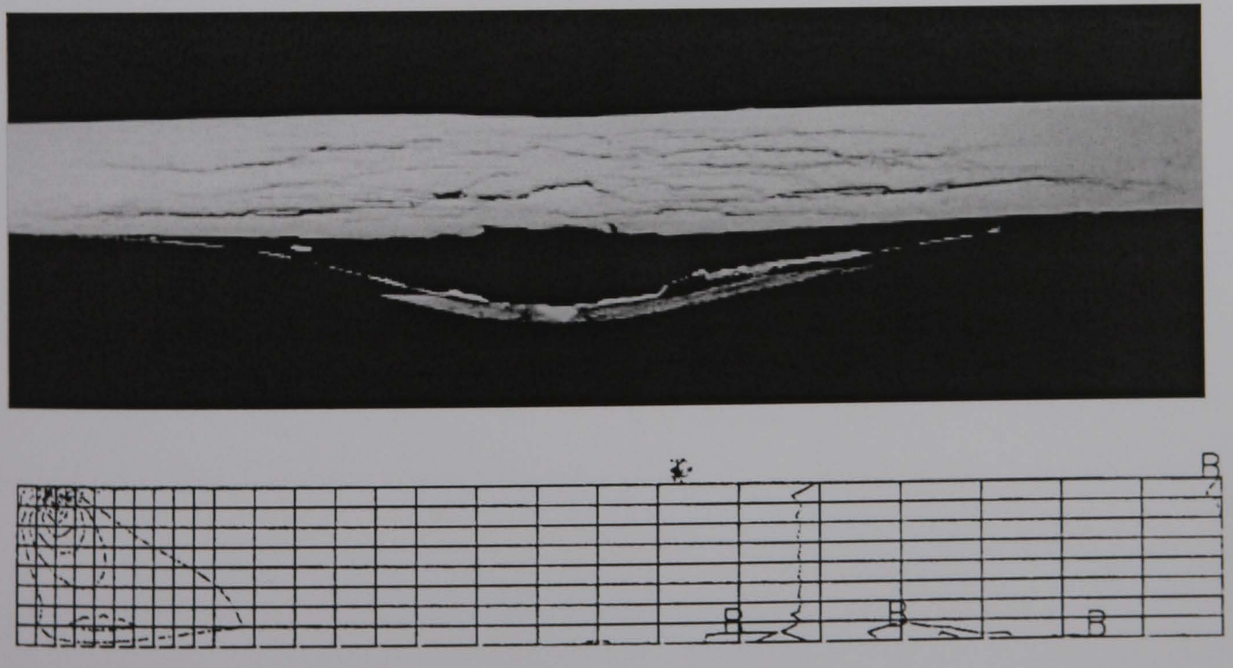

Figure 5.39 - Contours of shear stress and photographs of cross section for 4 mm SMC and 4 mm SMC with a layer of 0.6 mm stainless steel, top) SMC and bottom smc+steel.

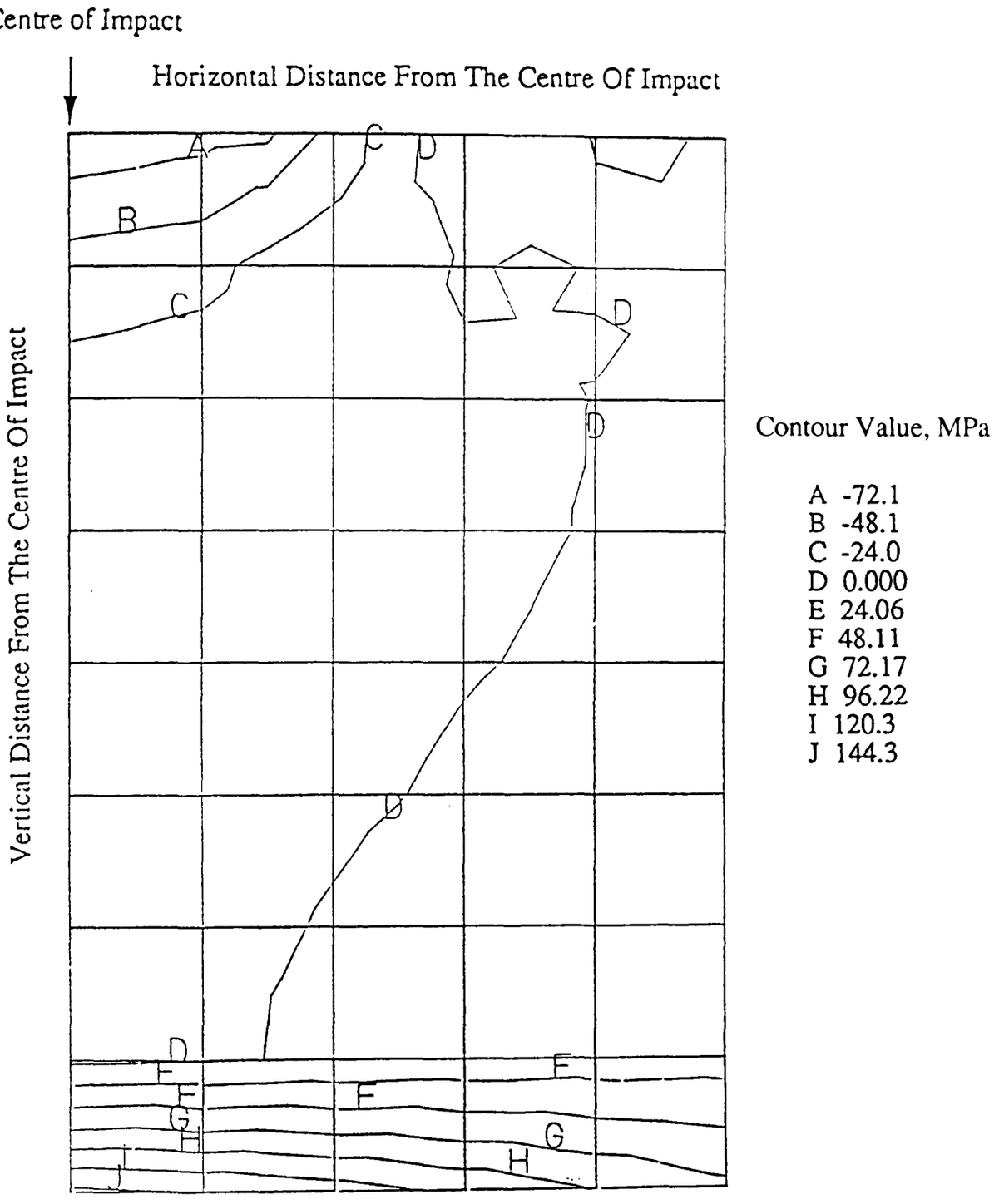

Figure 5.40 - contour of principal stress for 4 mm SMC with a layer of 0.6 mm stainless steel.

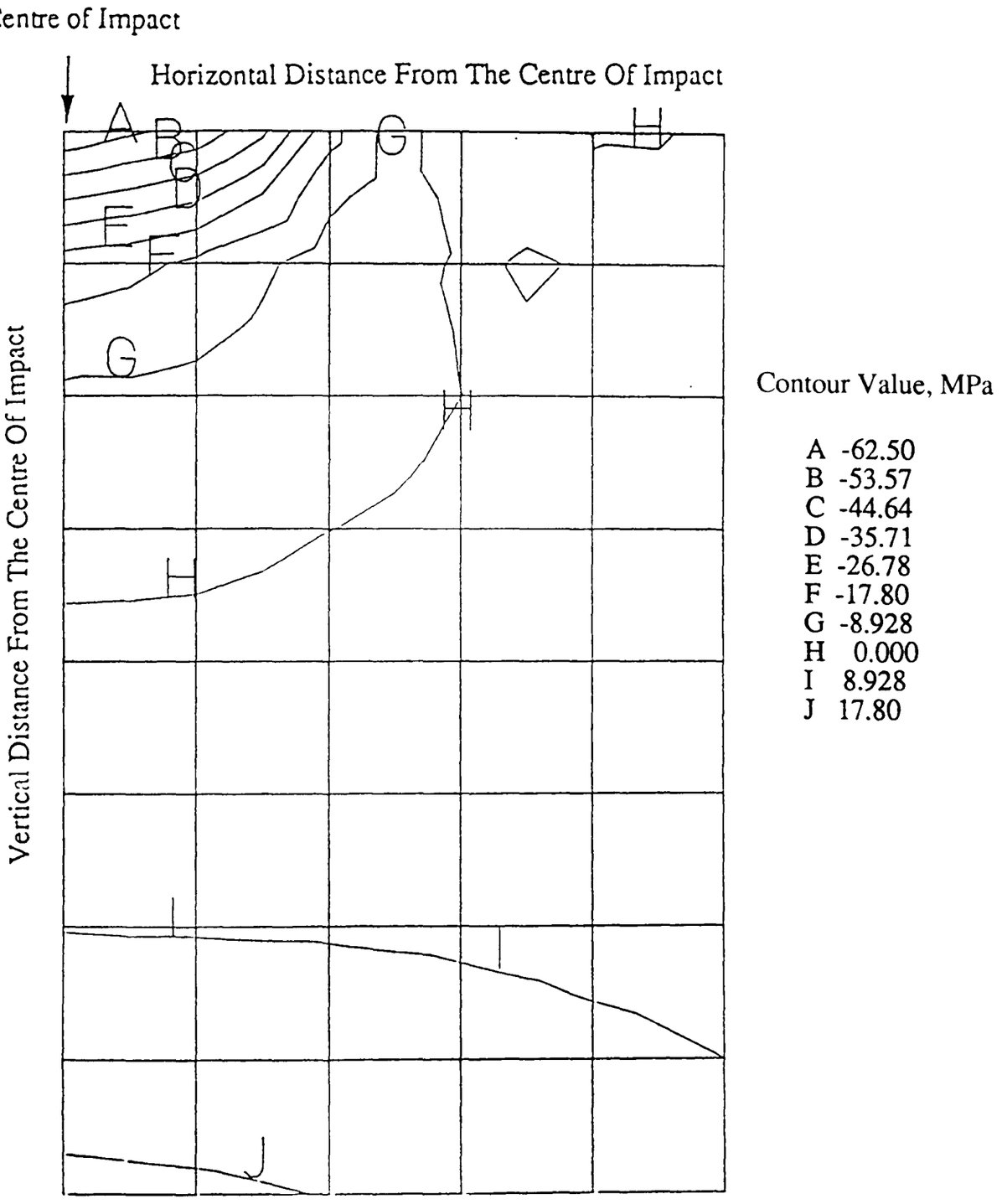

Figure 5.41 - contour of principal stress for 4 mm SMC.

When contours of stress for SMC-stainless steel laminate are studied in figure 5.40, the contour which has zero value (contour D) lies at the interface of stainless steel SMC layers. Therefore in this case the whole SMC layer has stress contours of negative sign and is in compression and the stainless steel layer is completely in tension.

In situations where the stiffness of the steel layer greatly exceeds that of the SMC layer (SMC'), the energy absorbing capability of SMC' is a function of its thickness irrespective of the thickness of the steel (figure 5.42). Where the relative thickness of the two constituents are such that the stiffness of the SMC' approaches that of the steel (as in the case of 6 mm thick SMC with 0.6 mm steel) then the energy absorbing capabilities decrease. This is due to the fact that the neutral axis is not at the interface of the SMC steel layer anymore and is placed within the SMC layer. Figure 5.43 shows stress contours for 6 mm SMC with a layer of 0.6 mm stainless steel. Contour I which has zero value is located within the SMC layer and consequently the whole thickness of SMC is not in compression. Therefore 0.6 mm thick stainless steel has greater effect on 4 mm SMC than 6 mm SMC. Cross sections of the SMC stainless steel laminates in figure 5.39 showed that 4 mm SMC impacted on its own, exhibit crack initiation from the tensile surface (surface opposite to the impact surface) whereas for the SMC layer in an SMC-stainless steel laminate the sub surface cracks in the form of delamination and matrix cracks are formed first. This is probably due to the high compressive stress at both surfaces of SMC'. When SMC stainless steel laminates were impacted from the stainless steel side the energy absorbed by the system was simply the sum of maximum energy absorption of the individual constituents when tested in isolation (fig. 5.42). Therefore the position of the applied load on the laminate is as important as its stiffness. If the stiffness of SMC is increased by a layer of steel, but the application of the load is such that the SMC is in tension, then it will increase the amount of energy absorbed by SMC. The other factors which should be taken into account will be discussed in chapter 6.

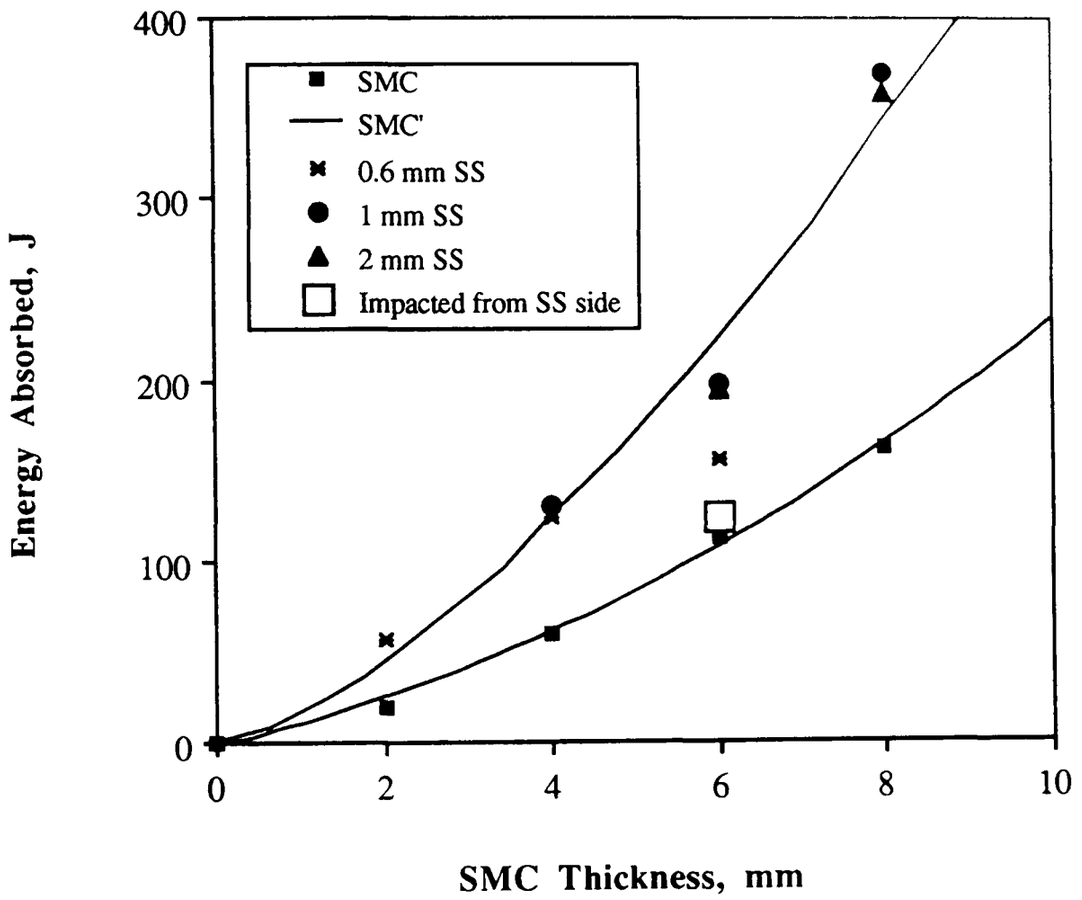

Figure 5.42 - Maximum energy absorbed as a function of thickness for SMC and SMC as a layer in macrocomposite (SMC') for all thicknesses of steel tested from 0.6 mm to 2 mm.

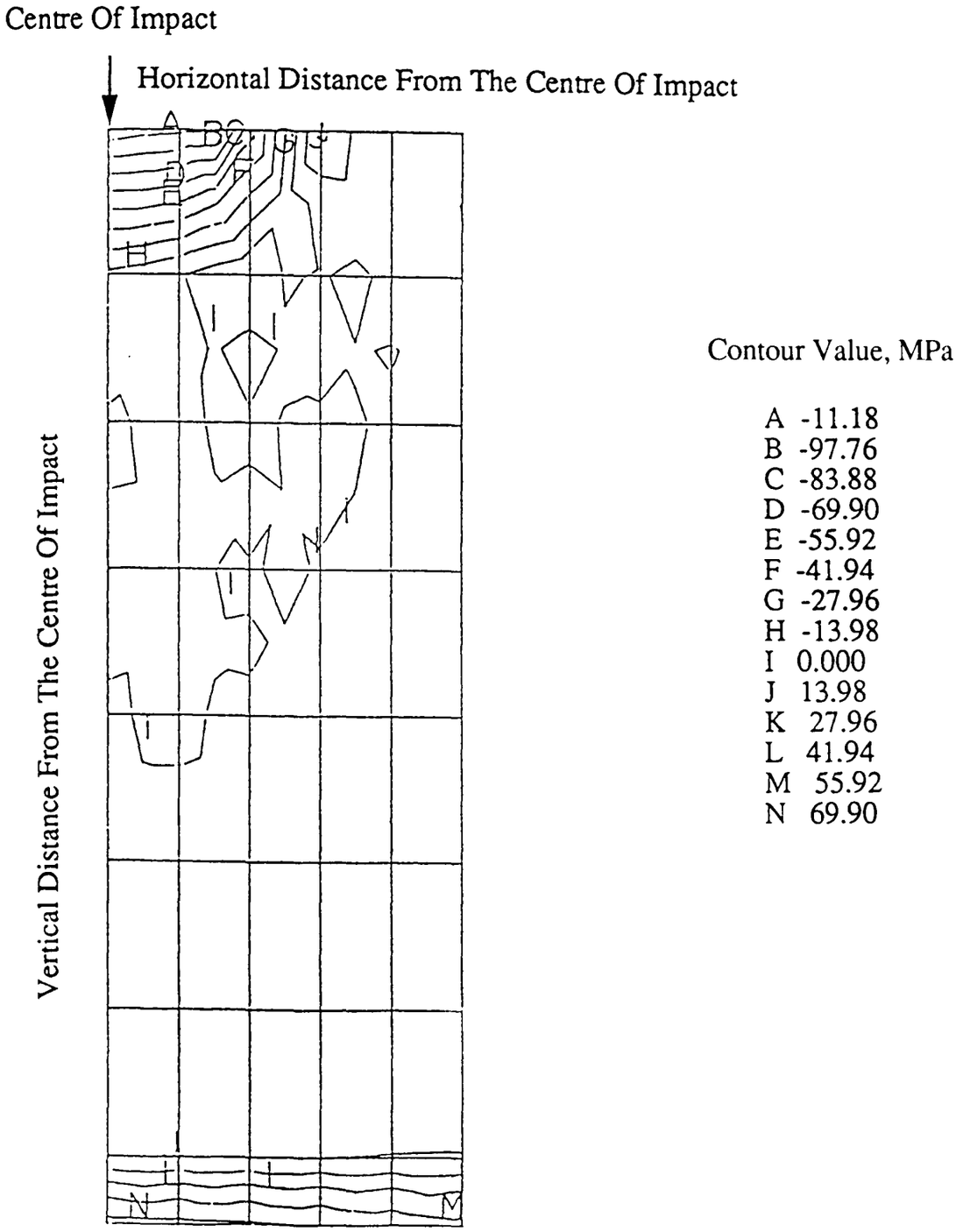

Figure 5.43 - Contour of stress for 6 mm SMC with a layer of 0.6 mm stainless steel.

4 -11 Conclusions

1 - The addition of a steel layer to the SMC to form a macrocomposite substantially increases the energy absorbing capacity of the laminate.

2 - The SMC layer within the macrocomposite absorbs considerably more energy than is possible in a comparable sheet of SMC tested in isolation.

3 - The stainless steel should be thick enough to shift the neutral axes towards the interface of the SMC-stainless steel and put SMC layer in compression.

4 - Finite element analysis can be used to calculate the position of the neutral axes and predict the effect of stainless steel layer.

Chapter 6

Response of SMC with a layer of Aluminium, SMC with a layer of Ionomer, SMC with a layer of Copper and SMC with a layer of Brass to drop weight impact.

In chapter 5 the impact behaviour of SMC with a layer of stainless steel was studied. Experimental results showed that the SMC layer in SMC-stainless steel laminate absorbs more energy than SMC of a similar thickness can when tested in isolation. This "macrocomposite" effect was linked to the action of the stiff steel layer which effectively puts the SMC into compression at least at the beginning of the impact event. In order to obtain further information regarding the importance of stiffness and ductility of the supporting layer of the macrocomposite a range of alternative macrocomposites were constructed. In the first stage of the impact programme laminates of SMC (4 mm thick) were prepared with an aluminium sheet (0.6 mm thick) of grade 5L16 which is almost a pure aluminium. The SMC aluminium (5L16) laminates were subjected to impact at different incident energies and examined in much the same way as for SMC stainless steel laminates. In the second stage laminates of 4 mm thick SMC with an aluminium sheet (0.6 mm thick) of grade L156, which is an aerospace alloy and a tougher and significantly stiffer material than 5L16, were prepared and subjected to impact at incident energy which was greater than the energy required for perforation of this laminate. In the third stage laminates of 4 mm thick SMC with a layer of Ionomer (4 mm thick) were constructed. Ionomer is much tougher and has much higher strain at failure (per cent of elongation is 400 in comparison to 3% for aluminium 5L16) than the two grades of aluminium that were used. The SMC-Ionomer laminates were subjected to impact at incident energies higher than the energy required for perforation. In the final stage the response of SMC with a layer of copper and SMC with a layer of brass was studied. The

SMC+copper and SMC+brass laminates were subjected to impact at incident energies higher than the energy required for perforation.

All testing on the laminates produced with SMC and different (non stainless steel) substrates, was undertaken using the CEAST impact machine. An overall comparison of the different materials was achieved by selecting a single impact energy (155 J) at a velocity of 4 ms^{-1} All impact tests in this series were performed with the SMC surface of the laminate acting as the impacted face and the specimens were lightly clamped to keep the condition of impact the same as SMC+stainless steel laminates.

6 -1 Response of SMC+Aluminium (grade 5L16) to drop weight impact.

Drop weight impact tests were carried out at 1, 2, 3 and 4 ms^{-1} on 2, 4 and 6 mm SMC with a layer of aluminium (0.6 mm thick) of grade 5L16. The composition and mechanical properties of this type of aluminium are shown in table 3.2.

Typical force-time and energy-time curves for unpenetrated and penetrated specimens are shown in figures 6.1 and 6.2. The general shape of the force-time curve for SMC+aluminium specimens was similar to that of SMC-stainless steel laminates. The force increased linearly up to a transition point, followed by a curve of lower slope before a maximum is reached (fig. 6.1). The general shape of the energy - time curve was also similar to that of SMC stainless steel laminates. For the unpenetrated SMC - aluminium specimens energy rose steadily to a peak value that corresponds to the kinetic energy of the striker (incident energy) immediately prior to impact. After this point specimens exhibit a degree of elastic recovery and the energy absorbed falls somewhat, levelling out a value equal to the total energy absorbed by the system during the impact event (fig. 6.1b). For perforated SMC aluminium laminates energy rose steadily until reaching a plateau corresponding the total energy absorbed by the laminate. The energy time curve for 4 mm SMC aluminium specimen which has been subjected to incident energy of 87

joules is shown in figure 6.2b. The energy absorbed by the laminate increased with time until reaching a plateau of magnitude 55 joules corresponding to total penetration of the specimen. Comparison between the load deflection of SMC aluminium laminates at different impact velocities showed that the transition load (P_i) did not change with increasing impact velocity which is an indication of the rate insensitivity of the laminate (fig. 6.3). However the maximum load increased with increasing impact velocity up to the perforation point and remained unchanged after this point (fig. 6.4).

6 - 2 Determination of the energy absorbed by the layer of SMC in the SMC - Aluminium (5L16) specimens.

The energy absorbed by SMC-aluminium specimens on impact is the sum of the energy absorbed by the layer of aluminium sheet and that absorbed by SMC. The profile of the aluminium sheet, when subjected to indentation and impact was exactly analogous to that in the aluminium when it is a component part of the macrocomposite. Therefore the energy absorbed by the layer of aluminium was determined in much the same way as for stainless steel sheet. Aluminium sheet was progressively loaded and unloaded to an increasing level and work done in producing a given permanent deflection in the aluminium sheet was obtained from the unloading curves, figure 6.5. By measuring the area under the curves, a calibration curve was produced, figure 6.6. The method of testing has been fully described in chapter 5. It was then straight forward to determine the work done in deforming the aluminium component of the laminate during impact by simply measuring the permanent deflection (dome height) of the aluminium and reading the relevant value from figure 6.6.

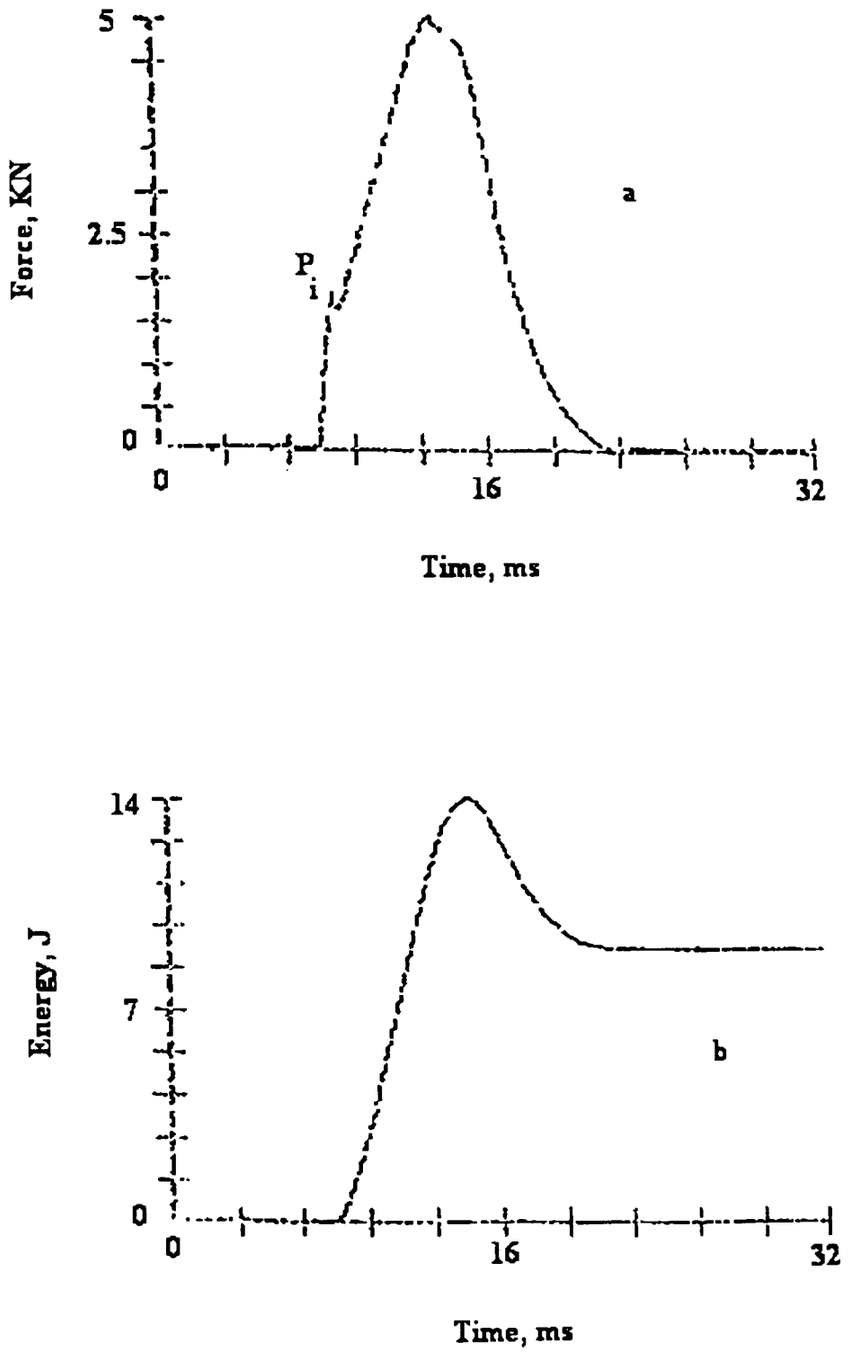

Figure 6.1 - Typical non-penetrating impact force-time and energy time curves for 4 mm SMC-Aluminium (grade 5L16) at 1 ms^{-1} a) force-time b) energy-time

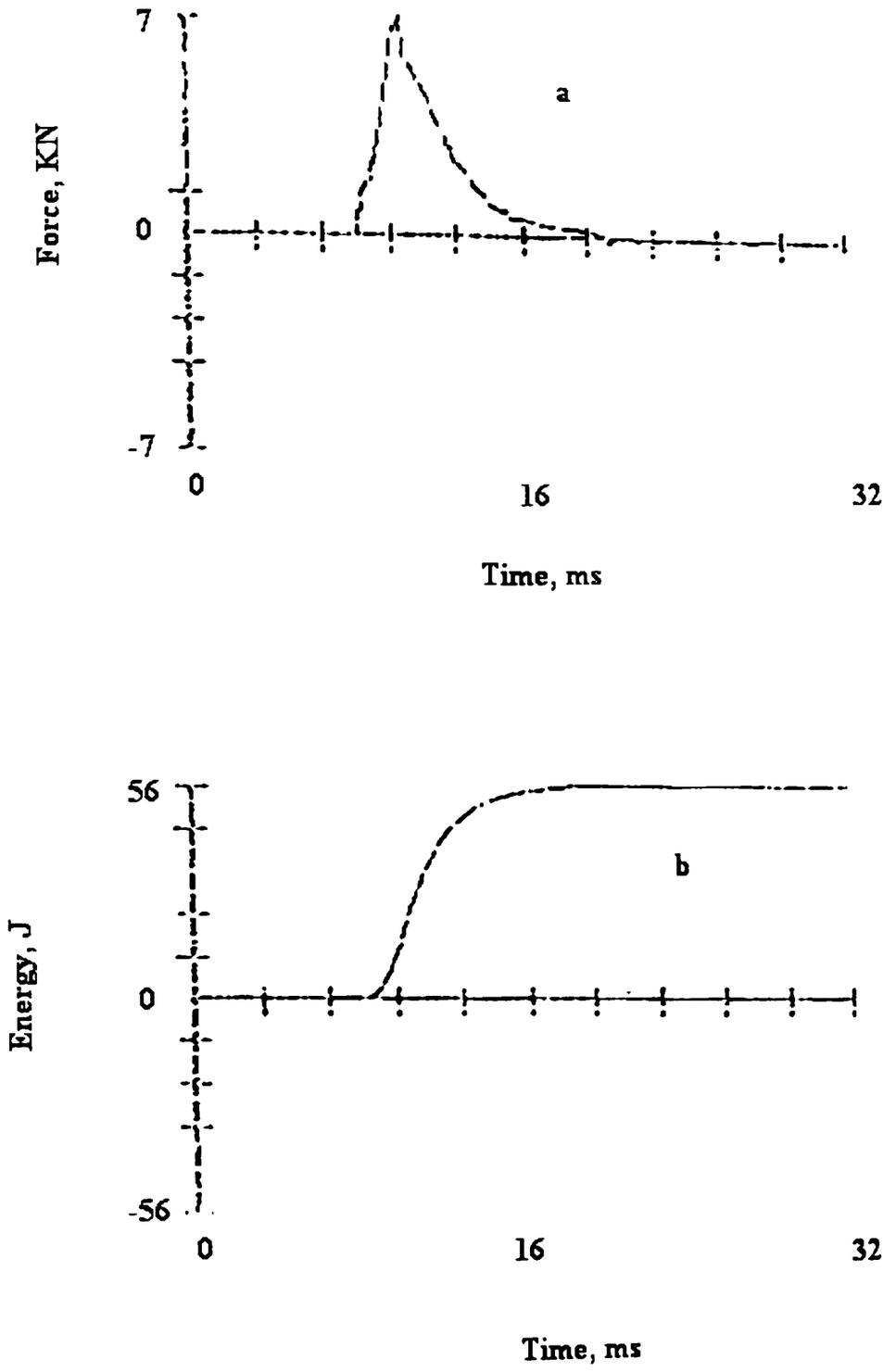

Figure 6.2 - Typical complete penetration force-time and energy time curves for 4 mm SMC-Aluminium (grade 5L16) at 3 ms^{-1} a) force-time b) energy-time

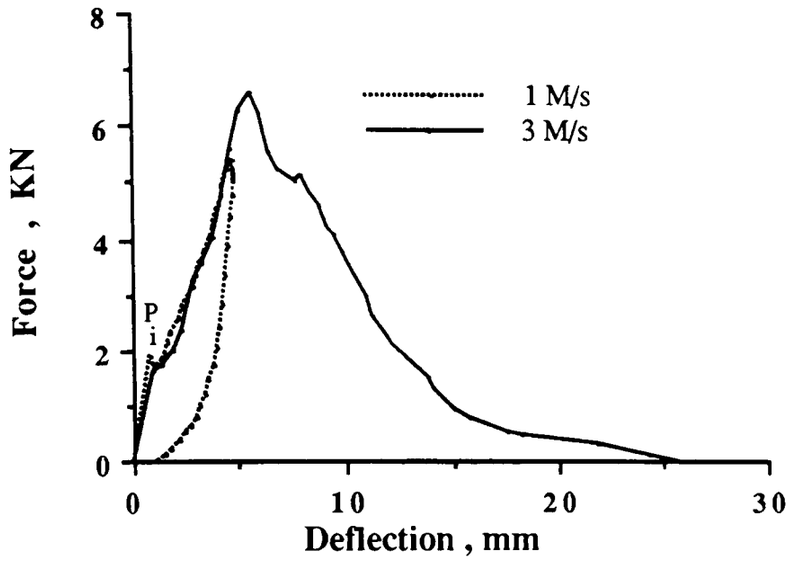

Figure 6.3 - Force-deflection curves for SMC-aluminium (grade 5L16) at 1 ms^{-1} and 3 ms^{-1}.

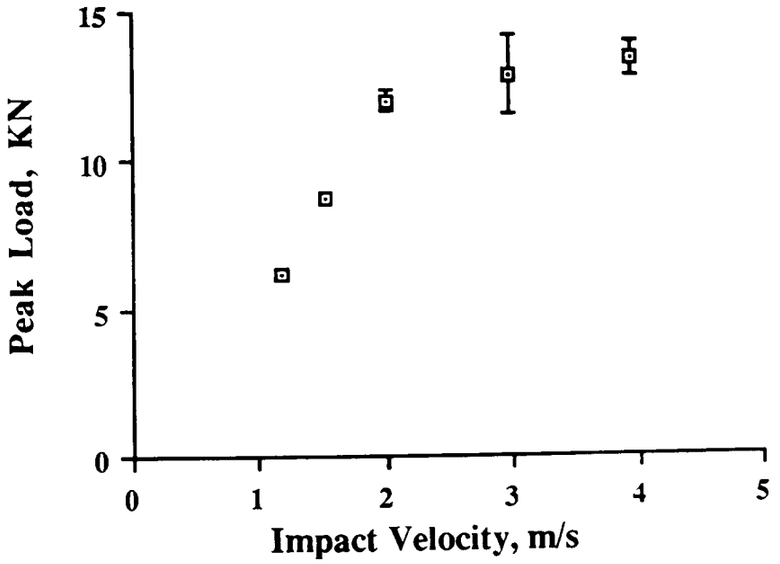

Figure 6.4 - Relation between maximum force generated during impact as a function of impact velocity for 6.6 mm SMC-aluminium (grade 5L16). Error bar denotes standard deviation.

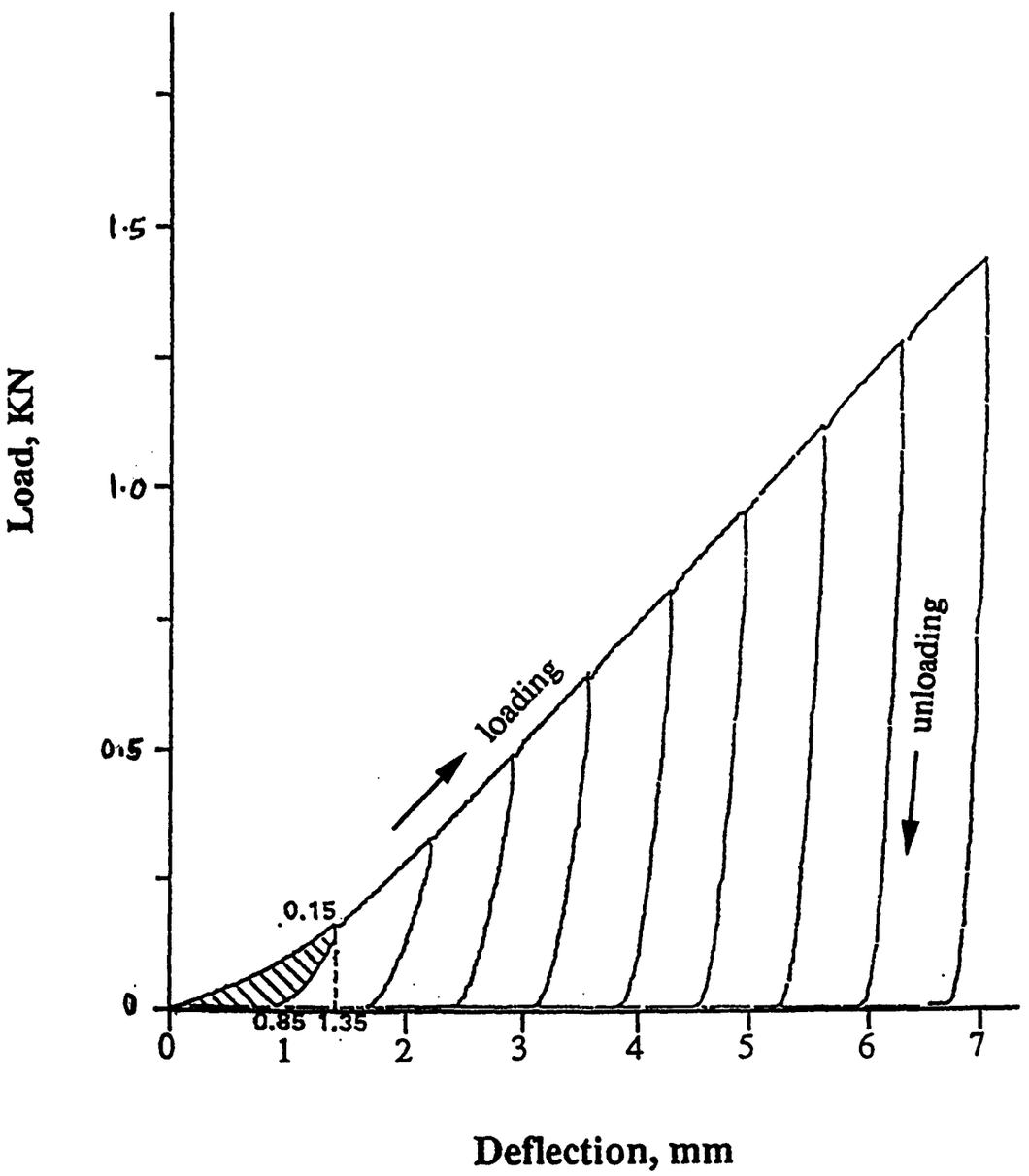

Figure 6.5 - Force deflection curve for aluminium sheet (grade 5L16) used to construct the calibration curve.

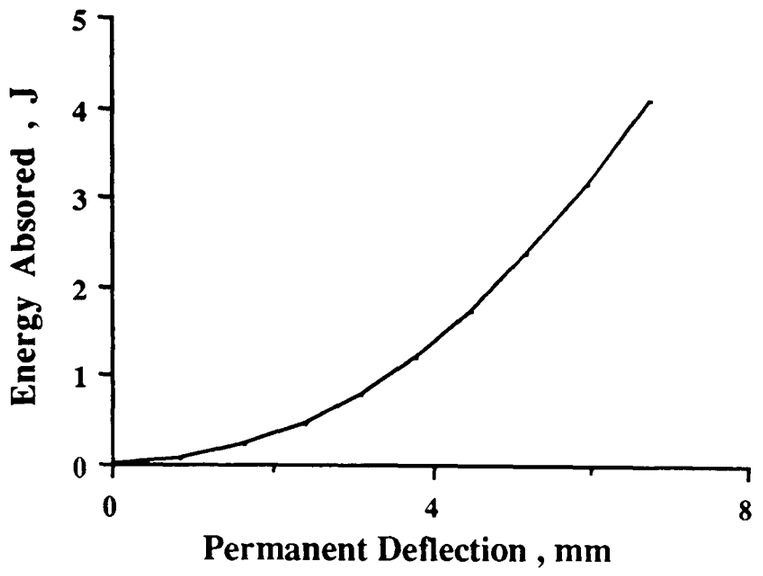

Figure 6.6 - Energy absorbed by 0.6 mm aluminium sheet as a function of permanent deflection.

For perforated SMC-aluminium laminates, the deflection just before the crack initiation in the layer of aluminium is equivalent to the deflection at maximum force on the force-deflection curve. Deflection at which the layer of aluminium as a part of SMC+aluminium laminate fractures is smaller than that of aluminium sheet. Therefore after impact the deflection at maximum force on the force-deflection curve was measured and the energy absorbed was determined from the calibration curve (figure 6.6). Since the crack propagates and develops some flaps during impact, the energy for this stage is added to the value which has already been read out from the calibration curve. The energy required for initiation of crack in the aluminium sheet and propagation of this crack to form flaps was calculated from the force-deflection curve on the aluminium sheet (figure 6.7).

Close examination of the force-deflection curve of aluminium sheet (figure 6.7) showed that after maximum force the load drops sharply to point A and then the load decreased at

much lower rate to point B. AB is the stage at which the flaps are formed and the energy required for initiation of crack and formation of the flaps is the dashed area in figure 6.7.

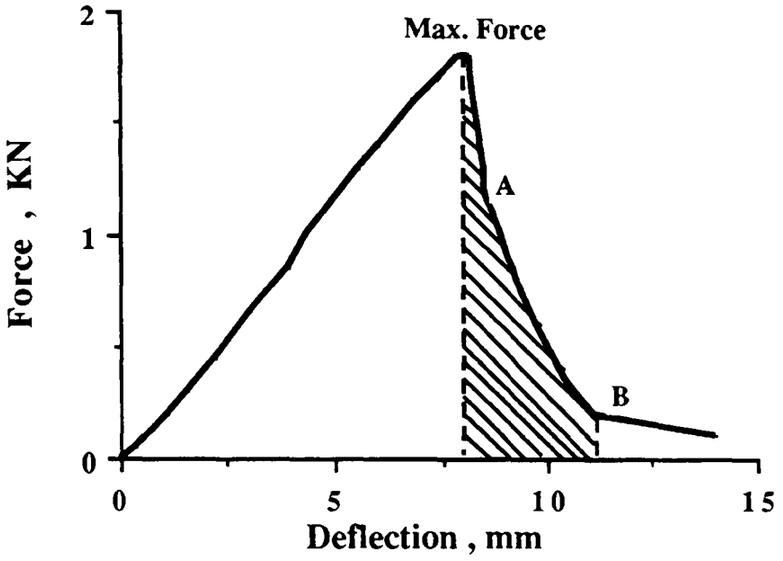

Figure 6.7 - Force deflection curve for 0.6 mm thick Aluminium (grade 5L16) after complete penetration.

Once the energy absorbed by the aluminium was known, the energy by the SMC could be calculated by simply subtracting the energy absorbed by aluminium from the total energy absorbed by SMC-aluminium laminate.

The results of this exercise showed that the amount of energy absorbed by the SMC-aluminium laminate depends on the thickness of SMC layer. For 2 mm thick SMC with a layer of 0.6 mm thick aluminium, the energy absorbed by SMC in the laminate was higher than the energy absorbed by 2 mm SMC when impacted on its own (fig. 6.8). When the thickness of SMC layer was increased to 4 mm the energy absorbed by the SMC in the laminate was the same as the energy absorbed by 4 mm SMC when impacted on its own (fig. 6.9). The results for 6 mm SMC in the SMC-aluminium laminate showed the same trend as 4 mm SMC in the SMC-aluminium laminate (fig. 6.10).

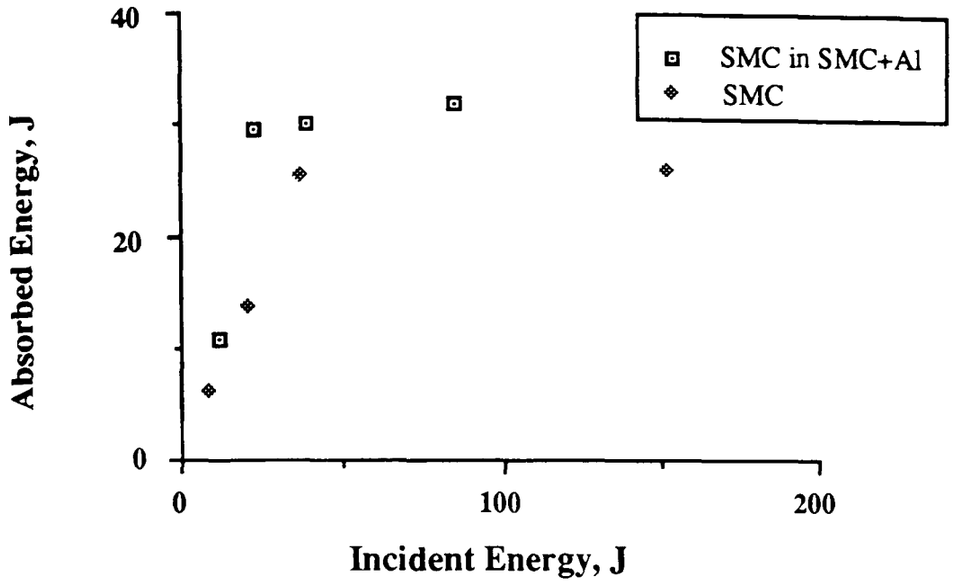

Figure 6.8 - The amount of energy absorbed as a function of incident energy for 2 mm SMC in SMC+aluminium (grade 5L16) and 2 mm SMC specimen.

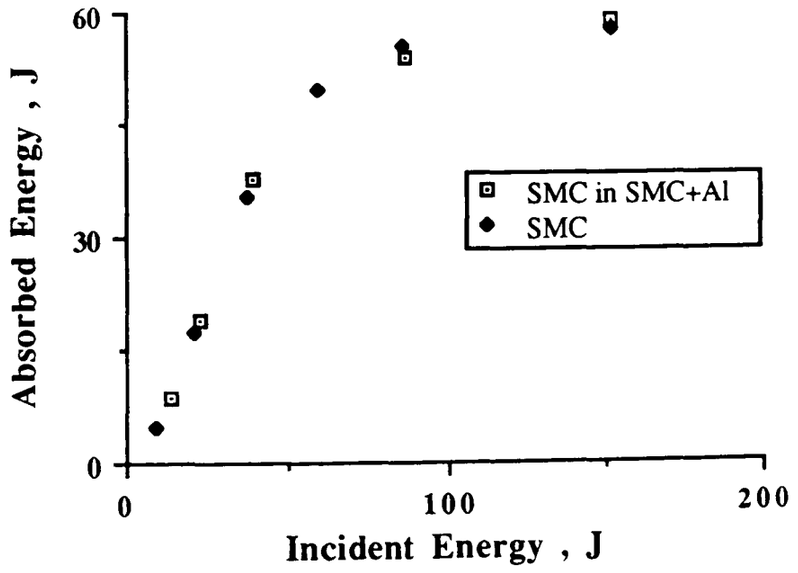

Figure 6.9 - Energy absorbed as a function of incident energy for 4 mm SMC in SMC+aluminium (grade 5L16) and 4 mm SMC.

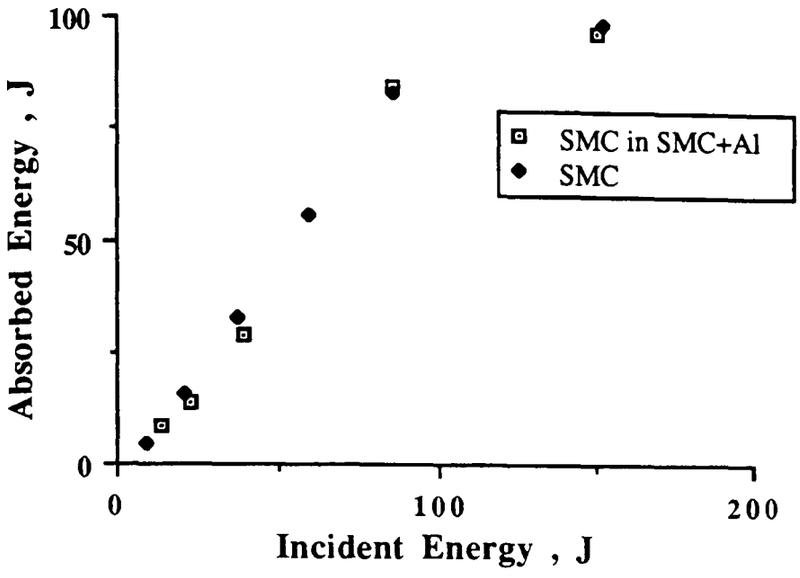

Figure 6.10 - Energy absorbed as a function of incident energy for 6 mm SMC in SMC+aluminium (grade 5L16) and 6 mm SMC specimen.

6 - 3 Response of SMC+Aluminium (grade L156) to drop weight impact

Laminates of 4 mm SMC with an aluminium sheet (0.6 mm thick) of grade L156 were constructed and subjected to 4 ms^{-1} impact velocity which produced incident energy about 155 joules. This incident energy resulted in complete penetration of the laminate. The composition and mechanical properties of aluminium grade L156 which is an aerospace alloy is shown in table 3.2.

Analysis of the energy absorbed by the layer of aluminium and SMC was similar to that of SMC-aluminium of grade 5L16 which has been fully described in section 6-2. After impact the deflection at maximum force on the force deflection curve was measured and the energy absorbed was determined from the calibration curve (fig. 6.11). The energy for formation of flaps was measured from the relevant force deflection (fig. 6.12) and added to the value obtained from the calibration curve.

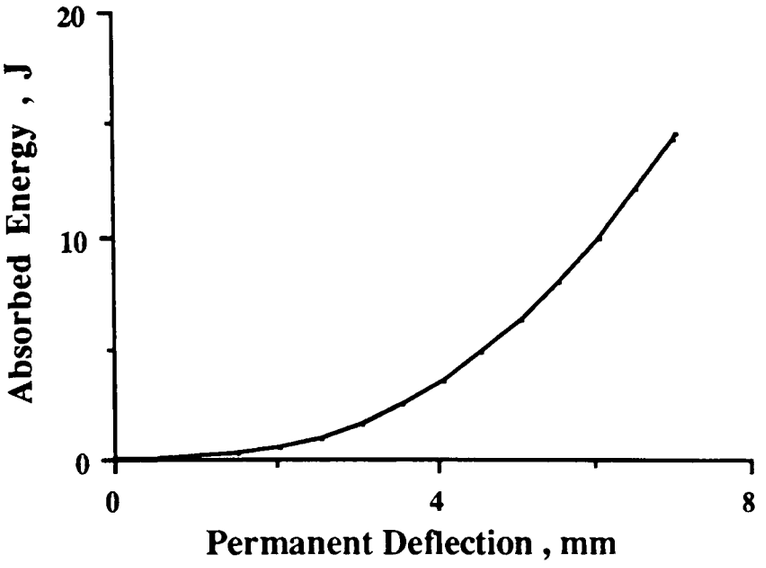

Figure 6.11 - Energy absorbed by 0.6 mm aluminium sheet (grade L156) as a function of permanent deflection.

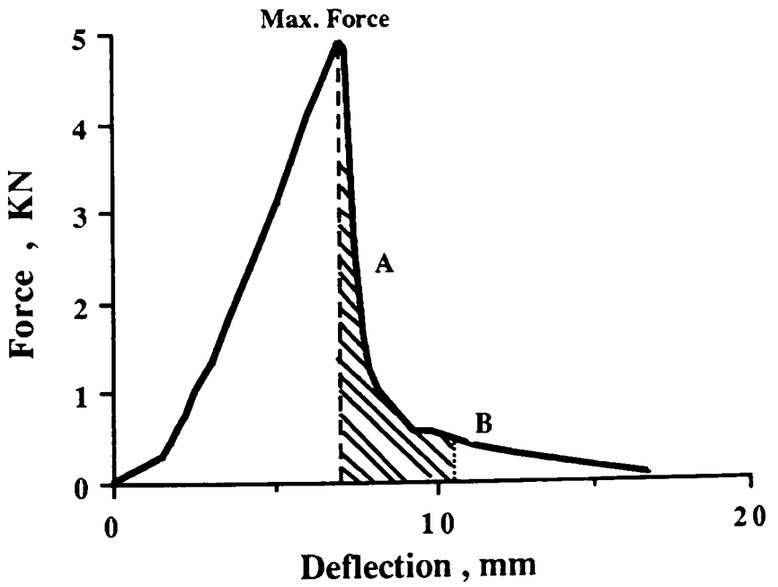

Figure 6.12 - Force deflection curve for 0.6 mm thick aluminium (grade L156) after complete penetration.

Once the energy absorbed by the aluminium was known, the energy absorbed by the SMC could be calculated by simply subtracting the energy absorbed by aluminium from the total energy absorbed by SMC-aluminium laminate.

Analysis of the energy absorbed by the layer of SMC and aluminium showed that 4 mm SMC in SMC-aluminium laminate absorbs slightly more energy than 4 mm SMC can when tested in isolation (fig. 6.13).

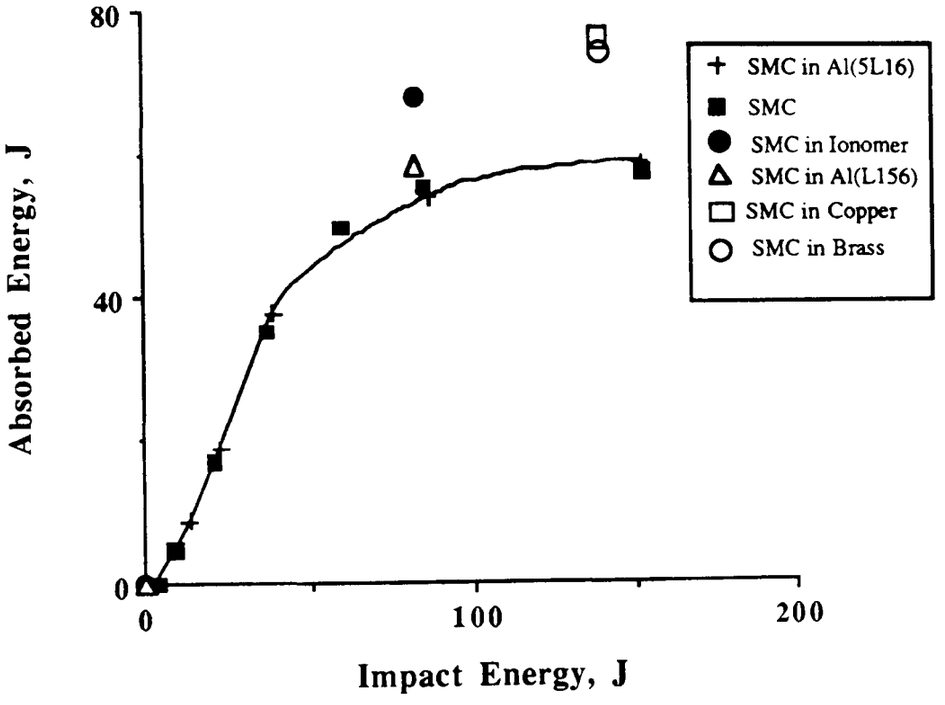

Figure 6.13 - Absorbed energy vs impact energy for SMC in a range of alternative macrocomposite systems based on 4 mm thick SMC.

6 - 4 Response of SMC + Ionomer to drop weight impact

Laminates of 4 mm thick SMC with a layer of 4 mm thick Ionomer were prepared. These differ from the SMC-aluminium laminates where the SMC had been directly cast on the aluminium sheet. In this case there was no bonding between two layers and 4 mm thick SMC was simply rested on 4 mm thick Ionomer and the laminate lightly clamped during

an impact test. The laminate was subjected to 4 ms^{-1} impact velocity (incident energy 155 joules). This incident energy resulted in complete penetration of the laminate.

Analysis of energy absorbed by the layer of Ionomer and SMC was similar to that of SMC-aluminium laminates with an exception that due to the rate sensitivity of Ionomer, a calibration curve was not obtained by slow test. A calibration curve was instead constructed by carrying a series of impact test on 4 mm thick Ionomer at different incident energies. After impact the deflection at maximum force on the force deflection curve was measured and the energy absorbed was determined from the calibration curve (fig. 6.14). As for the case of SMC-aluminium laminate some energy was absorbed for formation of flaps after crack initiation at maximum load. This energy which is about 6.2 joules is added to the value obtained from the calibration curve. The method of calculation of this value was similar to that of aluminium sheets. Force-deflection curve for the perforated specimen for 4 mm Ionomer is shown in figure 6.15.

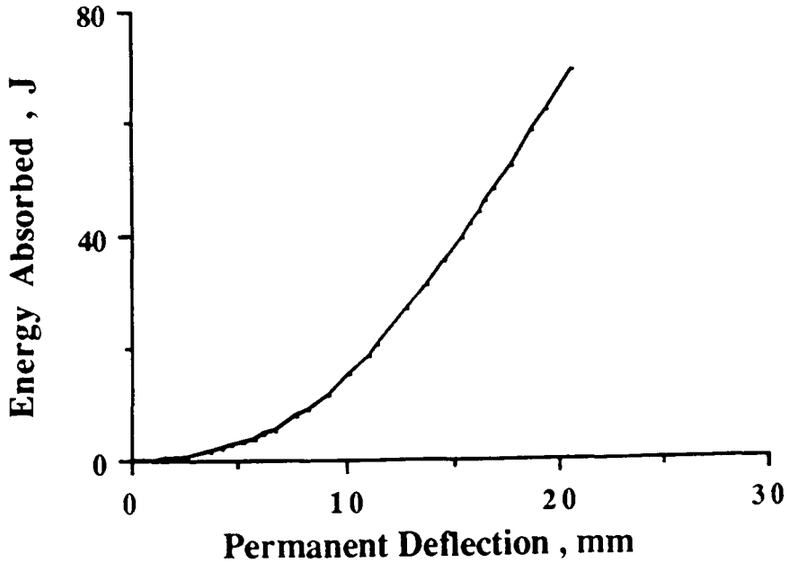

Figure 6.14 - Energy absorbed by 4 mm thick Ionomer as a function of permanent deflection.

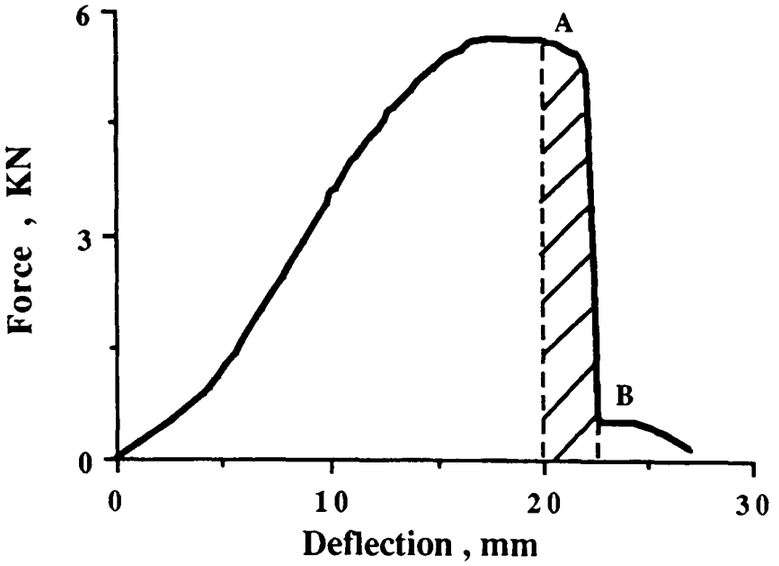

Figure 6.15 - Force deflection curve for 4 mm Ionomer after complete penetration by impact.

The results of this exercise showed that the amount of energy absorbed by 4 mm thick SMC in an SMC-Ionomer laminate was about 70 joules compared to 55 joules for SMC from the same batch tested in isolation.

6 - 5 Response of SMC+copper to drop weight impact

Laminates of 4 mm SMC with a layer of 0.75 mm thick copper were constructed and subjected to 4 ms^{-1} impact velocity which produced incident energy about 155 joules. This incident energy resulted in complete penetration of the laminate.

Analysis of the energy absorbed by the layer of copper and SMC was similar to that of SMC-aluminium of grade 5L16 which has been fully described in previous sections. After impact the deflection at maximum force on the force deflection curve was measured and the energy absorbed was determined from the calibration curve (fig. 6.16). The

energy for formation of flaps was measured from the relevant force deflection (fig. 6.17) and added to the value obtained from the calibration curve.

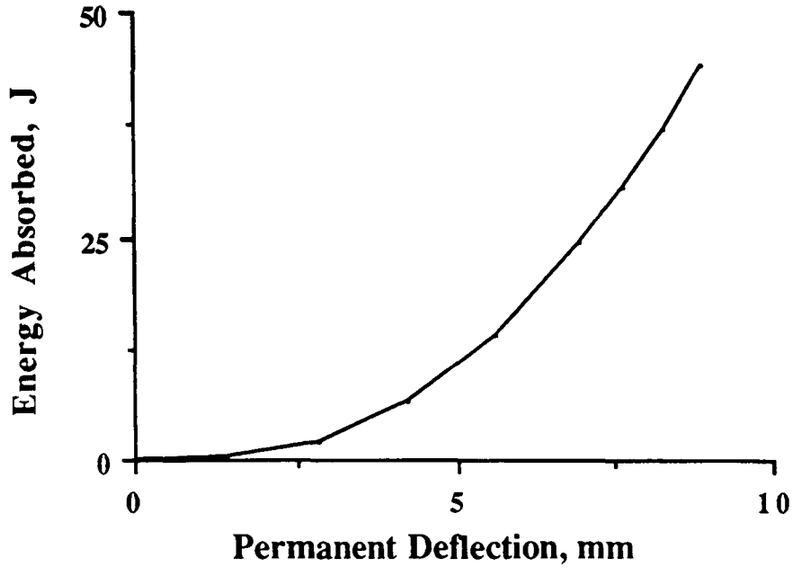

Figure 6.16 - Energy absorbed by 0.75 mm copper sheet as a function of permanent deflection.

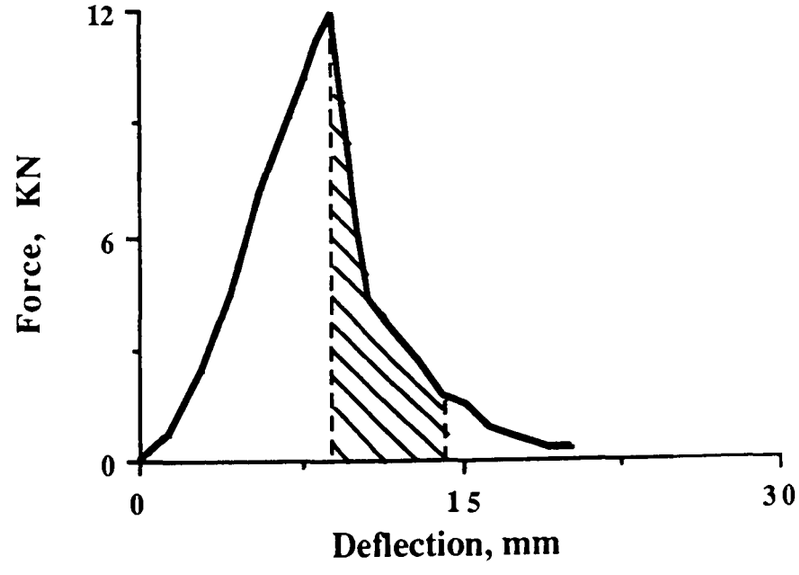

Figure 6.17 - Force deflection curve for 0.75 mm thick copper after complete penetration.

Once the energy absorbed by the copper was known, the energy by the SMC could be calculated by simply subtracting the energy absorbed by copper from the total energy absorbed by SMC-copper laminate.

Analysis of the energy absorbed by the layer of SMC and copper showed that 4 mm SMC in SMC-copper laminate absorbs about 79 joules which is about 20 joules more than SMC can when impacted on its own (fig. 6.13).

6 - 6 Response of SMC+Brass to drop weight impact

Laminates of 4 mm thick SMC with a layer of 0.75 mm thick brass were constructed and subjected to impact under the same conditions as SMC+copper which has been described in the previous section. The amount of energy absorbed by the layer of brass was calculated, using the calibration curve in figure 6.18. The amount of energy required for crack initiation and subsequent propagation to form flaps was determined from figure 6.19.

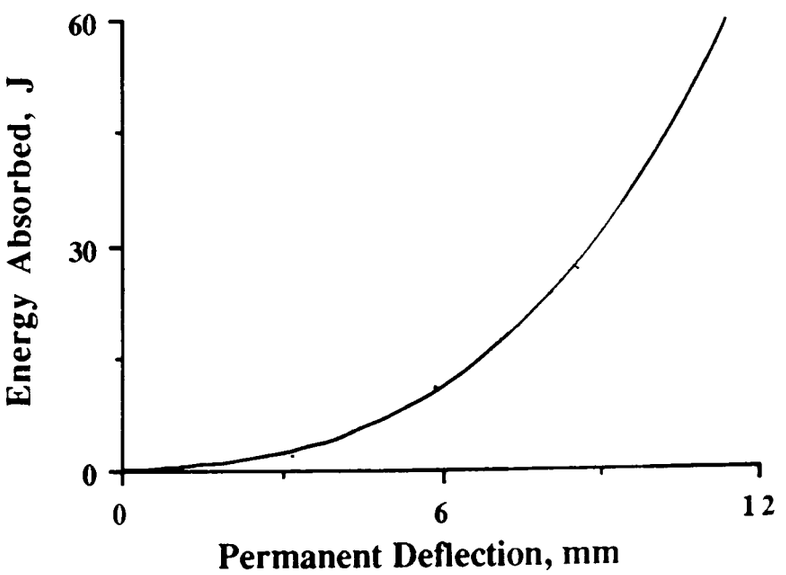

Figure 6.18 - Energy absorbed by 0.75 mm thick brass sheet as a function of permanent deflection.

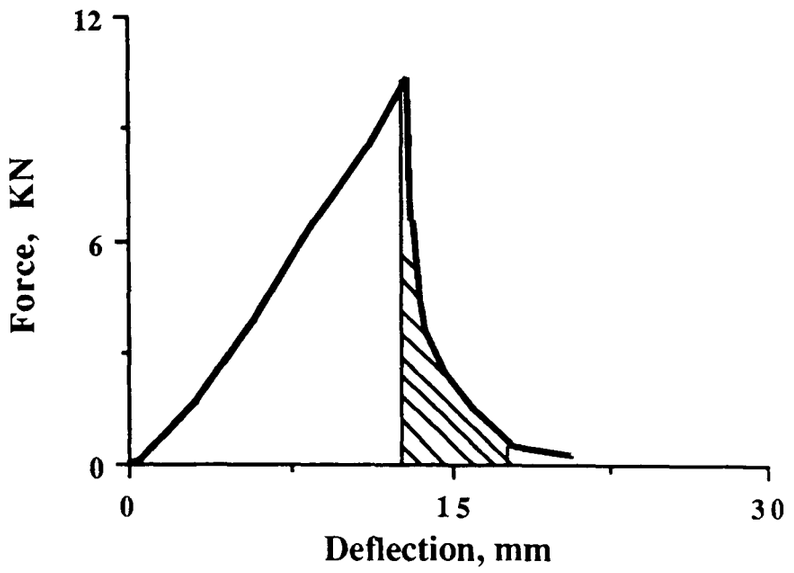

Figure 6.19 - Force deflection curve for 0.75 mm thick brass after complete penetration.

The result of energy analysis showed that the amount of energy absorbed by 4 mm thick SMC in SMC-brass laminate was about 76 joules compared to 55 joules for SMC from the same batch tested in isolation.

6 - 7 Discussion

Experimental results on SMC-aluminium (grade 5L16) showed that 2 mm thick SMC in SMC-aluminium laminate absorbs slightly more energy (fig. 6.8) and the thicker SMC in the laminates absorbed almost the same amount of energy as SMC of the same thickness can when tested in isolation (figures 6.9 and 6.10). Although the aluminium (grade 5L16) has a Young's modulus of 70 GPa which is about 7 times higher than SMC, the improvements in the energy absorption was observed only in the 2 mm thick SMC-aluminium laminate. The results obtained from testing 4 mm thick SMC-aluminium (grade L156) were slightly better than those from the 5L16 but the improvements was in the order of a few percent (fig. 6.13).

In order to explain these observed trends, the stress distribution within the laminate was determined using the finite element techniques which have been fully described in chapters 4 and 5. The result of finite element stress analysis showed that for 2 mm thick SMC-aluminium (grade 5L16) the layer of SMC is in compression and the so called neutral axis is in the interface of the SMC aluminium layers. Contours of stresses in figure 6.20 shows the position of the neutral axis which has been marked with letter D and has zero value. It is clearly seen in figure 6.20 that the contours above contour D have negative sign which is the indication that these areas are under compression and these contours are located in the SMC layer. The finite element results for 4 mm and 6 mm thick SMC -aluminium (grade 5L16) showed that the neutral axis is not at the interface of SMC-aluminium layers and is located within the SMC (fig. 6.21). The position of the neutral axis for 4 mm SMC-aluminium laminate which has been marked by contour I is shown in figure 6.21. As it is seen in figure 6.21 the zero contour is within the SMC layer, therefore the aluminium layer has not effectively put the SMC into compression. In comparison with 4 mm SMC tested in isolation (figure 5.41, chapter 5) the neutral axis has shifted slightly towards the aluminium layer which had very little effect on the impact behaviour of SMC layer. Results obtained from testing 4 mm thick SMC-aluminium (grade L156) were slightly better than those from the 5L16 (fig. 6.13) but the improvements are of the order of a few percent and are not significant given the possibility of batch to batch variations in the SMC itself. Earlier in the discussion it was mentioned that 2 mm thick SMC-aluminium (grade 5L16) showed some improvements in the energy absorbed by the laminate but this was much lower than 2 mm thick SMC with a layer of 0.6 mm stainless steel. The energy absorbed by 2 mm thick SMC in SMC-aluminium (grade 5L16) laminate was 31 joules whereas 2 mm thick SMC

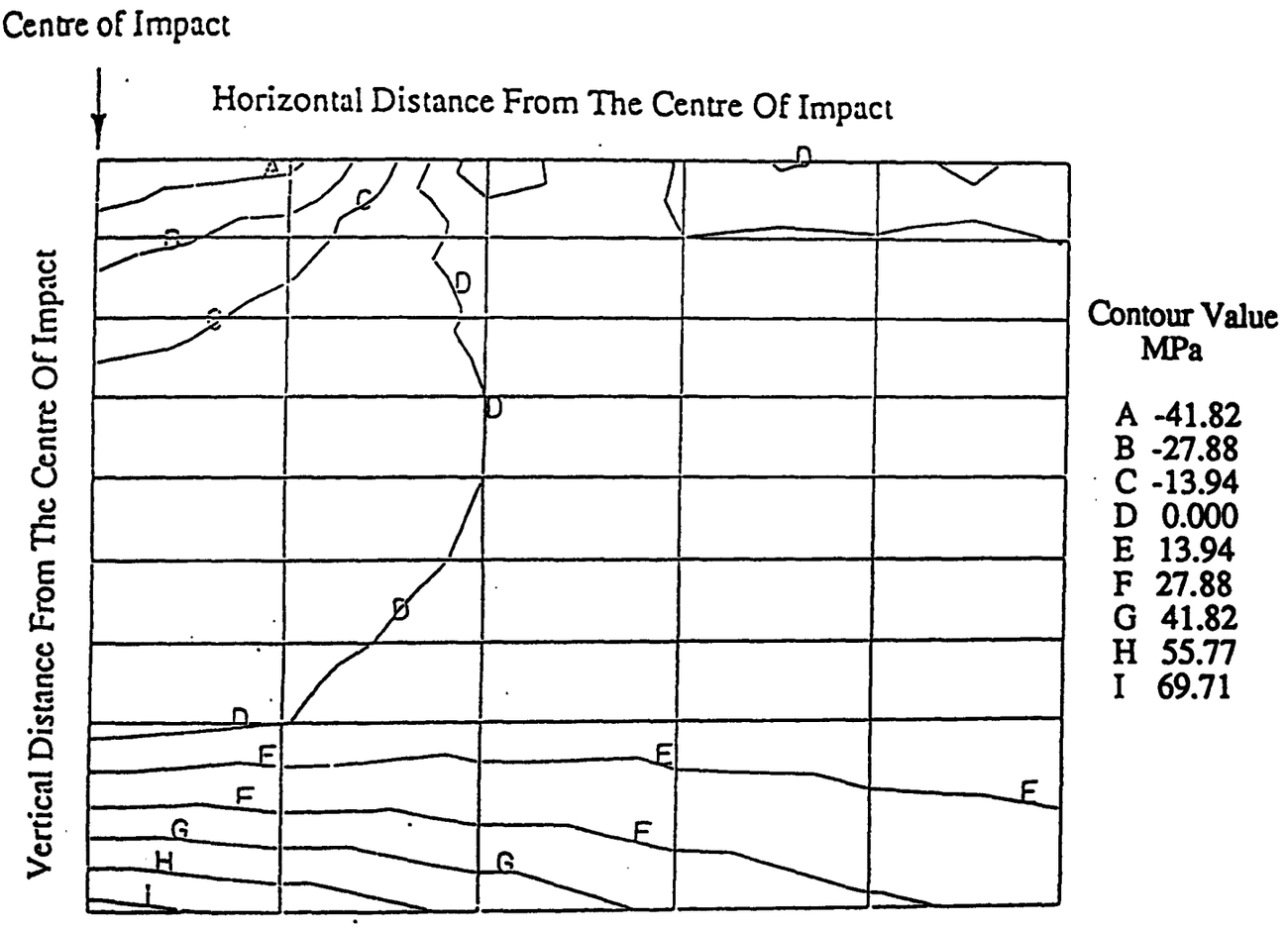

Figure 6.20 - Contour of principal stress for 2 mm SMC with a layer of 0.6 mm aluminium.

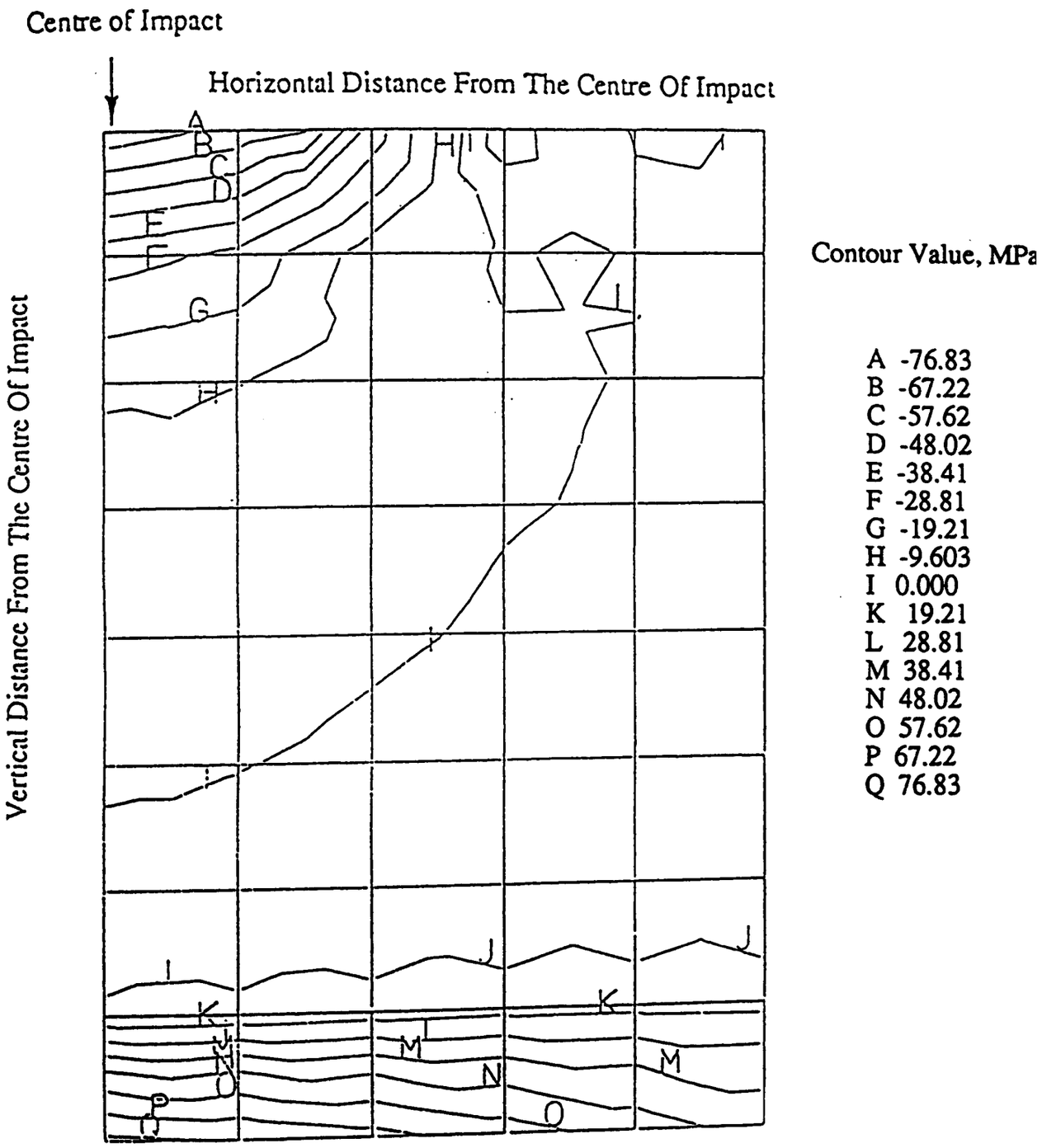

Figure 6.21 - Contour of principal stress for 4 mm SMC with a layer of 0.6 mm aluminium.

as a component part of SMC-stainless steel absorbed 56 joules. The finite element results showed that 2 mm thick SMC in both SMC-aluminium and SMC-stainless steel is in compression, therefore the difference in the amount of energy absorbed must be due to other factors than initially placing the SMC in compression and may be due to the general deformation characteristics of the steel and the two grades of aluminium.

Comparison of the force-deflection curves for 4 mm thick SMC-stainless steel (fig. 5.24, chapter 5), 4 mm thick SMC-aluminium (grade 5L16, fig. 6.22), 4 mm thick SMC-aluminium (grade L156, fig. 6.23) and 4 mm thick SMC (fig. 6.24) showed that the deflection at the peak load for SMC-aluminium laminates are the same as SMC when impacted on its own but these values for SMC-stainless steel laminate is much higher. The deflection at the peak load for 4 mm thick SMC, 4 mm thick SMC-aluminium laminates and 4 mm thick SMC-stainless steel laminates is shown in the following table :

Type of Laminate	SMC	SMC-Al (5L16)	SMC-Al (L156)	SMC-Steel
Max. Deflection, mm	5	6	6	13.5

The values of the deflection at maximum load suggests that the layer of stainless steel can sustain a far greater deflection before fracture than the SMC and both grades of aluminium. The steel therefore supports the SMC layer, to deflections beyond those at which fracture would normally occur. These observations may explain why 2 mm thick SMC in SMC-stainless steel absorbs more energy than the same thickness of SMC in SMC-aluminium laminates, although the SMC layer in both laminates is in compression. The reason is that the deflection at maximum load is quite different. For the case of 2 mm thick SMC-aluminium laminate the deflection is 6 mm whereas for SMC-stainless steel laminate is about 14 mm which supports the layer of SMC over that available in the SMC loaded in isolation.

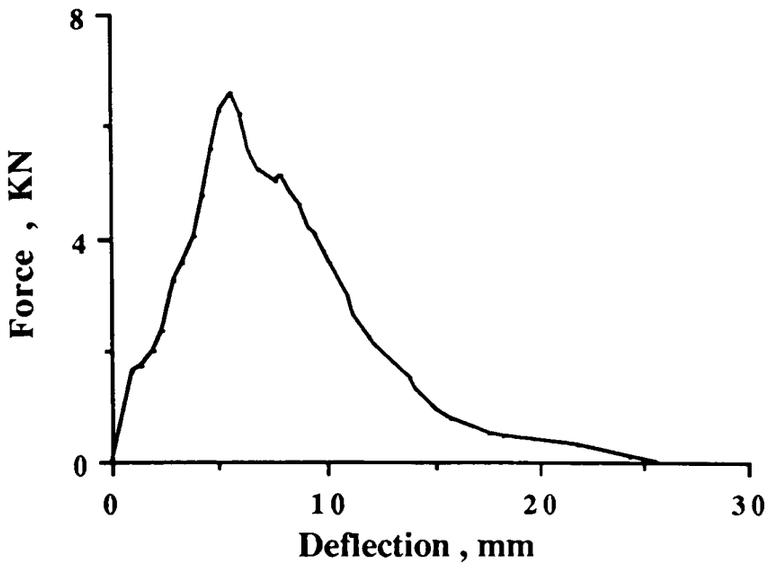

Figure 6.22 - Force deflection curve for 4 mm SMC-aluminium (grade 5L16) after complete penetration.

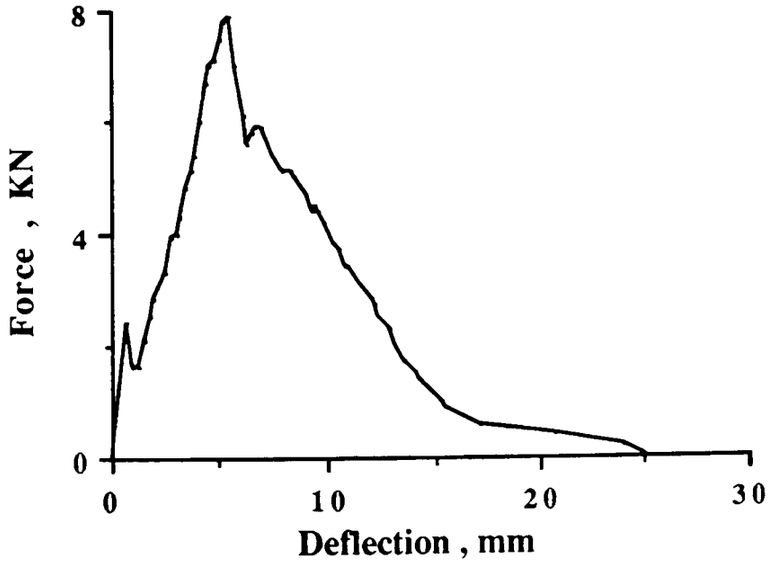

Figure 6.23 - Force deflection curve for 4 mm SMC-aluminium (grade L156) after complete penetration.

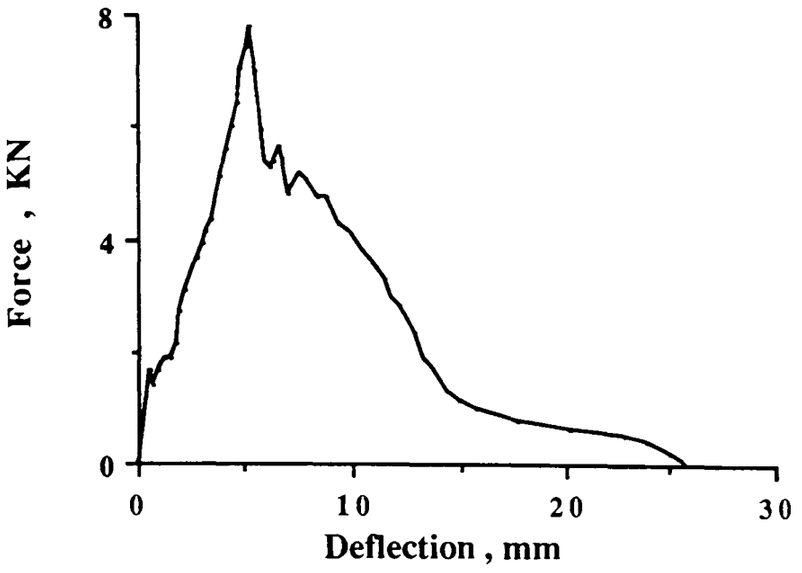

Figure 6.24- Force deflection curve for 4 mm SMC after complete penetration.

The result of SMC-Ionomer laminate showed that the layer of SMC in this laminate absorbs more energy than the same thickness of SMC can in isolation (fig. 6.13). The Ionomer is very tough polymer (deflection at peak load 19 mm, fig. 6.15) with a very low Young's modulus (0.3 GPa), but the comparatively thick layer used, 4 mm, provided a bending stiffness equivalent to that of 0.6 mm aluminium. Results of SMC-copper and SMC-brass laminates showed considerable improvement in the amount of energy absorbed by SMC in these two cases. This improvement may be related to the higher stiffness and higher toughness of these two materials in comparison with two grades of aluminium used. The copper and brass used in this experiment had a Young's modulus of about 140 GPa and 120 GPa respectively and the deflection at peak load were 9.5 mm and 13 mm respectively. Although brass has a lower Young's modulus than copper, the effect on SMC is the same. This is due to higher ductility of brass. These results with the results of Ionomer supports the idea that a combination of stiffness and ductility is necessary for improving the energy absorption capability of the SMC layer. The results also suggests that the substrate layer should be thick enough to give the required stiffness to the laminate and put the layer of SMC in compression. The thickness

of the substrate depends on the thickness of SMC. For example 0.6 mm thick aluminium has enough stiffness to put 2 mm thick SMC in compression, but for 4 mm SMC fails to do so.

Comparison of the results of SMC with a layer of stainless steel (see chapter 5) and the results of SMC with a layer of aluminium, Ionomer, brass and copper is shown in figure 6.25. Although aluminium, Ionomer, brass and copper improve the energy absorption of SMC, but stainless steel, due to its higher stiffness and deflection has more effect on the energy absorption of SMC.

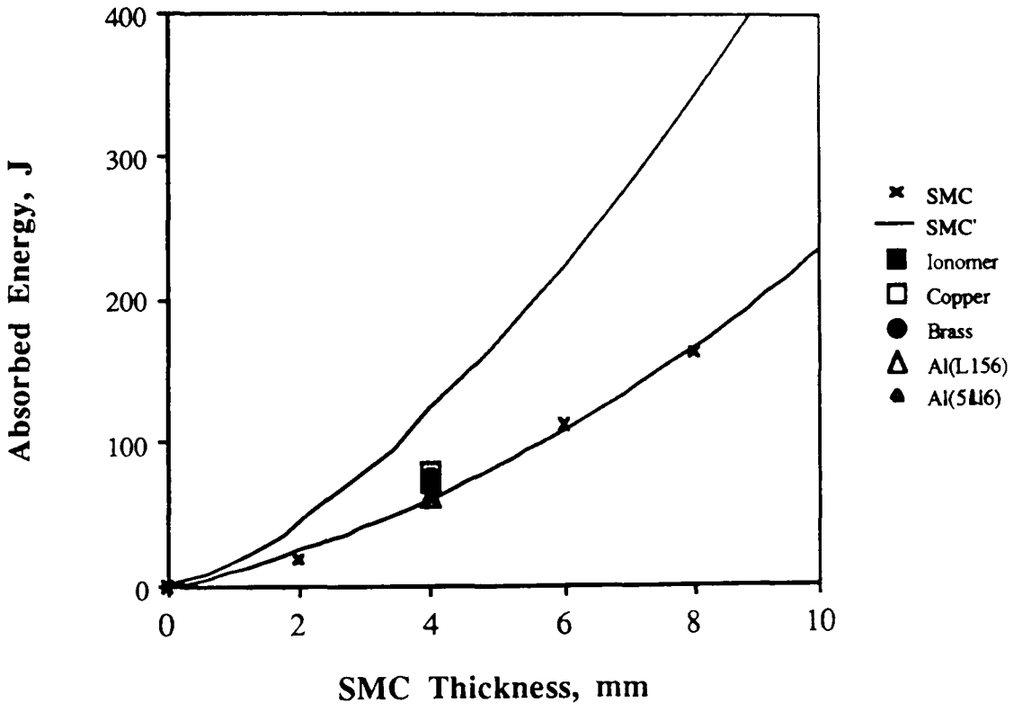

Figure 6.25 - Maximum energy absorbed as a function of thickness for SMC as a layer in macrocomposite (SMC') for all thicknesses of steel tested and aluminium, Ionomer, brass and copper.

6 - 8 Conclusions

When an appropriate backing plate is chosen with SMC to form a macrocomposite, the SMC absorbs considerably more energy. The backing plate would be effective if it satisfy two requirements:

1 - It should be stiff enough in order to place the SMC into compression in the initial stages of deformation.

2 - It should be ductile enough to support SMC over a extensive deformation range such that microcracking may occur over a large area.

Chapter 7

Residual tensile and compressive strength of SMC and SMC-Stainless steel laminates after impact.

Composites, unlike metallic materials, can suffer a severe reduction in compressive and tensile strength after impact. The results of damaged SMC and SMC-stainless steel laminates by impact in chapters 4 and 5 showed that impact loading generates areas of delamination, matrix cracking, fibre pull out and fibre debonding. The damage in the specimen may significantly reduce the residual properties of the material. Indeed, strength reductions of up to fifty per cent have been recorded in composites displaying little or no visible damage (134). A number of studies have been performed on various continuous fibre-reinforced laminated composite systems to determine their impact tolerance or resistance. A review of impact resistance and tolerance of continuous fibre-reinforced composites has been presented by Cantwell and Morton (42). Similar studies for chopped fibre composites are sparse. Efficient and reliable use of SMC composites requires characterisation of their mechanical behaviour for dynamic loading as well as static loading situations. Mechanical properties of SMC in static loading conditions have been presented in chapter 3. In this chapter attempts were made to measure the residual tensile and compressive strength of damaged SMC and SMC+stainless steel laminates and by using a suitable empirical fracture model to estimate the residual tensile strength after impact.

7 - 1 Residual tensile strength of SMC after impact

In order to measure the residual tensile strength of SMC, straight -sided samples 100 x 60 x t mm (t=2,4 and 6 mm), figure 7.1a, were cut from supplied sheets of material and subjected to drop weight impact at different impact velocities which yields different

incident energies and subsequently produced different areas of damage in the specimen. Residual tensile strength tests were performed on a Schenk Trebel Machine at cross head speed of 1 mm min^{-1}. The load elongation curves during the test were recorded and the specimens were loaded to fracture.

In order to compare the effect of a hole produced by the striker during complete penetration of the SMC specimens a few undamaged specimens were drilled by a 20 mm diameter drill (the same diameter as the striker head) and the tensile strength was measured (fig. 7.1b).

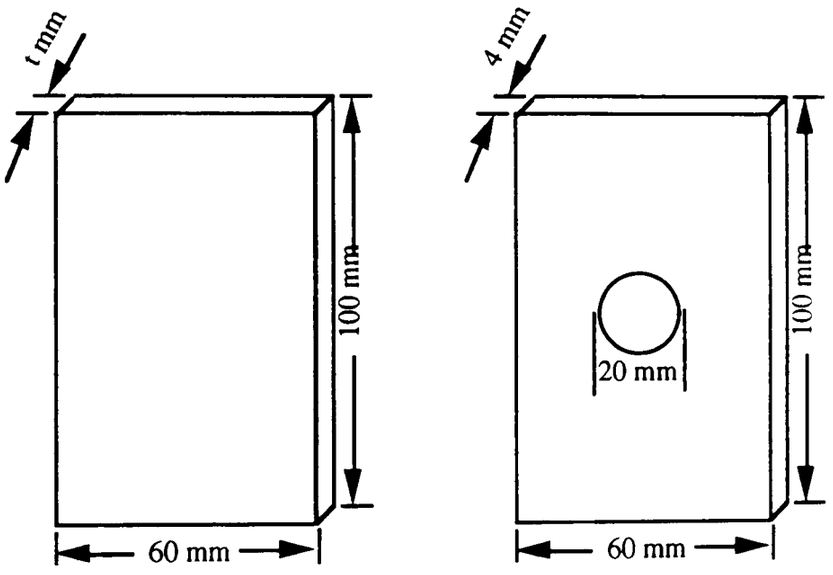

a b

Figure 7.1 - Geometry and nominal dimensions of the specimens used for measuring the tensile residual strength after impact a) without hole, b) with a 20 mm diameter hole

Results on the tensile residual strength of SMC showed that the strength decreases with increasing incident energy until the point at which complete penetration of the specimen takes place. After complete penetration the strength did not decrease with increasing incident energy. The thickness of SMC did not affect this trend and the specimens regardless of their thickness showed similar residual tensile strength-incident energy curves. The ratio of residual strength (σ_R) and undamaged strength (σ_0) as a function of incident energy for 2, 4 and 6 mm SMC are shown in figures 7.2 to 7.4.

For example for 4 mm SMC (fig. 7.3) there is almost no reduction in ratio of strength up to about 1.2 joules incident energy. Between 1.2 J and 38 J the strength reduces very rapidly from 100 % to about 40 %. Beyond 38 joules the material strength tends to level showing little decrease of strength with increasing incident energy, approaching the value resulted from a drill hole having the same diameter as the striker head (20 mm).

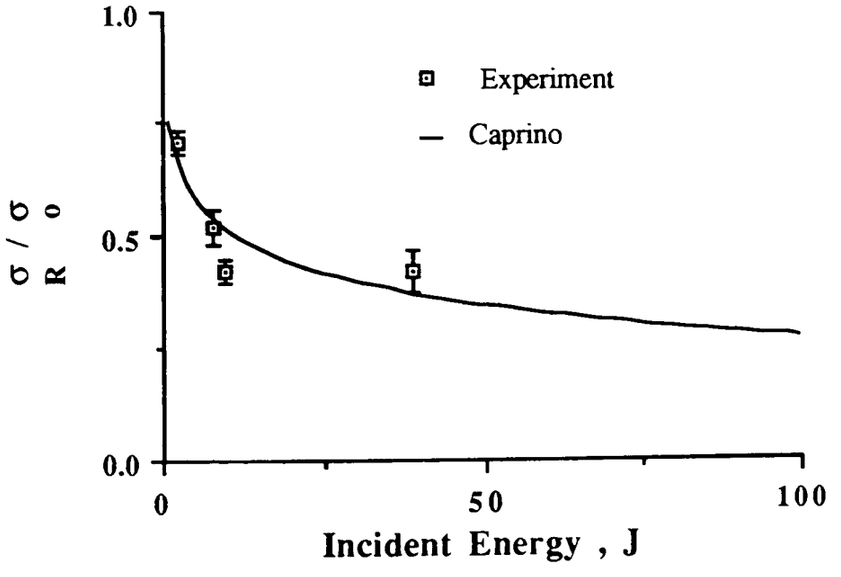

Figure 7.2 - Residual tensile strength σ_R / σ_0 against incident energy for 2 mm SMC.

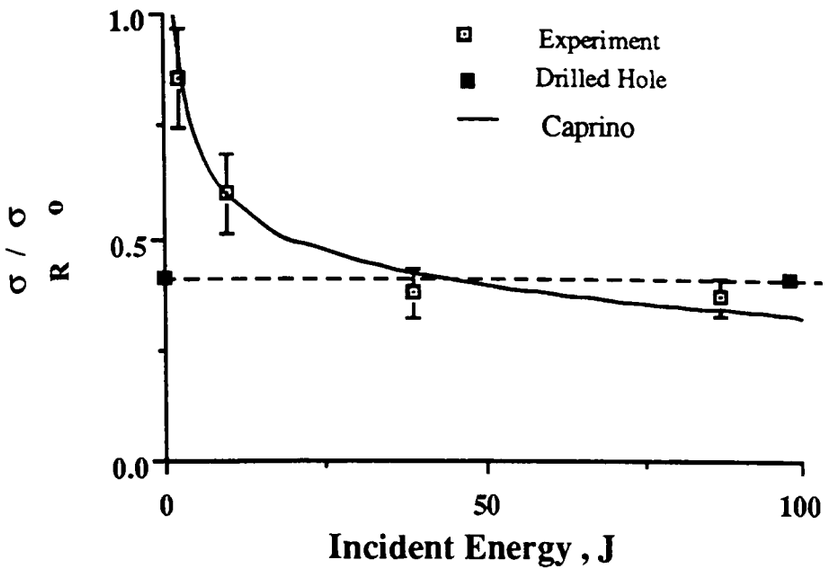

Figure 7.3 - Residual tensile strength σ_R / σ_0 against incident energy for 4 mm SMC.

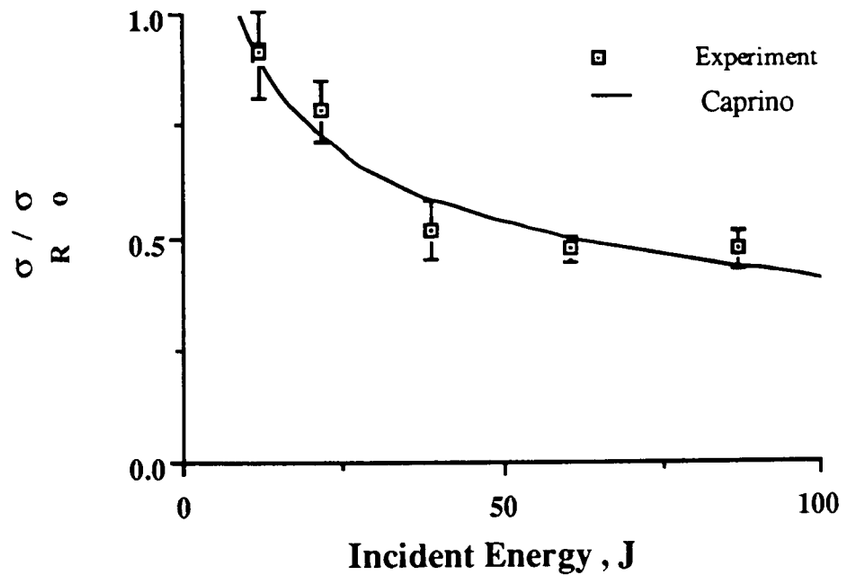

Figure 7.4 - Residual tensile strength σ_R / σ_0 against incident energy for 6 mm SMC.

Caprino's equation :

$$\sigma_R / \sigma_0 = (U_0 / U)^{\alpha} \qquad (1)$$

Which has been fully described in chapter 2 was employed to predict the tensile residual strength after impact. This was done by taking the log of equation (1) to get:

$$\log \sigma_R / \sigma_0 = \alpha \log U_0 - \alpha \log U \qquad (2)$$

Equation (2) provided a simple tool to calculate the parameters U_0 and α. Using the log-log plot of σ_R / σ_0 as a function of U a straight line with slope $-\alpha$, intersecting the y axis at ($\alpha \log U_0$) was obtained (fig. 7.5).

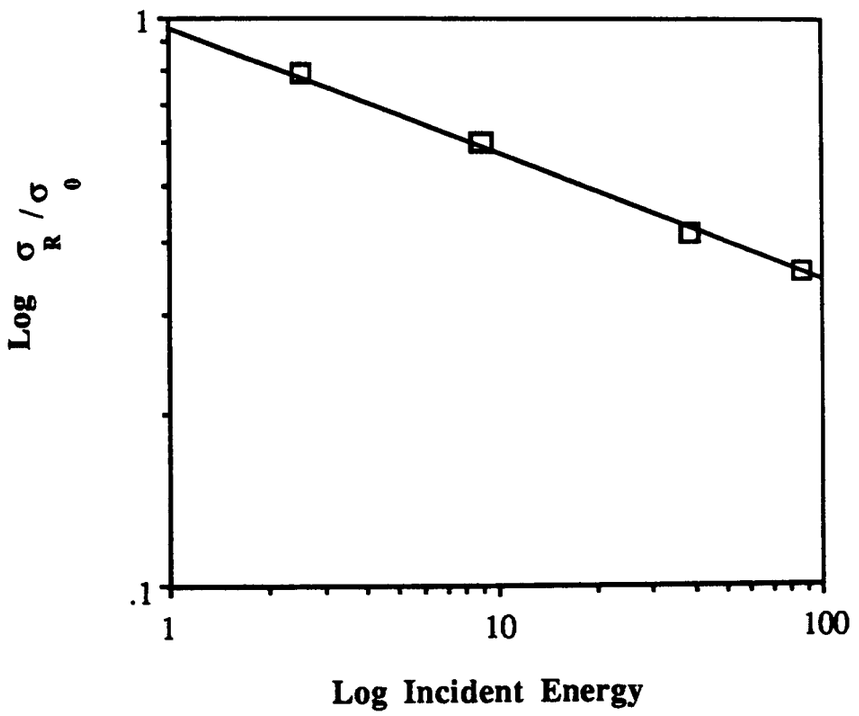

Figure 7.5 - Residual tensile strength σ_R/σ_0 for 4 mm SMC (log scale).

By the best fit method the values of U_0 and α were calculated which are shown in the following table:

SMC Thickness	2 mm	4 mm	6 mm
α	0.19	0.29	0.49
U_0	0.38	1.4	13.16

The best fit of equation (1) to the experimental results are plotted in figures 7.2 to 7.4. The equation gives a good fit to the experiment results.

Since Caprino's model gives different values of α and U_0 for different thicknesses of SMC and these values are not material properties, it was decided to apply other models such as Whitney and Nuismer criteria.

The Whitney Nuismer model assumes that failure occurs in a notched composite when stress field approaching the boundary of the damage rises to a point at which the local stress (at a point which is called point stress criteria or averaged over a small area which is called average stress criteria) is equal to the unnotched fracture strength of that composite (135). The point stress criteria and average stress criteria are described by equations 1 and 2 respectively.

$$\frac{\sigma_N}{\sigma_0} = \frac{2}{2+\xi_1^2+3\xi_1^4} \qquad (1) \qquad \xi_1 = \frac{R}{R+d_0}$$

$$\frac{\sigma_N}{\sigma_0} = \frac{2(1-\xi_2)}{(2-\xi_2^2-\xi_2^4)} \qquad (2) \qquad \xi_2 = \frac{R}{R+a_0}$$

Where R is the radius of the hole and d_0 and a_0 are characteristic distances which can be measured by processing the data. The Whitney-Nuismer criteria assumes that d_0 and a_0 are material properties and are independent of laminate geometry and stress distribution.

The post impact tensile data for 4 mm SMC and 6 mm SMC were processed by using equations 1 and 2 to plot figures 7.6 and 7.7 and derive the dimensions d_0 and a_0.

Values of d_0 and a_0 are 4.6 and 12 for 4 mm SMC and are 14 and 51 for 6 mm SMC. The form of Whitney-Nuismer equation does not fit well with the experimental data. The damage parameters are also thickness dependent.

Visual inspection of the specimens after residual tensile test showed that the appearance of the fractures are similar for all thicknesses of SMC. Cracks propagate from the damaged zone towards the edge of the specimens. The typical tensile failure of SMC specimens which had been subjected to different incident energies are shown in figure 7.8. It is clearly seen in figure 7.8 that failure modes are similar despite the difference in the initial damage prior to tensile test. Comparison of the tensile failure of the specimen with a drilled hole showed similar fracture pattern with the specimens which had been damaged by impact. Figure 7.9 shows the typical tensile failure in SMC specimens with a 20 mm diameter drilled hole.

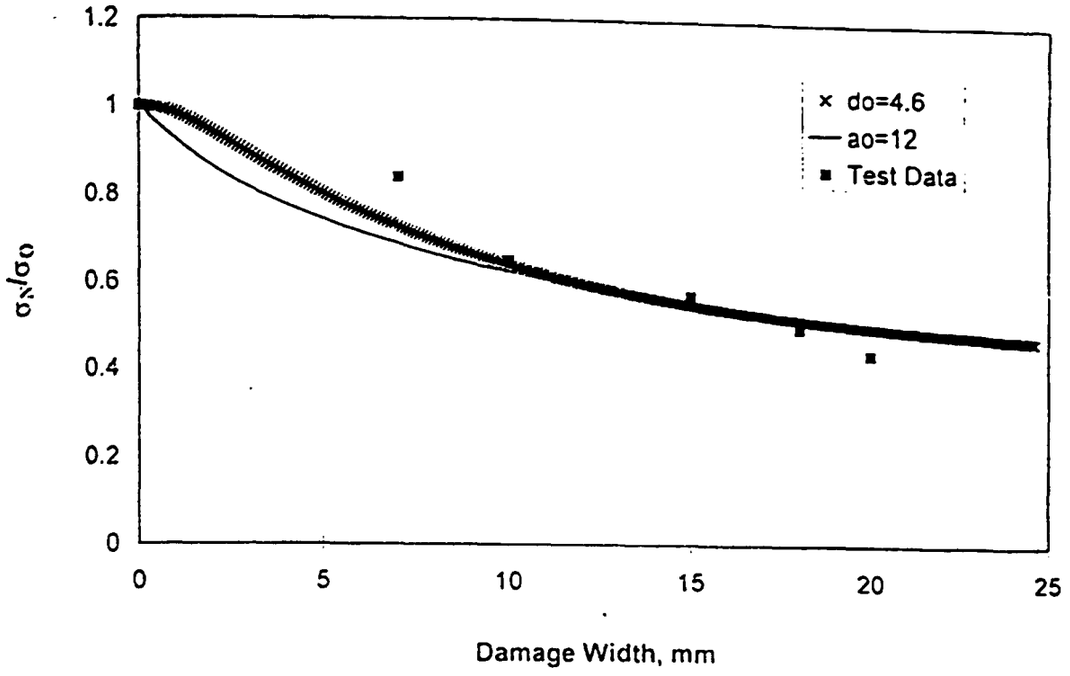

Figure 7.6 - Comparison of predicted and experimental residual tensile strength for 4 mm SMC.

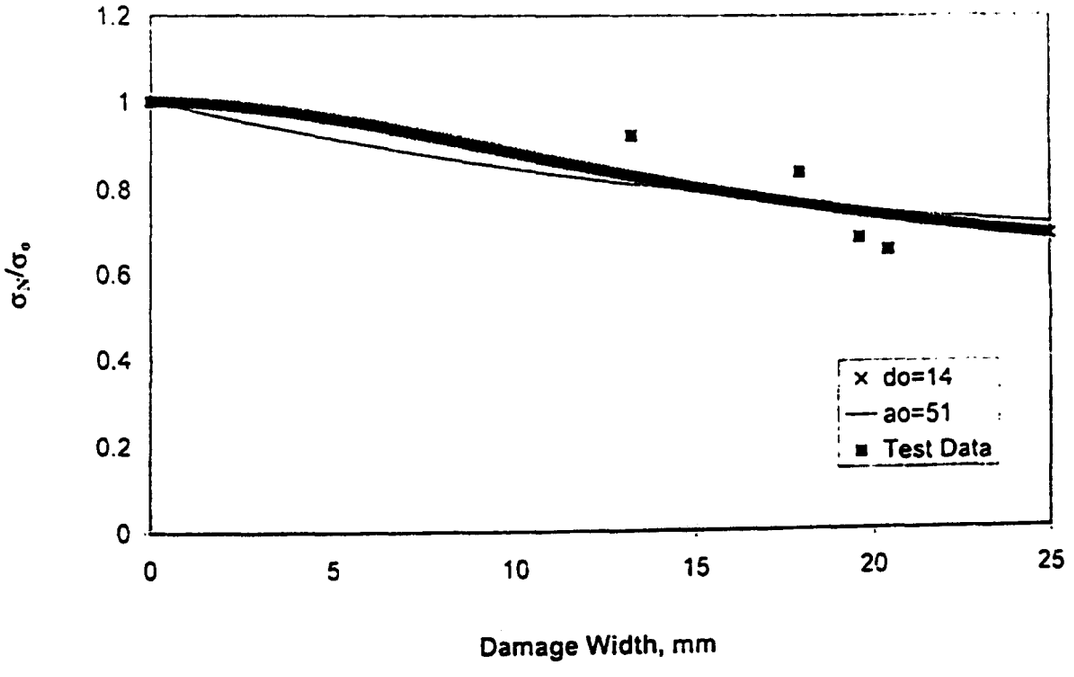

Figure 7.7 - Comparison of predicted and experimental residual tensile strength for 6 mm SMC.

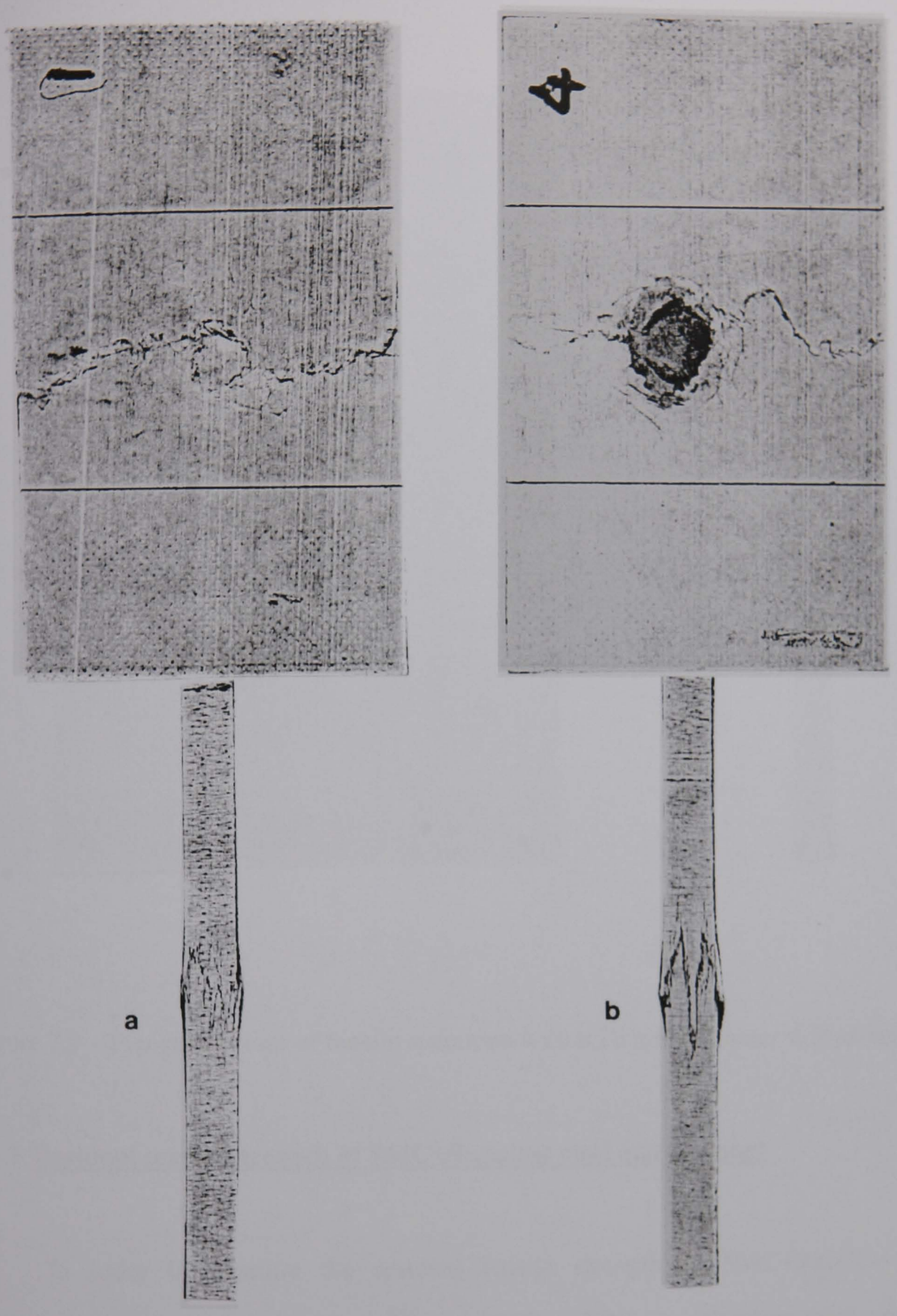

Figure 7.8 - Typical fracture of residual tensile specimens at two different incident energies a)38J, b)78J.

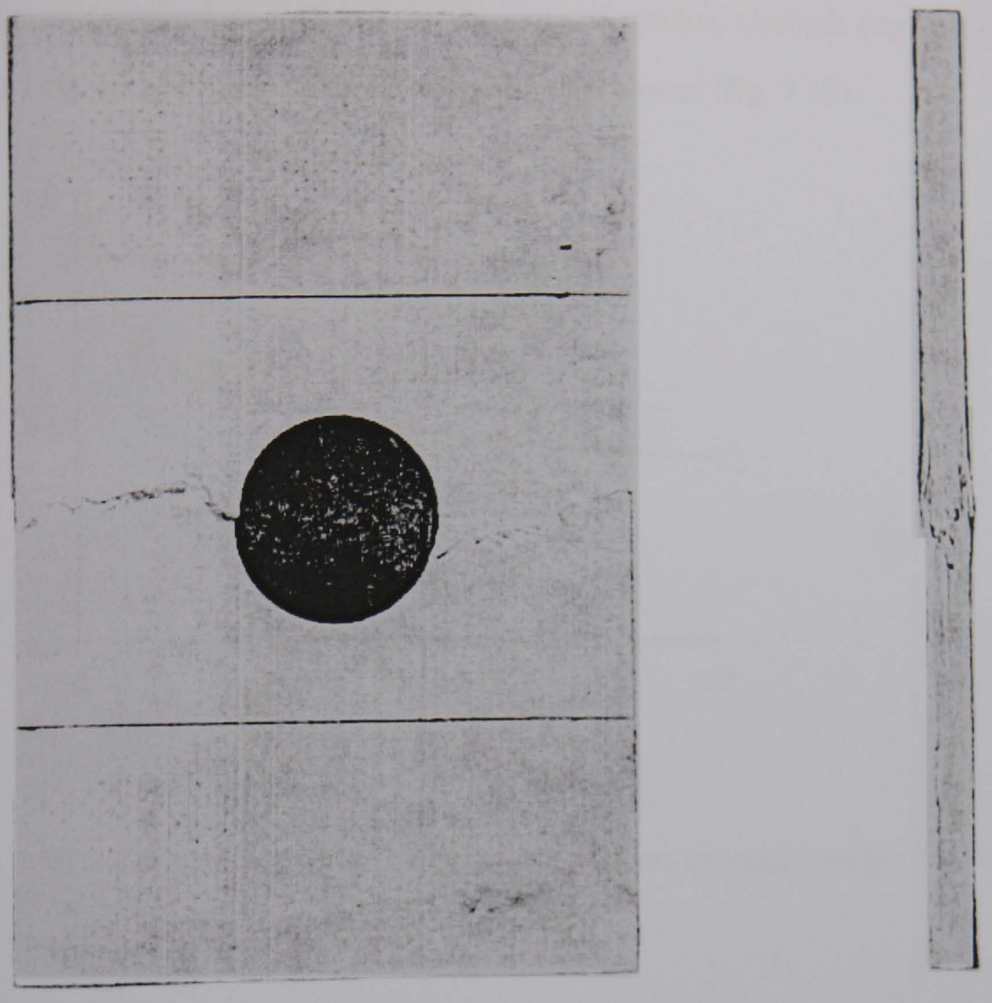

Figure 7.9 - Typical fracture of tensile specimen with a 20 mm diameter drilled hole.

7 - 2 Residual tensile strength of SMC+Stainless steel after impact

In order to measure the residual tensile strength of SMC+stainless steel laminates, straight -sided samples of 4 mm SMC and 0.6 mm stainless steel with the same dimensions as in figure 7.1 were cut from the supplied sheet of material. The SMC+stainless steel laminates were constructed by simply resting the layer of SMC on the stainless steel sheet. Then, the SMC-stainless steel laminates were subjected to drop weight impact from SMC side at different incident energies. After impact the layer of stainless steel was removed and the damaged SMC tested in tension.

The residual tensile test data was treated exactly the same as SMC which has already been described in section 7.1. The ratio of residual strength (σ_R) to undamaged strength (σ_0) as a function of incident energy was plotted (fig. 7.10).

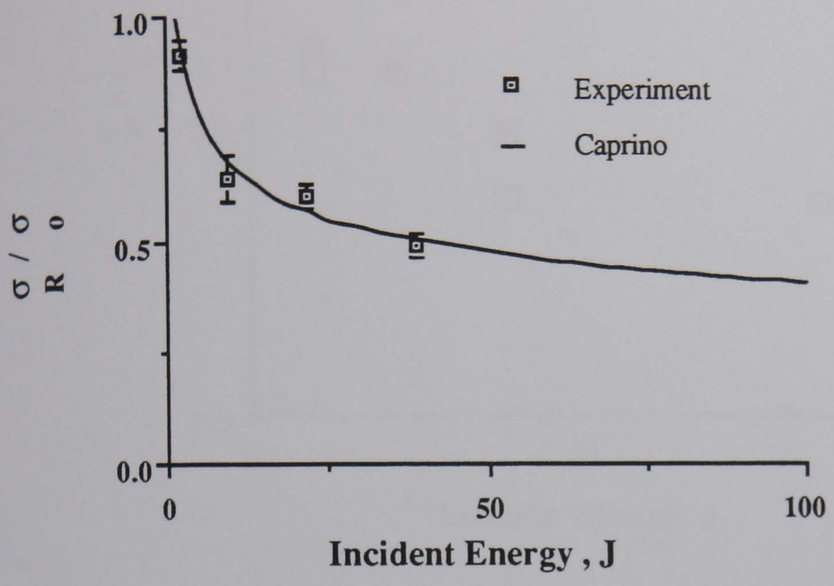

Figure 7.10 - Residual tensile strength σ_R / σ_0 against incident energy for 4 mm SMC with a layer of 0.6 mm stainless steel.

Equation (2) was applied to the experimental data shown in figure 7.10 and by the method which was explained previously the values of α and U_0 were found to be 0.16 and 1.3 respectively.

The best fit of equation (1) to the experimental results is shown as a solid line in figure 7.10. The equation gives a good fit to the experimental results.

Comparison of the residual strength of SMC and SMC as a layer of SMC+stainless steel laminates is shown in figure 7.11. Typical tensile failure of SMC in SMC+stainless steel laminates is shown in figure 7.12.

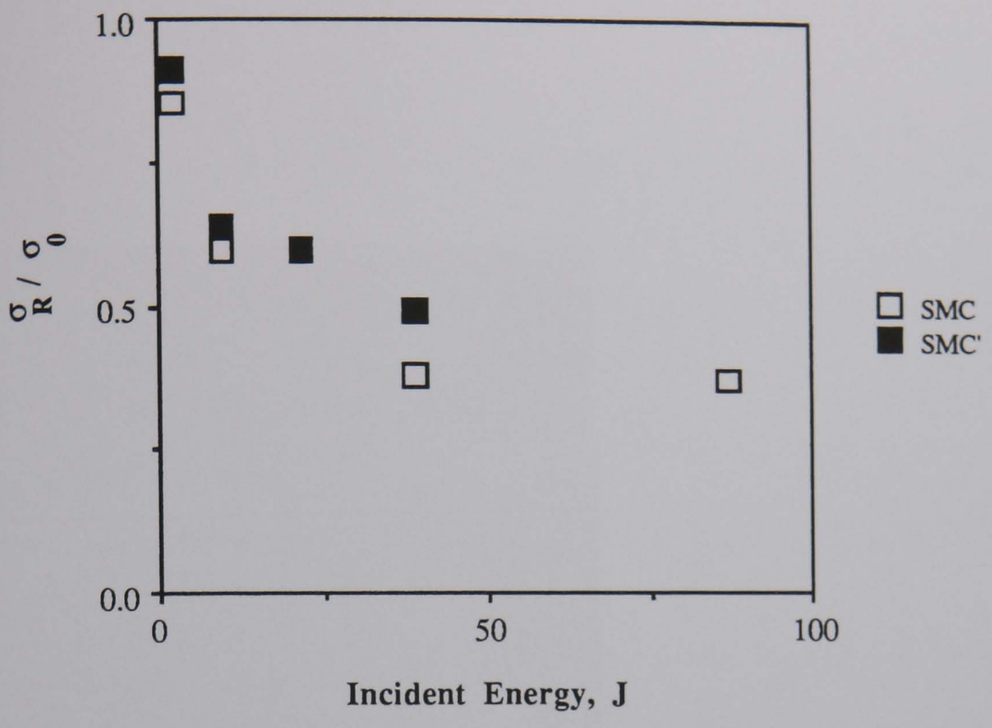

Figure 7.11 - Comparison of the residual tensile strength against incident energy for 4 mm SMC and 4 mm SMC with a layer of 0.6 mm stainless steel.

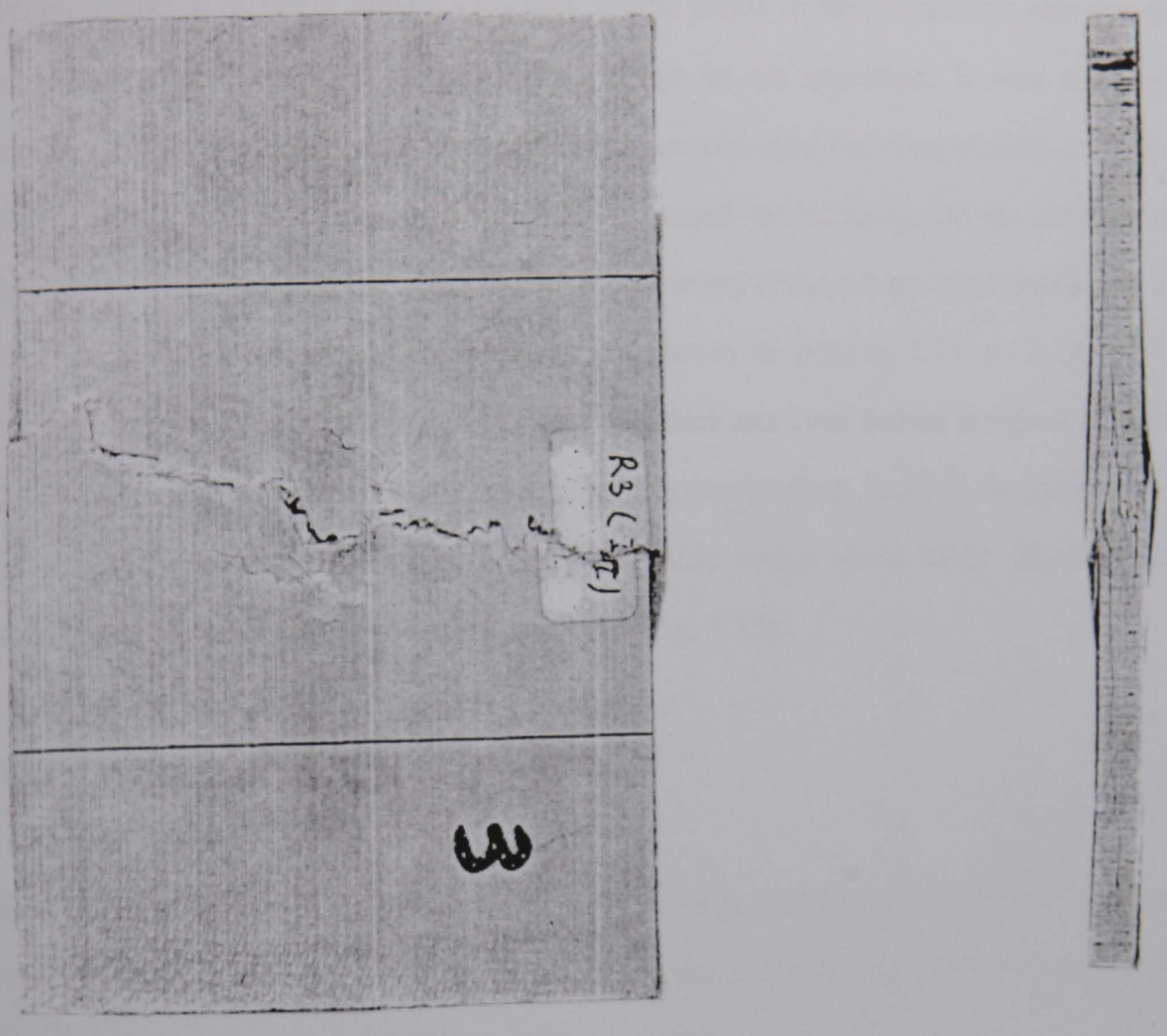

Figure 7.12 - Typical tensile failure of SMC in SMC+stainless steel laminates.

7 - 3 Residual compressive strength of SMC after impact

In order to measure the residual compressive strength of SMC, straight -sided samples 89 x 57 x 4 mm were cut from supplied sheets of material and subjected to drop weight impact at different impact velocities which yields different incident energies and subsequently produced different areas of damage in the specimen. It was mentioned previously (chapter 2) that such long specimens are not ideal for compression test unless they are supported to avoid premature failure caused by buckling. At the present time there is not a standard anti buckling device and a variety of them have been developed and used. A selection of anti buckling guides are shown in figures 2.11 to 2.14. At the beginning of the project an anti buckling guide which has been shown in figure 3.32 was designed to support the specimens during compression loading. Later in the programme a miniaturised version of Boeing anti buckling guide which gives better alignment and stability during compression loading was used (fig. 7.13).

7.3 -1 Details of compression test

Residual compressive strength tests were performed on a SCHENK TREBEL Machine at cross head speed of 1 mm / min. For the case of the anti buckling guide in figure 3.32 a compression cage as shown in figure 3.31 was used.

All post impact compression specimens were C-scanned using a Physical Acoustics Corporation machine (fig. 3.33). Specimens were placed in the tank filled with water (fig. 7.14) and then scanned. The Physical Acoustics unit had a 5 MHz flat probe which both acted as the transmitter and receiver. The tank was set up for double through transmission where the ultrasound is reflected from a glass plate below the specimen and received through an electronic gate. This information was passed to a computer storage device which built up the images on a 1 mm spaced grid. The typical C-scan results for different impact energies are shown in figure 7.15.

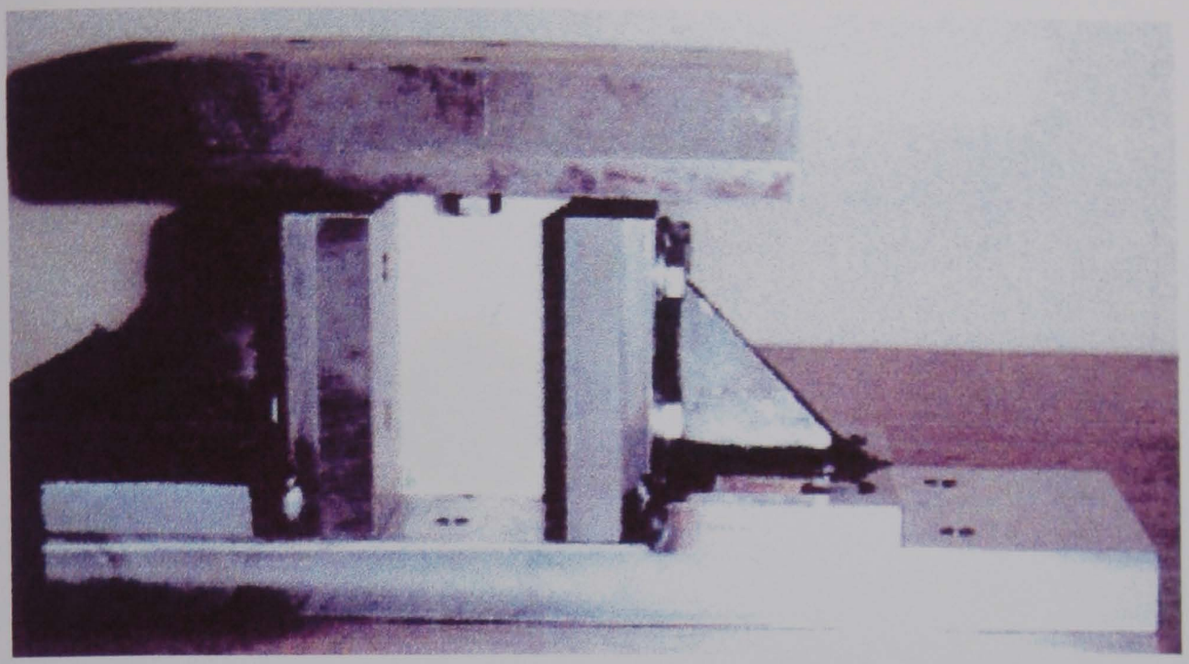

Figure 7.13 - Photograph of the QMW post impact compression support.

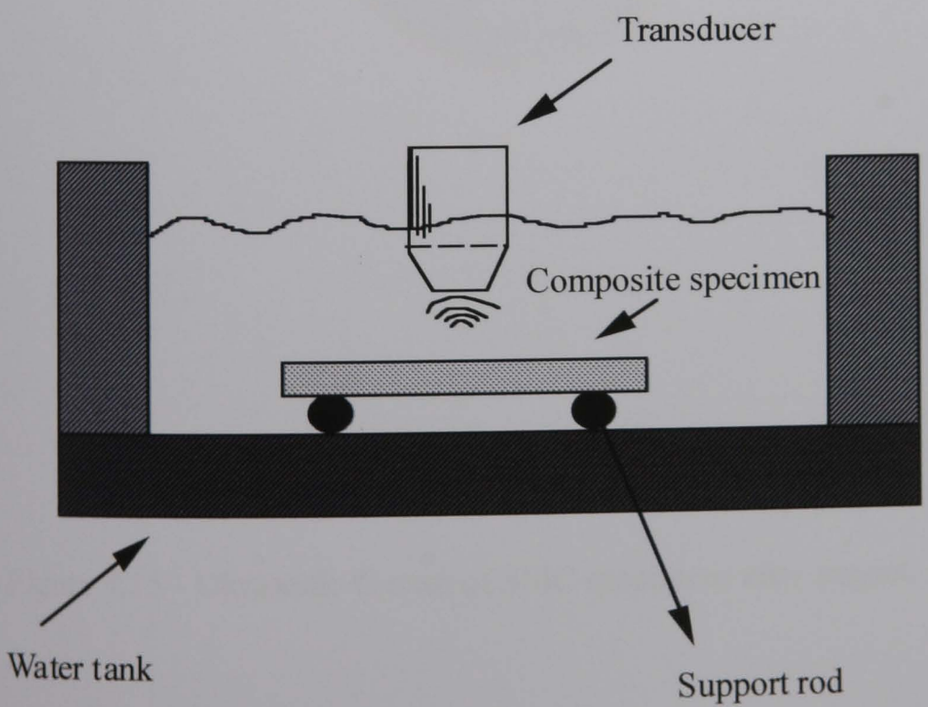

Figure 7.14 - Schematic representation of C-scan tank.

Figure 7.15 - Ultrasonic C-scan of SMC specimens after impact.

7.3 -2 Results

Damage width increased with increasing incident energy until a maximum width of approximately 40 mm was reached (fig. 7.16). This corresponds to the diameter of the support ring used during the impact test. The size of delamination area as a function of incident energy is shown in figure 7.17. Damage area increased almost linearly with incident energy until a maximum 1256 mm ^{2} which is the area of the support was reached. Compression strength after impact data is usually presented by plotting compression strength against incident energy or damage width. Figures 7.18 and 7.19 show the results of compression strength as a function of incident energy and damage width respectively.

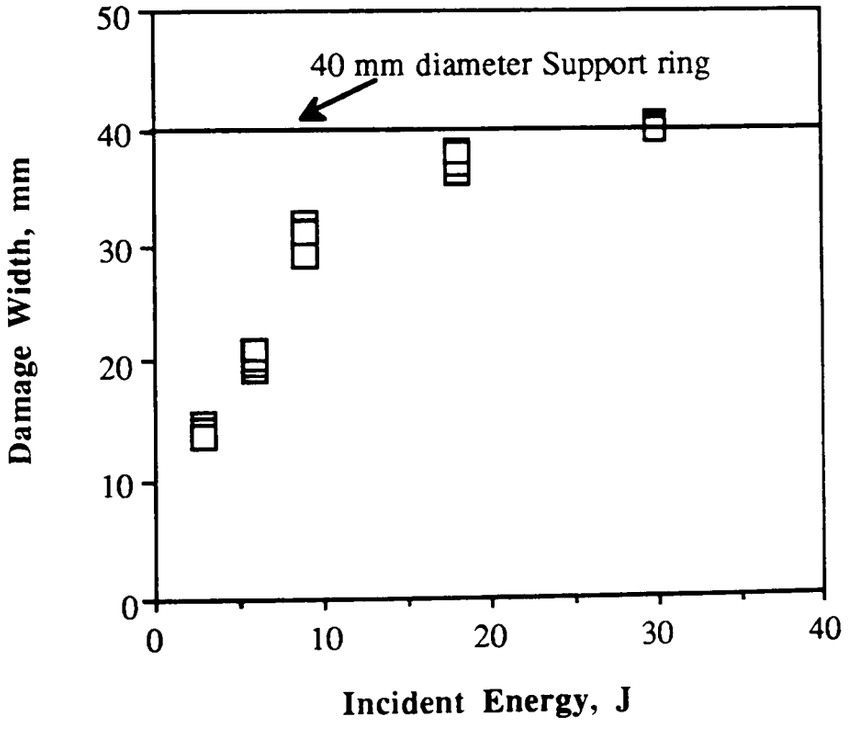

Figure 7.16 - Damage width as a function of incident energy.

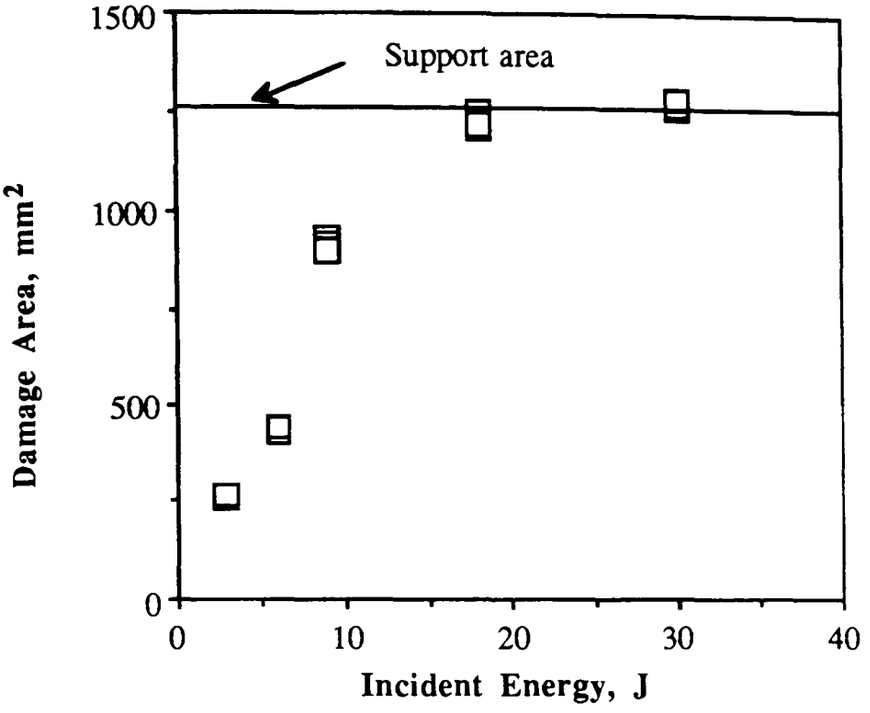

Figure 7.17 - Damage area as a function of incident energy.

Results on the compression tests showed that the strength decreases with increasing incident energy until the point at which complete penetration of the specimen takes place. After complete penetration the material strength tends to level off showing little decrease with increasing incident energy (fig. 7.18).

The typical compressive failure of SMC after impact is shown in figure 7.20. Comparison of the failure of the specimen with a drilled hole showed similar fracture pattern with the specimens which had been damaged by impact. Figure 7.21 shows the typical compressive failure in SMC specimens with a 20 mm diameter hole.

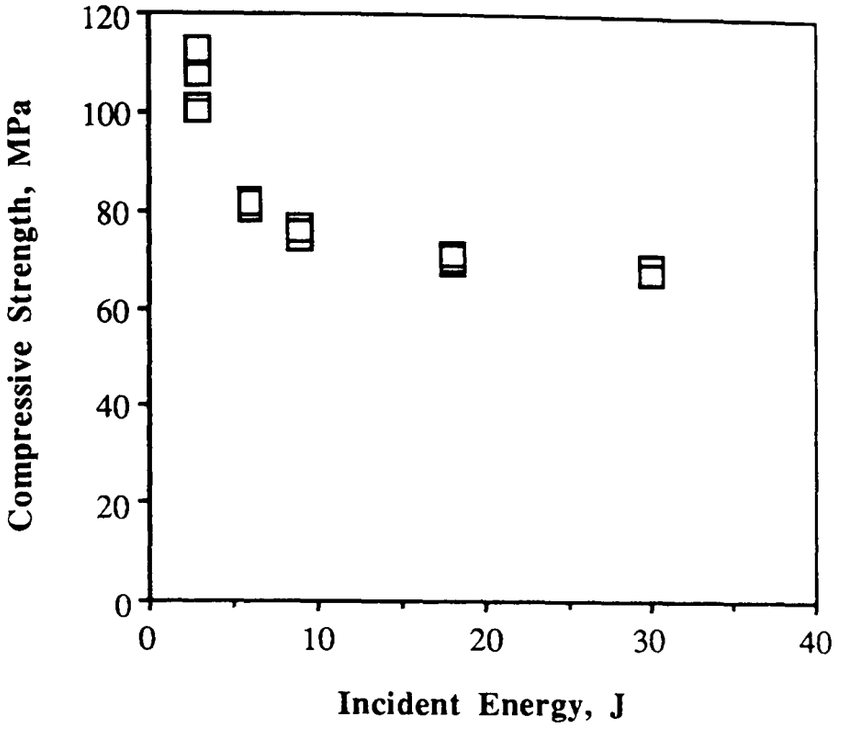

Figure 7.18 - Compression strength after impact as a function of incident energy.

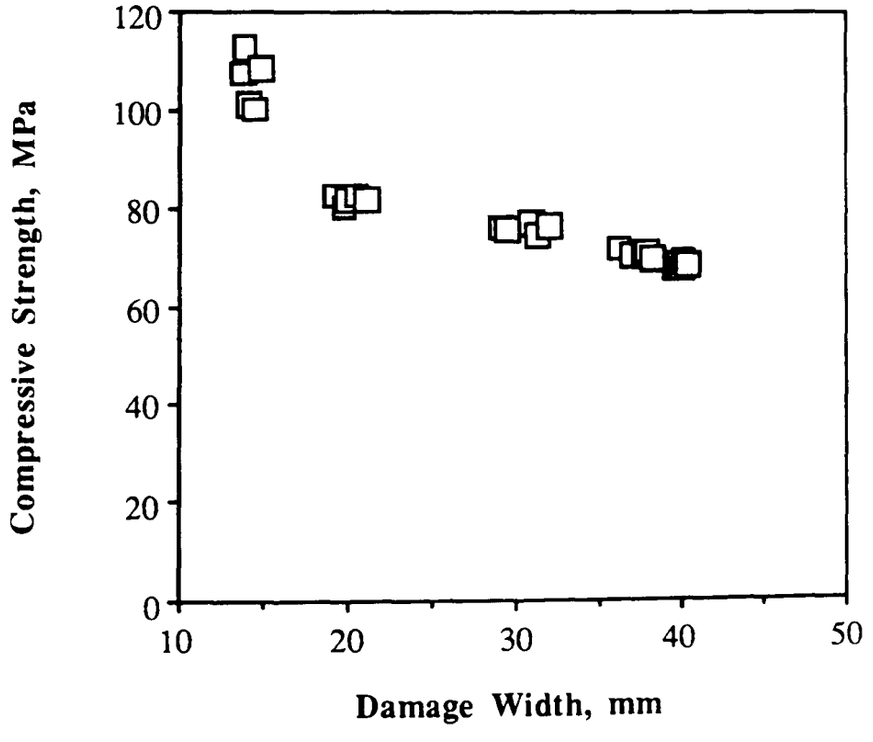

Figure 7.19 - Compression strength after impact as a function of damage width.

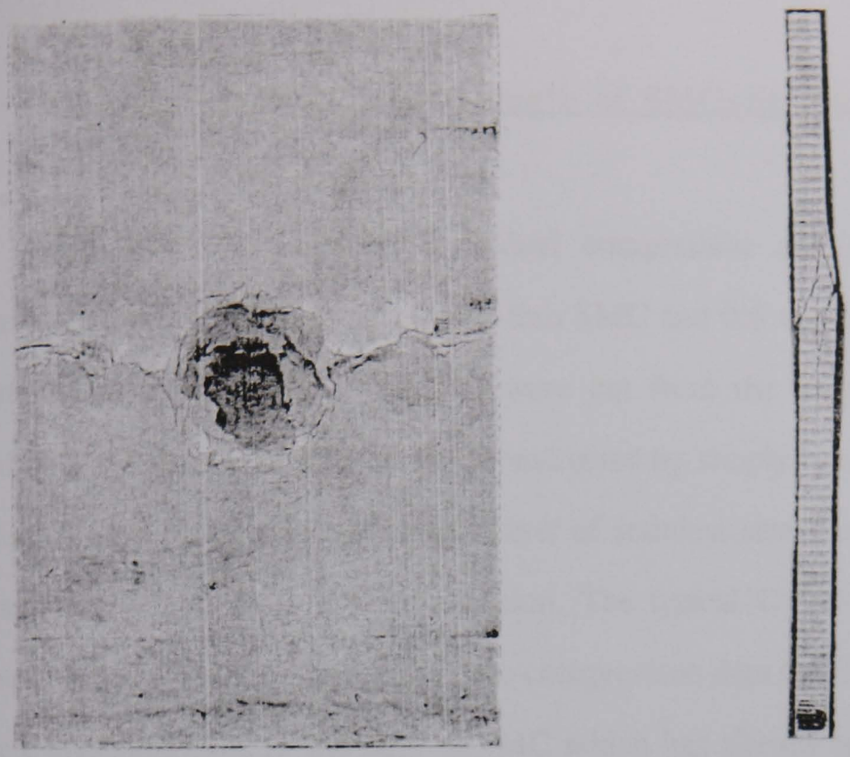

Figure 7.20 - Typical fracture of residual compressive specimens after impact for 4 mm SMC.

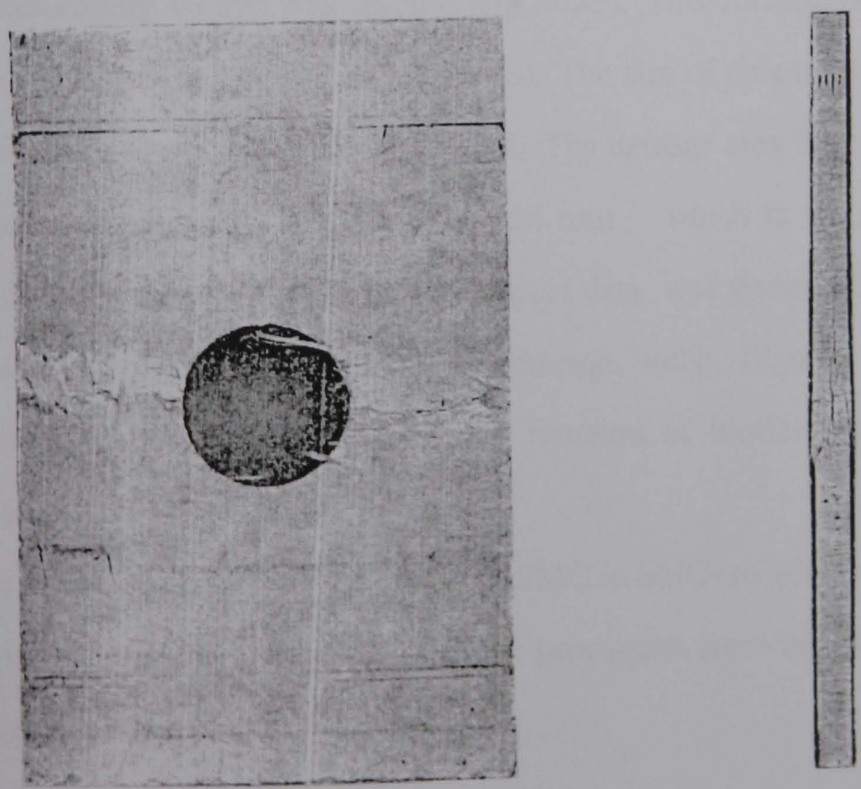

Figure 7.21 - Typical fracture of compressive specimen with a 20 mm diameter drilled hole.

7 - 4 Residual compressive strength of SMC+Stainless steel after impact

In order to measure the residual compressive strength of SMC+stainless steel laminates straight sided samples of 4 mm SMC and 0.6 mm thick stainless steel with the same dimension 89 x 57 x 4 mm were cut from the supplied sheet of material. The SMC+stainless steel laminates were constructed by simply resting the layer of SMC on the stainless steel sheet. After impact the layer of stainless steel was removed and SMC was c-scanned and then tested in compression. The typical C-scan results for different impact energies are shown in figure 7.22. The compression data for SMC+stainless steel laminates were presented exactly the same as SMC which has already been described in section 7.3-2.

Damage width increased with increasing incident energy until a maximum width of approximately 40 mm was reached (fig. 7.23). This corresponds to the diameter of the support ring used during the impact test. The size of delamination area as a function of incident energy is shown in figure 7.24. The damage area increased almost linearly with incident energy until a maximum 1256 mm^2 which is the area of the support was reached. Compression strength after impact data was presented by plotting compression strength against incident energy and damage width. Figures 7.25 and 7.26 show the results of compression strength as a function of incident energy and damage width respectively.

The compressive failure of the layer of SMC in SMC+stainless steel laminates (fig. 7.27) was similar to SMC (fig. 7.20). Crack propagates from the damaged zone towards the edge of the specimen.

Figure 7.22 - Ultrasonic C-scan of SMC' specimens after impact.

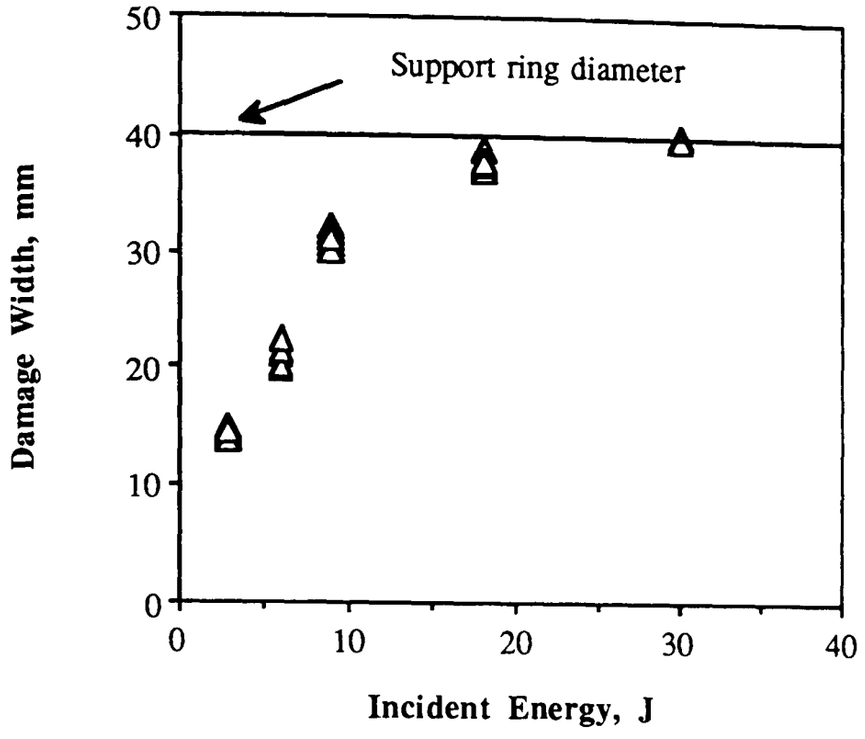

Figure 7.23 - Damage width as a function of incident energy for 4 mm SMC with a layer of 0.6 mm stainless steel.

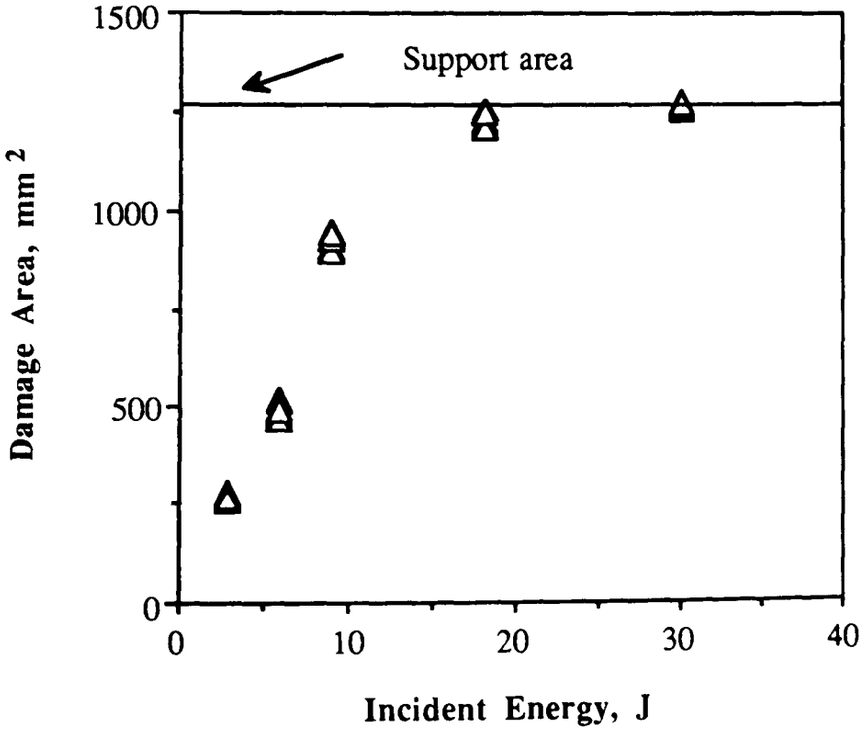

Figure 7.24 - Damage area as a function of incident energy for 4 mm SMC with a layer of 0.6 mm stainless steel.

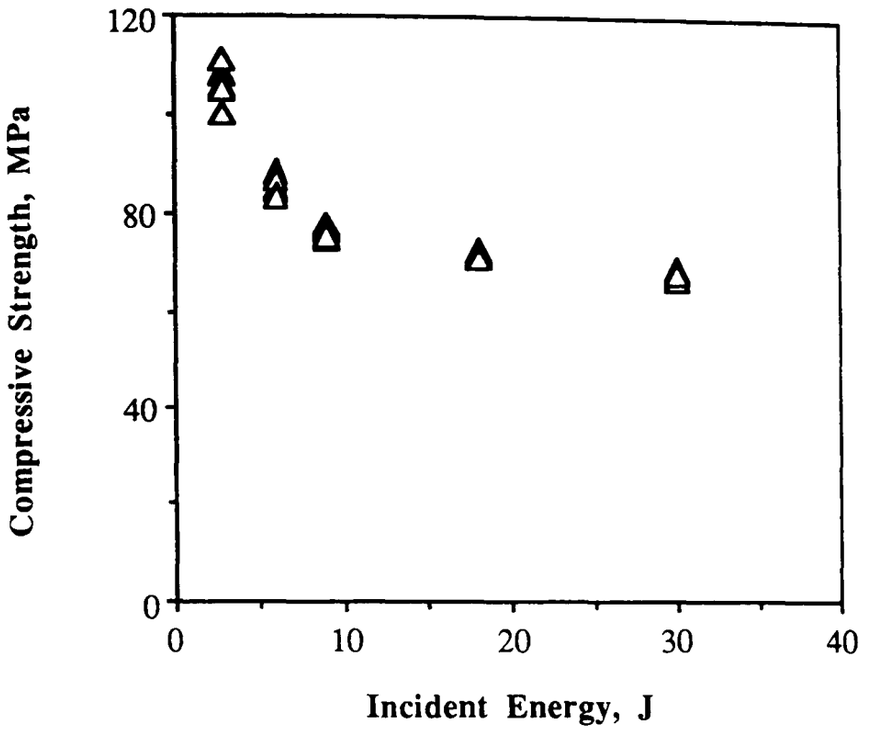

Figure 7.25 - Compression strength after impact as a function of incident energy for 4 mm SMC with a layer of 0.6 mm stainless steel.

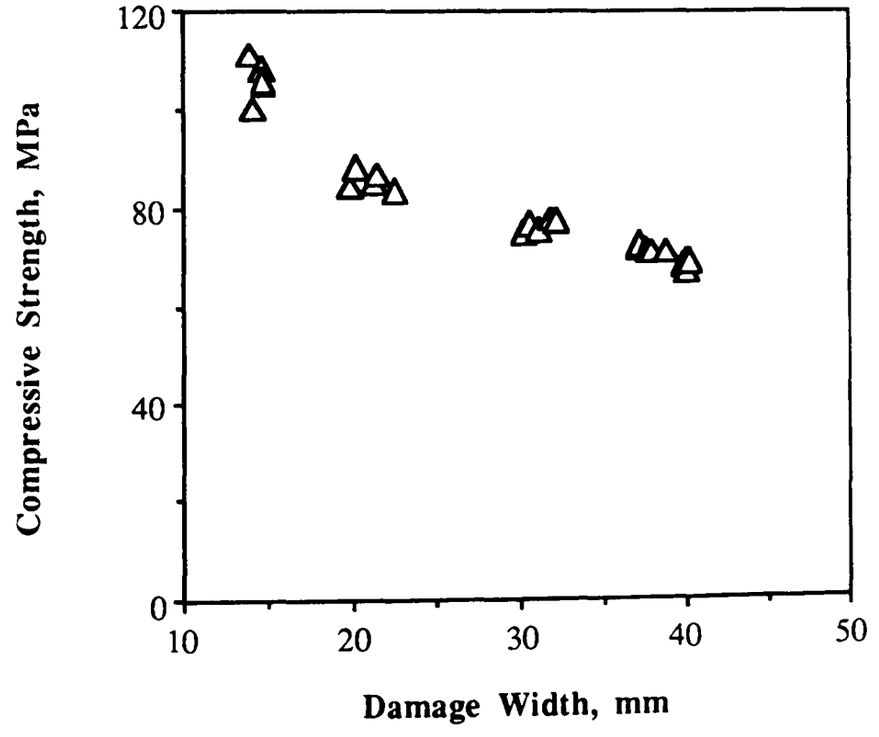

Figure 7.26 - Compression strength after impact as a function of damage width for 4 mm SMC with a layer of 0.6 mm stainless steel.

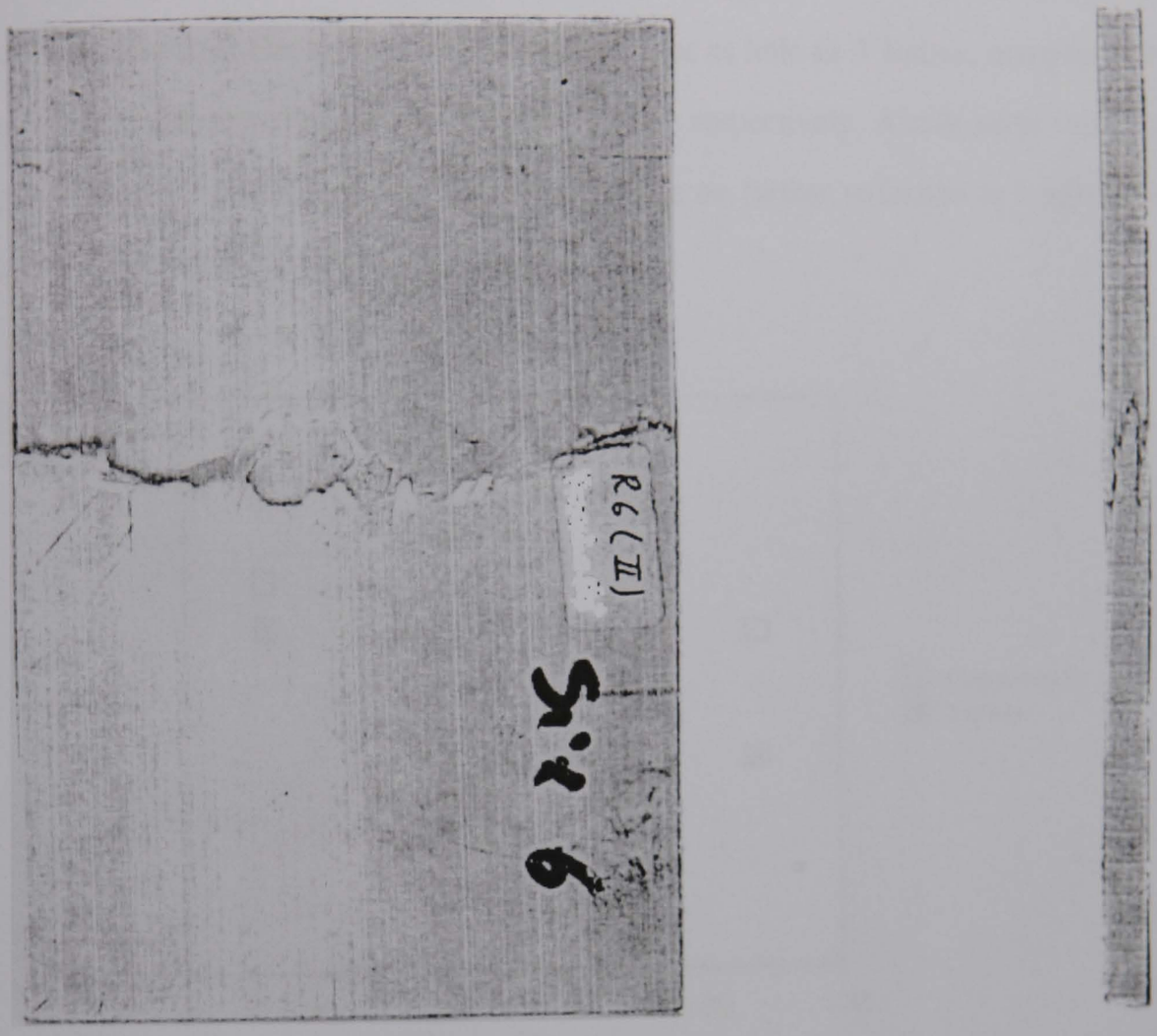

Figure 7.27 - Typical fracture of residual compressive specimens after impact for 4 mm SMC in SMC with a layer of 0.6 mm stainless steel.

7-5 Discussion

Experimental results showed that after impact tensile and compressive strength are decreased. The extent of reduction depends on the level of incident energy (fig. 7.28). Both tensile and compressive strength after impact did appear to be affected by almost any degree of damage. For example at incident energies as little as 3 Joules, compression and tensile strength were reduced by 5.7% and 13.7% respectively. Above some incident energy level, the plate will perforate, and there will be no further reduction in tensile and compressive strength (fig. 28).

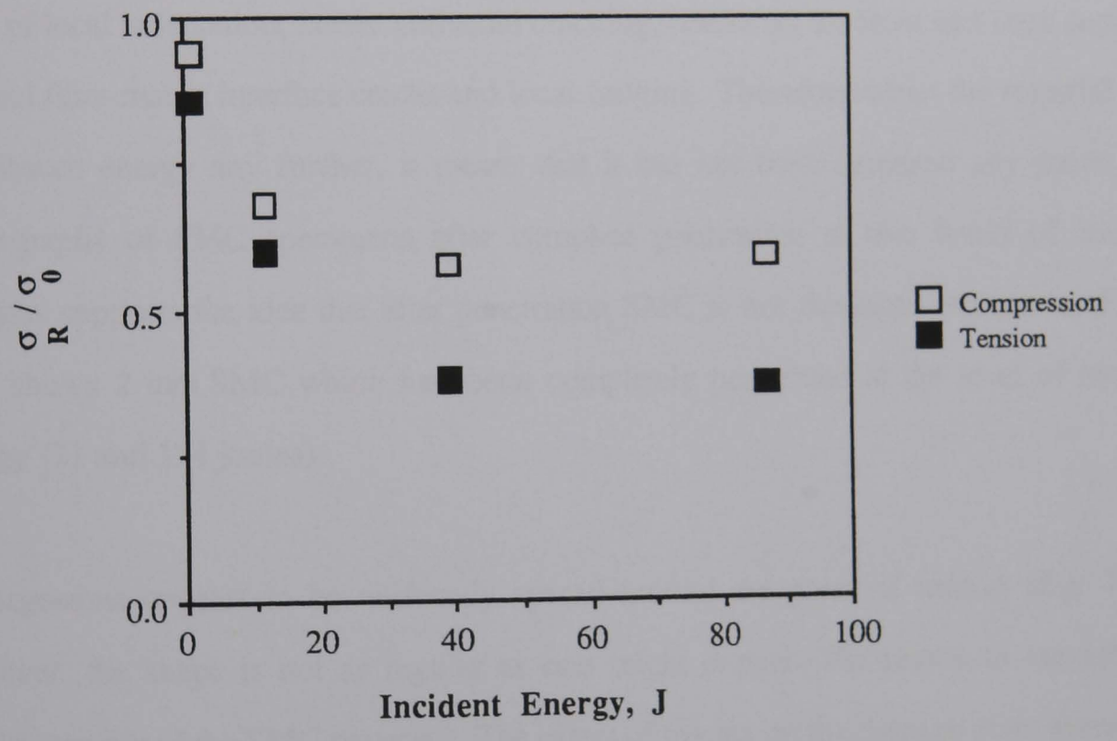

Figure 7.28 - Compression and tensile strength after impact as a function of incident energy for 4 mm SMC.

In general the strength reduction as a function of incident energy can be divided into four zones (fig. 7.29). In zone one the strength remains unchanged (for the case of specimens which have been impacted up to transition energy) or reduction in strength is very small. In the second zone which is between the energy level of zone one and the incident energy

just before penetration, the strength reduces very sharply. In zone 3 at which the level of incident energy is slightly higher than the energy required for penetration the strength of material is decreased further. At higher impact velocities (zone 4), a complete perforation of the specimen occurs with a hole produced for which the residual strength then remains constant for increasing incident energy. The reason for the absence of any reduction in strength after complete penetration can be attributed to the results of energy absorption as a function of incident energy for SMC laminates (see chapter 4 and 5) and optical microscopy results. It was mentioned in chapters 4 and 5 that SMC does not absorb any more energy after complete penetration regardless of the level of incident energy (e.g. fig. 4.20). The absorption of energy by SMC is accompanied by damage in the material in form of local indentation, lateral and axial cracking, cracks on the front and back surfaces, internal fibre-matrix interface cracks and local bulging. Therefore when the material does not absorb energy any further, it means that it has not been damaged any more. The photographs of SMC specimens after complete penetration at two levels of incident energies supports the idea that after penetration SMC is not damaged any more. Figure 7.30 shows 2 mm SMC which had been completely penetrated at the level of incident energy (21 and 154 joules).

Damage-zone appears to be uniformly spread around the point of impact (fig. 7.15), however, the shape is not as regular as one might expect. The reason is the inherent inhomogeneity of the SMC materials. The effect of impact on the damage-zone spread are shown in figures 7.15 and 7.16. Damage width increased with increasing incident energy until a maximum width of approximately 40 mm was reached (fig. 7.16). This corresponds to the diameter of the support ring used during the impact test. Damage area increased almost linearly with incident energy until a maximum 1256 mm^2 which is the area of the support was reached.

The data generated by the compression after impact test, when presented in the manner of incident energy versus compression strength, links a test parameter from one test (incident energy) to a property measured in another (compression strength). This in effect means that it is impossible to determine whether or not the relative performance of two laminate systems (SMC on its own and SMC in SMC +S.S.) is controlled by their resistance to damage during impact, or the resistance to propagation of that damage during compression. Prichard and Hogg argued that a relevant damage parameter that could be used to assess impact resistance was the width of the delaminated area (136). If this parameter was used then the impact and compression parts of the test could be separated. This was used to compare damage tolerance of SMC and SMC' (fig. 7.31). In figure 7.31 compression strength is plotted against damage width which shows that SMC and SMC' have similar damage tolerance.

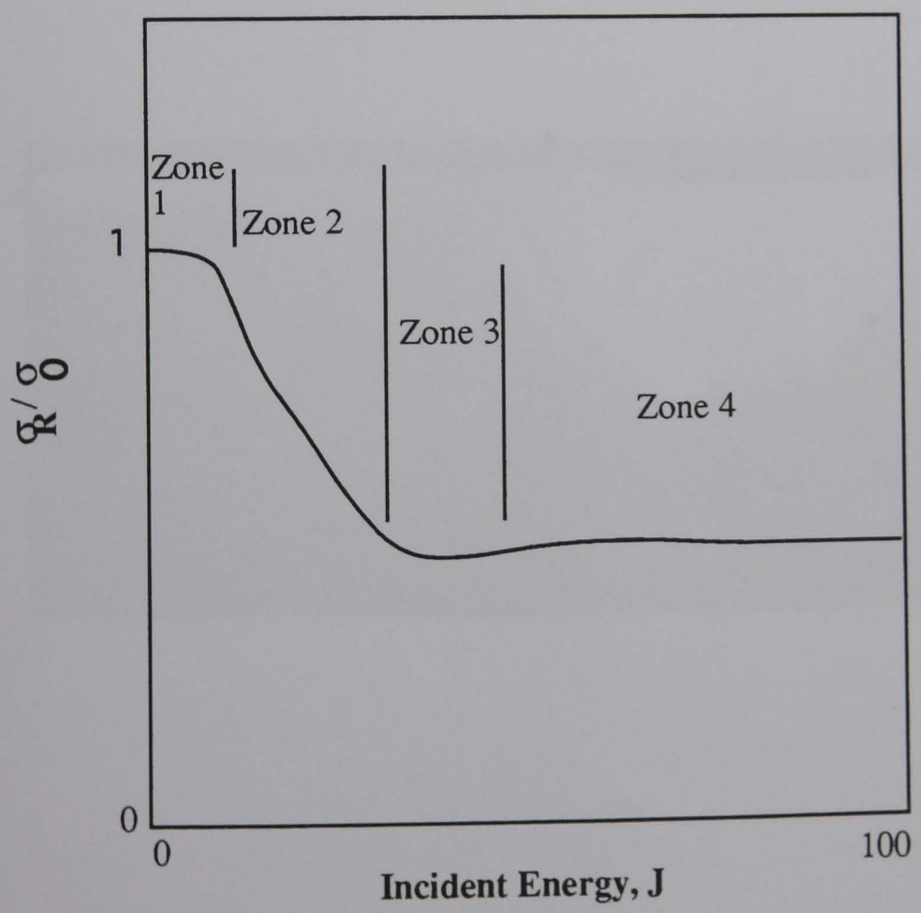

Figure 7.29 - Schematic diagram of Compression strength after impact as a function of incident energy.

a

b

Figure 7.30 - Photographs of 2 mm SMC after complete penetration for two level of incident energies a) 21 J, b) 154

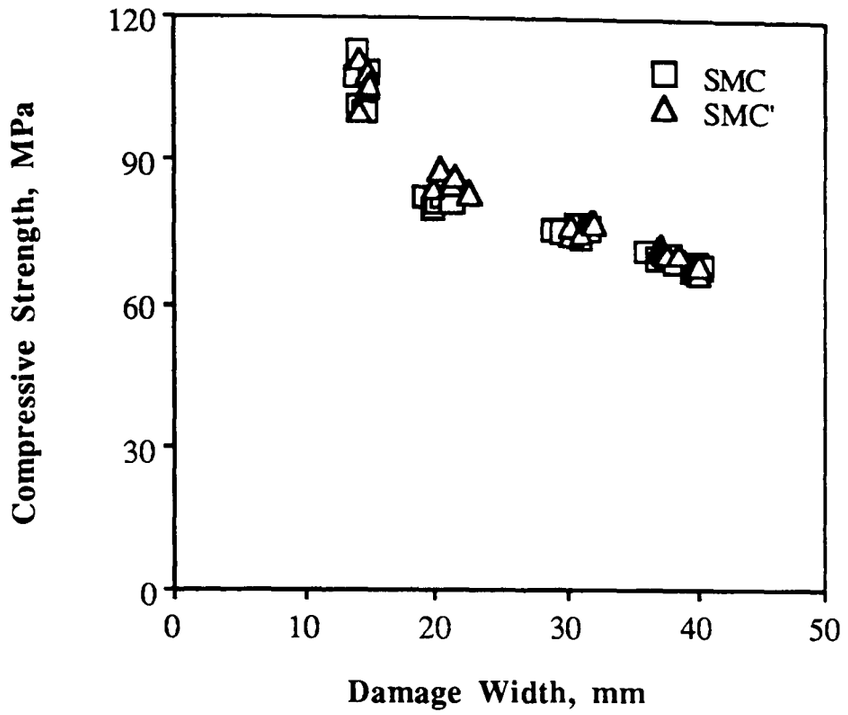

Figure 7.31 - Compression strength after impact as a function of damage width for 4 mm SMC and 4 mm SMC with a layer of 0.6 mm stainless steel (SMC').

Both Caprino and whitney-Nuismer models which were proposed to predict the residual strength of the materials were applied to tensile and compression data (figs. 7.2, 7.3, 7.4, 7.6, 7.7, 7.32 and 7.33). Caprino's model gives different values of α and U_0 for different thicknesses of SMC and these values are not material properties. Therefore, Caprino's model can not predict the residual strength of SMC after impact and is only a good fit to the experimental data. The same problem exist with Whitney-Nuismer criteria. The Whitney-Nuismer criteria assumes that d_0 and a_0 are material properties and are independent of laminate geometry and stress distribution. But, as it is shown in figures 7.6 and 7.7), these parameters are thickness dependent. The Whitney-Nuismer criteria, not only can not predict the residual strength of SMC, but also does not fit well with the experimental data (figs. 7.6, 7.7, and 7.33).

Comparison of the residual strength of SMC and SMC as a layer of SMC+stainless steel laminates showed that the trend of reduction for both are the same and both have the same damage tolerance (fig. 7.31). It was previously stated (see chapter 5) that SMC as a layer of SMC+stainless steel laminates absorbs more energy than SMC of the same thickness when impacted on its own. It was also mentioned that the higher the energy absorption the higher the amount of damage in the specimen. A question arises here as to how SMC as a layer of SMC+stainless steel laminate absorbs more energy while its strength is reduced to a similar degree to the SMC on its own. This contradiction may be explained by the nature of damage in SMC+stainless laminate (fig. 5.39) showed that damage in SMC is more localised and is well under the area of impact and this sort of damage might act as a source for high stress concentration and subsequently reduces the strength almost the same as larger area of damage in SMC'.

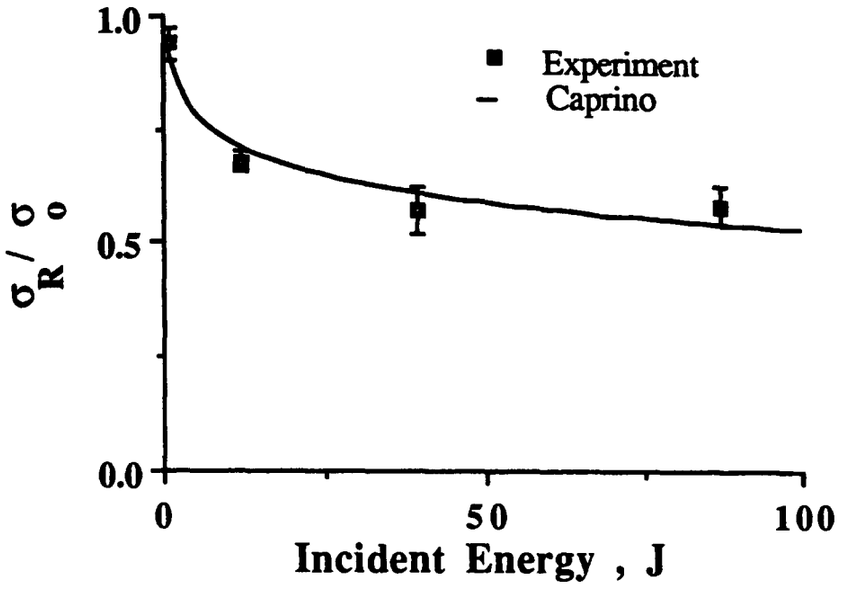

Figure 7.32 - Comparison of predicted and experimental residual compressive strength for 4 mm SMC.

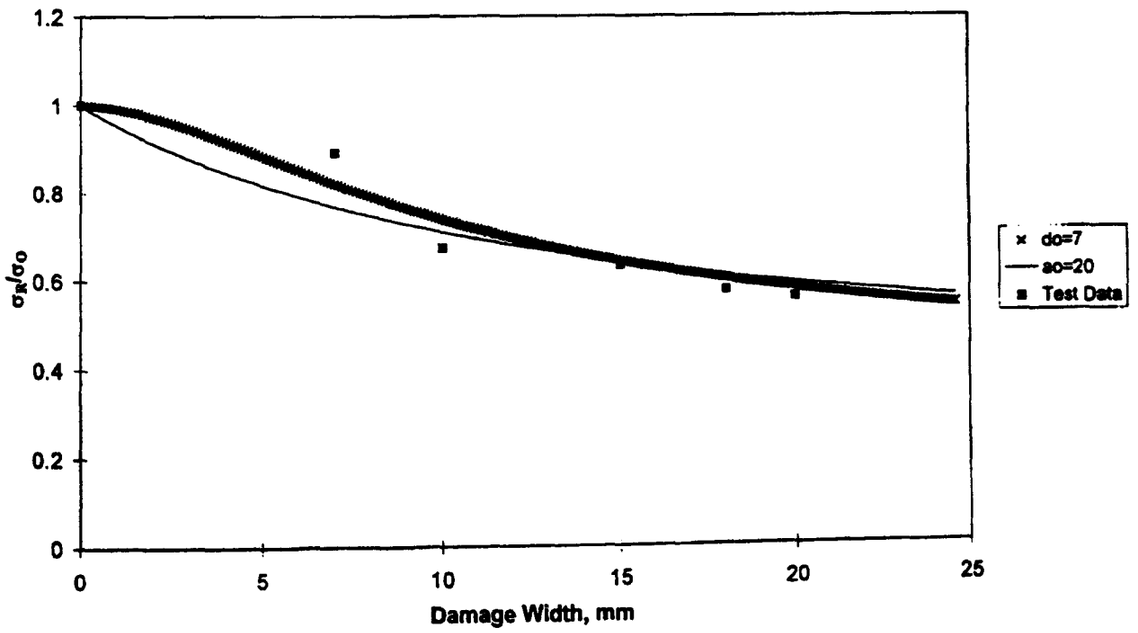

Figure 7.33 - Comparison of predicted and experimental residual compressive strength for 4 mm SMC.

7 - 6 Conclusions

1 - Both tensile and compressive strength of SMC is decreased by impact.

2 - After complete penetration of SMC the strength is not reduced any further with increasing the incident energy.

3 - The effect of drilled hole with same diameter as the impacter on the strength is the same as a hole produced by the impacter.

4 - Simple model may be employed to predict the residual strength of the impacted SMC.

Chapter 8

Summary of the results, conclusions and future work

8 - 1 Summary of results

Experimental results showed that the energy absorbed by SMC specimens is a function of the incident energy. Each thickness of SMC exhibited a linear relationship between these energy terms up until reaching a plateau corresponding to total penetration of the specimen by the impactor. The magnitude of this plateau increased with, and was proportional to, specimen thickness. The initial peak on the force-time curve exhibited by the SMC specimens is the onset of cracking, which occurs initially at the tensile loading surface. The specimens which were loaded below the initial peak showed no sign of damage. Initial peak did not change with increasing incident energy and had a linear relationship with the square of thickness. Peak force was a function of the incident energy. For each thickness of SMC, the peak force increased linearly with increasing the incident energy until reaching a plateau corresponding to the total penetration of the specimen by the impactor. The magnitude of this plateau increased with specimen thickness and has a linear relationship with the square of thickness.

The initial peak in SMC-steel specimens was a plastic deformation in the steel layer. The SMC layer in the SMC-stainless steel laminate absorbed considerably more energy than SMC of a similar thickness can when tested in isolation. Where the stiffness of the steel layer greatly exceeds that of SMC in the SMC-stainless steel laminate (SMC'), the energy absorbing capability of the SMC' is a function of its thickness irrespective of the thickness of the steel. Where the relative thickness of the two constituents are such that the stiffness of the SMC' approaches that of the steel, then the energy absorbing capabilities decrease.

The results of SMC with two grades of aluminium showed no improvement in the amount of energy absorbed by SMC, but for the case of SMC-Ionomer, SMC-copper and SMC-brass did.

Results of residual strength showed that both tensile and compressive strength decreased by impact damage. The level of reduction depends on the incident energy. After a certain level of incident energy, there was no further decrease in strength of the material.

8 - 2 Conclusions

Taken together the results from the various parts of the programme have enabled a general model to be formulated governing the selection of materials to form an energy absorbing macrocomposite laminate involving fibre reinforced composite layers such as SMC.

Potentially SMC can absorb a considerable quantity of energy by progressive microcracking. This requires the material to be uniformly stressed over a large area and that no section of the stressed composite becomes unstable which would allow a major crack to propagate and cause complete fracture.

Under normal impact loading the SMC rapidly develops a major crack near the tensile loading face resulting in collapse of the structure, penetrating of the impactor and only modest energy absorption.

The purpose of a dissimilar layer in a macrocomposite is firstly to support the SMC in such a way that tensile cracks do not form and become unstable which would result in fracture before significant microcracking can occur. This is readily achieved by using a stiff metallic layer of sufficient thickness such that the whole of the SMC layer is kept in compression until failure of the metallic layer itself. This is achieved by laminating SMC with both stainless steel and aluminium but the results indicate that, as aluminium is not effective in the macrocomposite, another property is important. The second requirement is that the SMC layer is supported over a extensive deformation range such that microcracking may occur over a large area. The steel layers deform over an extended

deflection range forcing the deforming SMC to adopt a similar gently curved profile that does not concentrate stress at one position. The net result being that a significant density of microcracking is generated in the SMC over a volume dictated solely by the support ring of the impact equipment. Results with ionomer indicate that the ability to deform extensively is useful in its own right and can lead to improved energy absorption in the SMC by providing some support over a deformation range that exceeds that available in the material loaded in isolation. However as the ionomer is not stiff enough to put the SMC into compression, tensile cracks can still form and the potential macrocomposite effect is not fully realised. A similar effect was observed with the thinnest steel layer in combination with the thick SMC. The final confirmation of these ideas comes from results obtained from macrocomposites tested with the SMC as the tensile, non-impacted, face of the macrocomposite. In all of these cases the energy absorbed by the system was simply the sum of the maximum energy absorption of the individual constituents when tested in isolation.

8 - 3 Future work

Continued interest in sheet moulding compounds (SMC), in automobile industry and other industries requires further research. One significant shortcoming of SMC is its low stiffness relative to carbon fibre composites and steel. The low density of SMC results in modest mass savings over steel, but may require the part to be made of relatively thick gauge. Consequently, the part will need longer cure time and this will result in higher manufacturing cost. For the SMC-composite to be more competitive and have broader application, it is essential that the stiffness properties of SMC be improved. In order to make optimum use of SMC materials, the mechanical behaviour of these materials under various loading conditions, particularly impact must be well understood. Since the fracture energy in impact test depends on the specimen geometry, support and indenter size and type of blows, therefore future work could be directed in these areas. For example the use of striker tip with different size and shape than the one used in this work (hemisphere of 20 mm diameter) will provide more information about the impact response of the macrocomposite. Different sizes of support and angle of impact are also needed to be investigated.

Another factor which severely affects the energy absorption capability of SMC and SMC+stainless steel specimens is sub zero temperatures. Most metallic materials behave in a very brittle manner at sub zero temperatures which might reduce the energy absorption of SMC+stainless steel specimens dramatically during impact.

Results of impact on SMC in chapter 4 showed that the energy which is required to initiate damage is very low. Subsequent results of post impact tension and compression showed that the damage associated with these low level energies do not affect the residual strength of the specimens. Research needs to be done to look at the effect of cyclic loads on these tiny impact damage. Although they do not affect the residual strength of the material under static load, but they might grow to a critical size when they are subjected to fatigue loading.

Finally, another direction for research on impact behaviour of SMC with a layer metallic or non-metallic material is to generate more data, that enable the investigator to provide a model that can select the right material as part of SMC macrocomposite. The current work has provided a useful and informative guide to the relative performance of different material systems, but which do not at this time provide a simple model for the design purposes.

References

1 - Norwood L. S., Taylor B. R. and Truman C. M., Toward a more general composite concept, 39th Annual conference, reinforced plastics, composite institute, The Society of the Plastic Industry, January 16-19, 1984.

2 - Gruenewald Rainer and Walter Oskar, Fifteen Years Experience with Sheet Moulding Compound, 30th Anniversary Technical Conference, 1975, Reinforced Plastics / Composite Institute, The Society of the Plastic Industry.

3 - Crystic Polyester Handbook, Scott Bader Company Limited, Wollaston, Wellingborough, Northamptonshire NN9 7RL, England.

4 - Seamark M. J., Face-lifting the World's First all SMC Clad Truck Cab after 5 years production - A Unique Study. SPI RP/C 36th Annual Conference, Section 11-C, 1981.

5 - SPI Composite Institute's, 47th Annual Conference, February 3-6 1992

6 - SPI Composite Institute's, 49th Annual Conference & EXPO,94, February 7-9 1994

7 - SPI Composite Institute's, 50th Annual Conference & EXPO,95, January 30-February 7-9 1994

8 - Denton, D. L., The mechanical properties of an SMC-R50 composite, Owens - Corning Fiberglas corporation (1979).

9 - Owen, M. J., Tobias A. M. and Rees, H. D., Design limits for polyester SMC's, International conference on fibre reinforced composites, University of Liverpool 1984.

10 - Chaturvedi, S. K., Sun C. T. and Sierakowaski R. L., Mechanical Characterisation of Sheet Moulding Compound Composites, Polymer composites, July, 1983, vol. 4, No. 3.

11 - Johnson A. E., Application of the instrumented falling weight technique to repeated low energy impacts upon SMC, Pilkinton Glass fibres new technology group, internal report 1982.

12 - Raghunath P. Khetan and David C. Chang, Surface damage of Sheet Moulding Compound Panels Subject to a Point Impact Loading, J. Composite Materials, vol. 17, pp. 182-194 (1983).

13 - Raghunath P. Khetan and David C. Chang, Surface Damage Of Steel, Aluminium and chopped-Fibre Composite Panels Due To Projectile Impact. Journal of Reinforced plastics and Composites, volume 3, July 1984.

14 - Myers F. A., Impact Response Of SMC / BMC Composites, 37th Annual Conference, Reinforced Plastics/ Composites Institute, The Society of the Plastics Industry, Inc. January 11-15, 1982.

15 - ASTM D256 (1978), Impact Resistance of Plastics and Electrical Insulating Materials.

16 - BS 2782 (1970), Method 306A Impact Strength (Pendulum Method); Method 306B and C Impact Strength (Falling Weight Method with Sheet Specimens).

17 - ASTM D1822 (1979), Tensile Impact Energy to break Plastic Materials.

18 - BS 4618: section 1.2 : 1972, British Standard Institution, London.

19 - Dieter G. E., Mechanical Metallurgy, McGraw-Hill series in materials science and engineering.

20 - Johnson A. F., Engineering design properties of GRP, The British Plastic Federation.

21 - ISO 6603/1 (1985), Plastics - Determination of Multiaxial Behaviour of Rigid Plastics: Part 1, Falling Dart Method.

22- Wyrick D. A. and Adams D. F., "Residual Strength of Carbon/Epoxy" Journal of Composite Materials, Vol. 22, 1988, pp 749-765.

23 - Reed P. E., Impact performance of polymers, From ` Developments in polymer fracture-1 ' Edited by E. H. Andrews, Applied science publishers, London.

24 - Driscoll S. B., ` Variable-Rate Impact of polymeric Materials-A Review ', Instrumented Impact of Plastics and Composite Materials, ASTM STP 936, pp 163-186.

25 - Johnson W., "Impact Strength of Materials", Edward Arnold, London 1972.

26 - Broutman L. J. and Rotem A., Impact strength and toughness of fibre composite material, ASTM STP 568, American Society for Testing and Materials, 1975, pp. 114-133.

27 - Reed P. E. Developments in Instrumented Impact Testing of Plastics and Composites, Progress In Rubber and Plastics Technology, Edited by J. M. Buist, Volume 5, No. 2, 1989.

28 - Hoover W. R., ` Effect of Test System Response Time on Instrumented Charpy Impact Data ', Instrumented Impact Testing, ASTM STP 563, American Society for Testing and Materials, 1974, pp. 203-214.

29 - Ireland D. R., Procedures and problems associated with reliable control of the instrumented impact test, ASTM STP 563, American Society for Testing and Materials, 1974, pp. 3-29.

30 - Ewing A. and Raymond L., Instrumented impact testing of titanium alloys, ASTM STP 563, American Society for Testing and Materials, 1974, pp. 180-202.

31 - Server W. L. and Ireland D. R., Nonstandard test techniques utilising the instrumented Charpy and Izod tests, ASTM STP 563, American Society for testing and Materials, 1974, pp. 74-91.

32 - Venzi S., Priest A. H. and May M. J., ASTM STP 466, American Society for Testing and Materials, 1970, p. 165.

33 - Turner C. E. in Impact Testing of Metals, ASTM STP 466, American Society for Testing and Materials, 1970, p. 93.

34 - Lueth R. C., An analysis of Charpy impact testing as applied to cemented carbide, ASTM STP 563, American Society for Testing and materials, 1974, pp. 166-179.

35 - Cheresh M. C. and McMichael S., Instrumented impact test data interperation, Instrumented Impact Testing of Plastics and Composite Materials, ASTM STP 936, American Society for testing and materials, 1987, pp. 9-23.

36 - Saxton H. J., Ireland D. R. and Sever W. L., Analysis and control of inertial effects during instrumented impact testing, ASTM STP 563, American Society for Testing and Materials, 1974, pp. 50-73.

37 - Kamal M. R., Samak Q., Provan J. and Ahmad Vagar, Evaluation of a Variable-Speed Impact Tester for Analysis of Impact Behaviour of Plastics and Composites, Instrumented Impact Testing of Plastics and Composite Materials,, ASTM STP 936, American Society for testing and materials, 1987, pp. 58-80.

38 - Knakal C. W. and Ireland D. R., Instrumented dart impact evaluation of some automotive plastics and composites, Instrumented Impact Testing of Plastics and Composite Materials, ASTM STP 936, American Society for Testing and Materials, pp. 44-57.

39 - Toland R. H., Impact testing of carbon-epoxy composite materials, STP 563, American Society for testing and materials, 1974, pp. 133-145.

40 - Jemian W. A., Jang B. Z. and Chou J. S., Testing Simulation and Interpretation of Materials Impact Characteristics, Instrumented Impact Testing of Plastics and Composite Materials, ASTM STP 936, American Society for testing and materials, 1987, pp. 117-143.

41 - Cantwell, W. J., Impact Damage in Carbon Fibre Composites, PhD thesis, University of London, UK, 1985.

42 - Cantwell, W. J. and Morton J., The Impact Resistance of Composite Materials - a Review, Composites, Volume 22, Number 5, September 1991.

43 - Adams D. F. and Miller A. K., An Analysis of the Impact Behaviour of Hybrid Composite Materials, Materials Science and Engineering, Volume 19, 1975, pp 245-260

44 - Hancox N. L., Izod Impact Testing of Carbon Fibre Reinforced Plastics, Composites, Volume 2, 1971, pp 41-45.

45 - Bader M. G. and Ellis R. M., The Effect of Notches and Specimen Geometry on the Pendulum Impact Strength of Uniaxial CFRP, Composites, Volume 5, 1974, pp 253-258.

46 - Davies P., Cantwell, W. J., Richard H., Moulin C. and Kausch H. H., Interlaminar fracture testing of carbon fibre/PEEK composites validity and applications, in Developments in the Science and Technology of Composite Materials, Proceeding ECCM3, Bordeaux, 1989 edited by Bunsell A. R., Lamicq P. and Massiaah A., (Elsevier Applied Science Publication) pp 747-755.

47 - Curson A. D., Leach D. C. and Moore D. R., Impact Failure Mechanism in Carbon fibre/PEEK Composites, Journal of Thermoplastic Composite Materials, Volume 3, 1990, pp 24-31.

48 - Greszczuk L. B., Response of isotropic and composite materials to particle impact, ASTM STP 568, American Society for Testing and Materials, 1975, pp. 183-211.

49 - Rogers K. F., Sidey G. R. and Kinston-LEE D. M., Ballistic Impact Resistance of Carbon-fibre Laminates, Composites, Volume 2, 1971, pp 237-241.

50 - Hirschbuehler K. R., A Comparison of Several Mechanical Tests Used to Evaluate the Toughness of Composites, Toughened Composites, ASTM STP 937 edited by Johnson M., American Society for Testing and Materials, 1987, pp. 61-73.

51 - Evan R. E. and Master J. E., A New Generation of Epoxy Composites for Primary Structural Application: Material and Mechanics, Toughened Composites, ASTM STP 937 edited by Johnson M., American Society for Testing and Materials, 1987, pp. 413-436.

52 - Williams J. G. and Rhodes M. D., Effects of Resin on Impact Damage Tolerance of Graphite/Epoxy Laminates, Composite Materials: Testing and Design, ASTM STP 787, American Society for Testing and Materials, 1982, pp. 450-480.

53 - Kam C. Y. and Walker J. V., Toughened Composites Selection Criteria, Toughened Composites, ASTM STP 937 edited by Johnston M., American Society for Testing and Materials, 1987, pp. 9-22.

54 - Hunston D. L., Composite Interlaminar Fracture: effect of matrix fracture energy, Composite Technical Review, volume 6, 1984, pp 176-180.

55 - Leach D. C. and Moore R.D.,Toughness of Aromatic Polymer Composites Reinforced with Carbon Fibres, Composite Science and Technology, Volume 25, 1985, pp 131-161.

56 - Davies P., Cantwell, W. J., and Kausch H. H., Measurement of Initiation Values of G_{IC} in IM6/PEEK Composites, Composite Science and Technology, Volume 35, 1989, pp 301-313.

57 - Dan-Jumbo E., Leewood A. R. and Sun C. T., Impact Damage Characteristics of Bismaleimides and Thermoplastic Composite Laminates, in Composite Materials: Fatigue and Fracture, 2nd Volume, ASTM STP 1012 edited by Lagace P. A., American Society for Testing and Materials, 1989, pp. 356-372.

58 - Bishop S. M., The Mechanical Performance and Impact Behaviour of Carbon Fibre Reinforced PEEK, Composite Structures 3, 1985, pp 295-318.

59 - Morton J. and Godwin E. W., Impact Response of Tough Carbon Fibre Composites, Composite Structure 13, 1989, pp 1-19.

60 - Dorey G., Bishop S. M. and Curtis P. T., On the Impact Performance of Carbon Fibre Laminates with Epoxy and Peek Matrices, Composites Science and Technology, 23, 1985, pp 221-237.

61 - Cantwell W. J., Davies P., Jar P. Y., Bourban P. E. and Kausch H. H., Joining and Repair of Carbon fibre PEEK-Composites, in Plastics-Metals-Ceramics edited by H. L. Hornfield, SAMPE 1990, pp 411-426.

62 - Lehmann S., Megerdigian C. and Papalia R., Carbon fibre/resin matrix Interphase: Effect of Fibre Surface Treatment on Composite Performance, SAMPE Quarterly 16, No 3 1985, pp 7-13.

63 - Harris B., Beaumont P. W. R., Moncuill de Ferran E., Strength and Fracture Toughness of Carbon Fibre Polyester Composites, Journal of Materials Science 6 1971, pp 238-251.

64 - Yeung P. and Broutman L. J., The Effect of Glass-Resin Interface Strength on The Impact Strength of Fibre Reinforced Plastics, Polymer Engineering Science, 18(2), 1978, pp 62-72.

65 - Kelly A., Interface Effects and the Work of Fracture of a Fibrous Composite, Proceeding of the Royal Society, Series A. Vol. 319, 1970.

66 - Hong, S. and Liu, D., On the Relationship between Impact Energy and Delamination area, Experimental Mechanics 13, 1989, pp 115-120.

67 - Hyung Yun Choi, Hong Sheng Wang and Fu-Kuo Chang, Effect of Laminate Configuration and Impactor's Mass on the Initial Impact Damage of Graphite/Epoxy Composite Plates Due to Line-Loading Impact, Journal of Composite Materials, Vol. 26, No. 6, 1992, pp 804-727.

68 - Cantwell, W. J. and Morton, J., Geometrical Effects in the Low Velocity Impact Response of CFRP, Composite Structure 12, 1989, pp 35-59 Composite Structure 13, 1989, pp 1-19.

69 - Dost, E. F., Ilcewicz, L. B., Avery, W. B. and Coxon, B. R., Effects of Stacking Sequence on Impact Damage Resistance and Residual Strength for Quasi-Isotropic Laminates, in Composite Materials: Fatigue and Fracture, Third Volume, ASTM STP 1110 edited by O,Brien, K., American Society for Testing and Materials, 1991, pp. 476-500.

70 - Cantwell, W. J., The Influence of Target Geometry on the High Velocity Impact Response of CFRP, Composite Structure 10, 1988, pp 247-265.

71 - Preston J. L. and Cook T. S., Impact response of graphite-epoxy flat laminates using projectiles that simulate aircraft engine encounters, ASTM STP 568, American Society for Testing and Materials, 1975, pp. 49-71.

72 -Cessna L. C., Lehane J. P., Ralstone R. H. and Prindle T., The Development of an Instrumented Projectile Impact Test: Data on Glass-Reinforced and Impact-Modified Polypropylene, Polymer Engineering and Science, June 1976, Vol. 16, No. 6, pp 419-425.

73 - Zukas Joanes A., Nicholas Theodore, Swift Hallock F., Greszczuk Longin B. and Curran Donald R.; Impact Dynamics, A Wiley - Interscience Publication, John Wiley & Sons, 1982, pp. 155-214.

74 - Zukas Joanes A., Nicholas Theodore, Swift Hallock F., Greszczuk Longin B. and Curran Donald R.; Impact Dynamics, A Wiley - Interscience Publication, John Wiley & Sons, 1982, pp. 367-417.

75 - Goldsmith W., Impact, The theory and Physical Behaviour of Colliding Solids, Edward Arnold (Publishers) Ltd., London.

76 - Timoshenko S. and Goodier J. N., Theory of elasticity, McGraw Hill, New York, 1982.

77 - Yang S. H. and Sun C. T., Indentation Law for Composite Laminates, Composite Materials: Testing and Design (Sixth Conference), ASTM STP 787, edited by Daniel I. M., American Society for Testing and Materials, 1982, pp. 425-449.

78 - Kubo J. T. and Nelson R. B., Analysis of impact stresses in composite plates, ASTM 568, 1975, pp. 228-244.

79 - Roark R. J., Roark's Formulas for stress and strain, McGraw Hill Book Company, New York, 1989.

80 - Dhatt Gouri and Touzot Gilbert, The finite element method displayed, John Wiley and Sons, 1984.

81 - 37 - Zienkiewicz O. C., The finite element method in engineering and Science, McGraw Hill, London, 1971.

82 - Girshovich S., Gottesman T., Rosenthal H. at al., Impact Damage Assessment of Composites, in Damage Detection in Composite Materials, ASTM STP 1128, edited by Msters Ed., American Society for Testing and Materials, 1992, pp. 183-199.

83 - Hogg P. J. and Kay M. L., The Effect of Environment on the Damage Tolerance of Glass and Carbon Fibre Reinforced Epoxy Laminates, Deformation and Fracture of Composites, Manchester, UK, 1997, Institute of Materials.

84 - Cantwell W. J. and Morton J., Detection of Impact Damage in CFRP laminates, Composite Structures, 3, 1985, pp 241-257.

85 - Prichard J. C., PhD Thesis 1991, Queen Mary and Westfield College, London.

86 - Non-Destructive Testing of Composite Materials, A 3 day Course, 27th February-1st March 1989, Centre for Composite Materials, Imperial College, London.

87 - Non-destructive Evaluation and Flaw Criticality for Composite Materials, edited by Pipes R. B., ASTM 696, American Society for Testing and Materials, 1978.

88 - Stone D. E. W. and Clark B., Proceeding of the ICCM6 / ECCM2, Non-Destructive Evaluation of Composite Structures - an Overview, (Edited by Matthews F. L., Buskell N. R. C., Hodgkinson J. M. and Morton J.), (Elsevier Applied Science, Oxford), 1987, pp. 1.28-1.59.

89 - Liber T., Daniel I. M. and Schramm S. W., Ultrasonic Tecniques for Inspecting Flat and Cylindrical Composite Specimens, in Nondestructive Evaluation and Flaw Criticality

for Composite Materials, edited by Pipes R. B., ASTM 696, American Society for Testing and Materials, 1978.

90 - Sendeeckyj G. P., Maddux G. E. and Tracy N. A., Comparison of Holographic and Ultrasonic Techniques for Damage Detection in Composite Materials, Proceeding of the ICCM2, (Edited by Noton B., Signorelli R., Street K. and Phillips L.), 1978, (The Metallurgical Society), pp 1037-1056.

91 - Scott W. R., in Nondestructive Evaluation and Flaw Criticality for Composite Materials, edited by Pipes R. B., ASTM 696, American Society for Testing and Materials, 1978, pp 96-98.

92 - Chang F. H., Couchman J. C., Eisenmann J. R. and Yee B. G. W., Application of a Special X-Ray Non-destructive Testing Technique for Monitoring Damage Zone Growth in Composite Materials, In Composite Reliability, ASTM STP 580, American Society for Testing and Materials, pp 176-190.

93 - Domanus J. C. and Lilholt H., Non-destructive Control of Carbon Fibre Reinforced Composites by Soft X-Ray Radiography, In Proceeding of the 1978 International Conference on Composite Materials, ICCM/2, The American Institute of Mining, Metallurgical and Petroleum Engineers (Torento, Canada), pp 1072-1092.

94 - Clark B., In Non-Destructive Testing of Composite Materials, A 3 day Course, 27th February-1st March 1989, Centre for Composite Materials, Imperial College, London, PP 68.

95 - Edwards J. H., The Use of Acoustic Emission to Detect the Onset of Interlaminar Shear Failure in Short Beam Fatigue Specimens, ASTM STP 972, American Society for Testing and Materials, 1988, pp. 369-379.

96 - Lorenzo L. and Hahn H. T., Damage Assessment by Acousto - Ultrasonic Technique in Composites, ASTM STP 972, American Society for Testing and Materials, 1988, pp. 380-397.

97 - Brown R. P., Handbook of Plastic Test Methods, Published by George Godwin Limited, London.

98 - Kay M. L., PhD Thesis 1995, Queen Mary and Westfield College, London.

99 - Gao S. L. and Kim J. K., Three-Dimensional Characterisation of Impact Damage in CFRPs, Key Engineering Materials Vols. 141-143 (1998) pp. 35-54.

100 - Bibo G. A., PhD Thesis 1997, Queen Mary and Westfield College, London.

101 - Stone D. E. W. and Clark B., Ultrasonic Attenuation as a Measure of Void Content in Carbon-fibre Reinforced Plastics, Nondestructive Testing, 1975, vol. 8, pp. 137-145.

102 - Gibbins, M. N. and Stinchcomb W. W., Fatigue Response of Composite Laminates with Internal Flaws, Composite Materials: Testing and Design (Sixth Conference), ASTM STP 787, edited by Daniel I. M., American Society for Testing and Materials, 1982, pp. 305-322.

103 - Nevadunsky, J. L. Lukas and Salkind M. J., Early Fatigue Damage Detection in Composite Materials, Journal of Composite Materials, 1975, vol. 9, pp. 394-408.

104 - Duke Jr. J. C., Nondestructive Characterisation of Chopped Glass Fibre Reinforced Composite Materials, Short Fibre Reinforced Composite Materials, ASTM

STP 772, edited by Sandes B. A., American Society for Testing and Materials, 1982, pp. 97-112.

105 - Husman G. E., Whitney J. M., and Halpin J. C., Residual Strength Characterisation of Laminated Composites Subjected to Impact Loading, ASTM STP 568, American Society for Testing and Materials, 1975, pp. 92-113.

106 - Dorey G., Impact and Crashworthiness of Composite Structures, In Structural Impact and Crashworthiness, Volume 1, Ed: G.A.O. Davies, Elsevier Applied Science Publisher, London, 1984.

107 - Sjobolm P. O. and Hwang B., Compression After Impact: $5000 data point, 34th International SAMPE Symposium, Reno, May 8-11, 19889, pp. 1411-1421.

108 - Anon, NASA Aircraft Industry Standard Specification for Graphite Fibre Toughened Resin Composite Material. NASA-RP-1142, 1985.

109 - Hogg P. J., Prichard J. C. and Stone D. L., A Miniaturised Post Impact Compression Test, ECCM-CTS, 1992, Ed's P. J. Hogg, G. D. Sims, F. L., Matthews, A. R. Bunsell and A. Massiah, pp. 357-370.

110 - Hogg P. J., Bibo G. A. and Tanaka K., A Comparison of full-scale and Miniaturised compression after Impact tests, Proceeding of the 4th Japan International SAMPE Symposium and Exhibition, Tokyo, 1995, ED's Z. Maekawa, E. Nakata and Y. Sakatani, Volume 2, pp. 907-914.

111 - Daniel I. M., Methods for Testing Composite Materials, In Handbook of Composites, Volume 3, Failure Mechanics of Composites, Editors: G.C. Sih and A. M. Skudra, Elsevier Science Publishers.

112 - Matondang T. H., and Schutz D., The Influence of Anti-buckling Guides on the Compression - Fatigue Behaviour of Carbon - Fibre Reinforced Plastic Laminates, Composites 15, 1984, pp. 217-221.

113 - Dorey G., Sigety P., Stellbrink K. and Hart W. G. J., Impact Damage Tolerance of a Carbon Fibre Composite Laminate, Royal Aircraft Establishment, Technical Report 84049, May 1984.

114 - Waddoups M. E., Eisenmann J. R. and Kaminski B. E., Macroscopic Fracture Mechanism of Advanced Composite Materials, Journal of Composite Materials, 5, 1981, pp. 446-454.

115 - Caprino G., Residual Strength Prediction of Impacted CFRP Laminates, Journal of Composite Materials, Vol. 18, November 1984, pp. 508-518.

116 - Caprino G., On the Prediction of Residual Strength for Notched Laminates, Journal of Material Science, Vol. 18, 1983, pp. 2269-2273.

117 - Weatherhead R. G., FRP Technology, Applied Science Publisher Ltd., 1980.

118 - Burns R., Hankin A. G. and Pennington D., Variability In Sheet Moulding Compound (SMC): Part II Processing and Moulding Variability, Plastics and Polymers, 1975, pp. 235-240.

119 - Riegner D. A. and Sanders B. A., Fibre Reinforced Plastics Test Specification, General Motors Technical Centre, Warren, Michigan 48090, Report No. MD 079-006.

120 - ASTM D638, Tensile Properties of Plastics, Section 8, Vol. 08.01, 1987, pp 155-166.

121 - Silverma E. M., Materials Properties of Chopped Glass Fibre/Polymer Sheet Moulding Compound., 37th Annual Conference, Reinforced Plastics/Composites Institute, SPI, Session 1 - D.

122 - ASTM D790, Flexural Properties of Unreinforced and Reinforced Plastics and Electrical Insulation Materials, Section 8, Vol. 08.01, 1986, pp 280-298.

123 - ASTM D3410, Compressive Properties of Unidirectional or Crossply Fibre-Resin Composites, Volume. 15.03, 1989, pp 131-138.

124 - ASTM D4255, Standard Guide for Testing In-Plane Shear Properties of Composites Laminates, Section 15, Vol. 15.03, 1983, pp 195-204.

125 - ASTM D2344, Apparent Interlaminar Shear Strength of Parallel Fibre Composites by Short Beam Method, Section 15, Vol. 15.03, 1984, pp 43-45.

126 - Lee K., Unpublished information, Queen Mary and Westfield College, London.

127 - Greszczuk L. B., Damage In Composite Materials Due to Low Velocity Impact, Impact Dynamics, A Wiley - Interscience Publication, John Wiley & Sons, 1982, pp. 55-94.

128 - Love A. E. H., The Stresses Produced in a Semi-Infinite Solid by Pressure on Part of a Boundary, Philosophical Transactions, Proceeding of the Royal Society, London, A228, 1929.

129 - Trubshaw R. N. and Birch G. L., Developing Instrumented Impact Testing of Composites, An International Conference on Impact Testing and Performance of Polymeric Materials, 2-3 September 1985, University of Surrey, Guildford, England.

130 - Detorres P. D., Instrumented Impact Interpretation and Application, An International Conference on Impact Testing and Performance of Polymeric Materials, 2-3 September 1985, University of Surrey, Guildford, England.

131 - Johnson A. E. and Lynskey B. M., Variation With Temperature of The Impact Behaviour of SMC, Glass Fibre New Technology Department, Pilkington Brothers PLC.

132 - Barbic L., Dunn C. and Hogg P. J., Damage Development and its Significance in GRP Subjected to Impact, Plastics and Rubber Processing and Applications, 12, 1989, pp 199-207.

133 - Dashin Liu, Impact-Induced Delamination, A View of Bending Stiffness Mismatching, Journal of Composite Material, Vol. 22, July 1988, pp 674-692.

134 - Bishop S. M., The significance of Defects on the Failure of Fibre Composites, Presented to the AGARD SMP subcommitte on Defects.

135 - Whitney J. M. and Nuismer R. J., Stress Fracture Criteria for Laminated Composites Containing Stress Concentrations, Journal of Composite Materials, Vol. 8, July 1974, pp 253-265.

136 - Prichard J. C. and Hogg P. J., The Role of Impact Damage in Post-Impact Compression Testing, Composites, 21, 1990, pp 503-511.